

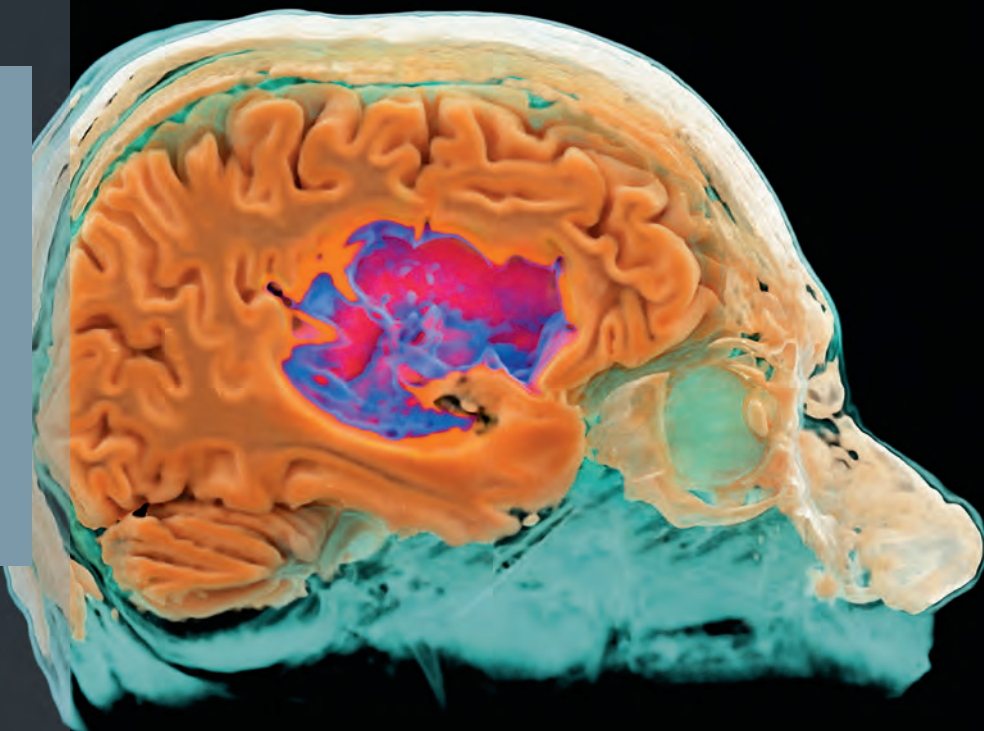
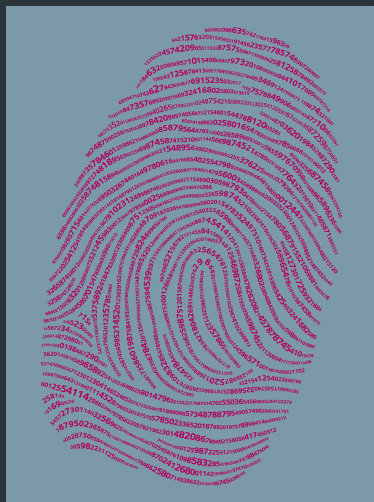
MAGNETOM Flash

The Magazine of MRI

Issue Number 2/2016 | ISMRM Edition

Not for distribution in the US

Overview of MR-Fingerprinting
Vikas Gulani et al.
Page 12



Editorial Comment
The Rapid Imaging Renaissance
Daniel K. Sodickson
Page 02

New Strategies
for Protocol Optimization
Otto Rapalino
Page 22

65



Daniel K. Sodickson, Ph.D., M.D., is Professor and Vice Chair for Research in the Department of Radiology at New York University School of Medicine. He directs the Bernard and Irene Schwartz Center for Biomedical Imaging and serves as principal investigator of the Center for Advanced Imaging Innovation and Research (CAI²R), a new Biomedical Technology Resource Center supported by the National Institute of Biomedical Imaging and Bioengineering in the US. Dr. Sodickson was privileged to participate in the early development and clinical translation of parallel MRI, and his current research centers around the development of rapid comprehensive imaging approaches to provide diverse information for the improvement of human health. He is grateful to numerous colleagues around the world who are making possible the current rapid imaging renaissance.

The Rapid Imaging Renaissance

“There is in this Earth no maneuver more unnerving than the Spin. Just when one thinks to have advanced into the twilight, Dawn comes round again.”

Samuel Bowditch

In imaging, we are all spies. Like true intelligence agents or their glamorized counterparts onscreen, imaging scientists and practitioners are charged with gathering critical information in space and time. We employ the latest technology to acquire encoded signals, and deploy laboriously optimized algorithms to decode them. We do what is necessary, piercing the veil of the skin, the skull, the cell, or whatever stands in our way, in order to see what was once invisible.

The MAGNETOM Flash Magazine represents a chronicle of this evolving intelligence work in the worldwide Siemens MR community. And one theme which emerges clearly from such a chronicle is the theme of advancing imaging speed.

Like floors at a construction site, or else like accreted archaeological layers, today's rapid imaging

techniques build upon yesterday's techniques, compressed sensing combining with parallel imaging joining forces with rapid gradient switching to yield ever higher accelerations. Recently, however, something new and unexpected has begun to emerge from this gradual accumulation. There is something more fundamental and more revolutionary afoot than mere acceleration.

This 'something' is reflected in quite a few of the articles in the current issue of MAGNETOM Flash. Relevant themes include

- streamlined workflow (see Rapalino et al. on clinical protocol optimization with GOBrain, Reiner et al. on the Whole-Body Dot Engine for combined chest, abdomen, and pelvis exams; Egelhof et al. on workflow improvements with Fit-Upgrades, and Schraa on Auto-Coverage in several Dot engines)
- fast, motion-insensitive imaging (such as FREEZEit in pediatric lung MRI* by Kinner et al.; parotid tumor imaging with GRASP by Patel et al.; or cardiac DTI by Ennis et al.)
- efficient multiparametric imaging, whether for diagnostics or for guidance of therapeutic interventions

(see Gulani et al. on MR Fingerprinting; Bickelhaupt et al. on fast and non-invasive characterization of suspicious breast lesions; and Pham et al., on the prediction of treatment response in rectal cancer.)

The thread of rapid, efficient imaging with rich and diverse information content may of course be traced not only through this MAGNETOM Flash issue, but also through numerous past issues, and indeed across much of the history of magnetic resonance. That said, we occupy a time of unique challenge and unique opportunity for MR. In the clinical arena to be sure, we are being subjected to unprecedented levels of pressure for efficient delivery of value. We are also, I would argue, witnessing a unique convergence of disruptive innovations that have the potential to reframe radically the value proposition in our field.

Before I release you to enjoy the contents of this issue, then, let me attempt to touch briefly on some of the dimensions of what I see as a rapid imaging renaissance [1].

*MR scanning has not been established as safe for imaging fetuses and infants less than two years of age. The responsible physician must evaluate the benefits of the MR examination compared to those of other imaging procedures.

A brief history of rapid imaging

One might argue that there is a natural evolutionary tendency for imaging modalities to get faster over time. This tendency is certainly driven by the inherent inventiveness of those who use imaging devices. It is also driven by a particular selection pressure – namely, the need for speed. In the context of biomedical imaging, this need is obvious and multifold. First of all, patients and organs move, and fast images are required to image moving structures such as the beating heart. Injected contrast agents used to highlight particular internal structures also move, and catching the contrast on its way through the vascular system requires speed. Second, patients get restless. Due to underlying disease or understandable agitation, subjects often cannot sustain long breath-holds, and long total examination times can be challenging. Third, time is money. Scanner throughput, and workflow in general, becomes an important practical consideration in an era like ours of intense cost-consciousness, in which the premium on efficiency is high. Finally, and perhaps most importantly, time is information. Greater imaging efficiency enables the acquisition of more information per unit time, which enhances the value of imaging studies, both for clinical evaluation and for basic research.

Figure 1 summarizes the evolution of imaging speed for MRI in particular, since its inception in the 1970s. Various hardware developments, such as strong and fast-switching magnetic field gradients, enabled progressively more rapid transitions between sequentially acquired data points. Meanwhile, changes to the acquisition sequence – including rapid MR pulse sequences incorporating rectangular raster patterns (Echo Planar Imaging) or spiral trajectories – further accelerated sequential scanning. It was not until the 1990s that arrays of RF detector coils were employed in practice to gather multiple data points simultaneously, rather than in the traditional sequential fashion. This use of parallelism, which harks back, of course, to the massively parallel con-

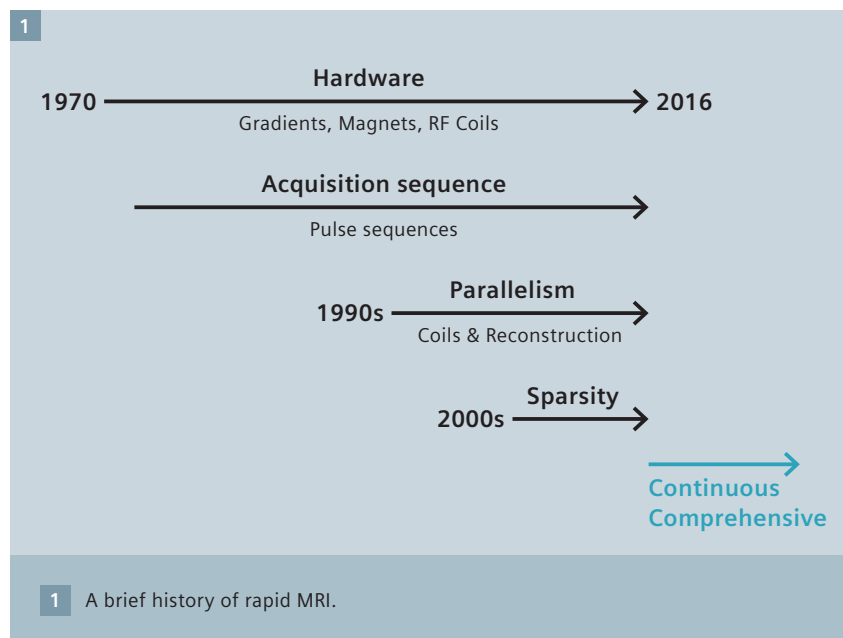
figuration of our eyes, enabled further advances in imaging speed beyond previous hardware and software limits. The next decade saw a race to incorporate ever larger numbers of detectors, until this trend, too, began to mature and new practical limits of acceleration began to be reached.

Suddenly, in the middle of the last decade, the landscape of rapid imaging started to shift again. The impetus this time could be traced to developments in the mathematics of image reconstruction. Previous rapid imaging approaches such as parallel MRI or non-Cartesian acquisitions had already necessitated substantial changes to image reconstruction algorithms. However, more recent developments had their root in a new appreciation of the role of sparsity and incoherence in the solution of inverse problems like image reconstruction. Modified acquisition approaches were soon being proposed to take advantage of the new reconstruction methods, which tended to be grouped under the label of compressed (or compressive) sensing. Many would argue that we now occupy the era of sparsity in rapid imaging. It is a 'post-Nyquist' era, somewhat unsettling to those raised on linear inverse problems, but extraordinarily rich in possibilities for innovation. The outcome in terms

of raw acceleration of MR image acquisition is already striking: appropriate combinations of compressed sensing with parallel imaging have, in many cases, been shown to yield order-of-magnitude accelerations as compared with parallel imaging alone. Meanwhile, compressed sensing and related approaches have begun to change the way we view the problem of image formation.

Sparsity and incoherence: the rise of compressed sensing

Compressed sensing may be argued to have arisen out of at least two central observations: 1) that most signals (including images) are simpler than they might at first appear, if they are viewed from the right perspective, and 2) that we can generally control how we encode and decode signals or images, such that undersampling does not necessarily lead to irretrievable loss of information. Over time, numerous particular reconstruction algorithms, taking advantage of various kinds of prior information to reconstruct undersampled datasets, had previously been proposed. However, it is the work of Candès [2], Romberg [2], Tao [2], and Donoho [3] that is generally credited with establishing the rigorous theoretical underpinnings of sparse signal recovery from



incoherent acquisitions – or, in other words, compressed sensing. Very soon thereafter, Lustig [4] demonstrated concrete applications of compressed sensing for rapid MRI, and in the process created a new subfield of biomedical imaging research.

The fact that we can represent images with less than the usual data is not in itself surprising. It is well known that most images are at least somewhat sparse, in the sense that they may be represented accurately by a number of parameters smaller than the number of voxels. The prevalence of image compression – an essential tool for modern data storage and transmission – serves as concrete evidence of this fact. Image compression algorithms exploit correlations between pixels to reduce the number of bits required for storage. Knowing as we do that most medical images are highly compressible, we are faced with a nagging question: why do we need to exert Herculean effort to acquire fully-sampled data, if in the end we are going to throw most of those data away? Until compressed sensing appeared on the scene, the prevailing answer was that accurate compression requires prior knowledge of image content, so that we can decide which components to discard and which to keep. By definition, however, the content of a new medical image is unknown, and it is in fact the unpredictable abnormalities that represent the most critical information for physicians and their patients. In medical imaging circles, use of prior knowledge is viewed with legitimate caution.

How, then, does compressed sensing effectively accomplish pre-compression without assuming particular image content? It simply asserts that the correct image (or image series) is sparse in a known domain. This domain may be the image domain itself, or it may be defined by transforming the image using Fourier transforms, wavelet transforms, or other operations often used in image compression. Compressed sensing makes no assumption about which coefficients in particular are significant or insignificant – it only

assumes that a suitably sparse solution is likely to be correct. Such an assumption does carry risks, but the risks are rather more modest than the risk of corrupting the true image with features of a specific image model.

In practice, successful compressed sensing requires three principal ingredients: 1) sparsity of true image content, 2) incoherent sampling (with incoherence, in this case, assessed between the acquisition basis and the sparse basis), and 3) non-linear reconstruction. The basic principles of compressed sensing are elucidated quite well in the literature, and for particular demonstrations of key concepts as applied to imaging, readers are referred to some of the seminal publications by Lustig et al. [4, 5]. A simple and compelling graphical example may be found in Figure 2 of Ref [4] or Figure 5 of Ref [5]. By now, some of the tradeoffs of compressed sensing, including the risk of subtle artifacts at excessively high accelerations and the challenges of quantitative image quality evaluation in the presence of nonlinear reconstruction, have also been well documented.

Stepping back from these details, however, there are a number of salutary consequences of adopting a compressed sensing *perspective*. First of all, one begins to focus less on the number of voxels in an image and more on information content. Second, one is confronted with what might be called a paradox of dimensionality: in the era of sparsity, bigger, more diverse datasets tend to result in better reconstruction performance. Multidimensional datasets tend to demonstrate more sparsity, and enable more incoherence, than datasets with fewer dimensions, and this has led to a new rule of thumb for data acquisition. Whereas in a traditional setting of ordered acquisition and linear reconstruction, simple repeatable sequences are often preferred, in a setting of compressed sensing it behooves one not to repeat oneself. Whenever possible, one should take advantage of temporal

coherence and sampling-pattern incoherence. Taken together, these observations connect rapid imaging, more than ever, not just with raw acceleration but also with enhanced information content.

Hints of a new paradigm

Just as our retinas are enviable models of parallel imaging systems, so we may look to our brains as examples of sparse information recovery systems. Human neural processes are highly efficient at data compression and information extraction. As we make our ways through any typical day, our brains are constantly distilling complex inputs rapidly into their essences, and they routinely reconstruct essential information from incomplete input. In considering what is next for biomedical imaging, we might be well served by looking once again to our day-to-day experience of the world. That experience is dynamic and multifaceted, with diverse information streaming in constantly along multiple sensory channels. Can we design imaging strategies to match these aspects of our experience?

Whereas biomedical imaging protocols have traditionally been designed around well-defined snapshots or ordered series thereof, a paradigm of rapid continuous imaging and flexible image reconstruction is emerging that may be better suited to capture the dynamic nature of experience. Recent continuous acquisition approaches exploit correlations along the time domain, and, in so doing, they may often outperform traditional intermittent acquisition protocols. In keeping with the paradox of dimensionality, it has been shown that acceleration capability, just like compressibility, is much greater with a time series than with a single snapshot, and an incoherently sampled time series plays particularly to the strengths of compressed sensing.

What about the multifaceted nature of experience? A trend towards rapid comprehensive imaging is now afoot, which aims explicitly to entangle multiple distinct streams of quantitative information, which have traditionally

been encoded separately and sequentially, within single dynamic multidimensional datasets. This trend represents a new form of parallelism, which promises to transform imaging devices from 'scanners' into something more closely resembling broadband communication channels.

As a complement to the diverse examples on display in the current edition of this magazine, let us briefly explore a few additional illustrative examples drawn from my own network of collaborators and from the Siemens collaboration network at large.

Rapid continuous imaging

There has been a recent resurgence in non-Cartesian imaging approaches, sparked in large part by considerations of sparsity. Radial k -space patterns in particular (arguably a throwback to Lauterbur's original encircling projections) tend to have favorably incoherent undersampling properties, well suited to compressed sensing reconstruction. Radial trajectories are also robust to motion, and they lend themselves to flexible angular ordering schemes such as the 'golden angle' scheme, in which each new radial spoke fills in the largest remaining gap in the angular distribution and provides complementary spatial information in a continuous nonrepeating sequence. The GRASP technique [6] described in a recent edition of *MAGNETOM Flash* [7] exploits such a golden angle radial sequence. Since this sequence has no preferred starting or ending point in time or angular distribution, and since even small sets of time-adjacent spokes provide nearly isotropic, if highly undersampled, coverage of k -space, the same dataset may be reconstructed with flexible temporal resolution (within the limits of achievable acceleration), at essentially any time point of interest. This flexibility and robustness tends to be greatly appreciated by clinicians (see Patel et al. on permeability imaging of parotid tumors using GRASP). Clinical GRASP studies have been performed for more than ten thousand patients at NYU Langone Medical Center to date, for applications ranging from head to toe, and GRASP is now being evaluated in

multicenter trials within the Siemens network.

Though GRASP is sufficiently motion-robust to obviate the need for breath-holding in many applications, motion can still degrade image quality, either by causing intraframe blurring for low-temporal-resolution reconstructions, or by degrading temporal sparsity and engendering residual inter-frame blurring in high-temporal-resolution reconstructions. Radial trajectories, however, have the additional advantage that each spoke passes through the center of k -space, and this repeated central data may be used as a sensitive indicator of changing motion states. The eXtra-Dimensional GRASP (XD-GRASP) reconstruction method [8] uses inherent self-navigation properties to sort GRASP data into multiple distinct motion states. Rather than simply grouping temporally sequential spokes, the XD-GRASP algorithm groups spokes within a given motion state, and organizes the data into additional temporal dimensions representing the different types of motion. Respiratory motion and contrast enhancement may be captured in distinct dimensions for dynamic contrast-enhanced studies; or the extra dimensions may represent respiratory motion and cardiac motion for cardiac MRI. (In this case, coils near the heart and the diaphragm are used to characterize the cardiac and the respiratory motion signals, respectively.) Sorting the continuously-acquired data into additional dimensions has a number of advantages. The extra dimensionality results in improved signal sparsity, since disparate motional frequencies and other dynamic characteristics are no longer intermingled. This results in improved image quality and increased acceleration capability. At the same time, extradimensional sorting is an efficient means of motion correction, which, unlike some traditional navigation methods, does not require that any data be discarded. Finally, XD-GRASP enables not just correction for but also characterization of motion. It has been shown to be useful, for instance, in separating and visualizing arrhythmic cardiac

cycles. It has also proven useful in characterizing respiratory dynamics, for example enabling direct visualization of left-right ventricular (LV-RV) interaction over the course of the respiratory cycle. Note that all of this information may be obtained from the same continuously acquired dataset, simply by adapting the reconstruction algorithm and by slicing through the resulting multidimensional image series as desired.

There is still more information to be gleaned from the same datasets. While XD-GRASP enables visualization of distinct motion states, it does not directly quantify the extent of the motion. One could, of course, attempt to coregister distinct frames to derive approximate motion fields. It turns out, however, that one may derive motion fields more directly from within the reconstruction algorithm itself, by appealing to a domain of mathematics closely related to that of sparse information recovery – namely, low-rank matrix completion. The 'motion-guided L+S' reconstruction of Otazo et al. [9] takes advantage of self-consistency within diverse continuously acquired datasets to self-discover accurate quantitative motion models, rather than trying to fit the data to a particular *a priori* model.

Rapid comprehensive imaging

The question of quantitation highlights one of the longstanding challenges of magnetic resonance. The highly flexible tissue contrast and rich endogenous information content associated with MRI also result in a high degree of potential operator- and scanner-dependence. Therefore, whereas the interpretation of most varieties of clinical MR images is qualitative, specialized MR pulse sequences are usually deployed for the quantitative mapping of tissue parameters such as relaxation times or diffusion constants. These specialized sequences come at a significant cost in scan time and, even when carefully calibrated, they suffer from residual errors and interferences which result in undesirable variability.

Recently – and arguably as a partial outcome of the ‘compressed sensing perspective’ alluded to earlier – it has been recognized that the multifactorial complexity of spin dynamics may represent an asset rather than a liability for quantitation. In particular, there is an emerging trend towards fitting multiple physical parameters (and, as desired, deriving multiple contrasts) from the same acquired data. This trend is in direct contradiction to the traditional approach of designing sequences around as simple a dynamical effect as possible, then correcting for undesired effects through painstaking calibration. Such a trend can also be viewed as another manifestation of the paradox of dimensionality. Whenever possible, the reasoning goes, mix together disparate encoding mechanisms such that the whole dataset is greater than the sum of its parts.

The current archetype of this new comprehensive quantitative mapping approach is the MR Fingerprinting (MRF)¹ technique, as championed by Griswold and colleagues at Case Western Reserve University [10]. Gulani et al. provide a helpful introduction to MRF in this issue of MAGNETOM Flash. MRF entangles the effects of multiple physical parameters (T1 and T2 relaxation, proton density, magnetic field inhomogeneity, etc.) in long pulse sequences with irregular timing. Spin evolution under the influence of these sequences results in complex temporal signals that serve as distinctive ‘fingerprints’ for particular sets of parameter values. Individual voxel fingerprints from a series of successive image frames are matched to a database of simulated spin dynamics with a range of known parameter values. Since the MRF sequences are arranged such that undersampling artifacts are incoherent with the spin dynamics, the fingerprints may be matched reliably to the database even for highly undersampled image sets, enabling high degrees of acceleration that compensate for the duration of the lengthy pulse trains. In this way, multiple quantitative parameter maps are derived rapidly and simultaneously from images

that, on their own, would be essentially uninterpretable.

Though the simple pattern-matching reconstruction in MRF is quite different from the iterative sparsity-enforcing reconstructions discussed earlier, there is nonetheless a strong connection to compressed sensing. MRF makes liberal use of incoherent acquisition, and Bloch equation models serve to capture the key dynamical coherences in the data, effectively standing in for a sparsifying transform. MRF also has some of the provocative effect of compressed sensing, spurring out-of-the-box thinking about potential new encoding or reconstruction methods. Ben-Eliezer et al. have demonstrated that, even with more highly coherent acquisitions, for example traditional multi-spin-echo sequences optimized for rapid T2 mapping, one can map multiple quantitative parameters, including not only T2 and proton density but also the B_1^+ RF transmission field distribution, by fitting to Bloch equation models [11]. Recent work by Cloos et al., moreover, has shown that MRF pattern matching may be extended to map the B_1^+ transmit field pattern of multiple RF coils [12]. In addition to enriching the information content of fingerprinting sequences at no cost in acquisition time, this new ‘multi-illumination’ fingerprinting approach has been shown to enable robust imaging in the presence of strong RF field inhomogeneities. As a result, it promises to reduce the calibration-heavy and workflow-intensive field of parallel RF transmission to a simple ‘plug and play’ mode of operation [12].

The multiparametric mapping approaches discussed so far all adhere to the general theme of allowing, or even embracing, inhomogeneities and signal imperfections. Rather than employing Herculean efforts to calibrate out imperfections, these approaches quantify inhomogeneities along with the usual desired parameter values, based on the distinctive characteristics of a multifaceted acquired signal. Like XD-GRASP or combined MR-PET, these rapid comprehensive imaging

approaches represent a form of all-in-one acquisition. The example of plug and play parallel transmission, moreover, introduces once again the important theme of workflow simplification.

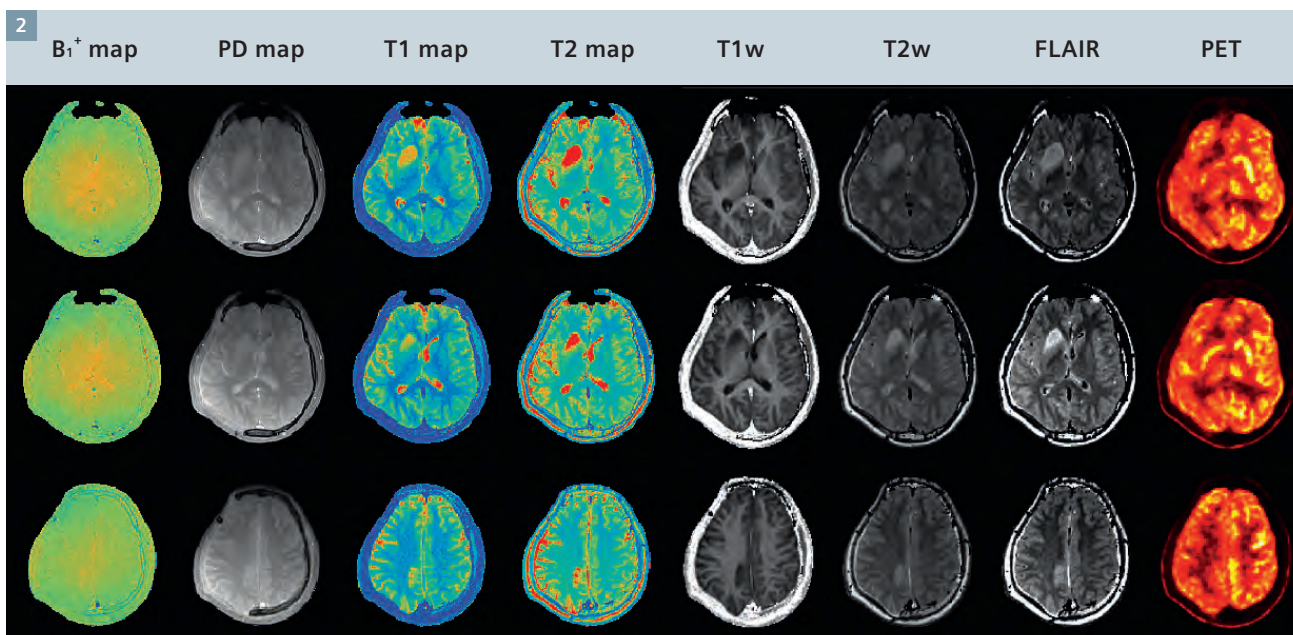
Toward rapid, continuous comprehensive imaging: the rapid imaging renaissance

Let me now offer two final examples of how the advances described so far can enable dramatic simplifications of MR (and multimodality) workflow, while preserving and ultimately enhancing image information content.

Cardiac MRI boasts some of the most complex workflow in the field. Both cardiac and respiratory monitoring are routinely performed, and advanced training is required merely to orient key multi-oblique image planes correctly during the planning of scans aimed at characterizing diverse aspects of cardiac anatomy and function. A few-minute comprehensive cardiac examination has long been a holy grail for those interested in cardiac MR. Collaborative work between NYU and the research group of Stuber et al. in Lausanne is addressed at a prototype few-minute continuous comprehensive cardiac MR examination, using four [13] - or five-dimensional XD-GRASP [14]. The ‘spiral phyllotaxis’ trajectory [15] used in this work is a generalization to three dimensions of the golden-angle radial trajectory used in prior XD-GRASP studies. In 5D cardiac XD-GRASP, continuously acquired data obtained during free breathing are sorted into cardiac and respiratory motion dimensions, in addition to the three spatial dimensions defining the imaging volume. This approach yields high-resolution isotropic whole-heart image sets in which cardiac motion, respiratory motion, and cardiac anatomy are all resolved. One can obtain robust

¹Magnetic Resonance Fingerprinting is currently under development. It is not for sale in the U.S. and other countries. Its future availability cannot be guaranteed. As this is a research topic in predevelopment, all results shown are preliminary in nature and do not allow for generalizations or conclusions to be drawn.

Product realization and features therein cannot be assured as the product may undergo further design iterations.



2 MRF-PET [16]. Three representative slices are shown from a 30-slice whole-brain axial image set obtained after surgery in a patient with a brain tumor. The diverse information obtained from a single continuous six-minute MRF-PET acquisition includes quantitative T1, T2, relative proton density, and B_1^+ maps, jointly reconstructed PET images, and a variety of synthesized contrast weightings, including T1, T2, and FLAIR weightings. *Figure courtesy of Drs. Martijn Cloos and Florian Knoll.*

views of cardiac and great vessel dynamics in any desired orientation, and from the same data one can derive high-resolution depictions of coronary arteries throughout the cardiac and respiratory cycles. This early work has not yet incorporated myocardial perfusion and viability studies, but in light of experience so far using XD-GRASP for other contrast-enhanced studies, this seems a natural extension.

The second example of rapid continuous comprehensive imaging was also motivated originally by workflow considerations. When we began performing simultaneous MR and PET scans on our Siemens Biograph mMR scanner at NYU, we quickly realized that the MR imaging protocol in many cases represented a temporal bottleneck. By the time the scan operator was done with gathering the multiple contrast weightings called for in clinical protocols, the typical time needed for FDG-PET acquisitions had long been exceeded. Though of course we could always continue averaging PET counts for the entire duration of the MR protocol, we were in a sense only biding our time. To address this inefficiency, we turned to MRF, and

designed a joint MRF-PET acquisition and reconstruction approach [16]. MRF-PET combines joint MR-PET reconstruction with spin dynamical pattern matching to derive multiple quantitative MR maps together with improved PET images. The joint reconstruction, moreover, improves MR aliasing artifact removal, as a supplement to the incoherence effects in MRF alone. The net result is a diverse, quantitative multimodality image volume obtained in the time normally occupied by a single PET 'bed position'. Figure 2 illustrates the range of information which may be obtained from a single six-minute continuous radial MRF-PET acquisition. In the figure, only three representative slices are shown out of a total of 30 slices covering the whole head. In addition to the PET image set, matched quantitative T1 and T2 maps are obtained, along with relative proton density maps and B_1^+ maps. Entanglement of multiple streams of information in this case results not only in improved quantitation but also in marked practical convenience. When all the information of interest may be obtained in a few minutes per bed position, one can

begin to contemplate efficient whole-body MR-PET screening. One can also perform retrospective data mining, in which any suspected lesion detected on MR and/or PET can be examined after the fact with a range of potential synthetic contrasts, or even directly from the multiparametric data, to clinch the diagnosis without need for any additional scanning.

The limits of just how much information can be embedded robustly in sequences like MRF-PET are still being explored. Meanwhile, it is natural to contemplate combining MRF or MRF-PET with approaches like XD-GRASP or motion-guided L+S. Such a combination would address known challenges associated with motion in MRF. It would also represent a unified approach to quantifying physiologic dynamics along with spin dynamics (not to mention PET tracer kinetics). Traditionally, physiologic motion has been considered the nemesis of quantitative imaging, but in such a unified approach, the two would be synergistically entangled, requiring only appropriate reconstruction algorithms to disentangle them as needed.

Conclusions, and a look to the future

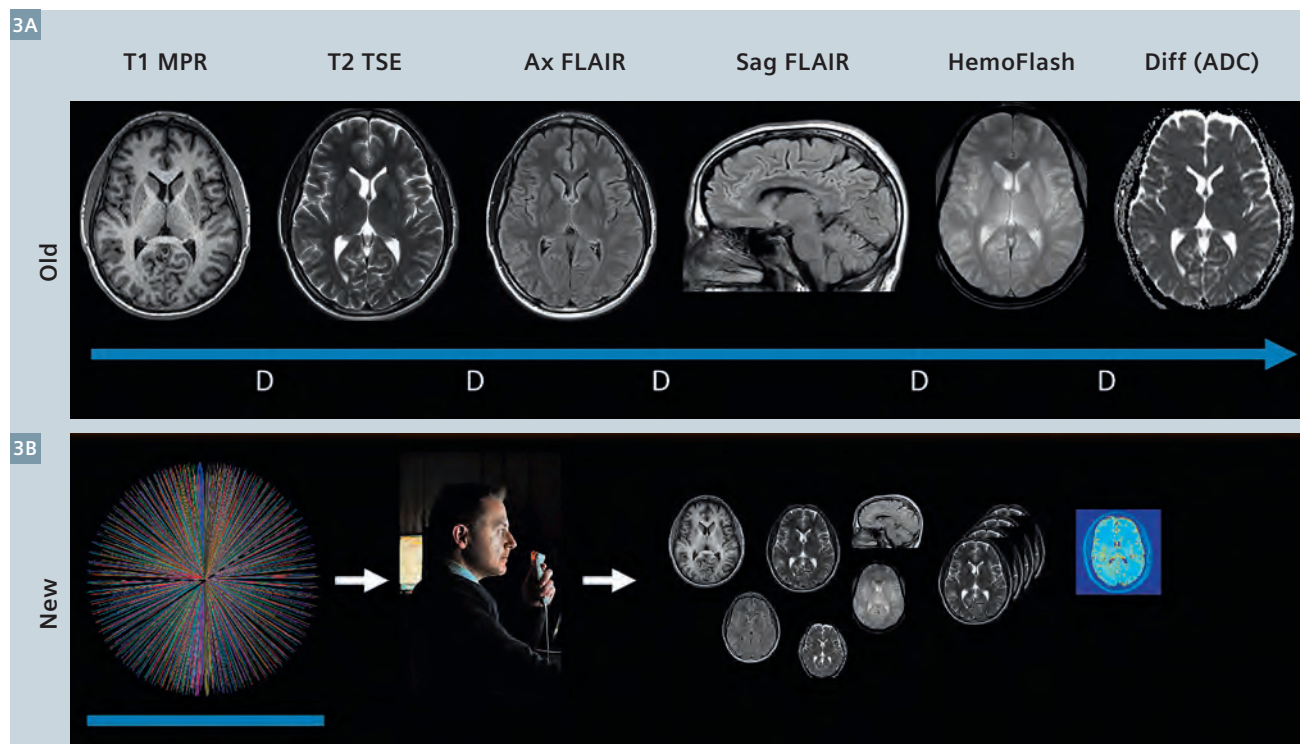
In closing, I would argue that an intriguing possible future of rapid imaging lies in continuous comprehensive data acquisition coupled with flexible image reconstruction. I hereby challenge you to identify some of the outlines of this future in the current issue of MAGNETOM Flash, not to mention in issues to come. The rapid continuous comprehensive paradigm (see the blue arrow at the bottom of Figure 1) has the potential to catalyze a new use of time in imaging, as is illustrated in Figure 3. At the top of the figure is a schematic representation of the traditional MR imaging protocol, with distinct contrast weightings achieved in distinct acquisitions using tailored pulse sequences. The scanner is not active during the dead time (D) between each sequence, which may become extended if careful planning of new scan geometries or other user input is required. Motion between scans can hinder registration, and motion

during scans typically leads to artifacts. By contrast, the bottom of Figure 3 illustrates the new paradigm of rapid continuous comprehensive imaging. A simple-to-plan comprehensive dataset is acquired efficiently, with no dead time. Patient motion during the acquisition is tracked using self-navigation or motion model discovery. Depending upon the clinical indication for imaging, a preset portfolio of reconstructed images may be presented initially to the radiologist. If he or she detects anything in these images which raises suspicion, and which calls for any new views or contrasts, these may be generated on the spot from the raw data by appropriate reconstruction or other processing algorithms. The acquired data, moreover, need not be limited to MR data. If multiple modalities are available, then joint reconstruction may be applied to take advantage of shared information, to highlight noteworthy differences, and, ultimately, to generate multimodality 'fingerprints' of pathology.

Despite the technological and computational complexity underlying such a continuous comprehensive imaging paradigm, its net effect will be a marked operational simplicity. One can envision a future scanner operator's tasks being distilled down to a) positioning the subject within the scanner, and b) pressing the 'go' button. The key challenge then will lie in navigating the resulting multifaceted datasets. This is a worthy challenge, which is already being taken up across a broad range of disciplines in our increasingly information-saturated age. In the meantime, much work remains to be done before the current rapid imaging renaissance reaches its peak. It will fall to our community of clinicians and scientists either to resist or to embrace the disruption and the opportunity that will ensue. The result may be nothing less than a change in the way we see the world around us.

Daniel K. Sodickson

Daniel Sodickson



3 Towards a new use of time in imaging. (3A) Schematic illustration of a traditional ('old') MR imaging protocol. (D = dead time between distinct contrast-weighted sequences.) (3B) Illustration of the new paradigm of rapid continuous comprehensive imaging.

References

- 1 Sodickson, D. K., Feng, L., Knoll, F. et al., "The rapid imaging renaissance: sparser samples, denser dimensions, and glimmerings of a grand unified tomography," *Proc. SPIE Medical Imaging*, 9417, 94170G (2015).
- 2 Candes, E., Romberg, J., and Tao, T., "Robust uncertainty principles: Exact signal reconstruction from highly incomplete frequency information," *IEEE Trans Inf Theory*, 52, 489–509 (2006).
- 3 Donoho, D., "Compressed Sensing," *IEEE Trans Inf Theory*, 52, 1289–1306 (2006).
- 4 Lustig, M., Donoho, D., and Pauly, J. M., "Sparse MRI: The application of compressed sensing for rapid MR imaging," *Magn Reson Med*, 58(6), 1182-95 (2007).
- 5 Lustig, M., Donoho, D. L., Santos, J. M. et al., "Compressed Sensing MRI: A look at how CS can improve on current imaging techniques," *IEEE Signal Processing Magazine*, March, 72-82 (2008).
- 6 Feng, L., Grimm, R., Block, K. T. et al., "Golden-angle radial sparse parallel MRI: Combination of compressed sensing, parallel imaging, and golden-angle radial sampling for fast and flexible dynamic volumetric MRI," *Magn Reson Med*, 72(3), 707-17 (2014).
- 7 Block, K. T., Feng, L., Grimm, R. et al., "GRASP: Tackling the Challenges of Abdominopelvic DCE-MRI," *MAGNETOM Flash*, 5/2015(60), 16-22 (2014).
- 8 Feng, L., Axel, L., Chandarana, H. et al., "XD-GRASP: Golden-angle radial MRI with reconstruction of extra motion-state dimensions using compressed sensing," *Magn Reson Med*, 75(2), 775-88 (2016).
- 9 Otazo, R., Koesters, T., Candes, E. J. et al., "Motion-guided low-rank plus sparse (L+S) reconstruction for free-breathing dynamic MRI," *Proceedings of the Twenty Second Scientific Meeting of the International Society for Magnetic Resonance in Medicine*, 742 (2014).
- 10 Ma, D., Gulani, V., Seiberlich, N. et al., "Magnetic resonance fingerprinting," *Nature*, 495(7440), 187-92 (2013).
- 11 Ben-Eliezer, N., Sodickson, D. K., and Block, K. T., "Rapid and accurate T2 mapping from multi-spin-echo data using Bloch-simulation-based reconstruction," *Magn Reson Med*, 73(2), 809-17 (2015).
- 12 Cloos, M., Wiggins, C., Wiggins, G. et al., "Plug and Play Parallel Transmission at 7 and 9.4 Tesla based on Principles from MR Fingerprinting," *Proceedings of the Twenty Second Scientific Meeting of the International Society for Magnetic Resonance in Medicine*, 542 (2014).
- 13 Piccini, D., Feng, L., Bonanno, G. et al., "Four-dimensional respiratory motion-resolved whole heart coronary MR angiography," *Magn Reson Med*, (2016).
- 14 Feng, L., Coppo, S., Piccini, D. et al., "Five-Dimensional Cardiac and Respiratory Motion-Resolved Whole-Heart MRI," *Proceedings of the Twenty Third Scientific Meeting of the International Society for Magnetic Resonance in Medicine*, 27 (2015).
- 15 Piccini, D., Littmann, A., Nilles-Vallespin, S. et al., "Spiral phyllotaxis: the natural way to construct a 3D radial trajectory in MRI," *Magn Reson Med*, 66(4), 1049-56 (2011).
- 16 Knoll, F., Cloos, M. A., Koesters, T. et al., "PET-MRF: One-step 6-minute multi-parametric PET-MR imaging using MR fingerprinting and multi-modality joint image reconstruction," *Proceedings of the Twenty Third Scientific Meeting of the International Society for Magnetic Resonance in Medicine*, 3391 (2015).

Editorial Board

We appreciate your comments.

Please contact us at magnetomworld.med@siemens.com



Antje Hellwich
Editor-in-chief



Wellesley Were
MR Business Development
Manager Australia and
New Zealand



Sunil Kumar S.L., Ph.D.
Senior Manager Applications,
Canada



Reto Merges
Head of Scientific Marketing



Gary R. McNeal, MS (BME)
Advanced Application
Specialist, Cardiovascular
MR Imaging Hoffman
Estates, IL, USA



Peter Kreisler, Ph.D.
Collaborations & Applications,
Erlangen, Germany

Review Board

Lisa Chuah, Ph.D.

*Global Segment Manager Neurology,
Pediatrics and Orthopedics*

Berthold Kiefer, Ph.D.

*Head of Oncological and Interventional
Applications*

Matthias Lichy, M.D., M.Sc.

Clinical Competence Center

Heiko Meyer, Ph.D.

Head of Neuro Applications

Edgar Müller

Head of Cardiovascular Applications

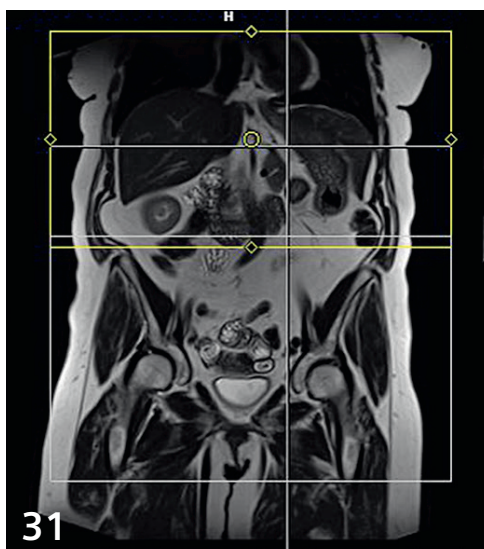
Gregor Thörmer, Ph.D.

*Global Segment Manager Men's and
Women's Health*

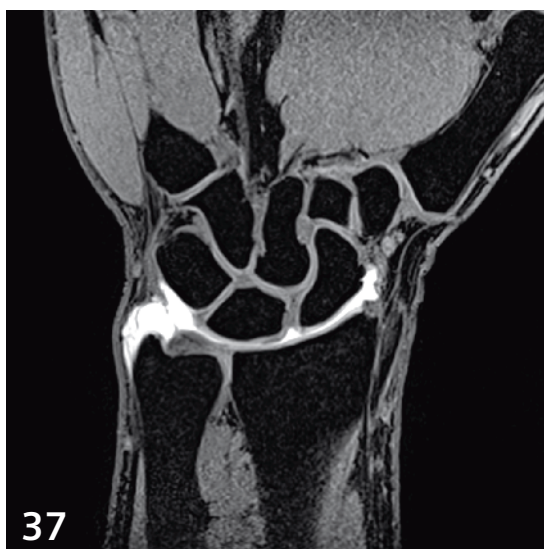
Heike Weh

Clinical Data Manager

Content



Whole-Body Dot Engine



The Skyra^{fit} Experience

Editorial Comment

- 2** The Rapid Imaging Renaissance
Daniel K. Sodickson,
New York University
Langone Medical Center,
New York, NY, USA

Technology

- 12** Overview of MR Fingerprinting*
Vikas Gulani, et al.,
Case Western Reserve University,
University Hospitals Case
Medical Center, Cleveland,
OH, USA
- 22** New Strategies for Protocol Optimization for Clinical MRI
Otto Rapalino, et al.,
Massachusetts General Hospital,
Boston, MA, USA
- 26** Slice Specific Adjustment* Improves the Image Quality of Whole-Body Diffusion-Weighted Examinations at 3T
Xue Huadan, et al.,
Peking Union Medical College Hospital, Beijing, China

Pediatric Imaging

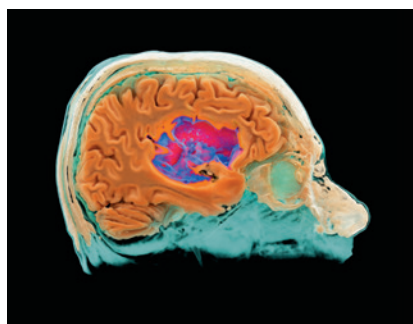
- 34** Pictorial Essay:
 Pulmonary Imaging for Children¹
Sonja Kinner, et al.,
University Hospital Essen, Germany

Business

- 37** The Skyra^{fit} Experience in Basel
Thomas Egelhof, et al.,
Merian Iselin Spital,
Basel, Switzerland

Review

- 40** Biograph mMR:
 System and Clinical Use Today
Björn W. Jakoby, et al.,
Siemens Healthcare,
Erlangen, Germany



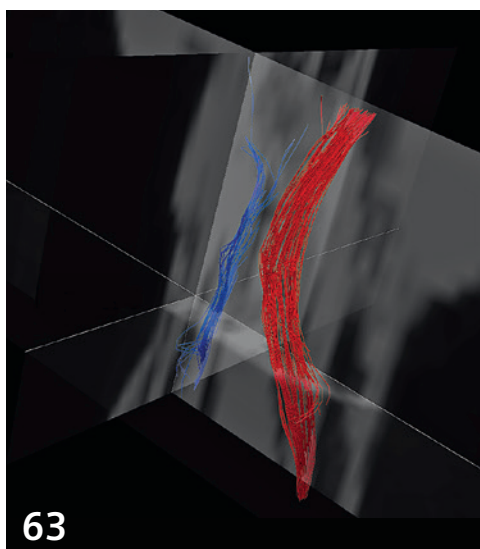
Cover image courtesy of
 Andreas J. Bartsch
(Radiologie Bamberg, Germany;
Departments of Neuroradiology,
Universities of Heidelberg and
Wuerzburg, Germany; Oxford Centre
for Functional MRI of the Brain
(FMRIB), University of Oxford, UK)

Abdominal Imaging

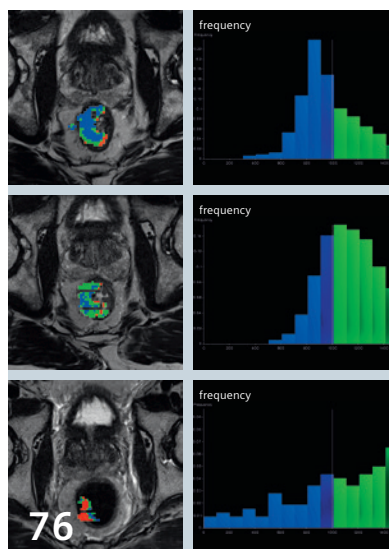
- 31** Whole-Body Dot Engine:
 First Clinical Experience with
 Automated Chest, Abdomen
 and Pelvis Examinations
Caecilia S. Reiner, et al.,
University Hospital Zurich,
Switzerland

Head and Neck Imaging

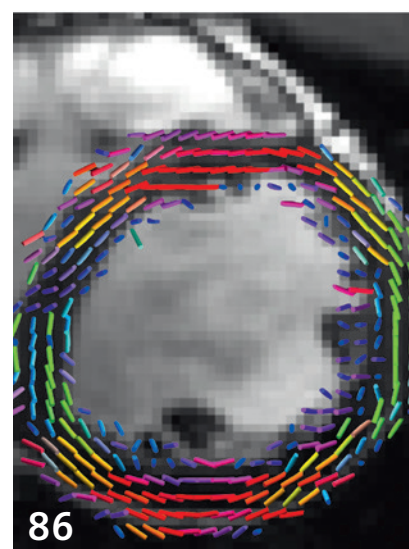
- 44** Permeability Imaging of Parotid Tumors with GRASP MR Imaging
Sohil H. Patel, et al.,
New York University Langone
Medical Center, New York,
NY, USA



63 SMS RESOLVE* Diffusion Neurography



76 Prediction of Treatment Response in Rectal Cancer



86 Cardiac Diffusion Tensor* MRI

How-I-do-it

46 Further Customization of Dot Engines: AutoCoverage
Bart Schraa, Siemens Canada Limited, Oakville, ON, Canada

52 syngo.MR Neuro 3D
Lisa Chuah, et al., Siemens Healthcare, Erlangen, Germany

Musculoskeletal Imaging

63 Case Report:
High-Resolution SMS RESOLVE* Diffusion Neurography
Andreas J. Bartsch, Radiologie Bamberg, Germany

Women's Health

68 Case Report:
3D SPACE MR Acquisition in Genitourinary Tract Imaging
Priti Apte-Upasani, et al., Sun Scan Center, Thane, India

70 Diffusion-Weighted MR Mammography. Potential in the Clarification of Suspicious Lesions Detected by X-Ray Mammography
Sebastian Bickelhaupt, et al., German Cancer Research Center (DKFZ), Heidelberg, Germany

80 Significant Benefit of Optimized 3D SPACE Sequences in Radiation Therapy Treatment
Maja Sohlén, et al., Sahlgrenska University Hospital, Gothenburg, Sweden

82 The Potential Role of Ultrashort Echo Time Sequences in MRI Guided Radiotherapy
Gary Liney, et al., Liverpool Cancer Therapy Centre, Liverpool Hospital, Sydney, Australia

Radiation Therapy

76 Multiparametric MRI at 3T for Prediction of Treatment Response in Rectal Cancer
Trang Pham, et al., Liverpool Cancer Therapy Centre, Liverpool Hospital, Sydney, Australia

Cardiovascular Imaging

86 Cardiac Diffusion Tensor MRI
Daniel B. Ennis, et al., University of California, Los Angeles, CA, USA

*WIP, the product is currently under development and is not for sale in the US and in other countries. Its future availability cannot be ensured.

[†]MR scanning has not been established as safe for imaging fetuses and infants less than two years of age. The responsible physician must evaluate the benefits of the MR examination compared to those of other imaging procedures.

The information presented in MAGNETOM Flash is for illustration only and is not intended to be relied upon by the reader for instruction as to the practice of medicine. Any healthcare practitioner reading this information is reminded that they must use their own learning, training and expertise in dealing with their individual patients. This material does not substitute for that duty and is not intended by Siemens Healthcare to be used for any purpose in that regard. The treating physician bears the sole responsibility for the diagnosis and treatment of patients, including drugs and doses prescribed in connection with such use. The Operating Instructions must always be strictly followed when operating the MR system. The source for the technical data is the corresponding data sheets.

Overview of Magnetic Resonance Fingerprinting

Simone Coppo¹; Bhairav B. Mehta¹; Debra McGivney¹; Dan Ma¹; Yong Chen¹; Yun Jiang²; Jesse Hamilton²; Shivani Pahwa¹; Chaitra Badve¹; Nicole Seiberlich¹; Mark Griswold^{1,2}; Vikas Gulani¹

Departments of Radiology (1) and Biomedical Engineering (2), Case Western Reserve University, University Hospitals Case Medical Center, Cleveland, OH, USA

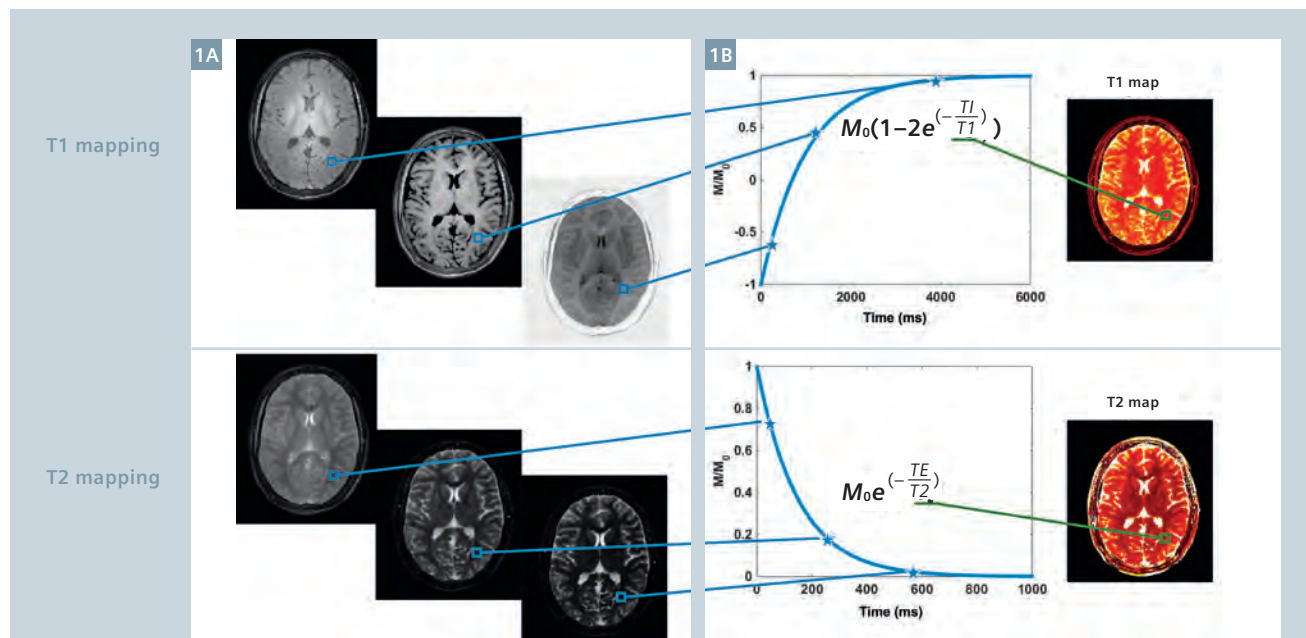
Introduction

Magnetic Resonance Imaging (MRI) is a powerful diagnostic, prognostic and therapy assessment tool due to its versatile nature as compared to other imaging modalities, as MRI allows the user to probe and measure various kinds of information (T1, T2, B₀, diffusion, perfusion, etc.). However, MRI has the drawback of being slow compared to other diagnostic tools, and is generally qualitative, where the contrast between tissues, rather than absolute measurements from single tissues, is the primary means of information that is used to characterize an underlying

pathology. While this information has proven extremely valuable for diagnosis, prognosis, and therapeutic assessment, the lack of quantification limits objective evaluation, leads to a variability in interpretation, and potentially limits the utility of the technology in some clinical scenarios.

To overcome this limitation, significant effort has been put into developing quantitative approaches that can measure tissue proprieties such as T1 and T2 relaxation times. Quantifying tissue proprieties allows physicians to better distinguish between healthy and pathological

tissue [1] in an absolute sense, makes it easier to objectively compare different exams in follow-up studies [2], and could be more representative of the underlying changes at the cellular level [3, 4] than standard weighted imaging. Quantitative imaging is crucial in the assessment of disease settings presenting subtle features such as cardiac diffuse fibrosis [5], iron [6] or fat deposition in the liver [7]. Additionally, there are various clinical settings in which multiple features such as T1, T2, diffusion, etc. add up synergistically to drastically improve the information for diagnosis, prognosis and/or therapeutic assessment.



- 1 Conventional parametric mapping approaches. Example of conventional T1 (above) and T2 (below) mapping techniques. (1A) Several fully sampled images are acquired one after the other with different inversion time (for T1) or echo time (for T2). (1B) An exponential fitting is performed using the multiple values of each voxel and the relaxation or decay time is the one that provides the best fit.

While quantitative imaging has been a long-standing goal of the MR community, a drawback encountered in early conventional quantitative imaging was the reduced time efficiency compared to qualitative imaging. Early conventional approaches for T1 and T2 mapping involved measuring one parameter at a time. These techniques relied on the acquisitions of several images, each with one specific acquisition parameter that varies for each image while the others were kept constant (Fig. 1A). The obtained images were subsequently fitted with a mathematical model to estimate the one parameter of interest, for example the relaxation time (T1) [8] or the time of signal decay (T2) [9] (Fig. 1B). This process had to be repeated for each parameter of interest. The need for keeping all except one sequence parameter and signal state constant and the limitation of assessing one parameter at a time made these approaches extremely time-inefficient because of the prolonged scan time and thus not suitable for a clinical environment where interscan motion can render such approaches infeasible. In recent times, several approaches have been proposed to shorten the acquisition time [10–13] or to provide combined T1 and T2 measurements [14–18] within a single acquisition. However, major barriers remain to clinical adoption, most notably a simultaneous need for rapid and accurate quantification.

To overcome the common drawbacks of quantitative imaging, Magnetic Resonance Fingerprinting (MRF)¹ [19–21] has been recently developed. This technique aims at providing simultaneous measurements of multiple parameters such as T1, T2, relative spin density, B_0 inhomogeneity (off-resonance frequency), etc., using a single, time-efficient acquisition. MRF completely changes the way quantitative MRI is performed with

an entirely different approach from that of conventional techniques. Instead of performing an acquisition with all but one sequence parameter constant, MRF relies on deliberately varying acquisition parameters in a pseudorandom fashion such that each tissue generates a unique signal evolution. It is possible to simulate signal evolutions from first principles using different physical models for a wide variety of tissue parameter combinations, which are collected together in a database called dictionary. After the acquisition, a pattern recognition algorithm is used to find the dictionary entry that best represents the acquired signal evolution of each voxel. The parameters that were used to simulate the resulting best match are then assigned to the voxel. This process is analogous to the fingerprinting identification process used by forensic experts to identify persons of interest. The acquired signal evolution is unique for each tissue and can be seen as the collected fingerprint that has to be identified. The dictionary is equivalent to the database where all the known fingerprints are stored, together with all the information relative to each person. In the forensic case, each fingerprint points to the feature identification of the associated person such as name, height, weight, eye color, date of birth, etc. Similarly, in the case of MRF, each fingerprint in the dictionary points to the MR related identification features of the associated tissue such as T1, T2, relative spin density, B_0 , diffusion, etc. After the acquisition, the fingerprint contained in a voxel is compared with all the entries in the dictionary. The dictionary entry that best matches the acquired fingerprint is considered a positive match, meaning that the tissue represented in the voxel has been identified. All the known parameters relative to that fingerprint can then be retrieved from the dictionary and assigned to the voxel. The uniqueness of the different signal components and the accuracy with which the dictionary is simulated are two crucial components for the correct estimation of the tissue parameters.

This paper attempts to describe the basic concepts of MRF and illustrate some clinical applications.

Acquisition sequence

Standard quantitative MR imaging approaches require several acquisitions, each one of which constantly repeats the same acquisition pattern, such as radiofrequency excitation angle (flip angle, FA), repetition time (TR) and gradient patterns, until all required data in the Fourier domain (also called k -space) are obtained. Each image is then reconstructed using the Fourier transform and a nonlinear fitting process is applied to each voxel. With MRF, instead, the flip angle, the TR and the trajectory (Fig. 2A, B) vary in a pseudorandom fashion throughout the acquisition; when implemented properly, this generates uncorrelated signals for each tissue, providing the unique fingerprints that are used to recognize the tissue. The initial implementation of MRF [19] was based on a balanced steady-state free-precession (bSSFP or TrueFISP) sequence because of its sensitivity to T1, T2 and off-resonance frequency, and because the steady-state signal generated by this sequence has been thoroughly studied [22]. The FA (Fig. 2A) varies in a sinusoidal fashion to smoothly vary the transient state of the magnetization, ranging from 0° to 60° and from 0° to 30° alternatively, with a period of 250 time points, or images. On top of this signal, a random variation is added to induce differences in the time evolutions from tissues with similar parameters. After each half period (250 images), 50 flip angles are set to 0° to allow for signal recovery. The TR variations, instead, are based on Perlin noise [23] which ranges from 9.34 ms to 12 ms. These are only examples of how the parameters can be randomly varied. Other random patterns have been tested [19, 24] showing that MRF is not limited to one specified set of parameters.

An inversion recovery pulse is played out at the beginning of the acquisition sequence to enhance T1 differences between tissues (Fig. 2B). For each TR, a heavily undersampled

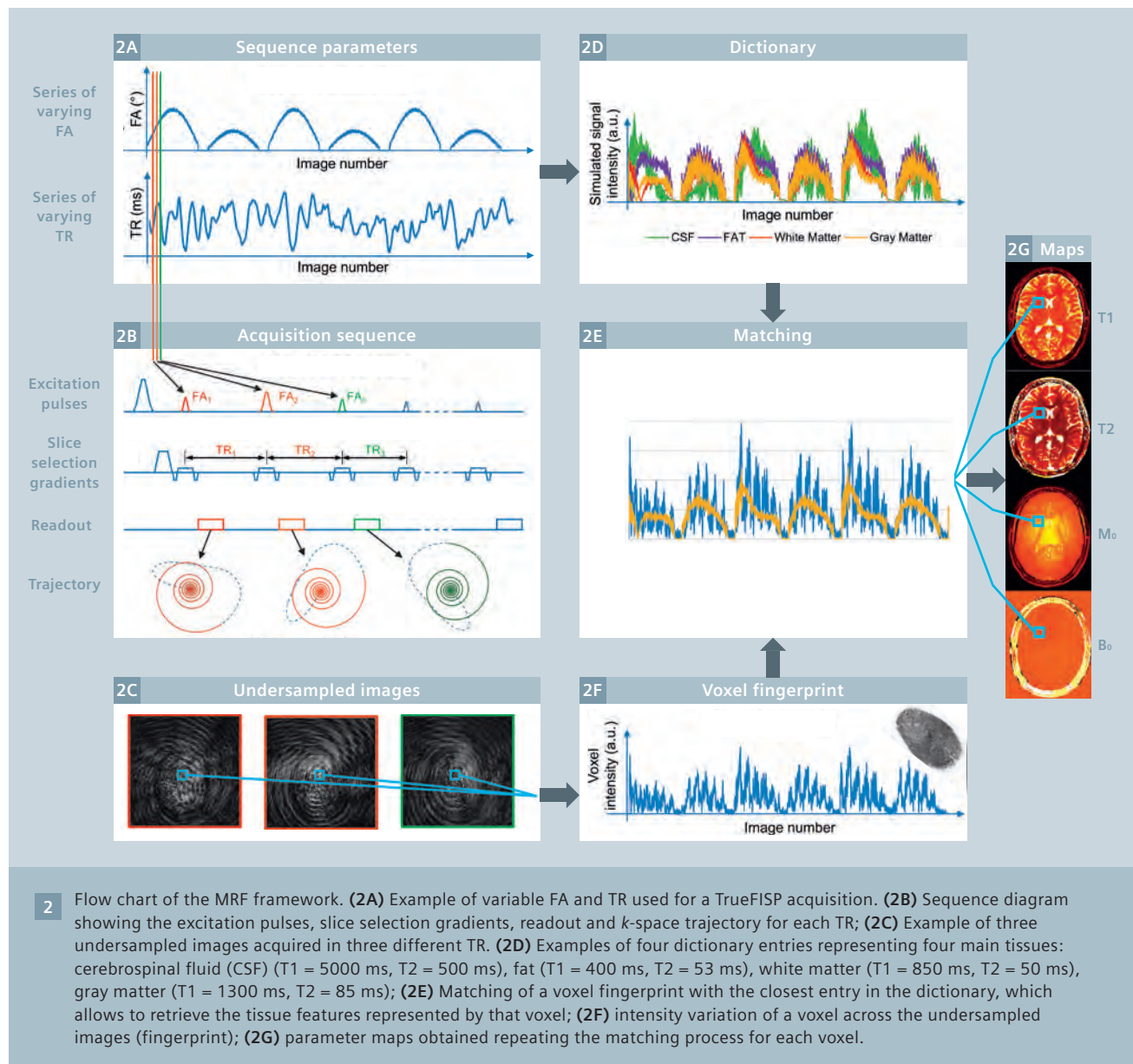
¹ The product is still under development and not commercially available yet. Its future availability cannot be ensured. As this is a research topic in predevelopment, all results shown are preliminary in nature and do not allow for generalizations or conclusions to be drawn. Product realization and features therein cannot be assured as the product may undergo further design iterations.

image is reconstructed (Fig. 2C). It can be noticed how the base image series are not useful by themselves, but each voxel contains a signature fingerprint that will be used later on for the matching (identification). The total number of images acquired (also referred to as 'time points') can vary from acquisition to acquisition, ranging from 1000 [19] to 2500 [21] as function of the image resolution, the undersampling ratio, the matching approach used, etc. In most cases, we have used a variable-density spiral trajectory [25] designed to have a minimum time gradient and zero moment compensation for the acquisition. For example, we

have successfully used a trajectory for a 128×128 matrix size that requires one interleaf to fully sample the center of k -space and 48 interleaves to fully sample the outer region of k -space. In the case of a 256×256 matrix, a trajectory requiring 24 interleaves to fully sample the inner region and 48 interleaves to fully sample the outer region can be used instead. Within each TR, one interleaf is acquired and used to reconstruct an image (or time point). The interleaf in the following TR is then rotated by 7.5° ($\approx 2\pi/48$) compared to the previous one.

The MRF framework is not only limited to a TrueFISP-based acquisi-

tion, but can be virtually applied to any kind of sequence. As an example, the MRF framework has been applied to a steady-state precession sequence (FISP) [20] to avoid the banding artifacts that can appear in wide field-of-view scans or in a high-field-strength scanner. The FISP sequence is still sensitive to T1 and T2 components but is less sensitive to off-resonance frequency. This is caused by the unbalanced gradient within every TR which results in the signal to be the sum of the spins within a voxel, making the sequence immune to banding artifacts. The unbalanced gradient, though, leads the FISP sequence to have a shorter transient state com-



pared to the TrueFISP. For this reason, the pseudorandom FA variation needs to be generated slightly differently than in the case of the TrueFISP sequence, in order to keep incoherence between the signal and under-sampling artifacts and to be able to identify the underlying fingerprint. The FA variation is thus generated based on sinusoidal variation in which the maximum reached FA for each half period randomly changes, ranging from 5° to 90°. The TR variation is always based on a Perlin noise pattern which ranges from 11.5 ms to 14 ms.

Dictionary generation

The dictionary can be seen as the heart of the MRF framework; it is the database that contains all physiologically possible signal evolutions that may be observed from the acquisition and that makes it possible to recognize the tissue within each voxel. MRF, like the forensic fingerprinting identification process, is effective only when a database large enough to contain all the potential candidates is available. In MRF, the dictionary is generated on a computer using algorithms that simulate the spin behavior during the acquisition and thus predict the realistic signal evolution. In case of a TrueFISP-based acquisition, the Bloch equations [26] are used to simulate the various effects of the acquisition sequence on the spins, given a set of tissue parameters of interest (Fig. 2D). The information that can be retrieved with MRF is thus related to how and what physical effects are simulated. In the initial stages of development, MRF includes the simulation of T1, T2 and off-resonance, but more tissue features can be simulated and extracted, such as partial volume [19], diffusion [27] and perfusion [28].

A critical aspect of the dictionary is its size: to ensure the identification of any possible tissue parameter present in the acquisition, a wide combination of T1, T2 and off-resonance frequency need to be simulated. A standard TrueFISP dictionary with the parameter ranges as shown in Table 1 leads to a total of 363,624 possible combinations and includes the parameter values that are commonly found in the human body. The computation of

Parameter	TrueFISP			FISP		
	Min value	Max value	Step size	Min value	Max value	Step size
T1 (ms)	100	2000	20	20	3000	10
	2000	5000	300	3000	5000	200
T2 (ms)	20	100	5	10	300	5
	100	200	10	300	500	50
	200	1900	200	500	900	200
Off-resonance (Hz)	-250	-190	20			
	-50	50	1			
	190	250	20			

Table 1: Ranges and step sizes used for the dictionary creation in case of a TrueFISP sequence (left) or FISP sequence (right).

such a dictionary for 1000 time points takes about 2.5 minutes on a standard desktop computer using a C++ based script and reaches 2.5 GB of memory size. A further increase in the dictionary size and/or resolution would increase the accuracy of the obtained maps at the expenses of an increase in the reconstruction time and memory requirements [19].

The simulation of a FISP acquisition is computed differently compared to the one described above. Since the FISP acquisition requires the simulation of multiple isochromats at different frequencies, which are then combined together, the simulation process through Bloch equations can be time consuming. An alternative time-efficient simulation is the extended phase graph (EPG) formalism [29], where a spin system affected by the sequence can be represented as discrete set of phase states, ideal to simulate the signal evolution of spins strongly dephased by unbalanced gradients. The FISP sequence is less sensitive to off-resonance effects compared to the TrueFISP acquisition, so the corresponding dictionary includes only the T1 and T2 relaxation times (Table 1) as the parameters of interest. This leads to 18,838 dictionary entries that can be computed in about 8 minutes on a standard desktop computer, and that generates a dictionary of about 1.2 GB.

Regardless of which sequence is used, the dictionary needs to be computed only once beforehand. It can then be used on the scanner, where it is used to reconstruct each MRF acquisition acquired with the sequence parameters that were simulated.

Matching

After the data acquisition, the fingerprint of each voxel (Fig. 2F) is normalized to unit norm and compared with all the normalized dictionary entries to identify the tissue in a given voxel (Fig. 2E). The simplest version of the matching is performed by taking the inner product between the voxel signal and each simulated fingerprint signal; the entry that returns the highest value is considered to be the one that best represents the tissue properties, and the respective T1, T2 and off-resonance values are assigned to the voxel (Fig. 2G). The relative spin density (M_0) map, instead, is computed as the scaling factor between the acquired and the simulated fingerprints. The inner product has been demonstrated to be a robust operation and is able to correctly classify the tissues even in case of low SNR due to undersampling or even in the presence of a limited amount of motion artifacts [19].

This approach has also the potential of distinguishing different tissue components present within a single voxel (partial volume effect) thanks

to the incoherence between different signal evolutions. The fingerprint (S) of a voxel containing different tissue can be seen as the weighted sum (w) of the different components (D): $S = Dw$. It has been shown [19] that, if the different components are known a priori, the appropriate inverse solution of the previous equation – $(D)^{-1}S = w$, where $(D)^{-1}$ represents the pseudoinverse of D – will provide the weight of each different tissue for each voxel [19,31].

The pattern recognition algorithm is performed on the scanner for every acquisition, so it is crucial for the clinical usefulness of the MR framework that this operation is performed in a reasonable time. While the direct matching using the inner product is accurate, it can take up to about 160 seconds to match a 2D slice of 128 x 128 base resolution, 1000 time points with a dictionary counting 363 624 entries. Similarly it takes about 30 seconds to match a 2D image with 256 x 256 voxels, 1000 time points and 18,838 dictionary entries for a FISP reconstruction.

The matching can be potentially accelerated by compressing the dictionary either in the time dimension or in the parameter combinations dimension, thus reducing the total number of comparisons that need to be performed. It has been shown [31] that the singular value decomposition (SVD) can be applied to compress the dictionary in the time dimension and reduce the matching time by a factor of 3.4 times for a TrueFISP dictionary and up to a factor of 4.8 times for a FISP dictionary. The SVD-based dictionary compression has less than 2% of reduction in the accuracy of the estimated parameters. In this approach, the dictionary is projected into a subspace of lower dimension spanned by the first 25-200 singular vectors obtained from the SVD. The acquired fingerprint is projected onto the same subspace, and the matching is performed using the projected signal and the compressed dictionary. This framework reduces the number of calculations, thus reducing the final computation time despite the added

operation of data projection on the subspace.

An alternative approach for reducing computational time for matching is by reducing the parameter combination dimension. A fast group matching algorithm [32] has been developed, where dictionary entries that have strong correlations are grouped together and a new signal that best represents the group is generated. The matching is thus subdivided in two steps; at first the acquired fingerprint is matched with the representing signal of each group, and only groups that return the highest correlation are kept in consideration. Then matching is used to find the best fit between the fingerprint and the remaining dictionary entries for the assignment of the parameters. This algorithm reduces the matching computation speed of one order of magnitude compared to the SVD compression and two orders of magnitude compared to the direct matching with no significant loss in the quality of the match. Techniques such as this make it feasible to implement MRF in a clinical manner.

Undersampling and motion

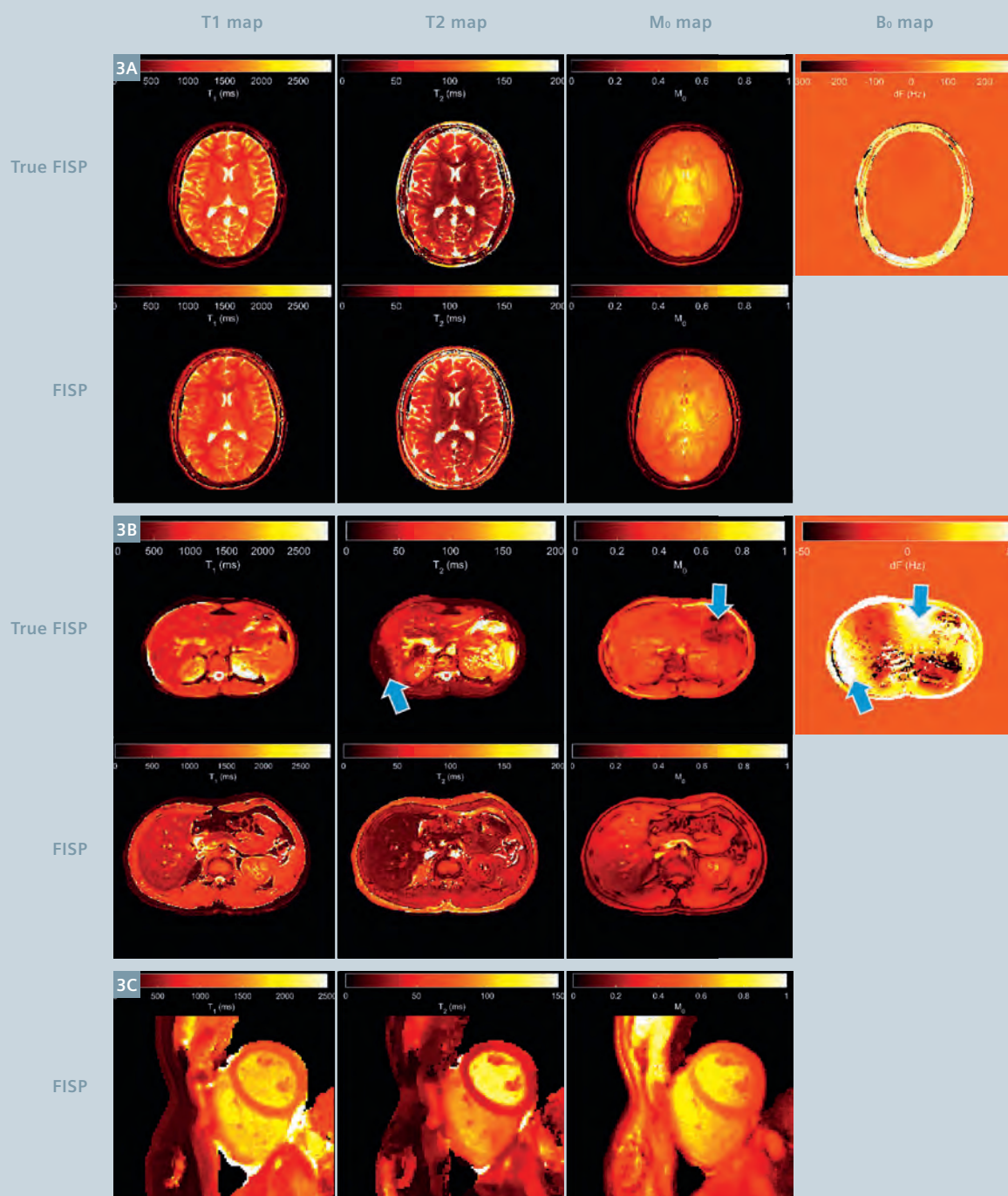
In MRF, the obtained parameter maps are the result of a pattern recognition algorithm as opposed to conventional reconstruction techniques, which allows MRF to be more robust to various image artifacts. This effect is strengthened by the random variation of FA, TR and trajectory which not only aim at differentiating the fingerprints from different tissues, but also aim at increasing the incoherence between the fingerprints. The matching can recognize the underlying signal evolutions even in low signal-to-noise or accelerated conditions as long as the noise or undersampling artifacts are incoherent with the signal. Additionally, just like in forensic fingerprinting, a correct identification is possible even with the use of blurry or partial fingerprints, the MR counterpart is also capable of providing parametric maps without any residual motion artifacts in case of a fingerprint partially corrupted by motion [19].

Volunteer acquisitions

MRF acquisitions have been tested in volunteers in 2D brain, abdominal, and cardiac scans. All *in vivo* experiments were performed under the Institutional Review Board guidelines and each subject signed informed consent prior to the data acquisition. The scans were performed on a 3T MAGNETOM Skyra system with a 20-channel head coil or a phased array 18-channel body coil plus spine coil. For the brain scans, the variable acquisition parameters (FA and TR) were set as described above and 3000 time points were acquired; the FOV was 300 x 300 mm, the slice thickness was 5 mm and the matrix size was 256 x 256. The acquisition time was 38 s for a 2D TrueFISP slice and 41 s for the FISP acquisition. The cardiac MRF scans were acquired using a modified pulse sequence with ECG triggering to restrict data collection to mid-diastole [35]. A total of 768 time points were acquired over a 16-heartbeats breath-hold using a scan window of 250 ms with FOV 300 x 300 mm, slice thickness 8 mm, and matrix size 192 x 192 [35]. For the abdominal and cardiac imaging, the trajectory and acquisition protocols were adapted as described in references [21, 35] respectively. The dictionaries were computed as described above and SVD based matching was used for parameter estimation.

Figure 3 shows the maps obtained from volunteer scans in the brain (Fig. 3A), abdomen (Fig. 3B), and heart (Fig. 3C). Both FISP and TrueFISP MRF provide comparable high resolution multiparametric tissue maps. The FISP acquisition has the drawback of not providing the off-resonance information, but it has the advantage of being insensitive to banding artifacts. Therefore, FISP MRF is advantageous for body imaging, where the sharp susceptibility transitions and the need for a large field-of-view would lead to banding artifacts with a balanced SSFP acquisition.

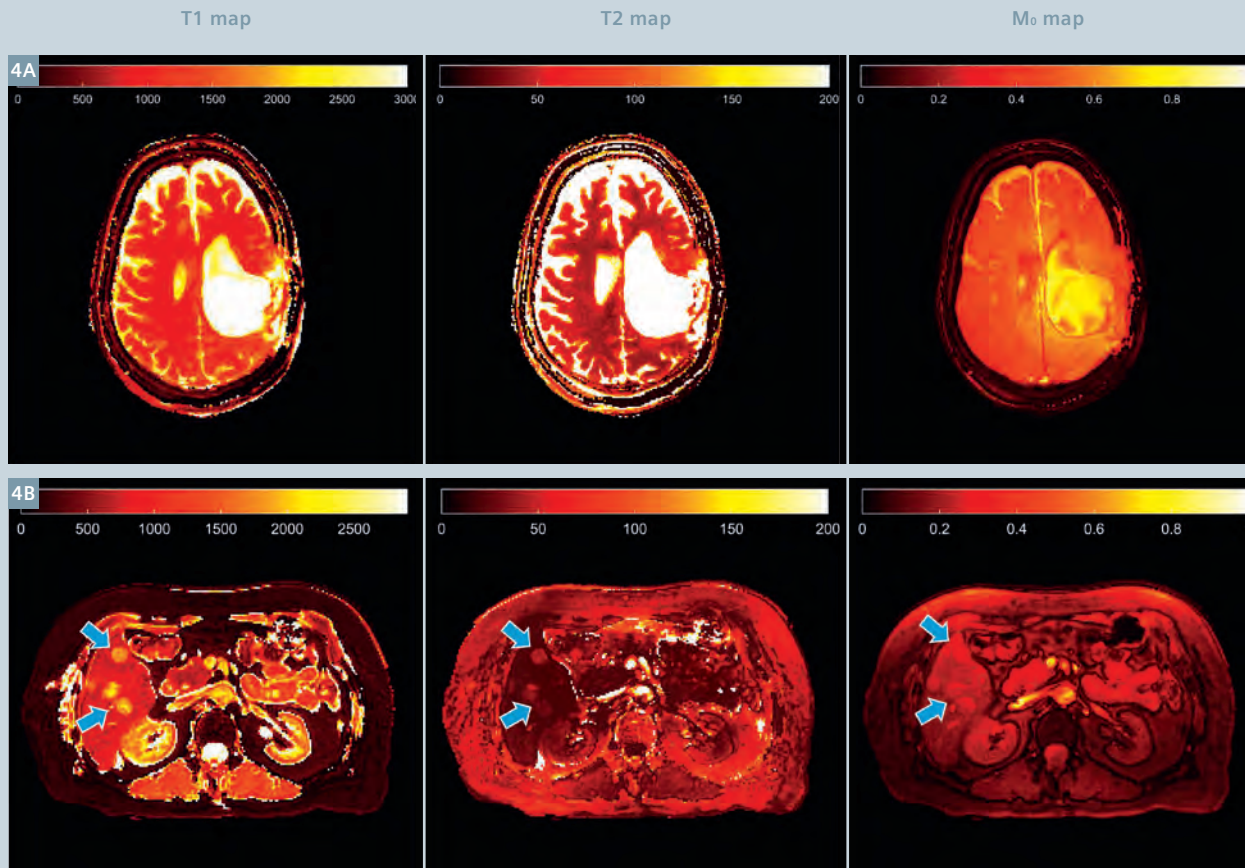
The values obtained with MRF maps are generally in good agreement with the standard mapping techniques [20] and with the literature value of tissue parameters [19, 24], as shown in table 2. It can be noticed, though,



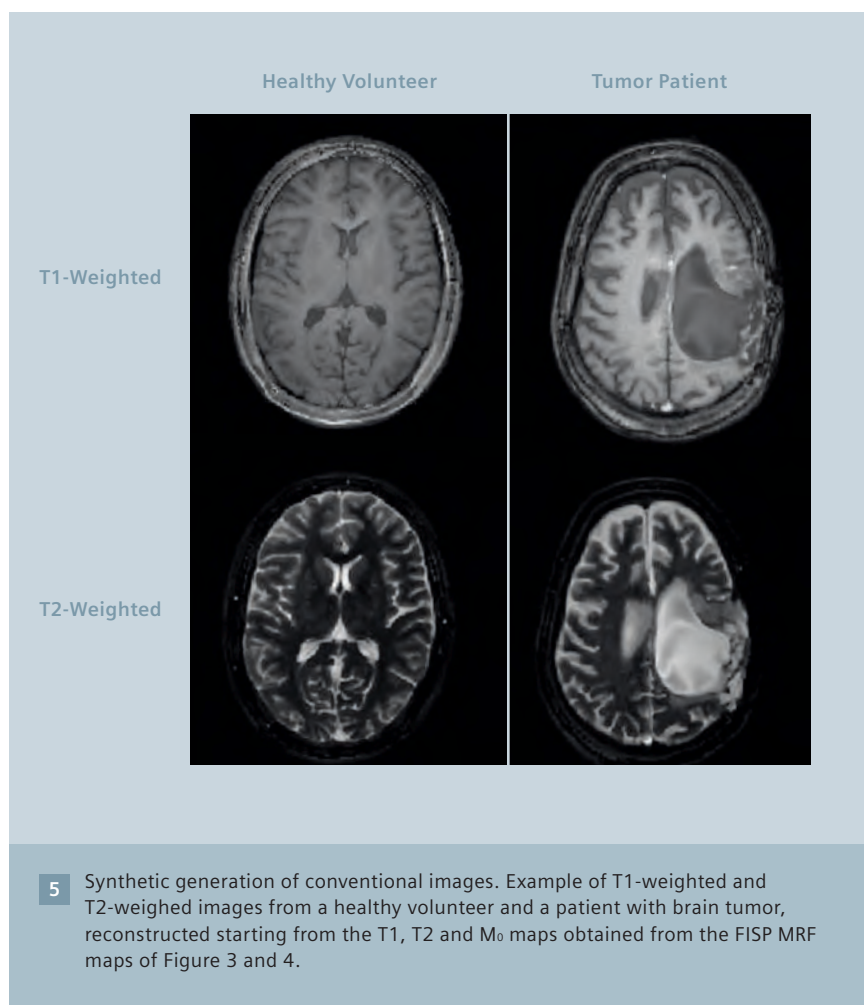
3 Examples of T1, T2, relative spin density (M_0) and off-resonance (B_0) maps acquired in two volunteers with a TrueFISP and a FISP acquisition. **(3A)** Single 2D slice of a head scan. **(3B)** Single 2D slice of an abdominal scan. **(3C)** Single 2D slice of diastolic cardiac scan in short axis view. In the T2 and B_0 map obtained from the TrueFISP acquisition, banding artifacts due to field inhomogeneity are visible (blue arrows).

Tissue	T1 (ms)		T2 (ms)	
	MRF	Literature	MRF	Literature
White matter	685 ± 33 [19]	608–756 [34, 40–42]	65 ± 4 [19]	54–81 [34, 40–42]
	781 ± 61 [20]	788–898 [43]	65 ± 6 [20]	78–80 [43]
Gray matter	1180 ± 104 [19]	998–1304 [34, 40–42]	97 ± 5.9 [19]	78–98 [34, 40–42]
	1193 ± 65 [20]	1286–1393 [43]	109 ± 11 [20]	99–117 [43]
Cerebrospinal fluid	4880 ± 379 [19]	4103–5400 [34, 40–42]	550 ± 251 [19]	1800–2460 [34, 40–42]
Liver	745 ± 65 [21]	809 ± 71 [44]	31 ± 6 [21]	34 ± 4 [44]
Kidney medulla	1702 ± 205 [21]	1545 ± 142 [44]	60 ± 21 [21]	81 ± 8 [44]
Kidney cortex	1314 ± 77 [21]	1142 ± 154 [44]	47 ± 10 [21]	76 ± 7 [44]
Skeletal muscle	1100 ± 59 [21]	1017 ± 78 [45]	44 ± 9 [21]	50 ± 4 [46]
Fat	253 ± 42 [21]	343 ± 37 [45]	77 ± 16 [21]	68 ± 4 [44]

Table 2: List of T1 and T2 relaxation times measured with MRF for different tissues and comparison with the value available in literature.



4 Example of patient results. Quantitative T1, T2 and relative spin density (M₀) maps obtained using the FISP protocol for brain [16] and abdomen acquisitions [20]. (4A) Maps of a patient with a brain tumor; (4B) 69-year-old patient with metastatic breast cancer. The metastasis (blue arrows) presents an increase in all tissue parameters, compared to the surrounding tissues.



that there is a mismatch in the values of CSF and fat. The CSF T2 discrepancy between MRF and literature value can be explained by through-plane motion of the fluid that was not taken into account in the dictionary simulation [19]. The fat T1 discrepancy, instead, is mainly due to the intentionally low T1 dictionary resolution (100 ms) for the range 100–600 ms used for that study [21].

The MRF efficiency is extremely high compared to traditional mapping approaches [19–21] as well as rapid combined T1 and T2 mapping methods like DESPOT [19, 36]. The high efficiency and accuracy of the MRF framework enable parametric mapping to be performed in a clinically relevant acquisition time without loss of information. In this way, multiparametric mapping can be translated to the clinical environment.

Patient acquisitions

The MRF framework has also been successfully tested on patients. Figure 4 shows the feasibility of brain and abdominal MRF in a clinical environment. Data were acquired with the previously described FISP acquisitions on patients with a brain tumor and breast cancer metastatic to the liver (Fig. 4). Longer T1 relaxation time can be observed in the metastatic lesions compared to the surrounding tissues. It has been shown in six patients with metastatic adenocarcinoma that the mean T1 and T2 values in the metastatic adenocarcinoma were on the order of 1673 ± 331 ms and 43 ± 13 ms, respectively. Those values are significantly higher than the ones of the surrounding tissues (840 ± 113 ms and 28 ± 3 ms, respectively) [21]. Recent studies investigate the possibility of predicting response of tumor

to treatment using tissue relaxation times; e.g. the T1 relaxation time can potentially be an indicator of chemotherapy response [35, 36]. Fast multiparametric mapping can thus open the path to the creation of a multiproperty space that might allow a deeper characterization and understanding of the conditions and evolutions of determined pathologies.

Synthetic weighted images

It is also possible to retrospectively calculate and estimate 'standard' weighted images from the multiple parameter maps obtained from an MRF scan. Figure 5 shows an example of T1-weighted and T2-weighted acquisition calculated from the FISP T1 and T2 maps of the volunteer and patient head scan shown above.

Conclusions

Magnetic resonance fingerprinting is a novel framework for MRI, where the pulse sequence design is not aimed at acquiring images, but at directly measuring tissue properties. In MRF, the sequence generates unique signal evolutions, or fingerprints, for each different tissue and matches it with a set of theoretical signal evolutions to measure several tissue properties within a single acquisition. Once the tissue features are measured, it is possible to directly know several tissue-specific properties that can synergistically provide all the information to improve diagnosis, prognosis and/or therapeutic assessment. In this work, only two MRF implementations have been shown, but the MRF framework has the potential to allow more freedom in the sequence design compared to standard MRI sequences, since the parameters can be randomly varied. Thanks to this freedom, a whole new world of possibilities of acquisition and reconstruction strategies that can probe and measure new features have been opened up for our community to explore.

This paper focused on T1, T2, M_0 and B_0 characterization, but the MRF is not limited to that. Several work are being performed to exploit the potential of MRF including: diffusion

[27], arterial spin labeling [28, 42, 43] and chemical exchange [44].

The pattern recognition nature of MRF makes the acquisition robust to artifacts like undersampling and motion, yielding high efficiency, accuracy and robustness that are critical for the successful integration of a multiparametric mapping technique into the clinical environment. Moreover, the increased efficiency and robustness to artifacts compared to standard MR imaging approaches could potentially reduce the time and thus the costs of MRI exams, making it more affordable and more competitive in comparison to other imaging modalities.

References

- Larsson H, Frederiksen J. Assessment of demyelination, edema, and gliosis by in vivo determination of T1 and T2 in the brain of patients with acute attack of multiple sclerosis. *Magn Reson Med* [Internet]. 1989;348:337–48. Available from: <http://onlinelibrary.wiley.com/doi/10.1002/mrm.1910110308/abstract>
- Usman AA, Taimen K, Wasielewski M, et al. Cardiac magnetic resonance T2 mapping in the monitoring and follow-up of acute cardiac transplant rejection: a pilot study. *Circ Cardiovasc Imaging* [Internet]. 2012;5(6):782–90. Available from: <http://www.ncbi.nlm.nih.gov/pubmed/23071145>
- Payne AR, Berry C, Kellman P, et al. Bright-blood T2-weighted MRI has high diagnostic accuracy for myocardial hemorrhage in myocardial infarction: a preclinical validation study in swine. *Circ Cardiovasc Imaging*. 2011;4(6):738–45.
- Van Heeswijk RB, Feliciano H, Bongard C, et al. Free-breathing 3 T magnetic resonance T2-mapping of the heart. *JACC Cardiovasc Imaging* [Internet]. 2012 Dec;5(12):1231–9. Available from: <http://www.ncbi.nlm.nih.gov/pubmed/23236973>
- Iles L, Pfluger H, Phrommintikul A, et al. Evaluation of Diffuse Myocardial Fibrosis in Heart Failure With Cardiac Magnetic Resonance Contrast-Enhanced T1 Mapping. *J Am Coll Cardiol*. 2008;52(19):1574–80.
- Hernando D, Levin YS, Sirlin CB, Reeder SB. Quantification of liver iron with MRI: state of the art and remaining challenges. *J Magn Reson Imaging* [Internet]. 2014 Nov;40(5):1003–21. Available from: <http://www.pubmed-central.nih.gov/articlerender.fcgi?artid=4308740&tool=pmcentrez&rendertype=abstract>
- Reeder SB, Cruite I, Hamilton G, Sirlin CB. Quantitative assessment of liver fat with magnetic resonance imaging and spectroscopy. *J Magn Reson Imaging* [Internet]. 2011 Oct;34(4):729–49. Available from: <http://www.ncbi.nlm.nih.gov/pubmed/21928307>
- Look DC, Locker DR. Time saving in measurement of NMR and EPR relaxation times. *Rev Sci Instrum*. 1970;41(2):250–1.
- Huang TY, Liu YJ, Stemmer A, Poncelet BP. T2 measurement of the human myocardium using a T2-prepared transient-state trueFISP sequence. *Magn Reson Med*. 2007;57:960–6.
- Mehta BB, Chen X, Bilchick KC, Salerno M, Epstein FH. Accelerated and navigator-gated look-locker imaging for cardiac T1 estimation (ANGIE): Development and application to T1 mapping of the right ventricle. *Magn Reson Med*. 2015;73(1):150–60.
- Zhu DC, Penn RD. Full-brain T1 mapping through inversion recovery fast spin echo imaging with time-efficient slice ordering. *Magn Reson Med*. 2005;54(3):725–31.
- Cheng H-LM, Wright GA. Rapid High-Resolution T1 Mapping by Variable Flip Angles: Accurate and Precise Measurements in the Presence of Radio-frequency Field Inhomogeneity. *Magn Reson Med*. 2006;55:566–76.
- Doneva M, Börner P, Eggers H, Stehning C, Sénégas J, Mertins A. Compressed sensing reconstruction for magnetic resonance parameter mapping. *Magn Reson Med*. 2010;64(4):1114–20.
- Deoni SCL, Rutt BK, Peters TM. Rapid combined T1 and T2 mapping using gradient recalled acquisition in the steady state. *Magn Reson Med*. 2003;49(3):515–26.
- Blume U, Lockie T, Stehning C, et al. Interleaved T1 and T2 relaxation time mapping for cardiac applications. *J Magn Reson Imaging*. 2009;29:480–7.
- Wartjes JBM, Dahlqvist O, Lundberg P. Novel method for rapid, simultaneous T1, T2*, and proton density quantification. *Magn Reson Med*. 2007;57(3):528–37.
- Schmitt P, Griswold MA, Jakob PM, et al. Inversion recovery TrueFISP: quantification of T(1), T(2), and spin density. *Magn Reson Med*. 2004;51(4):661–7.
- Ehses P, Seiberlich N, Ma D, et al. IR TrueFISP with a golden-ratio-based radial readout: Fast quantification of T1, T2, and proton density. *Magn Reson Med*. 2013;69(1):71–81.
- Ma D, Gulani V, Liu K, et al. Magnetic resonance fingerprinting. *Nature* [Internet]. 2013;495(7440):187–92.
- Jiang Y, Ma D, Seiberlich N, Gulani V, Griswold M a. MR fingerprinting using fast imaging with steady state precession (FISP) with spiral readout. *Magn Reson Med* [Internet]. 2014;. Available from: <http://www.ncbi.nlm.nih.gov/pubmed/25491018>
- Chen Y, Jiang Y, Pahva Shivani, et al. MR Fingerprinting for Rapid Quantitative Abdominal Imaging. *Radiology*. 2016;000(0):1–9.
- Schmitt P, Griswold MA, Gulani V, Haase A, Flentje M, Jakob PM. A simple geometrical description of the TrueFISP ideal transient and steady-state signal. *Magn Reson Med*. 2006;55(1):177–86.
- Perlin K. An image synthesizer. *ACM SIGGRAPH Comput Graph*. 1985;19(3):287–96.
- Ma D, Pierre EY, Jiang Y, et al. Music-based magnetic resonance fingerprinting to improve patient comfort during MRI examinations. *Magn Reson Med* [Internet]. 2015; Available from: <http://doi.wiley.com/10.1002/mrm.25818>
- Lee JH, Hargreaves B a., Hu BS, Nishimura DG. Fast 3D Imaging Using Variable-Density Spiral Trajectories with Applications to Limb Perfusion. *Magn Reson Med*. 2003;50(6):1276–85.
- Bloch F. Nuclear induction. *Phys Rev*. 1946;70:460–85.
- Jiang Y, Wright KL, Seiberlich N, Gulani V, Griswold MA. Simultaneous T1, T2, diffusion and proton density quantification with MR fingerprinting. In: In proceedings of the 22nd annual meeting of ISMRM meeting & exhibition in Milan, Italy. 2014. p. 28.
- Wright KL, Ma D, Jiang Y, Gulani V, Griswold MA, Luis H-G. Theoretical framework for MR fingerprinting with ASL: simultaneous quantification of CBF, transit time, and T1. In: In proceedings of the 22nd annual meeting of ISMRM meeting & exhibition in Milan, Italy. 2014. p. 417.
- Weigel M, Schwenk S, Kiselev VG, Scheffler K, Hennig J. Extended phase graphs with anisotropic diffusion. *J Magn Reson*. 2010;205(2):276–85.
- Deshmane AV, Ma D, Jiang Y, et al. Validation of Tissue Characterization in Mixed Voxels Using MR Fingerprinting. In: In proceedings of the 22nd annual meeting of ISMRM meeting & exhibition in Milan, Italy. 2014. p. 0094.
- McGivney D, Pierre E, Ma D, et al. SVD Compression for Magnetic Resonance Fingerprinting in the Time Domain. *IEEE Trans Med Imaging*. 2014;0062(12):1–13.
- Cauley SF, Setsompop K, Ma D, et al. Fast group matching for MR fingerprinting reconstruction. *Magn Reson Med* [Internet]. 2014;00. Available from: <http://dx.doi.org/10.1002/mrm.25439>
- Hamilton JI, Jiang Y, Chen Y, et al. MRF for Rapid Quantification of Myocardial T1, T2, and Proton Spin Density. *Magn Reson Med*. 2016;In press.

- 34 Deoni SCL, Peters TM, Rutt BK. High-resolution T1 and T2 mapping of the brain in a clinically acceptable time with DESPOT1 and DESPOT2. *Magn Reson Med*. 2005;53(1):237–41.
- 35 Jamin Y, Tucker ER, Poon ES, et al. Evaluation of Clinically Translatable MR Imaging Biomarkers of Therapeutic Response in the TH- MYCN Transgenic Mouse Model of Neuroblastoma. *Radiology*. 2012.
- 36 Weidensteiner C, Allegrini PR, Sticker-Jantscheff M, Romanet V, Ferretti S, McSheehy PM. Tumour T1 changes in vivo are highly predictive of response to chemotherapy and reflect the number of viable tumour cells - a preclinical MR study in mice. *BMC Cancer*. 2014;14(1):88.
- 37 Christen T, Pannetier NA, Ni WW, et al. MR vascular fingerprinting: A new approach to compute cerebral blood volume, mean vessel radius, and oxygenation maps in the human brain. *Neuroimage* [Internet]. 2014 Apr 1 [cited 2015 Nov 19];89:262–70. Available from: <http://www.pubmedcentral.nih.gov/articlerender.fcgi?artid=3940168&tool=pmcentrez&rendertype=abstract>
- 38 Pan S, Mao D, Peiying L, Yang L, Babu W, Hanzhang L. Arterial Spin Labeling without control/label pairing and post-labeling delay: an MR fingerprinting implementation. In: In proceedings of the 23rd annual meeting of ISMRM meeting & exhibition in Toronto, Canada. 2015. p. 0276.
- 39 Hamilton JI, Deshmane AV, Stephanie H, Griswold MA, Seiberlich N. Magnetic Resonance Fingerprinting with Chemical Exchange (MRF-X) for Quantification of Subvoxel T1, T2, Volume Fraction, and Exchange Rate. In: In proceedings of the 23rd annual meeting of ISMRM meeting & exhibition in Toronto, Canada. 2015. p. 0329.
- 40 Vymazal J, Righini A, Brooks RA, et al. T1 and T2 in the Brain of Healthy Subjects, Patients with Parkinson Disease, and Patients with Multiple System Atrophy: Relation to Iron Content. *Radiology*. 1999;211(2):489–95.
- 41 Whittall KP, MacKay AL, Graeb DA, Nugent RA, Li DK, Paty DW. In vivo measurement of T2 distributions and water contents in normal human brain. *Magn Reson Med*. 1997;37(1):34–43.
- 42 Poon CS, Henkelman RM. Practical T2 quantitation for clinical applications. *J Magn Reson Imaging*. 1992;2(5):541–53.
- 43 Wansapura JP, Holland SK, Dunn RS, Ball WS. NMR relaxation times in the human brain at 3.0 tesla. *J Magn Reson Imaging*. 1999;9(4):531–8.
- 44 de Bazelaire CM, Duhamel GD, Rofsky NM, Alsop DC. MR imaging relaxation times of abdominal and pelvic tissues measured in vivo at 3.0 T: preliminary results. *Radiology*. 2004;230(3):652–9.
- 45 Chen Y, Lee GR, Aandal G, et al. Rapid volumetric t1 mapping of the abdomen using three-dimensional through-time spiral GRAPPA. *Magnetic Resonance in Medicine*. 2016 Apr;75(4):1457–65.
- 46 Stanisz GJ, Odobina EE, Pun J, et al. T1, T2 relaxation and magnetization transfer in tissue at 3T. *Magn Reson Med* [Internet]. 2005/08/09 ed. 2005;54(3):507–12. Available from: <http://www.ncbi.nlm.nih.gov/pubmed/16086319>.

Contact

Vikas Gulani, M.D.
 Department of Radiology
 Case Western Reserve University
 University Hospitals Case Medical Center
 11100 Euclid Ave
 Bolwell Building, Room B120
 Cleveland, OH 44106
 USA
vxg46@case.edu



New Strategies for Protocol Optimization for Clinical MRI: Rapid Examinations and Improved Patient Care

Otto Rapalino, M.D.¹; Keith Heberlein, Ph.D.²

¹ Neuroradiology Division, Department of Radiology, Massachusetts General Hospital, Boston, MA, USA

² Director of Neuro Applications Development, Siemens Healthcare USA

Heightened attention to healthcare costs and value based outcomes in medicine are driving revolutionary changes in the MR industry. The MR community of academics, clinicians and industry experts need to build cooperative programs to dispel the old perceptions of MR as a slow and overly expensive imaging modality. Cooperative changes can be implemented on two fronts through utilization of advanced technology, revised reading procedures, and a culture change around the standard operations of MR. Siemens MR, in cooperation with Massachusetts General Hospital (MGH) in Boston, are building such a program with the first results now being made available with the recent launch of GOBrain, a new application which enables a push-button diagnostic brain examination in 5 minutes. This article will detail the strategic approach behind the implementation of GOBrain and then discuss briefly

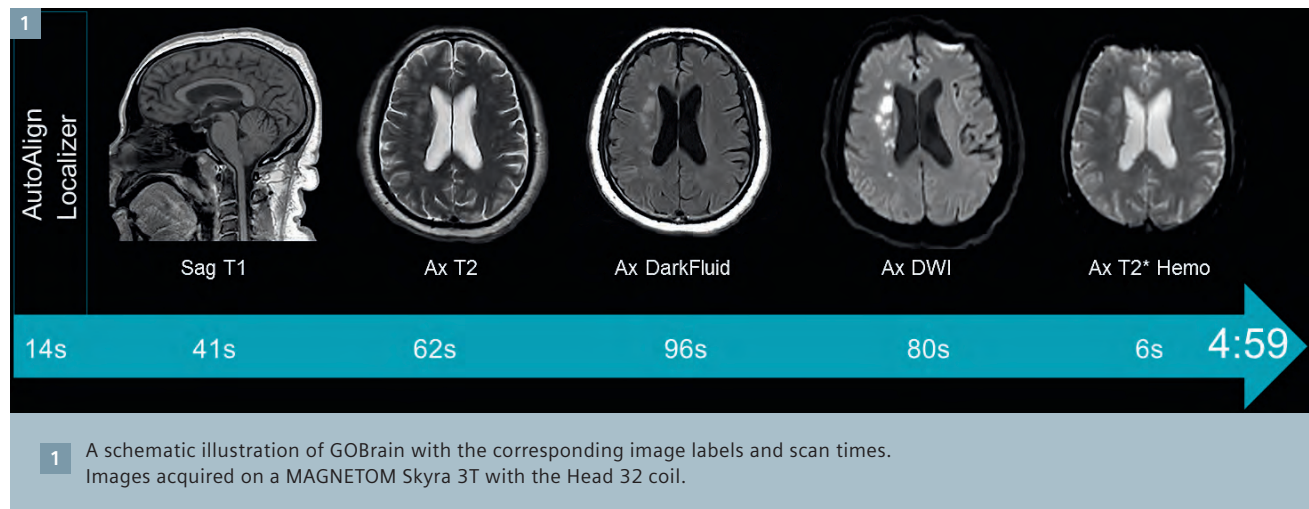
future potential extensions to GO (Generalized Optimized) strategies to develop fast and clinically validated examinations in MR.

GOBrain is a clinically validated diagnostic brain exam which takes 5 minutes¹. It consists of five diagnostically-important MR brain protocols [1, 2] acquired with optimized pulse sequences. Integrated with individual anatomical landmark-based AutoAlign technology providing automatic slice positioning, this push-button exam requires minimal interaction from the technologist. The included sequences are a sagittal T1-weighted, axial T2-weighted, axial T2-weighted DarkFluid, axial diffusion-weighted and an axial T2*-weighted contrast. Within the allotted five minutes for the complete exam, contrasts with stronger diagnostic utility were prioritized and afforded longer acquisition times, with the decided order of prioritization set as the DarkFluid, T2-weighted, diffusion,

T1-weighted and the T2*-weighted contrasts. The axial views cover the same field-of-view (FOV) and are acquired with identical slice thickness in order to read out multiple contrasts with synchronized display protocols (Fig. 1).

MR technologies which enabled the realization of GOBrain include parallel imaging [3] with high channel density coils [4, 5] and 3 Tesla imaging. The original expectation was that rapid exams could only be facilitated by higher field strength and high channel systems. However, during the course of the development effort, it became clear that the methodical approach towards a GO protocol optimization could also impact 1.5 Tesla systems and lower channel count head coils with some modest increase in total

¹ Achieved on a MAGNETOM Skyra with the Head 32 coil. Total examination time can take up to 6 minutes depending on system field strength and coil density.



scan time (see Appendix for the protocols across 1.5T and 3T systems). A key driving principle behind GOBrain was to preserve the image impressions in terms of contrast and resolution for radiological reading of routine MR exams and, at the same time, finding signal-to-noise ratio (SNR) limits acceptable for diagnostic imaging. A salient correlation can be made to the recent drive towards dose reduction in computed tomography (CT). With innovative developments in CT on the technology side, (e.g. dual energy), low-dose CT protocols were also developed for targeted applications where the diagnostic quality of the images is tuned to the application. Borrowing a similar approach and strategy in MR leads to a reframing of the protocol development goal towards a scan session which is as fast as reasonably achievable while maintaining at least the same diagnostic value.

A key step in the development of GOBrain was to establish the diagnostic equivalence of a rapid MR approach versus conventional examinations. The validation approach required two board-certified radiologists to perform double blind reads of clinical neuro exams and to score the images with regard to contrast, SNR and artifacts in 6 patient exams. To control for motion behavior in patients, the five-minute exam was placed randomly either prior to the conventional exam or after in order to average out any effects related to the order of acquisition. Additionally, both the rapid and conventional exams were read with clinical findings reported. The principle findings of the study (submitted to a peer reviewed journal for publication) [2] were that the rapid exam was

- 1) less prone to motion artifacts
- 2) of sufficient quality to make the diagnosis and
- 3) made no difference in the final radiological diagnosis.

These findings led to the primary conclusion that this fast examination may replace the conventional protocol, especially in motion-prone inpatient settings.

Adoption of rapid MRI protocols into the clinical service can trigger a culture change in the clinical team. Adaptations may be required to operations in terms of both workflow and training. GOBrain is a push button exam with automatic slice and orientation positioning and each sequence will run automatically one after the other. The scanner noise changes in pitch and volume during the continuously driven exam. However, if the technologists allow the scanner to run through the multiple contrasts without interaction, then the entire exam becomes a single protocol from the patient perspective. The acquisition is built with fast, individual sequences, which minimize the risk of motion artifacts. Also, if one contrast is corrupted by motion artifacts then only that single contrast needs to be reacquired. In a patient-centered approach, a rapid MR can substantially improve the patient experience at the scanner.

In the realm of personalized medicine, advanced imaging techniques will be required to address additional structural and functional markers of the disease process. The scan time requirements for acquiring enhanced imaging biomarkers need to be balanced with the increasing pressure on reducing scheduling time slots towards 30 minutes and below. A rapid MR approach for a core brain protocol opens possibilities to incorporate imaging into time-restricted scan slots. With the recent availability of Simultaneous Multi-Slice (SMS) technology [6 – 9] which can greatly accelerate diffusion and BOLD imaging, this further reduces the time required for important functional information. Other examples of GOBrain potential add-on exams are susceptibility-weighted imaging (SWI), post-contrast MPRAGE, perfusion-weighted imaging and high-resolution 3D DarkFluid. GOBrain can then be viewed as a scout exam and also function as a backup scan in cases where the high-resolution 3D protocols are corrupted by motion.

Extension of the GO protocol projects are now under consideration for other high volume MR indications. The vision is to build a comprehensive suite of fast, optimized diagnostic protocols which are clinically validated. The general structured approach for developing a GO protocol is as follows:

- 1) Establish the time budget for a given core exam. The scan time goal should be considered a restraint on the protocol development process and should not be revised until completion of the protocol development exercise.
- 2) Define the set of required contrasts for routine diagnosis and rank them in order of clinical priority based on literature evidence. Each contrast should be given an individual time budget based on their relative diagnostic importance.
- 3) Research the available methods for the acceleration of each sequence. Prototype and iterate on individual protocol candidates for each contrast from the protocol simulator.
- 4) Once candidate protocols are identified, conduct healthy volunteer scans to assess image quality in terms of tissue contrast and signal to noise levels. Several iterations may be required to finalize the protocol.
- 5) Once finalized, perform head-to-head comparisons to conventional examinations in the target patient population to compare the rapid MR protocol to the conventional exam with blind reads by at least two board certified radiologists. The reports should contain a qualitative assessment of the image quality, such as contrast and presence of artifacts and diagnostic findings appropriate for the indication. Concordance between both protocols across readers then validates the clinical utility of the rapid protocol.

MAGNETOM Skyra, 3T, Head/Neck 64											Total exam time: 4:36			
Plane	TR (ms)	TE (ms)	FOV (mm)	Phase FOV (%)	Slices	Slice (mm)	Gap (%)	Matrix	Phase Direc-tions	iPAT factor	b-values	Direc-tions (no)	TA (mins)	
AutoAlign Head Scout														
3D	3.15	1.37	260	100	128	1.6	20	160	A-P	3	NA	NA	0:14	
T1 GRE FLASH														
Sag	240	2.46	220	100	35	4.0	20	256	A-P	3	NA	NA	0:34	
T2 TSE														
Axial	6200	78	220	87.5	25	5.0	20	256	R-L	3	NA	NA	1:02	
T2 TSE DarkFluid														
Axial	8000	114	220	87.5	25	5.0	20	256	R-L	3	NA	NA	1:20	
ep2d Diffusion														
Axial	4000	65	240	100	31	5.0	12	160	A-P	3	0,800	12	1:20	
ep2d T2*-weighted														
Axial	6120	30	220	100	25	5.0	20	128	A-P	1	NA	NA	0:06	

MAGNETOM Skyra, 3T, Head 32											Total exam time: 4:59			
Plane	TR (ms)	TE (ms)	FOV (mm)	Phase FOV (%)	Slices	Slice (mm)	Gap (%)	Matrix	Phase Direc-tions	iPAT factor	b-values	Direc-tions (no)	TA (mins)	
AutoAlign Head Scout														
3D	3.15	1.37	260	100	128	1.6	20	160	A-P	3	NA	NA	0:14	
T1 GRE FLASH														
Sag	240	2.46	220	100	35	4.0	20	256	A-P	2	NA	NA	0:41	
T2 TSE														
Axial	6200	78	220	87.5	25	5.0	20	256	R-L	3	NA	NA	1:02	
T2 TSE DarkFluid														
Axial	8000	119	220	87.5	25	5.0	20	256	R-L	2	NA	NA	1:36	
ep2d Diffusion														
Axial	4000	65	240	100	31	5.0	12	160	A-P	3	0,800	12	1:20	
ep2d T2*-weighted														
Axial	6120	30	220	100	25	5.0	20	128	A-P	1	NA	NA	0:06	

Appendix

The GOBrain exam consists of a localizer scout with AutoAlign functionalities and five fundamental unenhanced MRI sequences (sagittal T1-weighted, axial T2-weighted, axial DarkFluid/FLAIR, axial DWI and axial T2*-weighted MRI sequences). Depending on the field strength (1.5T and 3T) and the number of elements in the coil used for imaging, total exam time lasts between 4:36 minutes on a 3T system with the Head/Neck 64 coil to 5:56 minutes for imaging on a 1.5T system with the Head/Neck 20 coil. Protocol parameters including scan times are detailed above for each system.

References

- Mehan WA, Gonzales RG, Buchbinder BR, Chen JW, Copen WA, Gupta R, et al. Optimal brain MRI protocol for new neurological complaint. PLOS One 2014; 9(10): e110803. doi:10.1371/journal.pone.0110803.
- Prakkamakul S, Witzel T, Huang S, Boulter D, Borja MJ, Schaefer P, et al. Comparative analysis of image quality and diagnostic concordance between 5-minute and conventional magnetic resonance protocols for brain imaging. Manuscript submitted for publication 2016.
- Griswold MA, Jakob PM, Heidemann RM, Nittka M, Jellus V, Wang J, et al. GeneRalized Autocalibrating Partially Parallel Acquisitions (GRAPPA). Magn Reson Med 2002; 47:1202-1210.
- Keil B, Wald LL. Massively parallel MRI detector arrays. J Magn Reson 2013; 229: 75-89.
- Wiggins GC, Triantafyllou C, Potthast A, Reykowski A, Nittka M, Wald LL. 32-channel 3 Tesla receive-only phased-array head coil with soccer-ball element geometry. Magn Reson Med 2006; 56(1): 216-223.
- Setsompop K, Cohen-Adad J, Gagoski BA, Raji T, Yendiki A, Keil B, et al. Improving diffusion MRI using simultaneous multi-slice echo planar imaging. Neuroimage 2012; 63:569-580.

MAGNETOM Skyra, 3T, Head/Neck 20												Total exam time: 5:11	
Plane	TR (ms)	TE (ms)	FOV (mm)	Phase FOV (%)	Slices	Slice (mm)	Gap (%)	Matrix	Phase Directions	iPAT factor	b-values	Directions (no)	TA (mins)
AutoAlign Head Scout													
3D	3.15	1.37	260	100	128	1.6	20	160	A-P	3	NA	NA	0:14
T1 GRE FLASH													
Sag	240	2.46	220	100	35	4.0	20	256	A-P	2	NA	NA	0:41
T2 TSE													
Axial	6200	78	220	87.5	25	5.0	20	256	R-L	3	NA	NA	1:02
T2 TSE DarkFluid													
Axial	8000	119	220	87.5	25	5.0	20	256	R-L	2	NA	NA	1:52
ep2d Diffusion													
Axial	4200	72	240	100	31	5.0	12	160	A-P	2	0,800	12	1:16
ep2d T2*-weighted													
Axial	6120	30	220	100	25	5.0	20	128	A-P	1	NA	NA	0:06

MAGNETOM Aera, 1.5T, Head/Neck 20 (XJ and XQ gradients)												Total exam time: 5:56	
Plane	TR (ms)	TE (ms)	FOV (mm)	Phase FOV (%)	Slices	Slice (mm)	Gap (%)	Matrix	Phase Directions	iPAT factor	b-values	Directions (no)	TA (mins)
AutoAlign Head Scout													
3D	4.52	2.38	260	100	128	1.6	20	160	A-P	3	NA	NA	0:19
T1 SE													
Sag	595	11	230	100	27	5.0	20	256	A-P	2	NA	NA	1:11
T2 TSE													
Axial	4700	101	220	87.5	25	5.0	20	256	R-L	2	NA	NA	0:56
T2 TSE DarkFluid													
Axial	5700	80	220	87.5	25	5.0	20	256	R-L	1	NA	NA	2:03
ep2d Diffusion													
Axial	4500	89	240	100	31	5.0	12	128	A-P	2	0,800	12	1:21
ep2d T2*-weighted													
Axial	6120	75	220	100	25	5.0	20	128	A-P	1	NA	NA	0:06

- 7 Setsompop K, Cauley S, Wald L. (2015). Advancing diffusion MRI using SMS EPI. MAGNETOM Flash (Special SMS Supplement) 2015; 63:16-22.
- 8 Smith SM, Beckmann CF, Andersson J, Auerbach EJ, Bijsterbosch J, Douaud G, et al. Resting state fMRI in the Human Connectome Project. Neuroimage 2013; 80:144-168.
- 9 Ugurbil K, Auerbach EJ, Modeller S, Xu J, Vu A, Glasser MF, et al. Slice acceleration in the 3 Tesla component of the human connectome project. MAGNETOM Flash (Special SMS Supplement) 2015; 63:49-56.



Contact

Otto Rapalino, M.D.
 Neuroradiology Division
 Department of Radiology
 Massachusetts General Hospital
 55 Fruit Street
 Boston MA, 02114-2696
 USA
 Phone: +1 617-726-8320

Slice Specific Adjustment Improves the Image Quality of Whole-Body Diffusion-Weighted Examinations at 3T

Zhang Haibo¹; Xue Huadan²; Alto Stemmer³; Liu Hui⁴; Stephan Kannengiesser³; Berthold Kiefer³; Jin Zhengyu²

¹Department of Radiology, China-Japan Friendship Hospital, Beijing, China

²Department of Radiology, Peking Union Medical College Hospital, Peking Union Medical College and Chinese Academy of Medical Sciences, Beijing, China

³MR Application-Predevelopment, Siemens Healthcare, Erlangen, Germany

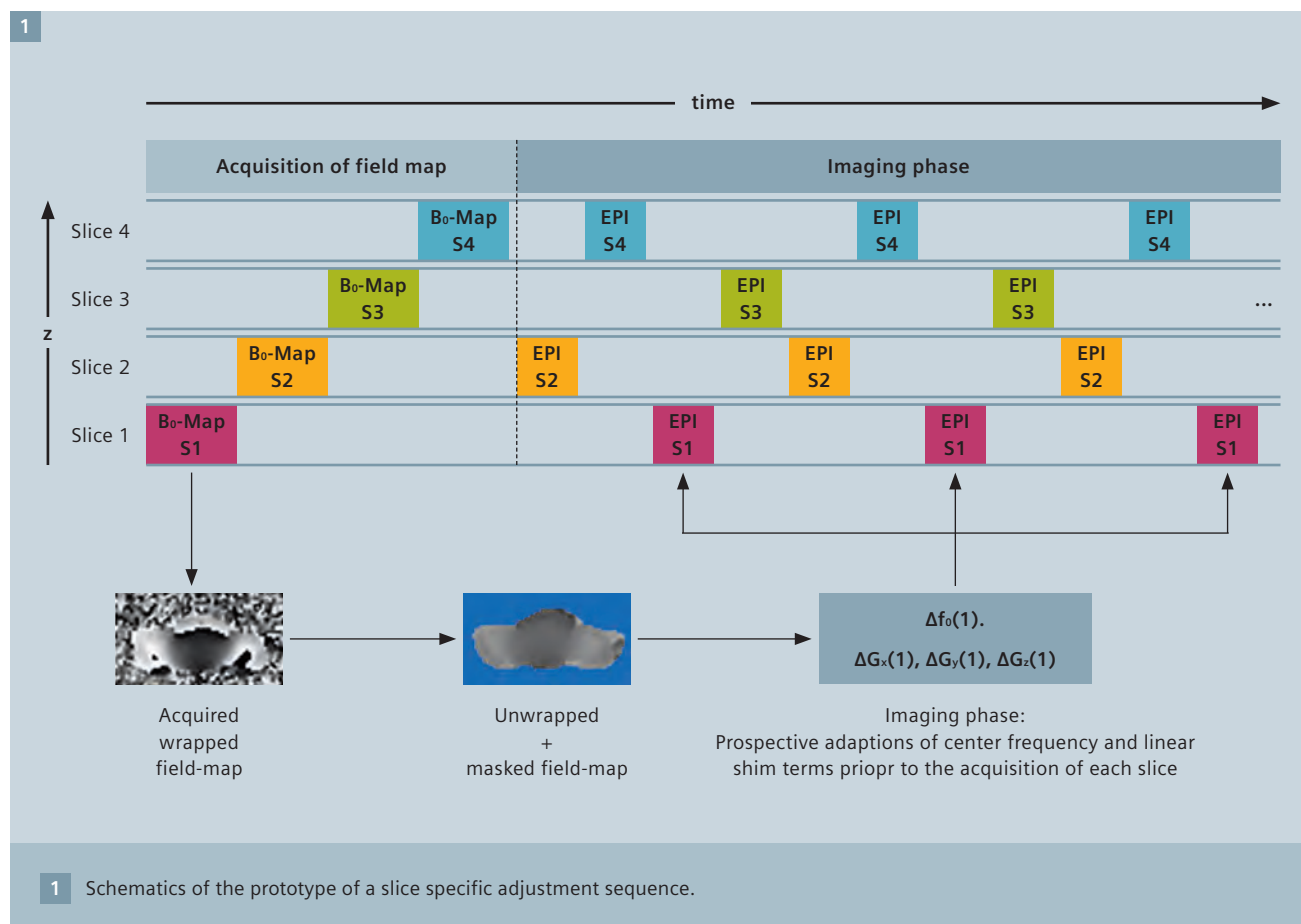
⁴MR Collaboration, Siemens Healthcare, Shanghai, China

Current whole-body diffusion-weighted imaging

Whole-body diffusion-weighted imaging (WBDWI) is considered a powerful clinical tool in the detection, characterization, and

treatment-response monitoring of tumors [1, 2]. It has been increasingly used in the evaluation of multiple myeloma, lymphoma, and skeletal metastases [3-8]. Being a measure of the microscopic water motion, WBDWI provides a quantita-

tive way of evaluating the tissue cellularity using the apparent diffusion coefficient (ADC). For example, whole-body magnetic resonance imaging including WBDWI is sensitive to multiple myeloma, especially in the case of diffuse bone marrow infiltration [9].



The combination of WBDWI with Fluorodeoxyglucose Positron Emission Tomography (FDG-PET) may provide a multiparametric assessment of tumors due to complementary imaging principles, where diffusion-weighted imaging (DWI) evaluates the tumor cellularity and the FDG-PET assesses the tumor metabolism [10].

At present it is challenging to meet the clinical demands for image quality with WBDWI at 3 Tesla. The signal-to-noise ratio (SNR) is increased at 3T, but it is still a challenge to perform WBDWI due to the drawback of single-shot echo planar imaging (EPI) acquisition and the stronger susceptibility effects, which lead to stronger geometric distortions and poor fat-suppression performance in specific body regions such as the neck. The distortions Δd in EPI are proportional to the physical field-of-view (FOV) in the phase-encoding direction (FOV_{PE}), the echo spacing Δt_{PE} , and the local off-resonance ΔB_0 ($\Delta d \sim FOV_{PE} \times \Delta t_{PE} \times \Delta B_0$). Recent technical developments in DWI acquisition such as readout segmented EPI [11, 12], other multi-shot [13] and zoomed techniques [14, 15] have shown improvements with less geometric distortion and higher image quality from the perspective of reducing Δt_{PE} or FOV_{PE} . However, the above techniques are not clinically feasible for whole-body imaging because of longer acquisition time, FOV restrictions, or sensitivity to motion.

Slice specific adjustment

Several past studies have shown the feasibility of reduced susceptibility artifact by dynamically updating optimized shim settings for each individual slice in a multi-slice acquisition [16]. Another study using slice-dependent adjustment has also shown improved image quality in 3T breast DWI [17]. However, its advantage to WBDWI is still unknown. The approach described here is to use slice specific adjustments for WBDWI, where a 2D multi-echo gradient echo (GRE) sequence preceding the WBDWI EPI scan is used to acquire a B_0 -map for each imaging slice. From the B_0 -map an optimal center frequency and linear shim

terms are determined for each imaging slice. Center frequency and gradient offsets are then updated before the acquisition of each EPI imaging slice in real time. In a recent study, its performance was evaluated, comparing slice specific adjustment¹ to a conventional pre-scan based shimming technique (3D Shim) [18].

For the 3D Shim protocol, one set of shim terms up to 2nd order is used for the entire slice stack of each patient table position, and the acquisition of the field map is included in the automatic scanner adjustment, which takes approximately 33 seconds per station (35 slices per station). Additionally, a single center frequency is determined in a separate frequency adjustment. Center frequency and shim currents are set once prior to the EPI scan.

For the slice specific adjustment protocol, the patient-specific 3D Shim procedure in the automatic scanner adjustment is disabled. The acquisition of the field map is integrated into the single-shot DWI EPI sequence. This prototype sequence first acquires 2D multi-gradient-echo images for each imaging slice with its FOV and orientation adapted from the respective imaging slice. The echo-time difference of the first and last echo is chosen such that fat and water are in-phase. Then a phase difference image is calculated from these two echoes. The remaining processing of the field map data is done in 3D and comprised phase unwrapping, background masking and a calibration to avoid global 2π offsets after unwrapping. For the dynamic shimming, a 2D plane is fitted to each field map slice to determine the center frequency and gradient offsets (1st order shim terms). Center frequency and gradient offsets are then updated before the acquisition of each EPI imaging slice in real time (Fig. 1). The time for the acquisition of the field map is approximately 540 ms per slice, or 19 s for a 35 slices station. Processing time of the field map is negligible.

Clinical evaluation

The evaluation of the slice specific adjustment technique for WBDWI in comparison to the conventional 3D Shim was performed at Peking Union Medical College Hospital. The slice specific adjustment and the 3D Shim WBDWI acquisitions with the exact same scan parameters were performed sequentially, and the impact of different shimming techniques on the image quality and detectability of conspicuous lesions were quantitatively analyzed and evaluated. Body-region-dependent signal-to-noise ratio (SNR), body-region-dependent shimming parameters, image quality, and the number of suspicious lesions were compared in 2 volunteers and 29 patients with suspected plasma-disorder. The results were as follows:

1. SNR

Two volunteers' position-dependent SNR ratio of slice specific adjustment over 3D Shim showed a significant SNR improvement with slice specific adjustment in the neck region, and a comparable SNR in other body regions. For the neck region, none of the 29 patients showed obvious signal loss with slice specific adjustment, while 25 patients showed partial to complete signal loss with 3D Shim scanning (Fig. 2).

2. Position-dependent slice specific adjustment parameters

The position-dependent slice specific adjustment parameters, center frequency shift, and linear frequency shift in phase-encoding direction, deviated significantly from the corresponding values of the 3D Shim settings only in the neck region, while they were comparable in the other body regions.

3. Image quality

Spatial displacement of DWI images was quantified by comparison with reformatted T2 SPACE images. This displacement was evaluated from cervical to coccyx vertebrae, excluding the neck region with signal loss

¹ WIP, the product is currently under development and is not for sale in the US and in other countries. Its future availability cannot be ensured.

(Figs. 2, 3). The mean absolute spatial displacement of the spine was 3.89 mm for slice specific adjustment and 7.21 mm for 3D Shim, respectively. The slice specific adjustment technique showed a significantly better illustration of the body shape than 3D Shim WBDWI.

4. Lesion detection assessment

Visual inspection of slice specific adjustment and 3D Shim DWI images side by side showed that the same lesions could be observed with both techniques in the thorax, abdomen and pelvis regions, while 24 of 72 lesions visible in slice specific adjustment DWI images of the neck region were not visible in 3D Shim DWI images; all lesions observed in 3D Shim DWI were also visible in slice specific adjustment DWI images.

Discussion

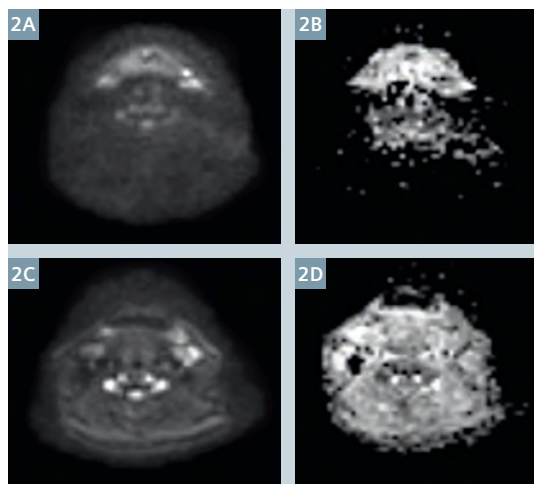
Signal loss is very common in the neck region of conventional 3D Shim WBDWI because there the B_0 varies rapidly along the head-foot direction caused by the sudden change of the body shape. Especially when a body station covers the neck and part

of the shoulder region, the 3D Shim adjustment may be insufficient since one single setting of resonance frequency and shim terms is not able to homogenize the B_0 field in the whole volume. In this study, the neck region showed a larger variation of center frequency shift and linear frequency shift in the phase-encoding direction than other body regions, and at the same time the lowest image quality of 3D Shim images, which supports this hypothesis. By applying a slice-based individual center frequency and gradient offset setting, the slice specific adjustment technique produced improved SNR and reliable image quality in the neck region and therefore outperforms 3D Shim. In other body regions such as thorax, abdomen and pelvis, there were no significant differences between slice specific adjustment and 3D Shim WBDWI for lesions and muscle.

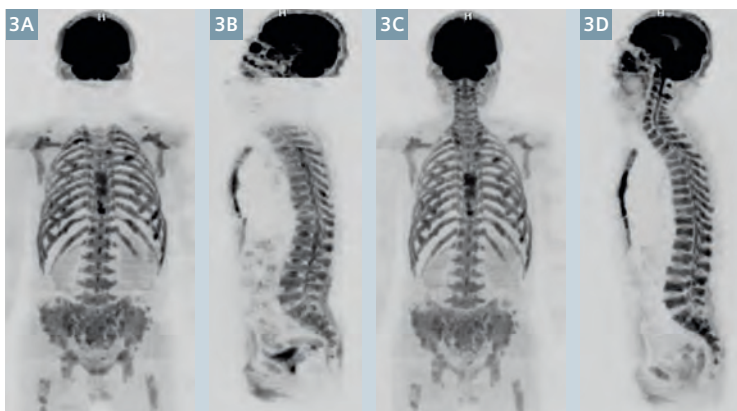
WBDWI provides a global assessment of whole-body tumor burden by visually assessing the signal intensity distribution on maximum intensity projections (MIPs) from high-b-value

images. But practically the whole-body images are acquired with multiple patient table positions, and are then composed to show the whole-body view (Fig. 3). Therefore, the signal homogeneity across different body parts is quite important, and lesions spanning images from adjacent patient table positions might be missed or misidentified as a result of large signal differences between these images. The image quality evaluation showed that the slice specific adjustment technique produced a smoother signal transition between adjacent patient table positions than the 3D Shim technique.

It is possible to further reduce the remaining distortions significantly with a recent extension of the slice specific adjustment prototype sequence as described in [19]. The modification combines the prospective slice-specific center-frequency adjustment and 1st order shimming with retrospective distortion correction based on the field-map method [20]. The field-map method uses a measured field-map to undo the distortion on a pixel-wise scale during post-processing. In the combined



- 2 Transversal view of the selected single slice of the neck of the same patient: (2A) 3D Shim DWI ($b = 800 \text{ s/mm}^2$), (2B) ADC map of 3D Shim DWI ($b = 800 \text{ s/mm}^2$), (2C) slice specific adjustment DWI ($b = 800 \text{ s/mm}^2$) and (2D) ADC map of slice specific adjustment DWI ($b = 800 \text{ s/mm}^2$). 2A, B showed massive signal loss in the neck region of 3D Shim DWI, however slice specific adjustment technique improved the image quality of the neck region obviously.



- 3 Maximum intensity projections (MIPs) with inverted grayscale from high-b-value WBDWI images. (3A, B) 3D Shim WBDWI images. The image quality of WBDWI was remarkably improved on 3T MRI. However, in the neck region a strong image quality deterioration can be observed. (3C, D) Slice specific adjustment WBDWI images. Compared with 3D Shim WBDWI, slice specific adjustment WBDWI showed artifact-free images.

method, the field-map needed for the distortion correction is not re-measured after center frequency adjustment and shimming but calculated from the field-map measured at the beginning and the known frequency and shim settings. It therefore does not prolong the acquisition time. It is a matter of further evaluation to enroll new patients to test the slice specific adjustment method together with retrospective distortion correction.

Short TI Inversion Recovery (STIR) fat suppression, which was used here, leads to lower SNR compared with chemical-shift-based fat suppression methods since water signal which is also inverted by the inversion pulse is not fully recovered at excitation time. Chemical shift based fat suppression techniques, however, are very sensitive to B_0 inhomogeneity [21, 22], so that the image quality can be degraded by fat ghosting or water suppression. As slice specific adjustment helps to significantly reduce the B_0 inhomogeneity, chemical shift based fat suppression techniques might provide an efficient fat suppression from head to toe. Chemical shift based fat suppression techniques like Spectral Adiabatic Inversion Recovery (SPAIR) are not compatible with slice specific adjustment as they exploit non-selective RF-pulses. Instead, slice selective water excitation could be used with slice specific adjustment. The inher-

ently higher SNR of water excitation may allow reducing the number of averages and hence the total acquisition time, and it merits evaluation in a clinical setting.

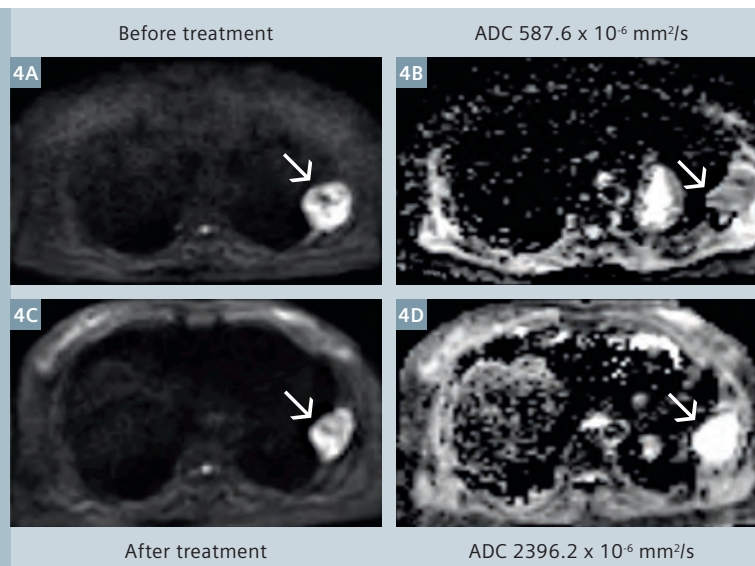
Conclusion

The slice specific adjustment technique is an effective method to reduce the negative impact of susceptibility effects on whole-body diffusion-weighted imaging at 3T, as supported by the apparent improvement in image quality, as well as improved SNR in the neck region. Compared with the 3D Shim technique, slice specific adjustment showed improved performance in detecting suspicious lesions in the neck region. The slice specific adjustment technique has entered the clinical arena, improving WBDWI. Slice specific adjustment and its future refinements may further improve the accuracy of lesion assessment and monitoring treatment response (Fig. 4).

References

- 1 Padhani AR, Liu G, Koh DM, et al. Diffusion-weighted magnetic resonance imaging as a cancer biomarker: consensus and recommendations. *Neoplasia* 2009;11(2):102–125.
- 2 Padhani AR, Koh DM, Collins DJ. Whole-body diffusion-weighted MR imaging in cancer: current status and research directions. *Radiology* 2011;261(3):700–718.
- 3 Attariwala R, Picker W. Whole body MRI: improved lesion detection and characterization with diffusion weighted techniques. *J MagnReson Imaging* 2013;38(2):253–268.
- 4 Petralia G, Padhani A, Summers P, et al. Whole-body diffusion-weighted imaging: is it all we need for detecting metastases in melanoma patients? *EurRadiol*. 2013;23(12):3466–3476.
- 5 Brioli A, Morgan GJ, Durie B, Zamagni E. The utility of newer imaging techniques as predictors of clinical outcomes in multiple myeloma. *Expert RevHematol* 2014;7(1):13–16.
- 6 Mayerhoefer ME, Karanikas G, Kletter K, et al. Evaluation of diffusion-weighted MRI for pretherapeutic assessment and staging of lymphoma: results of a prospective study in 140 patients. *Clin Cancer Res* 2014;20(11):2984–2993.
- 7 Littooij AS, Kwee TC, Barber I, et al. Whole-body MRI for initial staging of paediatric lymphoma: prospective comparison to an FDG-PET/CT-based reference standard. *EurRadiol* 2014;24(5):1153–1165.
- 8 Klenk C, Gawande R, Uslu L, et al. Ionising radiation-free whole-body MRI versus (18)F-fluorodeoxyglucose PET/CT scans for children and young adults with cancer: a prospective, non-randomised, single-centre study. *Lancet Oncol* 2014;15(3):275–285.
- 9 Zamagni E, Nanni C, Patriarca F, et al. A prospective comparison of 18F-fluorodeoxyglucose positron emission tomography-computed tomography, magnetic resonance imaging and whole-body planar radiographs in the assessment of bone disease in newly diagnosed multiple myeloma. *Haematologica*.2007; 92(1):50–55.
- 10 Schmidt H, Brendle C, Schraml C, et al. Correlation of simultaneously acquired diffusion-weighted imaging and 2-deoxy-[18F] fluoro-2-D-glucose positron

- 4 57-year-old female patient with multiple myeloma on the left chest wall (arrows). (4A, B) show a lesion with high signal on DWI ($b = 800 \text{ s/mm}^2$) image and low ADC value ($587.6 \times 10^{-6} \text{ mm}^2/\text{s}$) before treatment. (4C, D) show that the lesion still existed five months later after treatment, but ADC value was much higher than before. The change in ADC corresponds with the clinical results.



- emission tomography of pulmonary lesions in a dedicated whole-body magnetic resonance/positron emission tomography system. *Invest Radiol.* 2013;48(5):247-55.
- 11 Bogner W, Pinker-Domenig K, Bickel H, et al. Readout-segmented echo-planar imaging improves the diagnostic performance of diffusion-weighted MR breast examinations at 3.0 T. *Radiology* 2012;263(1):64-76.
 - 12 Porter DA, Heidemann RM. High resolution diffusion-weighted imaging using readout-segmented echo-planar imaging, parallel imaging and a two-dimensional navigator-based reacquisition. *Magn Reson Med.* 2009;62(2):468-475.
 - 13 Chen NK, Guidon A, Chang HC, et al. A robust multi-shot scan strategy for high-resolution diffusion weighted MRI enabled by multiplexed sensitivity-encoding (MUSE). *Neuroimage* 2013;72:41-7.
 - 14 Riffel P, Michaely HJ, Morelli JN, et al. Zoomed EPI-DWI of the head and neck with two-dimensional, spatially-selective radiofrequency excitation pulses, *EurRadiol* 2014; 24(10):2507-12.
 - 15 Thierfelder KM, Scherr MK, Notohamiprodjo M, et al. Diffusion-weighted MRI of the prostate: advantages of Zoomed EPI with parallel-transmit-accelerated 2D-selective excitation imaging. *EurRadiol* 2014; 24(12):3233-41.
 - 16 Morrell G, Spielman D. Dynamic shimming for multi-slice magnetic resonance imaging. *MagnResonMed* 1997;38(3):477-83.
 - 17 Lee SK, Tan ET, Govender A, et al. Dynamic slice-dependent shim and center frequency update in 3 T breast diffusion weighted imaging. *MagnReson Med* 2014;71(5):1813-1818.
 - 18 Zhang H, Xue H, Stemmer A, et al. Integrated Shimming Improves Lesion Detection in Whole-Body Diffusion-Weighted Examinations of Patients With Plasma Disorder at 3 T. *Investigative Radiology*, 2015 [Epub ahead of print]
 - 19 Stemmer A and Kiefer B. Combination of integrated slice-specific dynamic shimming and pixel-wise unwarping of residual EPI distortions. *Proc. Intl. Soc. Mag. Reson. Med.* 2015; 23:3729.
 - 20 Jezzard P and Balaban RS. Correction for geometric distortion in echo planar images from B0 field variations. *Magnetic Resonance in Medicine* 1995; 34:65-73.
 - 21 Takahara T, Imai Y, Yamashita T, et al. Diffusion weighted whole body imaging with background body signal suppression (DWIBS): technical improvement using free breathing, STIR and high resolution 3D display. *Radiat Med.* 2004;22:275-282.
 - 22 Thomas C. Kwee, Taro Takahara, Reiji Ochiai, et al. Diffusion-weighted whole-body imaging with background body signal suppression (DWIBS): features and potential applications in oncology". *EurRadiol.* 2008; 18:1937-1952
 - 23 Messiou C, Giles S, Collins D J, et al. Assessing response of myeloma bone disease with diffusion-weighted MRI [J]. *The British journal of radiology*, 2012, 85(1020): e1198-203.
 - 24 Giles S L, Messiou C, Collins D J, et al. Whole-body diffusion-weighted MR imaging for assessment of treatment response in myeloma [J]. *Radiology*, 2014, 271(3): 785-94.



Contact

Professor Xue Huadan, M.D.
Department of Radiology
Peking Union Medical College
Hospital, Peking Union
Medical College and Chinese
Academy of Medical Sciences
Shuaifuyuan 1#, Wangfujing
Street, Dongcheng District
Beijing, China, 100730
bjdanna95@hotmail.com

Contact

Zhang Haibo, M.D.
Department of Radiology
Chinese-Japan Friendship
Hospital
Yinghuayuan East Street #2
Chaoyang District
Beijing, China, 100029
zhh_hello@163.com



Whole-Body Dot Engine: First Clinical Experience with Automated Chest, Abdomen and Pelvis Examinations

Caecilia S. Reiner¹; Bernd Kuehn²; Daniel Nanz¹; Tim Finkenstädt¹; Berthold Kiefer²; Gustav Andreisek¹

¹ Institute of Diagnostic and Interventional Radiology, University Hospital Zurich, University of Zurich, Switzerland

² Oncology Application Predevelopment, Siemens Healthcare GmbH, Erlangen, Germany

Introduction

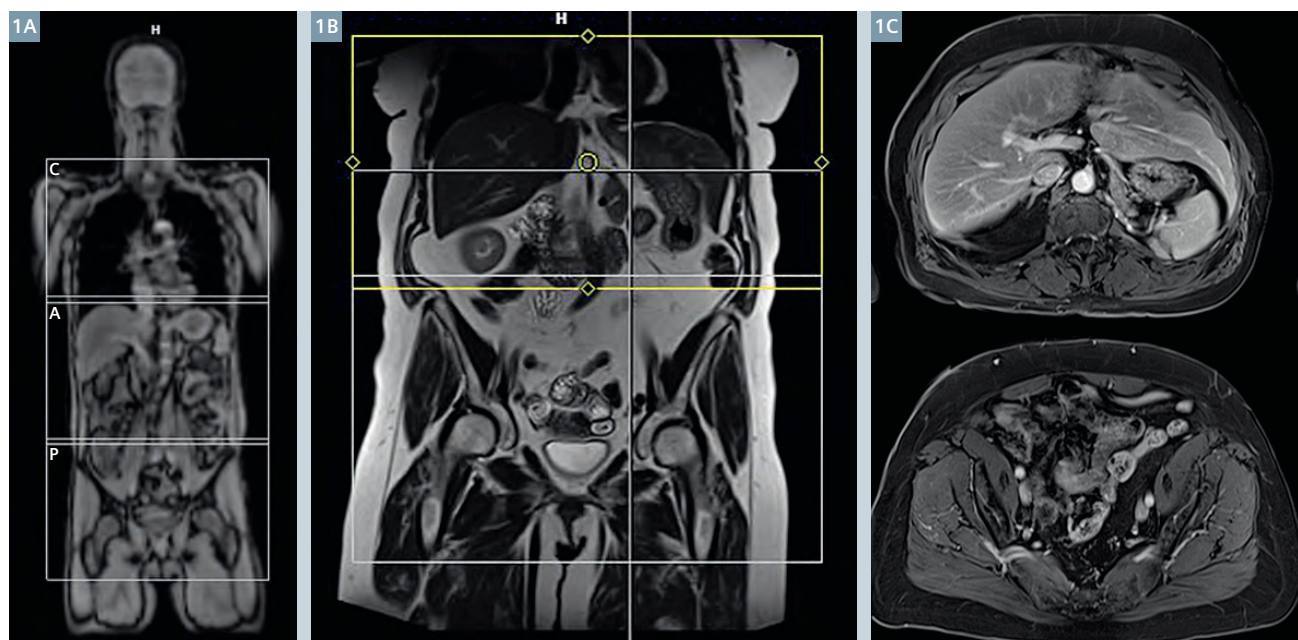
Time and cost efficiency are among the major challenges in clinical magnetic resonance imaging (MRI), mainly driven by the funding cuts in most health care systems [1]. At the same time, there is an increasing overall demand for a higher quality of MRI exams with regard to comparability, i.e. important for primary and/or follow-up studies in oncologic patients. To address these challenges, several vendors and researchers are developing automated scanner workflows for clinical MRI systems. The hypothesis is that these workflows allow a standardized and time-efficient

use and provide a robust image quality at only little user interaction. The Whole-Body Dot Engine was developed to meet these needs for multi-station MRI exams of chest, abdomen, pelvis, and even the whole body. Potential indications of multi-station body MRI exams are oncologic staging or follow-up, rheumatic disease and evaluation of myopathies.

MRI technique

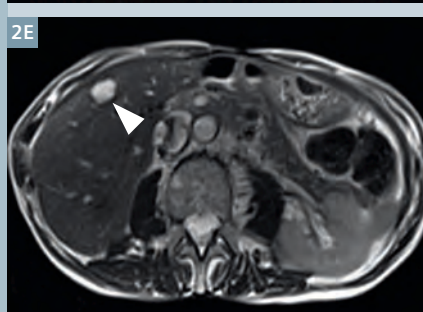
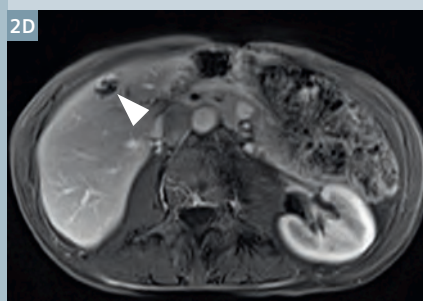
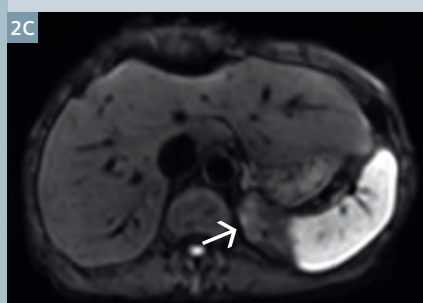
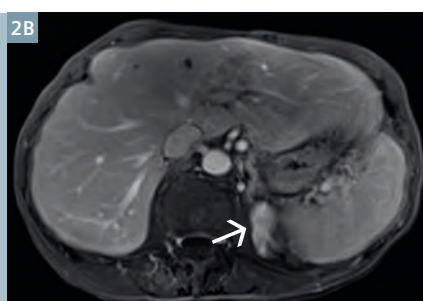
The Whole-Body Dot Engine automatically detects landmarks like lung apex, lung recesses, diaphragm, liver apex, iliac bone on a fast low-

resolution whole-body scout, which is acquired during moving table. Based on this scout the body regions selected for scanning, namely chest, abdomen and/or pelvis are automatically segmented (Fig. 1). With the information of the segmentation the sequence parameters (field-of-view [FOV] and number of slices) are automatically adjusted in order to ensure proper coverage of the body regions of interest. Additionally, the Whole-Body Dot Engine uses an anticipated patient's breath-hold capacity to automatically adjust the imaging protocols in body regions where breath-hold is required to generate optimal image quality.



1 (1A) Fast low resolution whole-body scout with automatically segmented chest (C), abdomen (A) and pelvis (P) for multi-station scanning. (1B) Coronal T2 single-shot turbo-spin-echo images with automatically segmented abdomen and pelvis split into two blocks for the transverse T1-weighted sequence (1C) with an acquisition time of 15 s for each lying within the preset 20-second breath-hold capacity. The cranio-caudal coverage per block is set to 400 mm with a fixed overlap of 2 cm between blocks and is adjusted to patient size and breath-hold capacity.

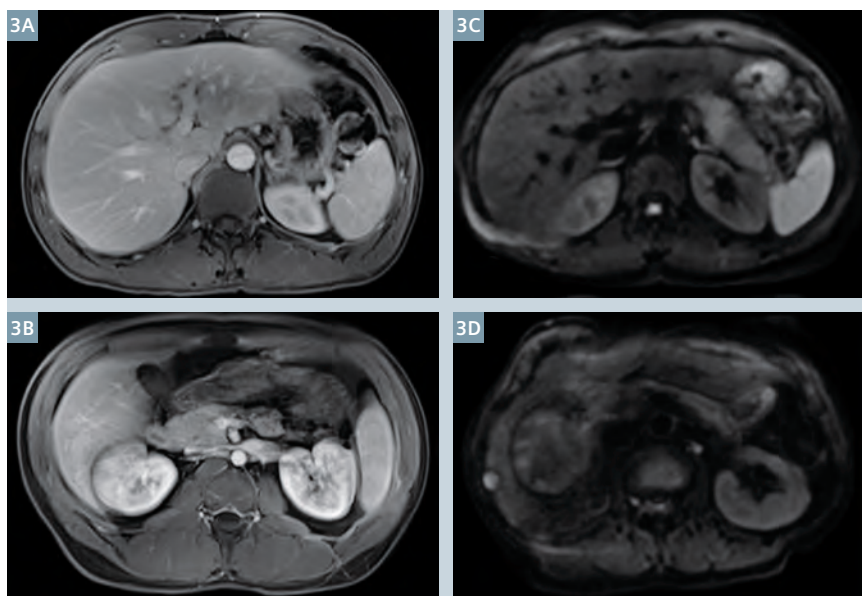
Table 1: MRI protocol	T2w HASTE	T2w HASTE	iShim ¹ EPI DWI	T1w VIBE Dixon without and with contrast	T1w VIBE Dixon with contrast
Scan plane	coronal	transverse	transverse	transverse	coronal
Repetition time/ Echo time (ms)	1230/92	1000/60	6100/56	4.27/1.28	3.93/1.23
Flip angle (°)	160	160	90	12	12
Slice thickness (mm)	6	5	6	3	1.5
Spacing (mm)	1	1	1	0	0
Acquisition matrix	256 x 256	256 x 109	128 x 84	320 x 180	192 x 162
Acceleration, factor	GRAPPA, 3	GRAPPA, 3	GRAPPA, 2	CAIPIRINHA, 2	CAIPIRINHA, 6
Number of excitations	1	1	6 and 15	1	1
b-values (s/mm ²)	na	na	50, 800	na	na



- 2** 73-year-old female patient with follow-up MRI of abdomen and pelvis after resection of a retroperitoneal liposarcoma. T1-weighted post-contrast 3D spoiled gradient-echo 2-point Dixon sequences in coronal (2A) and transverse (2B) plane show an enhancing mass cranial to the left kidney (white arrows), which shows a slightly restricted diffusion on the diffusion-weighted image (2C, b-value 800 s/mm²) and was highly suspicious of tumor recurrence. In addition a liver lesion was seen with peripheral nodular enhancement on the T1-weighted post-contrast 3D spoiled gradient-echo 2-point Dixon sequence (2D) and hyperintense on the T2-weighted single-shot turbo-spin-echo images (2E), which was diagnosed as hemangioma (white arrowheads).

The user can configure which parameters shall be adjusted for each protocol individually. In our protocol, base resolution was used for this purpose in 3D sequences, and number of concatenations was used in 2D sequences. We set the breath-hold capacity to 20 seconds. The protocol included a coronal and transverse T2-weighted single-shot turbo-spin-echo sequence (HASTE) acquired in breath-hold technique, transverse single-shot diffusion-weighted echo-planar imaging with slice-specific shim optimization (EPI-DWI, iShim¹ [2]) in free-breathing, and a transverse T1-weighted pre- and post-contrast 3D spoiled gradient-echo 2-point Dixon (VIBE) sequence acquired in breath-hold technique pre- and post-contrast (delay: chest 35 s, abdomen 70 s, pelvis 90 s after injection of 0.1 mmol/kg bodyweight gadoterate meglumine, Dotarem, Guerbet) (Table). Imaging after contrast-injection was timed by using automated bolus detection. The cranio-caudal coverage per block was adjusted to 400 mm. We chose a rather short scan protocol without dynamic acquisitions in a focus region (e.g. liver), because we wanted a fast and straightforward protocol for general oncologic imaging comparable to computed tomography. We used this scan protocol for oncologic follow-up imaging of abdomen and pelvis or chest, abdomen, and pelvis.

¹ The product is still under development and not commercially available yet. Its future availability cannot be ensured.



3 T1-weighted post-contrast 3D spoiled gradient-echo 2-point Dixon sequences with excellent image quality (**3A**) and with mild respiratory motion artifacts (**3B**). Single-shot diffusion-weighted echo-planar imaging sequence with slice-specific shim optimization with excellent image quality (**3C**) and with mild motion artifacts (**3D**).

Patients

20 patients (9 females, 11 males; mean age 52 years, range 21-79 years) were examined on a 3T MRI scanner (MAGNETOM Skyra, Siemens Healthcare) using the Whole-Body Dot Engine. Multi-station exams were performed on 11 patients for oncologic follow-up, in 2 for primary staging, and in 7 for tumor screening. The clinical diagnosis of these patients was: genitourinary malignancy (n=8), sarcoma (n=3), gastrointestinal malignancy (n=1), poly-posis syndromes (n=2), and chronic abdominal pain (n=6). In 18 patients abdomen and pelvis were scanned and in 2 patients chest, abdomen and pelvis. An image example is given in Figure 2. To validate whether our straightforward protocol results in an acceptable duration of

this multi-station MRI, patients scored their satisfaction with exam duration on a visual analogue scale from 0 (not acceptable, too long) to 10 (ideal exam duration).

Image quality

The scans were evaluated for overall image quality (IQ) (5 = excellent, 4 = good, 3 = moderate, 2 = poor, 1 = non-diagnostic) and artifacts (5 = no artifacts, 4 = mild artifacts, 3 = moderate artifacts, 2 = severe artifacts, 1 = non-diagnostic) on a 5-point scale by a board-certified abdominal radiologist with 8 years of experience. The image acquisition time was noted, as well as whether the coverage of the targeted body region was complete.

In all but one patient (19 of 20, 95%), the selected body regions were covered completely by the automated algorithm. An exception was the DWI, which showed markedly reduced signal in the sub-diaphragmatic part of the right liver in four patients (4 of 20, 20%), which impaired diagnostic ability of DWI in these liver parts.

The mean score for overall IQ was 4.7 ± 0.47 standard deviation (SD) and for artifacts overall was 4.4 ± 0.5 SD. Mild to moderate respiratory motion artifacts were seen in three patients (3 of 20, 15%) on T1-weighted post-contrast images with a mean IQ score of 4.8 ± 0.52 (Fig. 3). Mild motion artifacts were observed in four patients (5 of 20, 25%) on DWI with a mean IQ score of 4.75 ± 0.44 . The mean examination time was 27.4 ± 6.5 min for chest, abdomen and pelvis and 21.0 ± 6.9 min for abdomen and pelvis. The mean score of patient satisfaction regarding exam duration was 6.45 ± 2.19 (median, 6) and did not correlate with scan duration.

Conclusion

MR scanning with the automated Whole-Body Dot Engine results in good to excellent image quality within a reasonable total examination time with only small patient-dependent variations. An almost 'single-button protocol' for standardized fast, reproducible, and automated workflow of chest, abdomen, and pelvis could open up new possibilities in the diagnostic process. However, further comparison studies need to be performed to support our preliminary experience.

Contact

Cäcilia Reiner, M.D.
Institute of Diagnostic and
Interventional Radiology
University Hospital Zurich
Raemistrasse 100
8091 Zurich, Switzerland
caecilia.reiner@usz.ch



References

- 1 Andreisek G. Point-of-Care MR Imaging and how we can learn from other imaging modalities. Thoughts on a potential new strategy. MAGNETOM Flash (63) 3/2015:4-7. www.siemens.com/magnetom-world
- 2 Stemmer A, Kiefer B. Combination of integrated slice-specific dynamic shimming and pixel-wise unwarping of residual EPI distortions. Proc Intl Soc Mag Reson Med. 2015;23:3729.

Pictorial Essay: Pulmonary Imaging for Children

Sonja Kinner, M.D.; Haemi Phaedra Schemuth, M.D.

Department of Diagnostic and Interventional Radiology, University Hospital Essen, Essen, Germany

Introduction

To detect pulmonary metastasis a computed tomography (CT) scan is still the gold standard for adults as well as children. However, for children we try to keep the radiation burden as low as possible and use magnetic resonance imaging (MRI) for as many examinations as possible¹. Especially in children with oncologic diseases that can be treated curatively, we use MRI for the cervical and abdominal staging examinations and often also use the

MRI for the thoracic staging of the axillary, hilar, and mediastinal lymph nodes. However, to assess pulmonary metastases it is still necessary to perform a chest CT scan.

The examination we usually use for a thoracic MRI for children typically consists of a short T1 inversion recovery (STIR) sequence, a T2-weighted half fourier single-shot turbo spin echo (HASTE) sequence, a T1-weighted turbo spin echo (TSE) sequence, a true fast imaging with steady-state free precession (TrueFISP) sequence, dynamic volume interpolated breath-hold examination (VIBE) sequences, and a T1-weighted fast low angle shot (FLASH) 2D sequence. However in all of these sequences we have quite a few, especially motion artifacts and

can only safely assess pulmonary metastases when they have a diameter of at least 10 mm. For the staging in oncologic patients it is though also important to assess small pulmonary nodules, therefore we still rely on CT scans.

With FREEZEit, which includes the free-breathing radial MRI sequence StarVIBE we have less motion artifacts and may be able to assess pulmonary metastases.

Reference

H Chandarana, KT Block, MJ Winfeld, SV Lala, D Mazori, E Giuffrida, JS Babb, SS Milla. Free-breathing contrast-enhanced T1-weighted gradient-echo imaging with radial k-space sampling for paediatric abdominopelvic MRI. *Eur Radiol* (2014) 24:320-326.

¹ MR scanning has not been established as safe for imaging fetuses and infants under two years of age. The responsible physician must evaluate the benefit of the MRI examination in comparison to other imaging procedures.

Case 1

5-year-old male patient with an anaplastic large T-cell lymphoma with cervical and axillary lymphomas.

For staging purposes a contrast-enhanced MRI of the abdomen and neck was performed as well as a contrast-enhanced CT and MRI scan of the chest. The cervical MRI scan

showed cervical and axillary lymphomas; the CT and MRI scan of the chest showed left hilar lymphadenopathy with a consecutive dystelectasis of the left upper lobe.



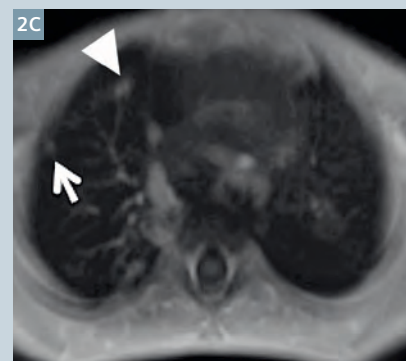
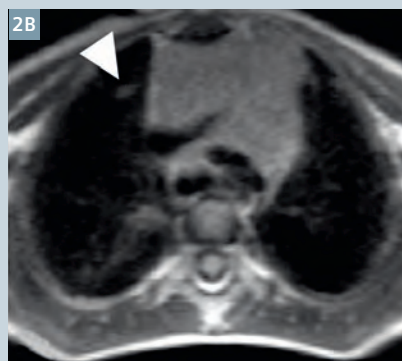
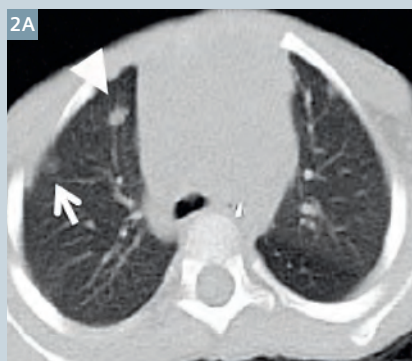
1 Contrast-enhanced CT scan in an arterial phase in (1A) lung window and (1B) edistinal window (SOMATOM Definition Flash; 3 mm slice thickness) show mediastinal lymphoma and dystelectasis of the left upper lobe. (1C) The StarVIBE sequence (MAGNETOM Aera 1.5T; 3 mm slice thickness) displays the mediastinal and axillary (arrow) lymph nodes in the post-contrast phase at least as well as in the CT scan.

Case 2

3-year-old male patient with post-transplant lymphoproliferative disorder (PTLD) after kidney transplantation.

The patient initially presented as a premature baby with a renal vein thrombosis. This led to a consecutive kidney failure and kidney transplant. Four months after the kidney transplant the patient developed a PTLD with cervical,

mediastinal, mesenteric, retroperitoneal, pelvic and pulmonal lymphomas. An FDG-PET/CT scan without an intravenous contrast agent was performed as well as an MRI of the chest and abdomen.



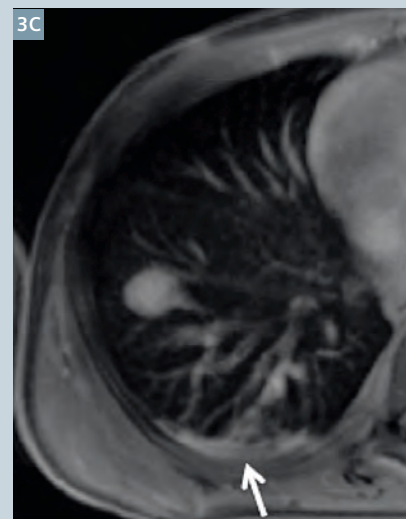
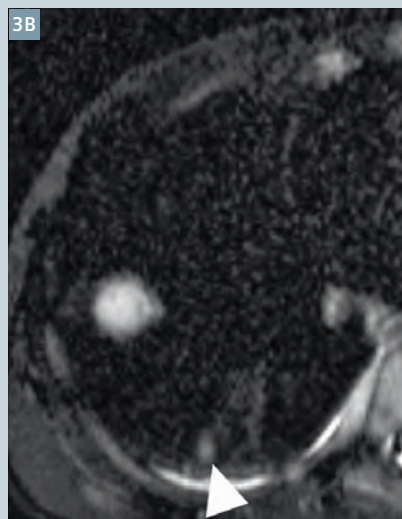
2 (2A) The non-contrast CT scan (3 mm slice thickness) in lung window shows pulmonary and mediastinal lymphoma manifestations. (2B) In a T2-weighted HASTE sequence (MAGNETOM Aera 1.5T; 5 mm slice thickness) only the bigger pulmonary lesion can be detected (arrowhead), while (2C) StarVIBE (MAGNETOM Aera 1.5T; 3 mm slice thickness) is able to show additional lung lesions (arrow).

Case 3

9-year-old male patient with a peripheral t-cell lymphoma.

The patient presented with cervical, thoracic, and abdominal lymphomas. Staging was done by a ^{18}F -FDG-PET/CT without intravenous

contrast agent and a contrast-enhanced cervical, thoracic, and abdominal MRI.



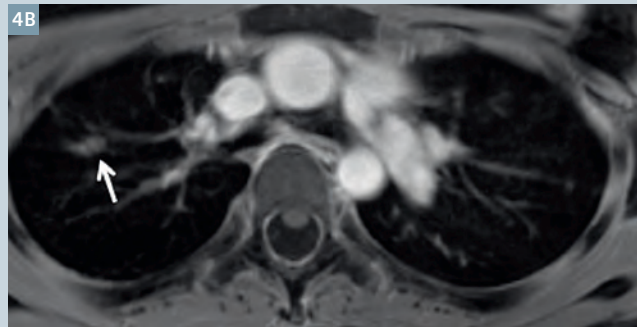
3 (3A) Non-contrast CT scan in lung window (3 mm slice thickness) shows two pulmonary lymphoma manifestations, which are also shown by (3B) the T2-weighted HASTE sequence however with less spatial resolution than (3C) the StarVIBE. In the StarVIBE sequence the second pulmonary lymphoma manifestation is masked by a dystelectasis (arrow). In our protocol, StarVIBE is the last sequence, which can lead to dystelectasis, especially after a quite extensive imaging protocol for whole-body staging. Therefore, it would be advisable to perform this sequence as early as possible.

Case 4

14-year-old female patient with acute lymphatic leukemia (ALL) and aspergillosis.

Patient presented with invasive aspergillosis after receiving chemotherapy with aspergillosis

manifestations in the lungs as well as the liver.



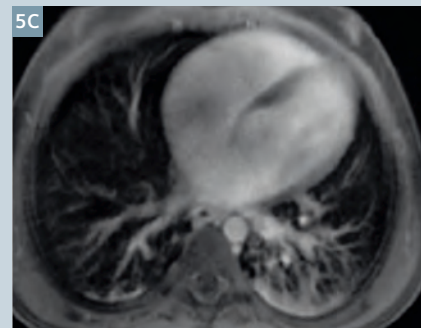
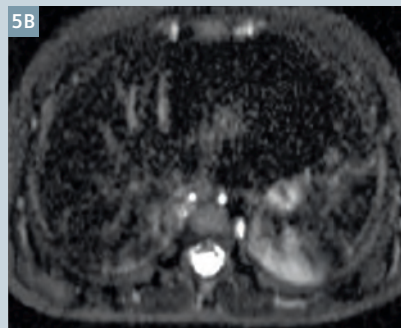
4 Single aspergillosis lesion in the upper right lobe in **(4A)** the non-contrast CT scan, with the same lesion shown in **(4B)** the StarVIBE sequence.

Case 5

2-year-old male patient with PTLD.

Patient presented with liver cirrhosis, and hepatocellular carcinoma (HCC). He received a liver transplant, and shortly after developed PTLD. An FDG-PET/CT

was performed, as well as a cervical, thoracic, and abdominal MRI. Pulmonary lymphomas were not detected, however infiltrates were diagnosed.



5 **(5A)** The CT scan and **(5C)** the StarVIBE sequence show the infiltrates in both lower lobes. **(5B)** The T2-weighted HASTE sequence does not offer as much spatial resolution as the CT scan and the StarVIBE.

Contact

Priv.-Doz. Dr. med. Sonja Kinner
University Hospital Essen
Diagnostic and Interventional Radiology
Hufelandstraße 55
45122 Essen
Germany
Phone: +49 (0)201/723-84544
Sonja.Kinner@uni-due.de



Sonja Kinner



Haemi Phaendra Schemuth

The Skyra^{fit} Experience in Basel

Thomas Egelhof, M.D.; Georg Katz, M.D.; Claudia Maise

Merian Iselin Spital, Radiology Department, Basel Switzerland

Introduction

Merian Iselin is one of the leading clinics for orthopedic and surgical procedures in Switzerland and it has 120 acute care beds. In 2014 there were 4,893 orthopedic cases (71% of all new cases), 615 surgical cases, and specifically 514 urological cases registered. By 2014 we observed that

other institutions were catching up with our clinical service and we therefore evaluated how we could take advantage of new opportunities in MR imaging to differentiate and to improve existing services. The option we considered was a fit-Upgrade of our installed MAGNETOM Verio MRI scanner.

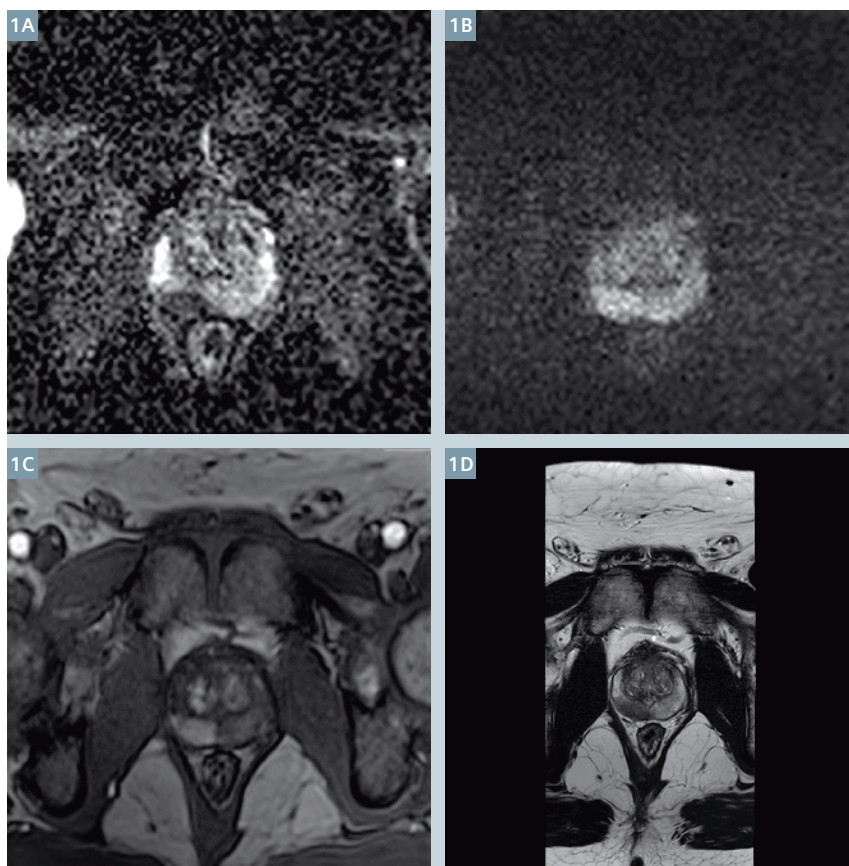
A fit-Upgrade is an upgrade of the installed 3T MRI system with the new Tim 4G coil technology, the new DotGO workflow and most recent applications available, including Quiet Suite. It also includes the installation of the new digital-in/digital-out RF system and new covers with Dot Display and Dot Control Centers, as well as the replacement of the control unit cabinet, body coil and surface coils, examination table and workstations.

Challenges

As a surgery reference hospital, prostate evaluation and therapy have become important topics for Merian Iselin, and consequently for the Radiology Department as well. One frequent request by our urology department and external referrers is pre-biopsy imaging of the prostate in order to guide targeted biopsies. However, before the upgrade the imaging department lacked the means to offer additional guidance for a targeted biopsy.

With our equipment prior to the fit-Upgrade, a prostate MR examination used to be rather uncomfortable for the patient because an endorectal coil was needed to achieve sufficient SNR. In many cases this device caused patient movement, affecting image quality and thus biopsy planning. Or, even worse, in some cases patients refused to undergo this kind of procedure at all.

Furthermore, scheduling of prostate patients required an extra time buffer to describe the procedure and to explain the use of an endorectal coil. While routine MR examinations take around 20 to 30 minutes, patient



1 Prostate images.
(1A) ADC RESOLVE b50, 800, 1500 transversal, SL 3 mm, FOV 150 x 150, matrix 100 x 100. (1B) DWI b 800 transversal, SL 3 mm, FOV 150 x 150, matrix 100 x 100. (1C) T1-weighted VIBE transversal post-contrast, SL 3.5 mm, FOV 180 x 180, matrix 122 x 160. (1D) T2w TSE transversal, SL 3 mm, FOV 240 x 120, matrix 384 x 192.

preparation for prostate examinations required additional time in the MR scanner – especially for non-German speakers because language barriers made it slower to explain.

Another key reason for the fit-Upgrade was the offered advantage in musculoskeletal imaging: As a hospital focused on orthopedic procedures, we need to evaluate the whole hand, especially for finger ligament diagnosis and degenerative pathologies. Ideally, a hand coil should support an examination where the wrist and finger can be examined as a whole.

Our analysis further revealed that time pressure had also been a major issue in Merian Iselin before the fit-Upgrade. In order to acquire images in all required orientations and contrasts as requested by the radiologist for some clinical questions, the team of technologists had occasionally found themselves under pressure to finish an examination within the patient time-slot. This was particularly the case for finger and hip examinations. And, in general, the team has been under pressure to reduce patient time in the scanner to the minimum.

Solutions

After upgrading the system to MAGNETOM Skyra^{fit}, we changed our prostate protocol and decided to abandon the use of an endorectal coil. With the upgraded 3T system and

using only the surface body 30 coil and the spine coil we now ensure patient comfort and compliance. We obtain images with high quality while eliminating the challenges associated with the endorectal coil.

We also replaced our standard diffusion-weighted imaging protocol, which is prone to susceptibility artifacts, with a high-resolution, diffusion-weighted imaging sequence (RESOLVE), and in general benefitted from a higher signal-to-noise ratio (SNR) and improved FatSat imaging. All these changes have very positively influenced the quality of our prostate MR exams provided to the urologists and improved diagnostic confidence (Fig. 1). Consequently, we are now able and confident to recommend if a biopsy is required or not, based on a MRI scan.

With the new hardware, providing higher coil density, we were able to improve the spatial and temporal resolution of our protocols in abdominal and pelvic imaging in general. One sequence of particular use is StarVIBE. Now it is possible to perform abdominal and pelvic examinations allowing patient's free breathing and reducing artifacts in the image.

The fit-Upgrade also included a new set of high element-density orthopedic coils. The 16-channel

hand and wrist coil, in particular, enables a complete hand examination, without additional coils or specific coil or patient repositioning (Fig. 2).

We have also been able to accelerate orthopaedic examinations such as hip exams with the high element-density of the body coil and the additional workflow support provided by the Large Joint Dot Engine (Fig. 3). In the case of ankle examinations we have been able to reduce the scan time while even improving image quality by using the 16-channel foot and ankle high element-density coil. This coil also requires less time for shimming.

Results

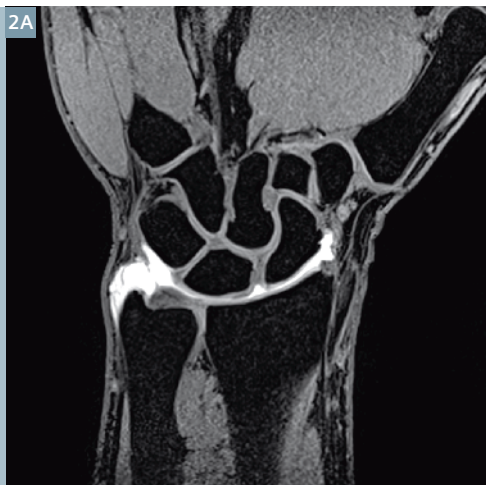
The improvements introduced with our Skyra^{fit} upgrade have been crucial for us, our referring physicians and our patients. We are now able to offer a very convenient and comfortable examination to patients referred for prostate MRI and can consistently acquire all images required for diagnosis and (as far as needed) targeted biopsy. The avoidance of an endorectal probe is especially appreciated by patients undergoing active surveillance where regularly repeated exams are standard.

Dr. Georg Katz particularly points out: "Now urologists ask us to revise cases

2

Wrist images.
(2A) T1w VIBE coronal, FOV 90 x 100, matrix 273 x 320.
(2B) T2w TSE sagittal, SL 3 mm, FOV 100 x 100, matrix 307 x 384.

2A



2B

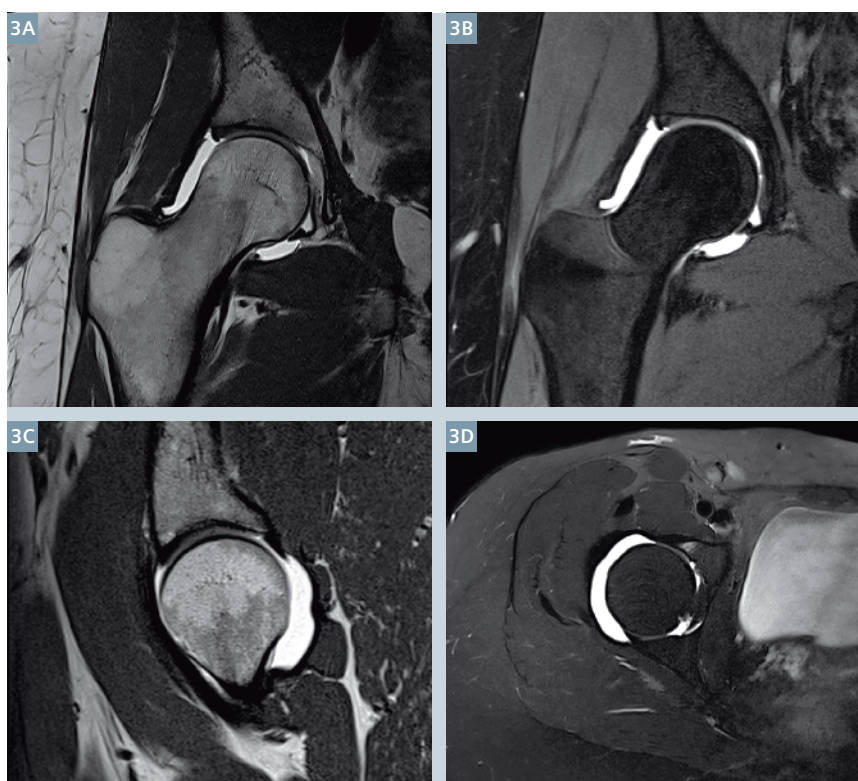


previously diagnosed in other sites or perform follow-up examinations.”

Since the introduction of the new orthopedic coils, wrist and finger lesions referrals have increased in the region and we have also seen an increase in scanning rheumatic hands. For finger evaluations, Technologist Claudia Maise commented: “It is now easier and faster to perform an MRI scan than an ultrasound and we provide to the orthopedic physicians complete wrist and finger evaluation.” In this way, orthopedic physicians offer patients a targeted treatment or physiotherapy.

Being able to scan faster has resulted in having more time available within the patient time-slot for techs to ensure all possible sets of images are available. They are under less stress and this also guarantees a good result.

We provide the treating physician and the patient all the possible images needed for the diagnosis, therapy, surgery and follow-up questions which may later arise. Thus ensuring that no recall of patients is needed.



3 Hip images.
(3A) T1w TSE coronal, SL 3 mm, slices 20, FOV 160 x 160, matrix 269 x 448, A 3:56 min. (3B) PDw TSE FatSat coronal, SL 3.5 mm, slices 20, FOV 150 x 150, matrix 272 x 320, TA 2:42 min. (3C) PDw TSE sagittal, SL 2 mm, FOV 130 x 130, matrix 230 x 256. (3D) T2w TSE FatSat transversal, SL 3 mm, FOV 192 x 200, matrix 279 x 384.

Conclusion

Given challenges and the tremendous improvements achieved, the fit-Upgrade with software version syngo MR E11 has proved to be the best cost-benefit solution. The building costs were very low, installation was fast and the upgraded system is practically the same as a new scanner. Even though patients don't recognize the changes to the system, our referring physicians have specifically noticed the difference. And all this has been achieved with a reduced investment.



Contact

Dr. med. Thomas Egelhof
Merian Iselin Spital
Radiology Department
Föhrenstrasse 2
CH-4054 Basel
Switzerland
Phone: T +41 61 305 12 96
thomas.egelhof@merianiselin.ch



Contact

Dr. med. Georg Katz
Merian Iselin Spital
Radiology Department
Föhrenstrasse 2
CH-4054 Basel
Switzerland
Phone: T +41 61 305 12 99
Georg.Katz@merianiselin.ch

Biograph mMR: System and Clinical Use Today

Björn W. Jakoby, Ph.D.; Christian Geppert, Ph.D.; Jens-Christoph Georgi, Ph.D.

Siemens Healthcare, Erlangen, Germany

Summary

This article describes the latest developments in the area of technical advancements and clinical research for the Biograph mMR. Seminal publications in the field of neurology, cardiology, and oncology will be discussed.

Introduction

The Biograph mMR (Siemens Healthcare, Germany) was introduced in 2011. So far, more than 80 systems have been sold. Early on, numerous scientific publications explored the field of technical performance and basic research. Nowadays, the majority of publications address the clinical benefits of the Biograph mMR in daily routine. An increasing number of the latest publications imply improvements in clinical practice. The clinical fields can be roughly divided into oncology (60%), neurology (25%), and cardiology (15%). These early customers have been the pioneers of guiding simultaneous whole-body MR/PET into clinical practice. While

the authors have tried to cover a wide range of the available published literature, it is unfortunately inevitable that we overlooked to mention other equally important articles.

The Biograph mMR already experienced updates in hardware as well as software. Currently, the 3rd generation of the Biograph mMR is under development.

Neurology

In the field of neurological mMR, three main areas of application have been identified so far: neurodegenerative diseases, brain tumors, and methodological developments.

Fowler et al. [1] describe the particular advantages of combined MR/PET for dementia imaging using ^{18}F -Florbetapir, a β -amyloid-plaque tracer. In an approach of multiparametric diagnosis the PET information is jointly evaluated with automatic MRI-based volumetry of relevant brain regions.

A feasibility study by Jena et al. [2] indicates that PET quantitation

accuracy of the Biograph mMR is similar to that of PET/CT, and is reliable in a clinical setting. Furthermore, optimal co-registration of simultaneously acquired MRI and PET data has been identified as a specific advantage in brain imaging. According to Bisdas et al. [3], the potential of MR-PET imaging for the accurate investigation of *in vivo* pathophysiology has opened new pathways for the management of gliomas. The role of combined metabolic mapping of gliomas without clear evidence of tumor grade by means of MR spectroscopy and Methionine PET was demonstrated.

Ongoing developments of brain attenuation correction methods [4–10] demonstrate promising results, which will further expand the applications in the field of neurology. The application of MR-PET currently finds increasing interest in patients with refractory epilepsy. Here, very often, only after the simultaneous MR-PET exams, the decision for a surgery can be made. Early results have been published by Ding et al. [11] and Shin et al. [12].

Cardiology

Compared to oncological applications, mMR examinations in the field of cardiology and vascular imaging are not as established in clinical routine. Most publications originate from clinical research projects.

White et al. [13] describe the benefits of simultaneous MR/PET in a case study for cardiac sarcoidosis. In the same context of cardiac sarcoidosis, Schneider et al. [14] concluded that serial assessment of edema and LGE by MRI as well as FDG-PET may be helpful for therapy monitoring and guidance of primary preventive device therapy. Inflammatory processes of



the heart and vasculature developed to a potential key application for mMR. Nensa et al. [13] identified benefits from multiparametric assessment for detection, differential diagnosis, and monitoring of acute myocarditis.

Furthermore, myocardial infarction is of growing interest for several mMR working groups. Nensa et al. [15] examined 20 patients for acute myocardial infarction. They identified potential improvements for risk stratification by assessing quantitative information on metabolic processes. Furthermore, they project for new, specific tracers to provide valuable information of pathophysiological level.

It is to be expected that the broad clinical adoption of these cardiac indications will be accelerated in the future by the methodological advances, e.g. in cardiac MR/PET motion correction as demonstrated by Huang et al. [17].

Oncology

As expected, the oncological applications for mMR were established early on in clinical practice and research. The corresponding publications will be discussed in the following.

In a comparison study with PET/CT, Beiderwellen et al. [18] looked into 70 patients with solid tumors, including 36 liver lesions. Both PET/CT and MR/PET identified the same lesions. However, the clear advantage of MR/PET imaging was the significantly higher conspicuity of the findings due to the additional MR information and improved diagnostic certainty of the reading physician.

For prostate imaging with C11-Choline, Souvatzoglou et al. [19, 20] demonstrated the additional value of MR/PET in comparison to PET/CT for

the spatial registration of lesions in the pelvis and bones. Souvatzoglou et al. foresee a diagnostic advantage for MR/PET in prostate imaging.

Further potential of mMR imaging in prostate cancer was also explored by Afshar-Oromieh et al. [21], Eiber et al. [22, 23] in particular report higher diagnostic accuracy of MR-PET in comparison to PET and multiparametric MR. These key publications concluded that prostate cancer can be detected more easily and more accurately with Ga-PSMA PET/MRI than with PET/CT and with lower radiation exposure. The specific benefit of this novel tracer has already been demonstrated by Schaefer et al. [24].

For a number of oncological diseases knowledge of bone metastases is key for thorough therapy selection. FDG PET/MRI shows high potential for the assessment of bone metastases by offering superior lesion conspicuity when compared to PET/CT, as demonstrated by Beiderwellen et al. [25] and Eiber et al. [26]. In particular, the anatomical delineation seemed to be improved by the use of a T1-weighted TSE sequence.

Catalano et al. [27] compare the influence of MR/PET and PET/CT on patient-management. The results (134 oncological patients) show that in 18% of the cases the use of PET/MR would lead to a change in therapy management.

A research field that has been gaining increasing attention is the application of mMR data in the process of radiotherapy planning. Several European groups are working on this topic. Based on their initial experience Thorwarth et al. [28] expect for integrated PET/MR to become particularly important and clinically useful for improved,

individualized RT therapy planning for brain lesions.

Recently, Catalano et al. and Pirelli et al. have reported promising results in Crohn's disease using PET/MR for pre-operative lesion assessment [29, 30].

It is not only the substantial dose saving of typically 30-50% by omitting the CT [31] and additional 50% due to potentially reduced tracer activity [32] that makes MR/PET interesting for pediatric* oncological imaging. Hirsch et al. [33] also demonstrated a clear advantage of MR over CT for this patient group. Specific benefits in pediatric astrocytoma patients have been described by Fraioli et al. [34]. The general potential in pediatric imaging also beyond oncology is elaborated by Purz et al. [35].

Another trend for oncological MR/PET, the segmentation of regions of different tumor biology based on multiparametric analysis is described in Schmidt et al. [36] for pulmonary lesions and Schwenzer et al. [37] for Peritoneal Carcinomatosis. Gawlitza et al. [38] use a similar analysis for the depiction of complex interactions between glucose metabolism, microcirculatory parameters and cellular density.

In the field of small lung lesions without FDG uptake, Raad et al. have published intriguing data in a follow-up setting of 207 patients using a motion-insensitive radial VIBE sequence. They could show that those lesions that would be missed if only MR-PET was applied, are most likely (97%) benign [39].

*MR scanning has not been established as safe for imaging fetuses and infants less than two years of age. The responsible physician must evaluate the benefits of the MR examination compared to those of other imaging procedures.

Discussion

After an initial phase of technical and performance evaluations within the first two years after introduction, the Biograph mMR established itself in high-end patient centered care, from diagnosis and staging to therapy planning and monitoring.

This was achieved by the groundbreaking work of all Biograph mMR users using the system in clinical research and routine operation.

References

- 1 K. J. Fowler, J. McConathy, and V. R. Narra, "Whole-body simultaneous positron emission tomography (PET)-MR: Optimization and adaptation of MRI sequences," *Journal of Magnetic Resonance Imaging*, vol. 39, pp. 259–268, Oct. 2013.
- 2 A. Jena, S. Taneja, R. Goel, P. Renjen, and P. Negi, "Reliability of semiquantitative 18F-FDG PET parameters derived from simultaneous brain PET/MRI: A feasibility study," *European Journal of Radiology*, vol. 83, no. 7, pp. 1269–1274, Jul. 2014.
- 3 S. Bisdas, R. Ritz, B. Bender, C. Braun, C. Pfannenberger, M. Reimold, T. Naegele, and U. Ernemann, "Metabolic Mapping of Gliomas Using Hybrid MR-PET Imaging: Feasibility of the Method and Spatial Distribution of Metabolic Changes," *Investigative Radiology*, vol. 48, no. 5, pp. 295–301, May 2013.
- 4 U. C. Anazodo, J. D. Thiessen, T. Ssali, J. Mandel, M. Günther, J. Butler, W. Pavlosky, F. S. Prato, R. T. Thompson, and K. S. St Lawrence, "Feasibility of simultaneous whole-brain imaging on an integrated PET-MRI system using an enhanced 2-point Dixon attenuation correction method," *Front Neurosci*, vol. 8, no. n/a, p. 434, Jan. 2015.
- 5 D. Benoit, C. Ladefoged, and J. N. Sune Keller Flemming Andersen Liselotte Hojgaard Adam Espe Hansen Søren Holm Ahmadreza Rezaei, "PET/MR: improvement of the UTE μ -maps using modified MLAA," *EJNMMI Physics*, vol. 2, no. 1, p. A58, May 2015.
- 6 N. Burgos, M. J. Cardoso, M. Modat, S. Pedemonte, J. Dickson, A. Barnes, J. S. Duncan, D. Atkinson, S. R. Arridge, B. F. Hutton, and S. Ourselin, "Attenuation correction synthesis for hybrid PET-MR scanners: Application to Brain Studies," *Med Image Comput Comput Assist Interv*, vol. 16, no. Pt 1, pp. 147–154, Jul. 2013.
- 7 J. Cabello, M. Lukas, S. Förster, T. Pyka, S. G. Nekolla, and S. I. Ziegler, "MR-based attenuation correction using ultrashort-echo-time pulse sequences in dementia patients," *J Nucl Med*, vol. 56, no. 3, pp. 423–429, Mar. 2015.
- 8 Y. Chen, M. Juttukonda, Y. Su, T. Benzinger, B. G. Rubin, Y. Z. Lee, W. Lin, D. Shen, D. Lalush, and H. An, "Probabilistic Air Segmentation and Sparse Regression Estimated Pseudo CT for PET/MR Attenuation Correction," *Radiology*, vol. 275, no. 2, pp. 562–569, May 2015.
- 9 D. Izquierdo-Garcia, A. E. Hansen, S. Förster, D. Benoit, S. Schachoff, S. Fürst, K. T. Chen, D. B. Chonde, and C. Catana, "An SPM8-Based Approach for Attenuation Correction Combining Segmentation and Nonrigid Template Formation: Application to Simultaneous PET/MR Brain Imaging," *Journal of Nuclear Medicine*, vol. 55, no. 11, pp. 1825–30, Oct. 2014.
- 10 M. R. Juttukonda, B. G. Mersereau, Y. Chen, Y. Su, B. G. Rubin, T. L. S. Benzinger, D. S. Lalush, and H. An, "MR-based attenuation correction for PET/MRI neurological studies with continuous-valued attenuation coefficients for bone through a conversion from R2* to CT-Hounsfield units," *Neuroimage*, vol. 112, no. n/a, pp. 160–168, May 2015.
- 11 Y. S. Ding, B. B. Chen, C. Glielmi, K. Friedman, O. Devinsky, "A pilot study in epilepsy patients using simultaneous PET/MR," *Am J Nucl Med Mol Imaging* 2014;4(5):459-470.
- 12 H. W. Shin, V. Jewells, A. Sheikh, J. Zhang, H. Zhu, H. An, W. Gao, D. Shen, E. Hadar, W. Lin W, "Initial experience in hybrid PET-MRI for evaluation of refractory focal onset epilepsy," *Seizure* 31 (2015) 1–4.
- 13 J. A. White, M. Rajchl, J. Butler, R. T. Thompson, F. S. Prato, and G. Wisenberg, "Active cardiac sarcoidosis: first clinical experience of simultaneous positron emission tomography-magnetic resonance imaging for the diagnosis of cardiac disease," *Circulation*, vol. 127, no. 22, pp. e639–e641, Jun. 2013.
- 14 S. Schneider, A. Batrice, C. Rischpler, M. Eiber, T. Ibrahim, and S. G. Nekolla, "Utility of multimodal cardiac imaging with PET/MRI in cardiac sarcoidosis: implications for diagnosis, monitoring and treatment," *European Heart Journal*, vol. 35, p. 312, Aug. 2013.
- 15 F. Nensa, T. D. Poeppel, P. Krings, and T. Schlosser, "Multiparametric assessment of myocarditis using simultaneous positron emission tomography/magnetic resonance imaging," *European Heart Journal*, vol. 35, no. 32, p. 2173, Feb. 2014.
- 16 F. Nensa, T. Poeppel, E. Tezgah, P. Heusch, K. Nassenstein, A. A. Mahabadi, M. Forsting, A. Bockisch, R. Erbel, G. Heusch, and T. Schlosser, "Integrated FDG PET/MR Imaging for the Assessment of Myocardial Salvage in Reperfused Acute Myocardial Infarction," *Radiology*, vol. 276, no. 2, pp. 400–407, Aug. 2015.
- 17 C. Huang, Y. Petibon, J. Ouyang, T. G. Reese, M. A. Ahlman, D. A. Bluemke, and G. E. Fakhri, "Accelerated acquisition of tagged MRI for cardiac motion correction in simultaneous PET-MR: Phantom and patient studies," *Med Phys*, vol. 42, no. 2, pp. 1086–1097, Jan. 2015.
- 18 K. Beiderwellen, L. Geraldo, V. Ruhlmann, P. Heusch, B. Gomez, F. Nensa, L. Umutlu, and T. C. Lauenstein, "Accuracy of [18F] FDG PET/MRI for the Detection of Liver Metastases," *PLoS One*, vol. 10, no. 9, p. e0137285, Sep. 2015.
- 19 M. Souvatzoglou, M. Eiber, A. Martinez-Moeller, S. Fürst, K. Holzappel, T. Maurer, S. Ziegler, S. Nekolla, M. Schwaiger, and A. J. Beer, "PET/MR in prostate cancer: technical aspects and potential diagnostic value," *Eur J Nucl Med Mol Imaging*, vol. 40, no. 1, pp. 79–88, Jul. 2013.
- 20 M. Souvatzoglou, M. Eiber, T. Takei, S. Fürst, T. Maurer, F. Gaertner, H. Geinitz, A. Drzezga, S. Ziegler, S. Nekolla, E. Rummeny, M. Schwaiger, and A. Beer, "Comparison of integrated whole-body [11C]choline PET/MR with PET/CT in patients with prostate cancer," *Eur J Nucl Med Mol Imaging*, vol. 40, pp. 1486–1499, Jul. 2013.
- 21 A. Afshar-Oromieh, U. Haberkorn, H. P. Schlemmer, M. Fenchel, M. Eder, M. Eisenhut, B. A. Hadaschik, A. Kopp-Schneider, and M. Röthke, "Comparison of PET/CT and PET/MRI hybrid systems

- using a (68)Ga-labelled PSMA ligand for the diagnosis of recurrent prostate cancer: initial experience.,” *Eur J Nucl Med Mol Imaging*, vol. 41, no. 5, pp. 887–897, Dec. 2013.
- 22 M. Eiber, S. Nekolla, T. Maurer, G. Weirich, H.-J. Wester, and M. Schwaiger, “68Ga-PSMA PET/MR with multimodality image analysis for primary prostate cancer,” *Abdom Imaging*, vol. 11, pp. 1–3, Nov. 2014.
 - 23 M. Eiber, G. Weirich, K. Holzapfel, M. Souvatzoglou, B. Haller, I. Rauscher, A.J. Beer, H.J. Wester, J. Gschwend, M. Schwaiger, T. Maurer, “Simultaneous 68Ga-PSMA HBED-CC PET/MRI Improves the Localization of Primary Prostate Cancer,” *Eur Urol*. 2016 Jan 18. pii: S0302-2838(16)00011-7.
 - 24 M. Schaefer, U. Bauder-Wuest, K. Leotta, F. Zoller, W. Mier, U. Haberkorn, M. Eisenhut, and M. Eder, “A dimerized urea-based inhibitor of the prostate-specific membrane antigen for 68Ga-PET imaging of prostate cancer,” *EJNMMI Res*, vol. 2, no. 1, p. 23, 2012.
 - 25 K. Beiderwellen, M. Huebner, P. Heusch, J. Grueneisen, V. Ruhlmann, F. Nensa, H. Kuehl, L. Umutlu, S. Rosenbaum-Krumme, and T. Lauenstein, “Whole-body [18F]FDG PET/MRI vs. PET/CT in the assessment of bone lesions in oncological patients: initial results,” *European Radiology*, vol. 24, no. 8, pp. 2023–2030, Jun. 2014.
 - 26 M. Eiber, T. Takei, M. Souvatzoglou, M. E. Mayerhoefer, S. Fürst, F. C. Gaertner, D. J. Loeffelbein, E. J. Rummeny, S. I. Ziegler, M. Schwaiger, and A. J. Beer, “Performance of Whole-Body Integrated 18F-FDG PET/MR in Comparison to PET/CT for Evaluation of Malignant Bone Lesions,” *Journal of Nuclear Medicine*, vol. 55, no. 2, pp. 191–197, Feb. 2014.
 - 27 O. A. Catalano, B. R. Rosen, D. V. Sahani, P. F. Hahn, A. R. Guimaraes, M. G. Vangel, E. Nicolai, A. Soricelli, and M. Salvatore, “Clinical Impact of PET/MR Imaging in Patients with Cancer Undergoing Same-Day PET/CT: Initial Experience in 134 Patients-A Hypothesis-generating Exploratory Study,” *Radiology*, vol. 269, no. 3, pp. 857–869, Dec. 2013.
 - 28 D. Thorwarth, A.-C. Müller, C. Pfannenberger, and T. Beyer, “Combined PET/MR imaging using (68)Ga-DOTATOC for radiotherapy treatment planning in meningioma patients,” *Recent Results in Cancer Research*, vol. 194, pp. 425–439, Aug. 2013.
 - 29 G. Pellino, E. Nicolai, O.A. Catalano, S. Campione, F.P. D’Armiento, M. Salvatore, A. Cuocolo, F. Selvaggi, “PET/MR Versus PET/CT Imaging: Impact on the Clinical Management of Small-Bowel Crohn’s Disease,” *Journal of Crohn’s and Colitis*, 2015, 1–10.
 - 30 O.A. Catalano, M.S. Gee, E. Nicolai, F. Selvaggi, G. Pellino, A. Cuocolo, A. Luongo, M. Catalano, B.R. Rosen, D. Gervais, M.G. Vangel, A. Soricelli, M. Salvatore, “Evaluation of Quantitative PET/MR Enterography Biomarkers for Discrimination of Inflammatory Strictures from Fibrotic Strictures in Crohn Disease,” *Radiology* 2016 Mar;278(3):792-800.
 - 31 S. C. Chawla, N. Federman, D. Zhang, K. Nagata, S. Nuthakki, M. McNitt-Gray, and M. I. Boechat, “Estimated cumulative radiation dose from PET/CT in children with malignancies: a 5-year retrospective review,” *Pediatr Radiol*, vol. 40, no. 5, pp. 681–686, May 2010.
 - 32 M. Oehmigen, S. Ziegler, B. Jakoby, J. C. Georgi, D. H. Paulus, and H. Quick, “Radiotracer Dose Reduction in Integrated PET/MR: Implications from National Electrical Manufacturers Association Phantom Studies,” *Journal of Nuclear Medicine*, vol. 55, no. 6, pp. 1–7, Jul. 2014.
 - 33 F. W. Hirsch, B. Sattler, I. Sorge, L. Kurch, A. Viehweger, L. Ritter, P. Werner, T. Jochimsen, H. Barthel, U. Bierbach, H. Till, O. Sabri, and R. Kluge, “PET/MR in children. Initial clinical experience in paediatric oncology using an integrated PET/MR scanner,” *Pediatr Radiol*, vol. 43, no. 7, pp. 860–875, Jul. 2013.
 - 34 F. Fraioli, A. Shankar, D. Hargav, H. Hyare, M. N. Gaze, A. M. Groves, P. Alongi, S. Stoneham, S. Michopoulou, R. Syed, and J. B. Bomanji, “18F-Fluoro-ethylcholine (18F-Cho) PET/MRI Functional Parameters in Pediatric Astrocytic Brain Tumors,” *Clinical Nuclear Medicine*, vol. 40, no. 1, pp. 40–45, Jan. 2015.
 - 35 S. Purz, O. Sabri, A. Viehweger, H. Barthel, R. Kluge, I. Sorge, and F. W. Hirsch, “Potential Pediatric Applications of PET/MR,” *Journal of Nuclear Medicine*, vol. 55, no. 6 (Suppl. 2), p. 8, Jun. 2014.
 - 36 H. Schmidt, C. Brendle, C. Schraml, P. Martirosian, I. Bezrukov, J. Hetzel, M. Müller, A. Sauter, C. D. Claussen, C. Pfannenberger, and N. F. Schwenzer, “Correlation of Simultaneously Acquired Diffusion-Weighted Imaging and 2-Deoxy-[18F] fluoro-2-D-glucose Positron Emission Tomography of Pulmonary Lesions in a Dedicated Whole-Body Magnetic Resonance/Positron Emission Tomography System,” *Investigative Radiology*, vol. 48, no. 5, pp. 247–255, May 2013.
 - 37 N. F. Schwenzer, H. Schmidt, S. Gatidis, C. Brendle, M. Mueller, I. Koenigsrainer, C. D. Claussen, A. C. Pfannenberger, and C. Schraml, “Measurement of apparent diffusion coefficient with simultaneous MR/positron emission tomography in patients with peritoneal carcinomatosis: Comparison with 18F-FDG-PET,” *Journal of Magnetic Resonance Imaging*, vol. n/a, p. n/a–n/a, Nov. 2013.
 - 38 M. Gawlitza, S. Purz, K. Kubiessa, A. Boehm, H. Barthel, R. Kluge, T. Kahn, O. Sabri, and P. Stumpp, “In Vivo Correlation of Glucose Metabolism, Cell Density and Microcirculatory Parameters in Patients with Head and Neck Cancer: Initial Results Using Simultaneous PET/MRI,” *PLoS One*, vol. 10, no. 8, p. e0134749, Aug. 2015.
 - 39 R.A. Raad, K.P. Friedman, L. Heacock, F. Ponzio, A. Melsaether, H. Chandarana, “Outcome of small lung nodules missed on hybrid PET/MRI in patients with primary malignancy,” *J Magn Reson Imaging*. 2016 Feb;43(2):504-11.

Contact

Björn Jakoby
Siemens Healthcare GmbH
HC DI MR PI TIO NEUR
Postbox 32 60
91050 Erlangen
Germany
Phone: +49 (0)9131 84-6308
bjoern.jakoby@siemens.com

Permeability Imaging of Parotid Tumors with Golden-Angle Radial Sparse Parallel MR Imaging (GRASP)

Sohil H. Patel, M.D.¹; Hersh Chandarana, M.D.¹; Kai Tobias Block, Ph.D.¹; Robert Grimm, Ph.D.²; Girish Fatterpekar, M.D.¹

¹ Department of Radiology, NYU Langone Medical Center, New York, NY, USA

² Siemens Healthcare, Erlangen, Germany

Introduction

A range of pathologic processes may affect the parotid gland. These vary from benign processes such as reactive lymph nodes, pleomorphic adenoma, and Warthin's tumor, to malignancies such as adenocarcinoma, adenoid cystic carcinoma, and mucoepidermoid carcinoma. Neoplasms of the parotid gland can pose a diagnostic challenge because conventional imaging features cannot differentiate benign from malignant lesions with complete certainty [1]. In conventional MRI examinations, most neoplasms of the parotid gland enhance with intravenous contrast. Therefore, the presence of enhancement, while essential to the identification and mapping of parotid neoplasms, does not differentiate between different

tumor subtypes. To further obfuscate clinical management, the most common benign tumor of the parotid gland (pleomorphic adenoma) can occasionally dedifferentiate into a malignant tumor [2]. Moreover, the accuracy of fine needle biopsy of parotid neoplasms can occasionally be limited due to sampling errors [3].

GRASP

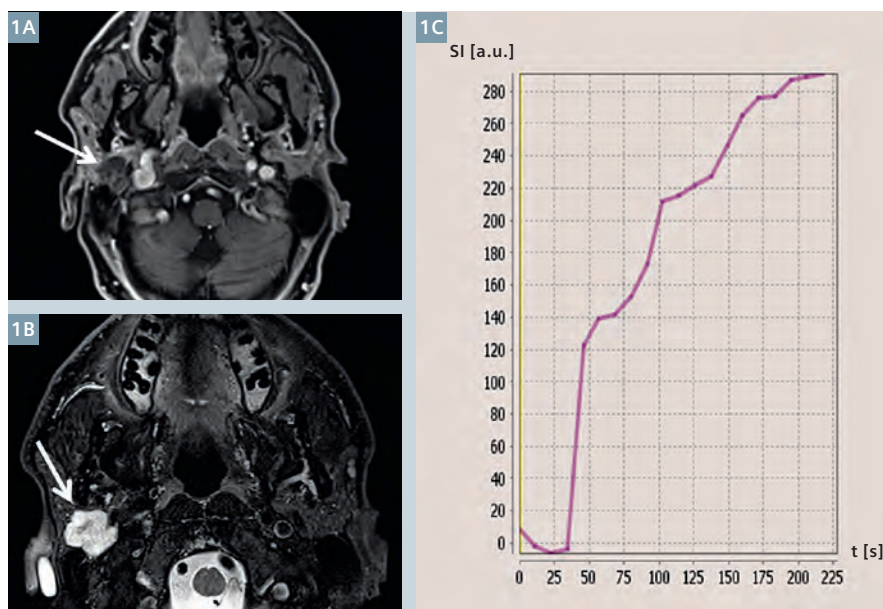
Golden-Angle Radial Sparse Parallel MR Imaging (GRASP¹) is a novel imaging technique that combines golden-angle radial stack-of-stars sampling with a compressed sensing reconstruction [4], enabling motion-robust imaging at high spatial and temporal resolution. GRASP allows

a characterization of the dynamic contrast curve of parotid tumors. Numerous features of the contrast curve can be easily assessed, such as the wash-in and wash-out contrast slopes, the time-to-maximum-enhancement, area under the curve, and peak enhancement. Each of these features may differ amongst various parotid neoplasms, and provide an additional non-invasive method of interrogating parotid neoplasms. In addition, GRASP produces high-resolution, fat-suppressed images with excellent motion robustness allowing for precise localization and mapping of parotid neoplasms.

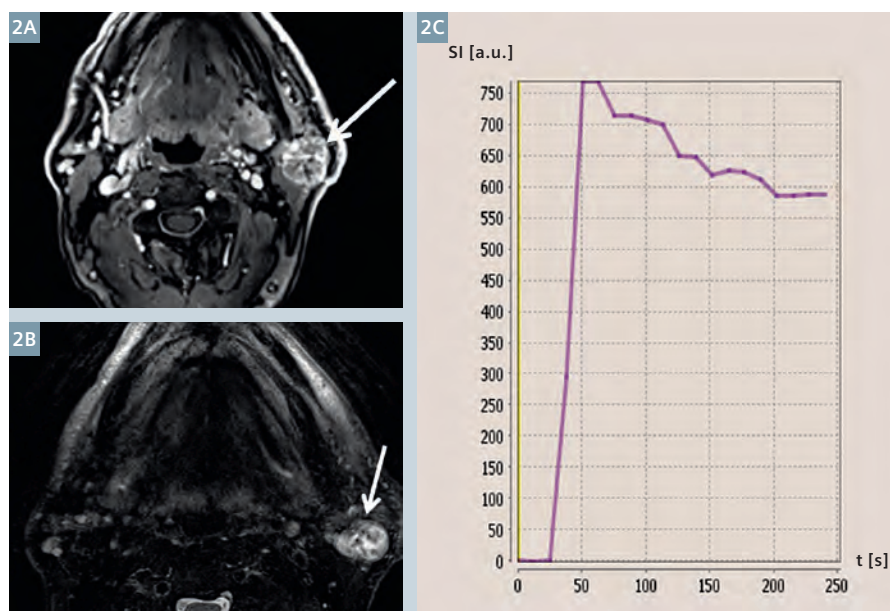
Clinical cases

Two cases are included for illustration. Figure 1 shows GRASP imaging data of a parotid mass in a 67-year-old male.

¹ The product is still under development and not commercially available yet. Its future availability cannot be ensured.



1 67-year-old male patient with a right parotid pleomorphic adenoma. **(1A)** Composite GRASP image shows a lobulated mass in the right parotid gland demonstrating mild enhancement (arrow). **(1B)** T2-weighted imaging demonstrates hyperintense signal in the lesion (arrow). **(1C)** Dynamic contrast curve shows continuous gradual wash-in of contrast material during the image acquisition.



- 2 68-year-old male patient with a left parotid Warthin's tumor. (2A) Composite GRASP image shows a lobulated mass in the left parotid gland demonstrating moderate enhancement (arrow). (2B) T2-weighted imaging demonstrates predominantly hyperintense signal in the lesion (arrow). (2C) Dynamic contrast curve shows steep wash-in slope, sharp early peak of contrast enhancement, and more gradual wash-out of contrast material.

Figure 1A is a high-resolution post-contrast image demonstrating that the mass has mild heterogeneous enhancement, and contains lobulated margins. Figure 1B shows that the lesion is hyperintense on T2-weighted imaging. Figure 1C demonstrates the dynamic contrast curve after processing of the GRASP data. The contrast curve demonstrates a gradual and continuously rising wash-in of contrast material. The imaging appearance and contrast curve characteristics were consistent with a pleomorphic adenoma [5], and this proved to be the case on pathologic analysis.

Figure 2 shows GRASP imaging data of a left parotid mass in a 68-year-old male. Figure 2A shows that the mass demonstrates moderately avid heterogeneous enhancement, and contains lobulated margins. Figure 2B shows that the lesion is predominantly hyperintense on T2-weighted imaging. Figure 2C demonstrates the dynamic contrast curve, which is strikingly different than the case shown in Figure 1. In this case, the contrast curve shows a sharp wash-in, an early peak, and relatively early wash-out of contrast material. Though the conventional imaging characteristics in this case were non-specific, the contrast curve was characteristic of a Warthin's tumor [5], which proved to be the case upon pathologic analysis.

Conclusion

Improving the diagnostic specificity in assessing parotid neoplasms is only one among many potential applications for GRASP in the head and neck. Examples include assessment of lymph node status in cancer patients, differentiation of tumor recurrence from inflammation in treated patients, or differentiation of tumor types in other organs of the head and neck. At our institution, GRASP is performed in all of our clinical head and neck MRI scans, and it routinely impacts on our diagnostic performance.

References

- Christe A, Waldherr C, Hallett R, Zbaeren P, Thoeny H. MR imaging of parotid tumors: typical lesion characteristics in MR imaging improve discrimination between benign and malignant disease. *AJNR American journal of neuroradiology*. 2011;32(7):1202-7. doi:10.3174/ajnr.A2520.
- Antony J, Gopalan V, Smith RA, Lam AK. Carcinoma ex pleomorphic adenoma: a comprehensive review of clinical, pathological and molecular data. *Head and neck pathology*. 2012;6(1):1-9. doi:10.1007/s12105-011-0281-z.
- Daneshbod Y, Daneshbod K, Khademi B. Diagnostic difficulties in the interpretation of fine needle aspirate samples in salivary lesions: diagnostic pitfalls revisited. *Acta cytologica*. 2009;53(1):53-70.
- Feng L, Grimm R, Block KT, Chandarana H, Kim S, Xu J, Axel L, Sodickson DK, Otazo R. Golden-angle radial sparse parallel MRI: combination of compressed sensing, parallel imaging, and golden-angle radial sampling for fast and flexible dynamic volumetric MRI. *Magn Reson Med*. 2014.
- Dong Y, Lei GW, Wang SW, Zheng SW, Ge Y, Wei FC. Diagnostic value of CT perfusion imaging for parotid neoplasms. *Dento maxillo facial radiology*.
- Chandarana H, Feng L, Block TK, Rosenkrantz AB, Lim RP, Babb JS, Sodickson DK, Otazo R. Free-breathing contrast-enhanced multiphase MRI of the liver using a combination of compressed sensing, parallel imaging, and golden-angle radial sampling. *Invest Radiol* 2013 Jan;48(1):10-6.
- Chandarana H, Block TK, Ream J, Mikheev A, Sigal SH, Otazo R, Rusinek H. Estimating liver perfusion from free-breathing continuously acquired dynamic gadolinium-ethoxybenzyl-diethylenetriamine pentaacetic acid-enhanced acquisition with compressed sensing reconstruction. *Invest Radiol*. 2015 Feb;50(2):88-94. 2014;43(1):20130237. doi:10.1259/dmfr.20130237.

Contact

Sohil H. Patel, M.D.
Department of Radiology
New York University
Langone Medical Center
660 1st Ave
New York, NY 10016
USA
sohil.patel@nyumc.org

Further Customization of Dot Engines: AutoCoverage

Bart Schraa, MSc., Senior MR Application Specialist

Siemens Canada Limited, Oakville, ON, Canada

Introduction

In 2009 Dot engines introduced a very powerful customization tool: AutoCoverage. AutoCoverage ensures the anatomy under examination is covered consistently throughout the entire examination. Moreover, the adjustments to the coverage will be done in a standardized way independent of the choices and/or skills of the operator.

Tailoring the coverage of the patient's anatomy can be done via the AutoCoverage parameter card. This card can be found in many of the Dot AddIns. The availability of Dot AddIns depends on the Dot engines purchased. This article uses the Generic Views Dot AddIn that is included in the Brain Dot Engine and is part of the standard system configuration for virtually all our MR systems on the D and E software levels.

Most of the available Dot engines, including the Brain Dot Engine, contain an AutoAlign (AA) Scout: e.g. AAHead_Scout, AASpine_Scout, AAHip_Scout and so on. These AutoAlign Scouts provide the landmarks and the orientation for positioning the slices in a standardized way independent of the operator.

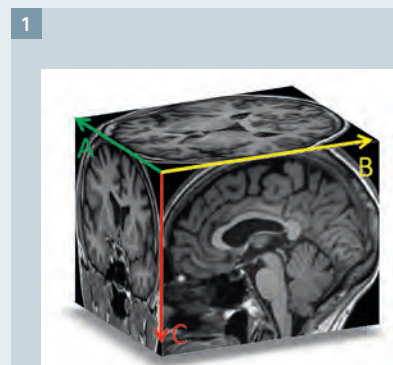
However, these AutoAlign scouts provide more information about the anatomy by means of an organ box. This organ box is a cuboid which defines the boundaries of the anatomy under examination, and which can be adjusted in size by the user. This information not only enables us to position the slices in a stan-

dardized way, but also to ensure that the coverage of the anatomy is tailored to the individual patient's anatomy. The adjustments can be done within these Dot AddIns, and ensure that the coverage is always adjusted in the same way throughout the whole examination, whether by changing the number of slices, slice thickness or distance factor (or a combination of these).

Organ boxes

An organ box defines the boundaries of the anatomy under examination. There are several organ boxes available with the AutoAlign Scouts which are delivered with the Dot engines. This article will focus on the organ box 'Brain' that is available with the Brain Dot Engine, but the principles and adjustments described can be applied to any of the other organ boxes that are available on the system.

One should note that there is a distinct difference between an AutoAlign Reference and an organ box. The AutoAlign Reference defines just the orientation and position based on landmarks as detected by the AAHead_Scout. However, the organ box will provide additional information for the AutoAlign Reference in terms of the boundaries of the anatomy. This information can then be used to adapt the coverage of the anatomy which is enclosed by the organ box to ensure the coverage is done correctly, independent of the size of the individual patient's anatomy.



1 Cuboid of the Brain organ box.

Adaptation to the coverage can be made via the edges of the cuboid of the organ box in any of the three orthogonal axes: phase, read and slice selection.

The edges of the cuboid that represents the Brain organ box as shown in Figure 1 are labeled A, B and C. These dimensions can be used for AutoCoverage to adjust the field-of-view (FOV) and coverage in the slice direction in a standardized way. For example, for the transversal plane A and B could be used to adapt the FOV, whereas C can control the 'coverage' in the slice direction. For the sagittal plane, B and C could be used by the FOV and A can control the 'coverage' in the slice direction and so on. How one can actually use this organ box to adjust the FOV and/or coverage in the AddIn will be described in the next section: AutoCoverage in the Brain Dot Engine.

AutoCoverage in the Brain Dot Engine

In order to utilize the AutoCoverage functionality we need to make sure that we measured an AAHead_Scout first. Remember, the AAHead_Scout will provide both the AutoAlign references and set the boundaries of the 'organ box'. Additionally, we need to ensure that every protocol that we want to make use of AutoCoverage is actually configured with a Dot AddIn that has that AutoCoverage functionality enabled. For demonstration

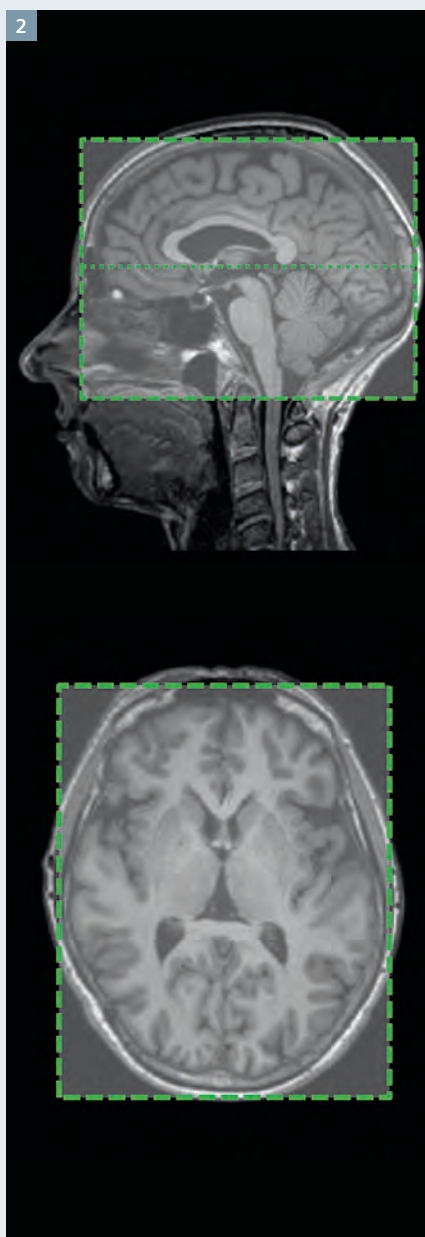
purposes, the remainder of this article uses the Generic Views AddIn to explain the AutoCoverage functionality.

The Brain Dot Engine comes with two organ boxes: Brain and Temporal Lobe. The dimensions of the Brain organ box are shown in Figure 2. As can be seen, the 'Brain' organ box uses the AutoAlign reference 'Brain' for the correct orientation and position of the transversal brain images.

We next look at how the organ box can be used in the Brain Dot Engine.

Firstly, ensure that a Generic Views AddIn is associated with the protocol: drag and drop a Generic Views from the Default AddIns directory, or any other Dot AddIn that has this AutoCoverage functionality, on the protocol you want to work on as shown in Figure 3.

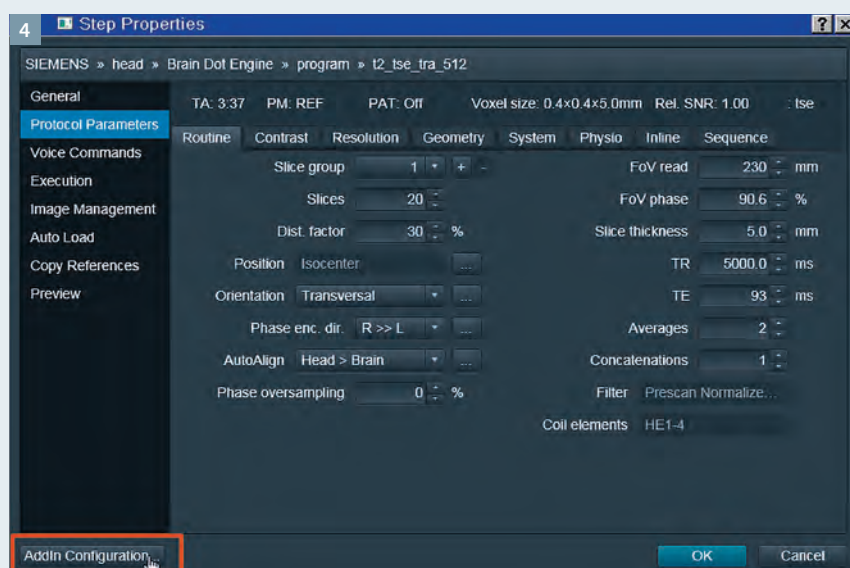
Secondly, open the AddIn Configuration. This can be done by clicking on the 'Add-In' configuration button found on the left bottom of the window of the protocol (Fig. 4) provided the protocol has an AddIn associated with it.



2 Dimensions of the Brain organ box.



3 Drag and Drop Generic Views AddIn.



4 Button AddIn Configuration.

The AutoCoverage parameter card is shown on the left side of the Dot AddIn Configurator window (Fig. 5). AutoCoverage is available in most Dot AddIns, for example the Generic Views or MPR Assignment (in this case the Generic View AddIn is used).

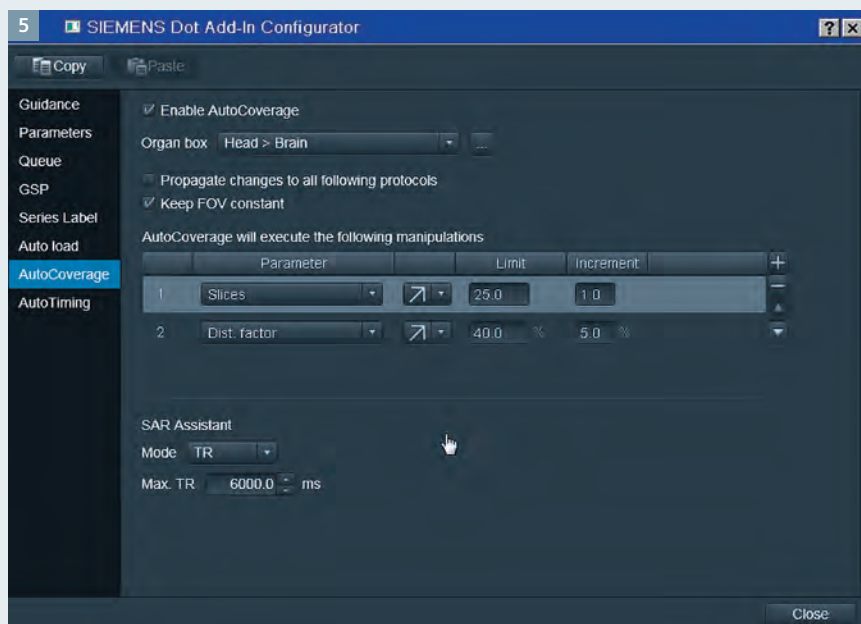
Thirdly, enable AutoCoverage on the Dot AddIn Configurator window (Fig. 6).

Fourthly, choose the organ box to be used for AutoCoverage. Within the Brain Dot Engine there are two organ boxes to choose from. For further illustration the organ box 'Brain' is chosen from the drop down menu as shown in Figure 7.

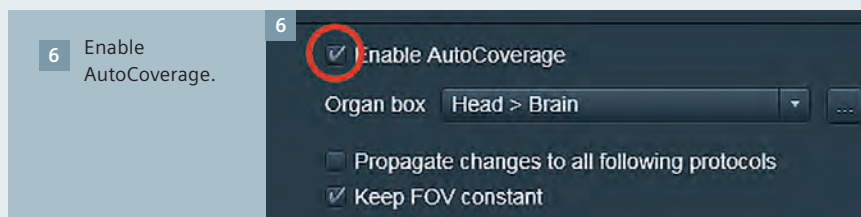
As mentioned above, the AAHead_Scout run at the beginning of the Dot Engine, not only sets the AutoAlign references, but also the dimensions of the organ boxes (Brain and Temporal Lobe in case of the AAHead_Scout). If you want to adjust the size of the organ box as set by the AAHead_Scout, select the button with the three dots (behind the chosen organ box). Another window (Fig. 8) will pop-up and the desired adjustments to the size of the organ box can be made to all three (read, phase and slice) encoding directions. The size can be increased or decreased (enter a negative value). Please note that the adjustments to the organ box (edges of the cuboid shown in Figure 2) are specific to the orientation of the slices and therefore are different for other orientations.

Fifthly, the option 'Propagate changes to all following protocols' (Fig. 9) ensures that any changes you made during the positioning of this protocol – which in effect changes the FOV and/or coverage – will be applied to the subsequent protocols.

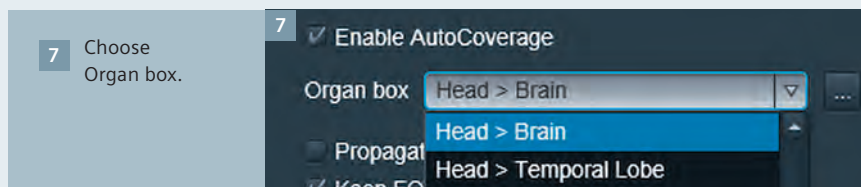
In a typical brain examination this is actually a **less** often used feature. The FOV used in Brain examinations is usually fixed and not set to a minimum as defined by the dimensions of the individual patient's anatomy. However, in abdominal examinations this is certainly more frequently done and it is quite a nice feature to tailor the protocol to the patient's anatomy. Please note that you require the



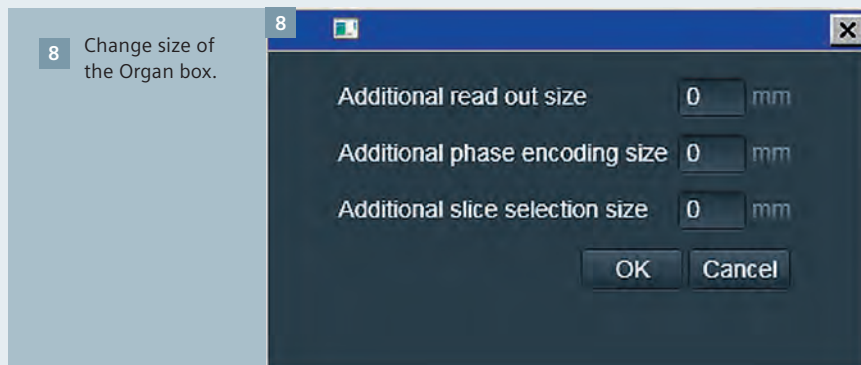
5 AutoCoverage parameter card.



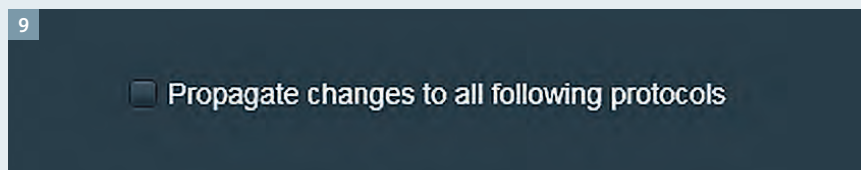
6 Enable AutoCoverage.



7 Choose Organ box.

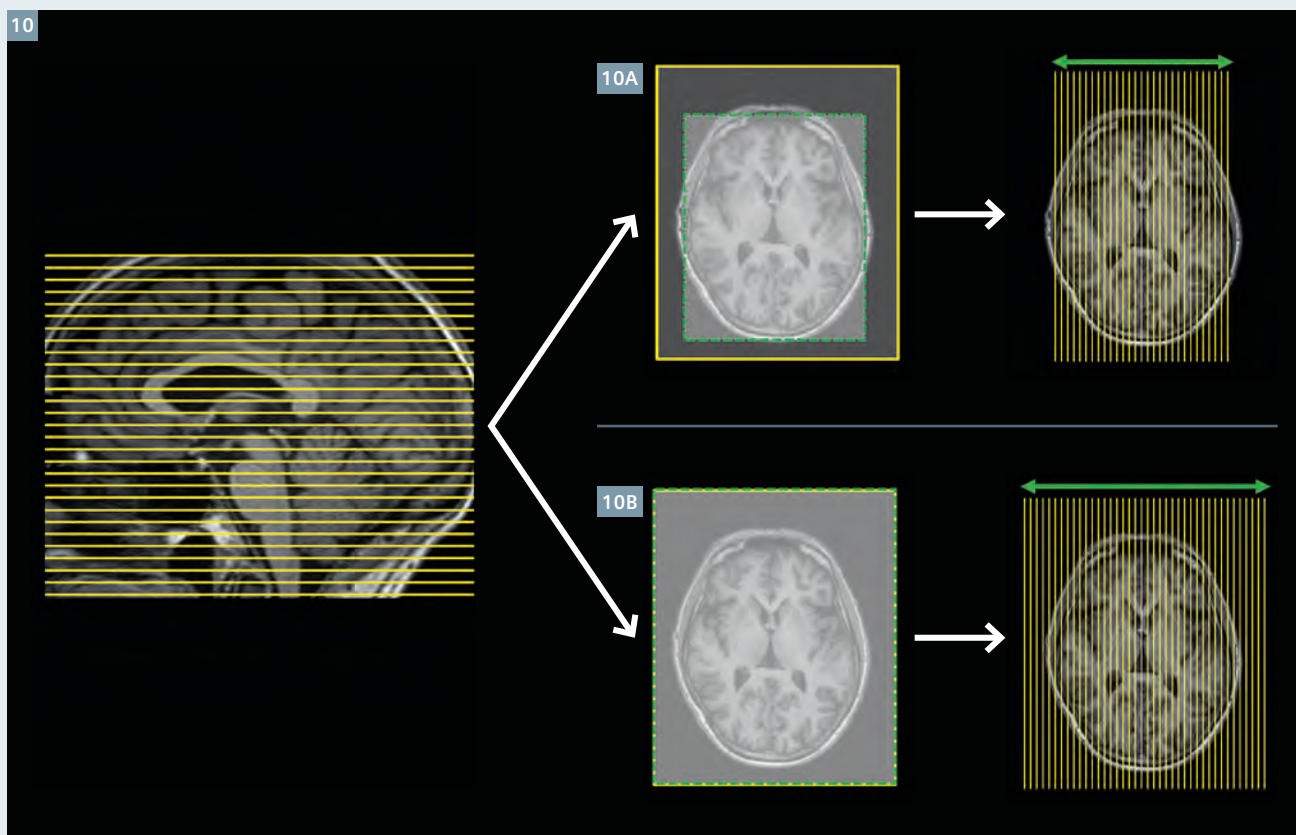


8 Change size of the Organ box.



9 Propagate changes.

10



10 Results of 'Propagate changes to all following protocols'.

Abdomen Dot Engine to make use of the AutoCoverage feature in abdominal examinations.

Warning: Changing the FOV in one direction might also influence the coverage of the slices in another direction when 'Propagate changes to all following protocols' is used. Figure 10 demonstrates what happens when we use 'Propagate changes to all following protocols'. One should be aware that while the prescription (using AutoCoverage) is the same for the transversal protocol in the user interface, the effect of the settings of 'Propagate changes to all following protocols' makes a big difference for the sagittal protocol following this transversal protocol. In Figure 10A the setting for 'Propagate changes to all following protocols' was unchecked. This will result in a proper coverage of the brain from right to left. In Figure 10B the setting for 'Propagate changes to all following protocols' was checked and results in coverage as large as the rectangular FOV (phase direction) set in the transversal protocol.

The reason for this is that when 'Propagate changes to all following protocols' is used, the FOV of the transversal protocol changes the size of the organ box in the read and phase direction (indicated by the dotted green box in Figure 10). Consequently, the organ box is changed in the slice direction for the sagittal protocol and AutoCoverage will now ensure that this complete organ box in the slice direction is covered.

As can be seen in situation A, where 'Propagate changes to all following protocols' is off, the organ box is still the size of the brain in both the read and phase direction. But in situation B, where it is 'on', the size of the organ has been adjusted to the FOV in both read and phase direction. While the size in the read direction does not have a direct influence on this sagittal protocol, the change in phase direction results in a larger coverage than necessary. Only in cases when the subsequent orientations are the same, the option

'Propagate changes to all following protocols' might be useful, but must be used carefully.

Sixthly, the next parameter 'Keep FOV constant' (Fig. 11) ensures that the FOV defined in the underlying protocol is not changed by the AutoCoverage settings. This option can be used in protocols where the FOV is **not** changed according to the size of the patient's anatomy. 'Keep FOV constant' in effect disables the AutoCoverage feature in the phase and read direction, while it still works in the slice orientation.



11 Keep FOV constant.

Seventhly, the next configuration step in the AutoCoverage card is the actual 'brain' of AutoCoverage. In order to adjust the coverage of the anatomical region in a standardized way, one needs to configure so-called manipulations to make modifications to the underlying protocol to ensure the complete anatomy is covered.

The default Generic Views Dot AddIn, as used for the transversal protocols in the Brain Dot Engine (this example is from a MAGNETOM Skyra running on software version syngo MR E11A), typically has three steps to achieve sufficient coverage (Fig. 12):

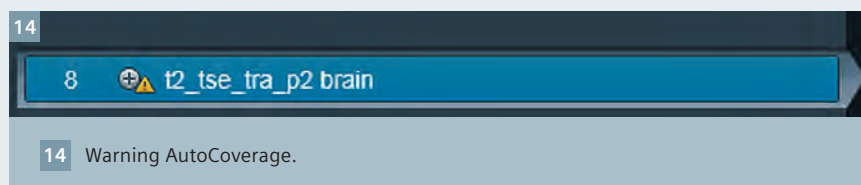
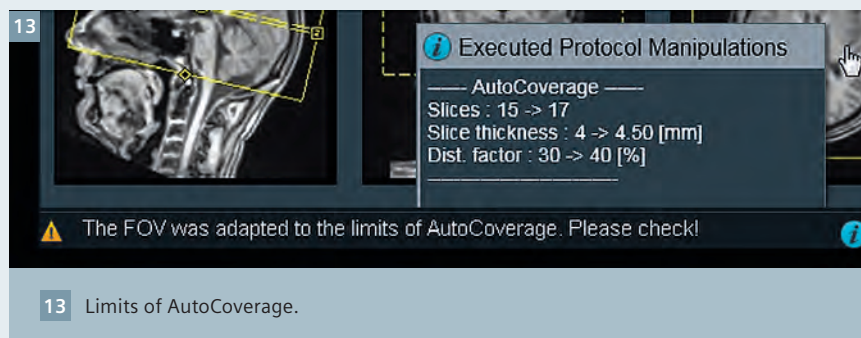
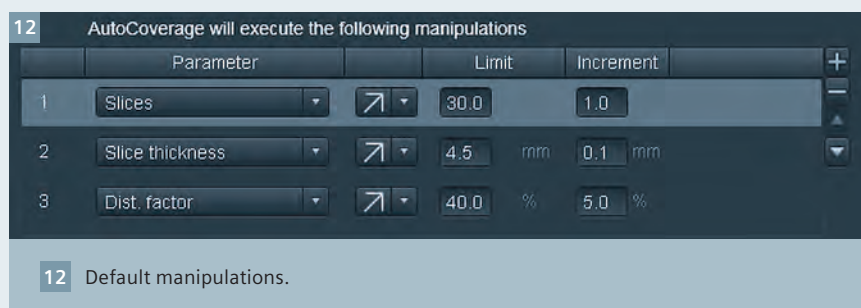
1. Increase the number of slices up to a maximum of 30 in increments of 1 slice at a time until sufficient coverage is achieved, if not proceed to the next step,
2. Increase the slice thickness up to a maximum of 4.5 mm in increments of 0.1 mm at a time until sufficient coverage is achieved, if not proceed to the next step,
3. Increase the distance factor up to a maximum of 40% in increments of 5% at a time until enough coverage is achieved.

If these three steps are not enough to cover the entire organ box, the user will get a warning ('The FOV was adapted to the limit of AutoCoverage. Please Check!') on the Guidance View card of the open protocol in the Queue (Fig. 13). The warning indicates that the AutoCoverage was not successful and needs to be checked by the user.

Additionally, an AutoAlign icon with the yellow warning triangle will be shown in the queue (Fig. 14).

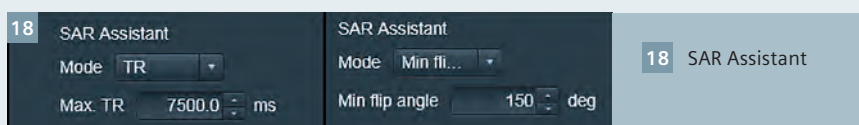
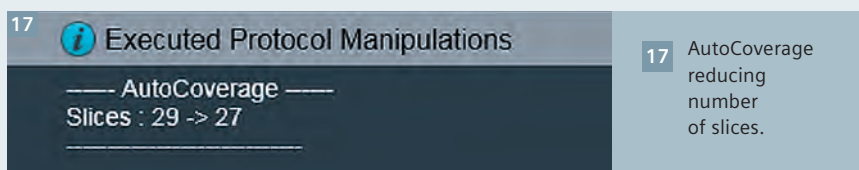
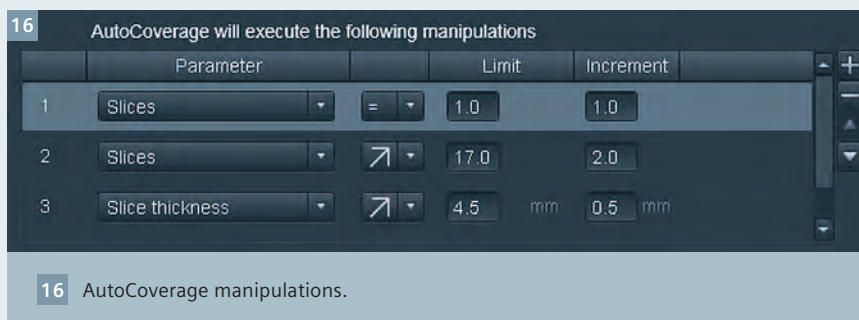
But where AutoCoverage was successful the user can also see which changes have been made to the original protocol. This information is visible when the mouse is hovered over the information button (italic *i* in blue circle) located at the bottom of the Generic Views Guidance card (Fig. 15).

By default the manipulations in the AutoCoverage are set up such that an adjustment will be made only where



the coverage of the organ box was insufficient; it will only increase the number of slices, slice thickness and/or distance factor. Where the anatomy in the slice direction is actually smaller than the organ box detected, no changes will be made. If the size of the organ box is by coincidence the same as the coverage defined by the protocol (number of slices, slice thickness and distance factor), the system will also indicate there are no changes necessary. From the information provided by the information button, the user would not be able to tell if either exact coverage or smaller anatomy produced the message 'AutoCoverage was successful without changing the protocol'.

To have AutoCoverage also adjust the coverage in situations where the size of the actual anatomy, as defined by organ box, is smaller than defined by the underlying protocol (number of slices, slice thickness and distance factor), a simple adjustment to the manipulations is all that is required. The user need only insert an extra manipulation at the top by clicking on the '+' sign in the manipulations setup box (Fig. 16). This extra manipulation must be moved with the arrow key to the top and is actually the first manipulation. The manipulation should then be changed such that the Slices '=' 1 as shown in Figure 16. This will effectively set the number of slices first to 1. When multiple concatenations



are used in the protocol, this minimum number should instead be set to at least the number of concatenations. Otherwise, the protocol will be adjusted to fewer concatenations than initially configured since the number of concatenations cannot be greater than the number of slices.

The second manipulation will then increase the number of slices to make sure there is enough coverage. Further manipulations (e.g. 3 and/or 4) will then be executed when required.

With this small adjustment to the AutoCoverage one can ensure that the anatomical region is covered by the number of slices required, independent of the relative size of the anatomical region.

In this example the number of slices is decreased from 29 to 27 (in this case the protocol had 29 slices as default) as shown in Figure 17. In reality it was first set to 1 and then increased to 27 following the defined manipulations. Had this small adjustment to the AutoCoverage not been made, 29 slices would have been scanned instead.

The AutoCoverage card enables you to ensure that the anatomy is covered, whether the protocol is 2D or 3D, as both have the same orientation. But of course the individual manipulations

to ensure enough coverage are different for 2D and 3D protocols.

To make sure that manual adjustments to the proposed coverage by the user, like increasing the number of slices, is done for all protocols in the same orientation (and require the same coverage), it is recommended to work with Copy References ('Slices' / 'Slices and saturation regions' / 'Slices and Adjust Volume') in order to keep the changes in coverage the same for all linked protocols. This is necessary since we switched off 'Propagate changes to all following protocols' and therefore the manual adjustment to the coverage by the user, are not propagated to the following protocols.

The system will give priority to Copy References over AutoCoverage. Please note that in this case the coverage for the 2D cannot be

propagated to 3D protocols by Copy References and would require a manual interaction by the user.

The last option on the AutoCoverage parameter card is very useful when using AutoCoverage. Increasing the coverage from the underlying protocol might result in a higher chance of SAR pop-ups. The number of SAR pop-ups can be reduced using the SAR Assistant, either by increasing the TR to a certain maximum, or by reducing the flip angle to a certain minimum to be able to scan the protocol within the current SAR limits without interaction of the user. Depending on the underlying protocol, either option can be chosen and configured as shown in Figure 18.

Conclusion

This article details the steps to adjust and manipulate the coverage in the slice direction by using the AutoCoverage functionality available in many Dot AddIns by the use of the organ box as provided by the AAHead_Scout. In practice when there are other AutoAlign Scouts available on the system, the modifications to the coverage can be made by using any of the organ boxes available with these AutoAlign scouts. The AutoCoverage parameter card is a very powerful option, and will ensure that the complete anatomy, as detected by the organ box, will be covered in the underlying protocol. At the same time, steps to ensure that the coverage is achieved, will be executed in a standardized way and adjustments are independent of the choices and/or skills of the operator. However, it will remain the responsibility of the user of the MR system to confirm the correct coverage of the anatomy of interest.

Contact

Bart Schraa
Siemens Canada Limited
HC CX NAM CA CX-CS APP
1577 North Service Road East Oakville
L6H 0H6 Oakville, ON
Canada
bart.schraa@siemens.com



syngo.MR Neuro 3D: Your All-In-One Post Processing, Visualization and Reporting Engine for BOLD Functional and Diffusion Tensor MR Imaging Datasets

Julien Gervais; Lisa Chuah

Siemens Healthcare, Magnetic Resonance, Erlangen, Germany

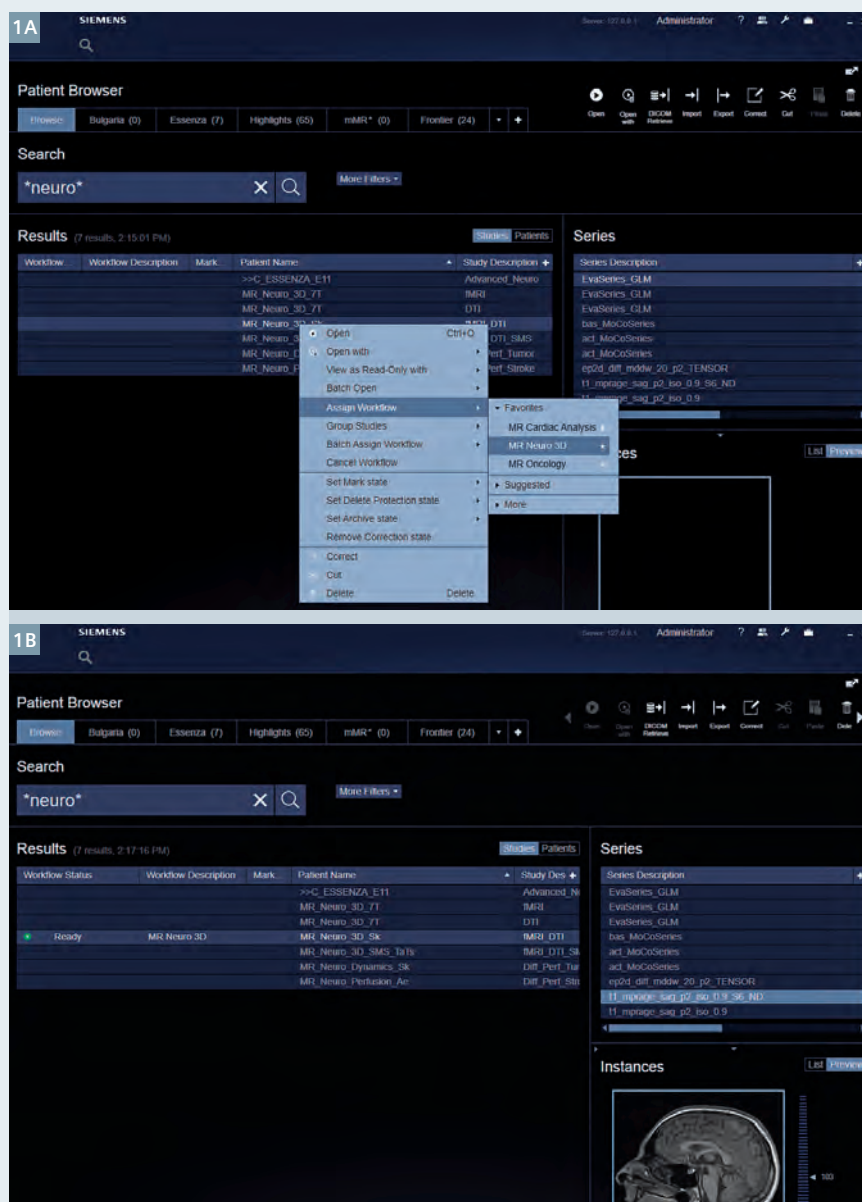
syngo.MR Neuro 3D enables a streamlined post processing and visualization of functional BOLD and diffusion tensor images. For clinical insights into the use of fMRI and DTI in the clinical settings, we would like to refer the interested reader to these case series [1, 2, 3].

Within this article, we have described our preferred workflow and steps for the processing and analysis of BOLD fMRI and diffusion tensor imaging (DTI) data. Obviously, it is *not* necessary to have both BOLD fMRI and DTI datasets available for each patient, syngo.MR Neuro 3D can be used even if there is only BOLD fMRI or DTI data for a patient.

First step: Open the case

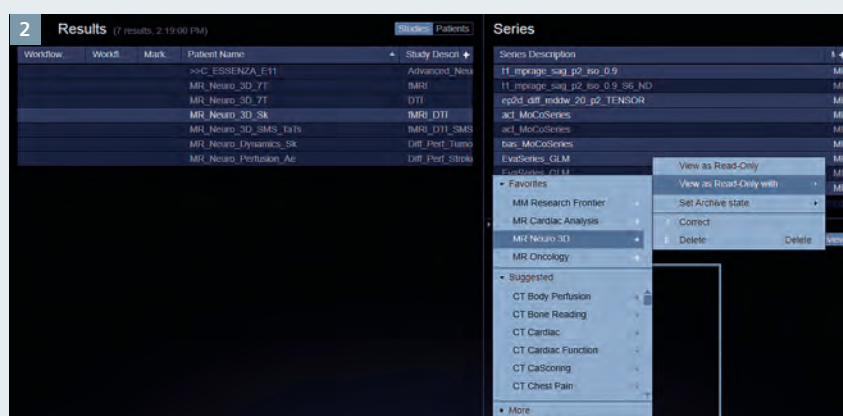
Assign the complete case to syngo.MR Neuro 3D with a right-mouse click and selection of the option 'Assign' with further selection of 'MR Neuro 3D' (Fig. 1A). Once the case has been assigned, the status of the case changes from 'Scheduled' to 'Ready' (Fig. 1B). Open the case by double clicking on it.

For faster loading, select only the relevant series (BOLD MOCO, GLM, Tensor, anatomical data) by multi-selection with 'Ctrl' key and left mouse clicks (Fig. 2). Follow this with a right mouse click and selection of the option 'Read only' with further selection of 'MR Neuro 3D' (Fig. 2). syngo.MR Neuro 3D can accept more than one BOLD series with the capability of visualizing activations for up to 4 different



1 (1A) Case assignment to Neuro 3D with a right mouse click. (1B) When the case is ready, the 'Workflow Status' changes from 'Scheduled' to 'Ready'.

paradigms simultaneously. However, the corresponding GLM must also be loaded. For tractography analysis, only the TENSOR data is required. The raw diffusion series does not have to be loaded. *syngo.MR Neuro 3D* can accept data collected in different scan sessions (e.g., the patient anatomical and DTI data were collected in separate scan sessions from the BOLD data).



2 Multi-selection of the relevant datasets to be opened as 'read only' for Neuro 3D.

Second step: Alignment

The BOLD and DTI data should be registered to a reference scan, usually the anatomical scan such as the MPRAGE. Accurate alignment is especially critical for the analysis of data acquired in different scan sessions.

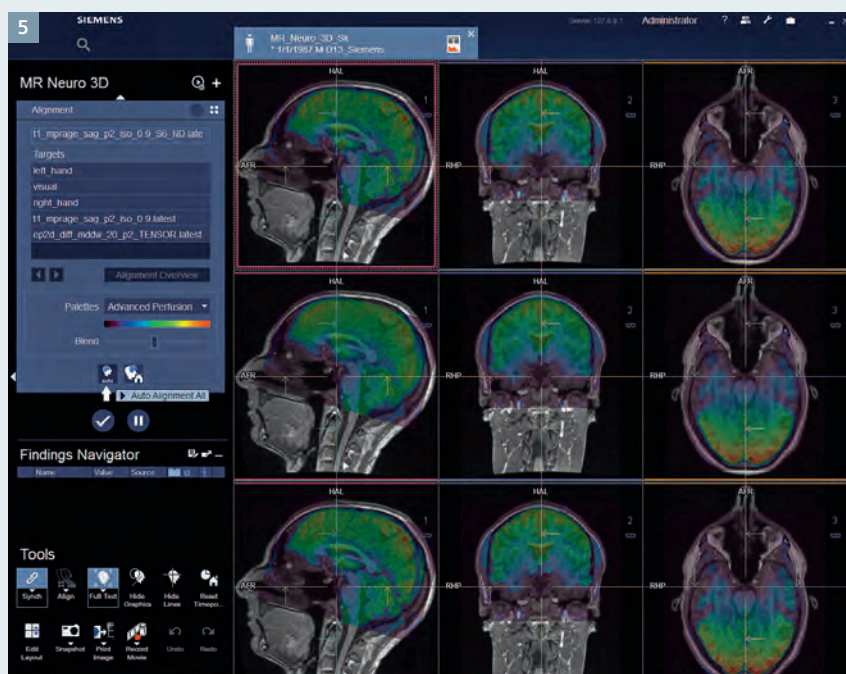
The alignment overview displays all available series overlaid on the reference scan. This is the starting point for registration (Fig. 3). A drop down menu in the Control Area on the far left enables the selection of different overlay palettes, such as 'Edges' or 'Perfusion', to help visual assessment of co-registration accuracy (Fig. 4). In addition, a blending functionality is available.



3 The alignment overview with all available series overlaid on the reference scan.



4 Dropdown menu for different overlay palettes in the Control Area on the far left of the screen. These different overlay palettes can aid assessment of co-registration accuracy. The different examples shown are (4A) Advanced Perfusion (default) and (4B) Edges.



5 Automatic alignment for all series to the reference series is performed by clicking on the 'Auto Alignment All' button (indicated with arrow).

Image alignment can be performed automatically or manually. First, click on the 'Auto Alignment All' button in the Control Area (Fig. 5, indicated by arrow) in order to perform automatic alignment for all series simultaneously. The algorithm works with an iterative approach: Every time you click on the 'registration' button, the registration is further improved until a steady state is reached (Fig. 6).

We recommend the individual verification of each and every series. To do this, click on the series in the 'target images'. This opens the single series in a dedicated 3D MPR view with the functional data overlaid on the reference scan. For BOLD acquisitions, the raw series is also displayed together with motion correction graphs (rotation and translation) (Fig. 7).

For each segment, scroll through the slices to check the alignment. You can scroll using three alternatives:

1. using the mouse wheel,
2. moving the mouse up and down while pressing the right mouse button,
3. pressing the keyboard arrows 'up' and 'down'.

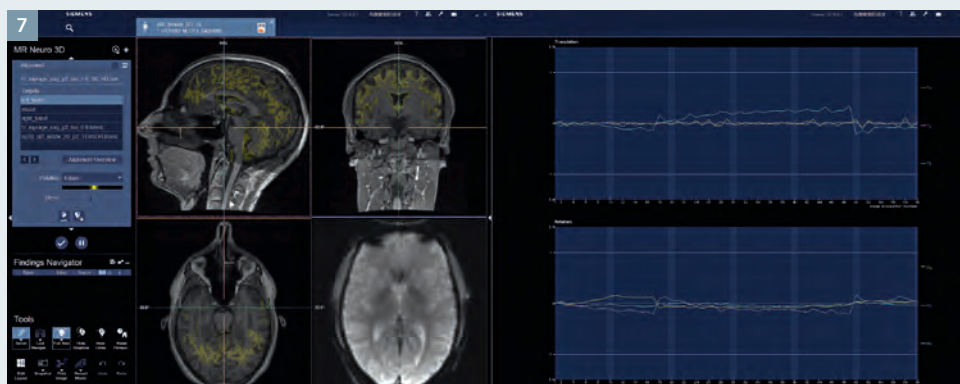
For the BOLD raw series, you can additionally scroll through time using two alternatives:

1. moving the mouse left and right while pressing the right mouse button,
2. pressing the keyboard arrows 'left' and 'right'.

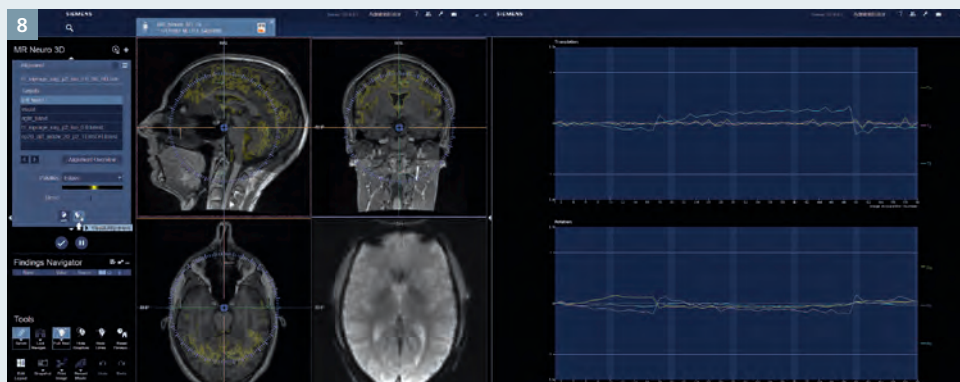


6 Improvements to the automatic coregistration with several iterations. (6A) Prior to application of alignment algorithm, (6B) after one iteration, (6C) after three iterations.





7 Verification of the alignment of a single series in a dedicated display.



8 Manual alignment is activated by pressing the 'Visual Alignment' button which triggers the appearance of a compass guide.

To modify the alignment, click on the 'Visual Alignment' button in the Control Area (Fig. 8, indicated by arrow). This opens a compass guide in the MPR segments.

- For translation: Position the cursor in the desired MPR segment and drag the overlay using the left mouse button.
- For rotation: Position the cursor over the compass in the desired MPR seg-

ment. The compass changes to white and you can drag it clockwise or counter clockwise using the left mouse button. The center of the rotation can be adjusted by dragging the center of the compass.

Many users find the 'Edges' palette useful for the verification of the alignment. After you have performed the manual alignment, deactivate the

'Visual Alignment' button to avoid any further accidental modifications.

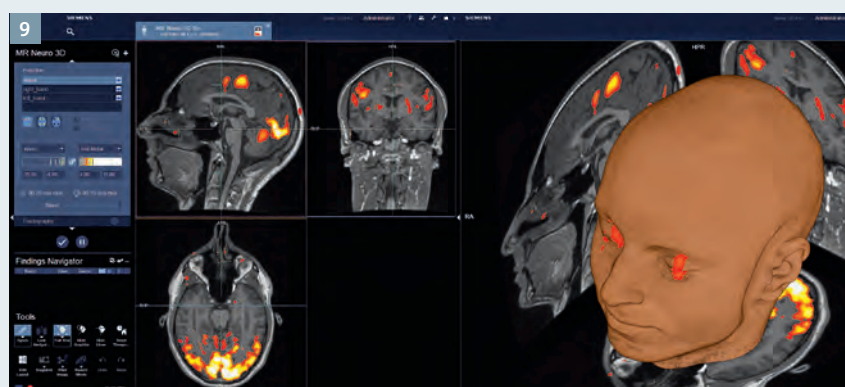
Repeat this step for all the other series: Click in the 'target images' list to select the next series. To go back to the overview display, click on the 'Alignment Overview' button. When all the series are properly registered, processing and visualization can then be performed.

Third step: fMRI

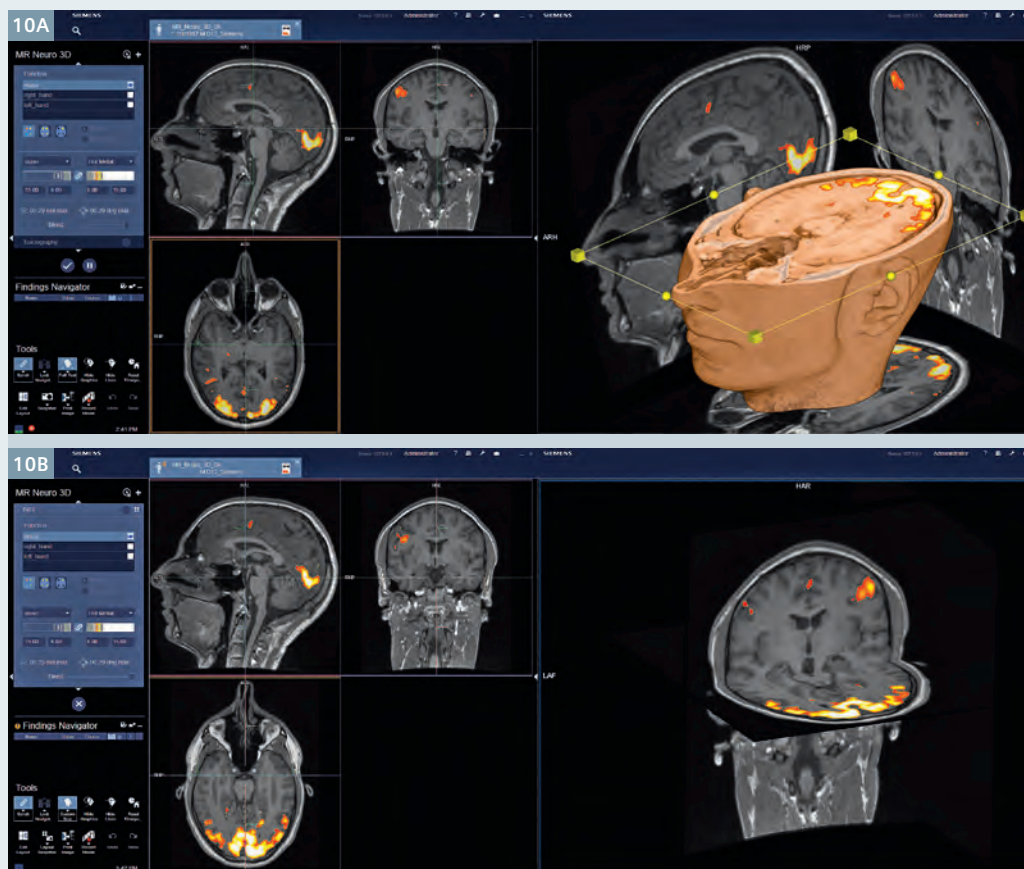
Click on the 'fMRI' step to perform visualization of BOLD activation areas. All BOLD paradigms are presented in the 'function' list and the corresponding activation maps are displayed overlaid on the reference scan in a 3D MPR view and as a volume rendered image (Fig. 9).

The visualization and processing tools offer the following functionalities:

- Hide or display dedicated activation maps by clicking the 'eye' icon in the function list.



9 Visualization of BOLD activation maps within the fMRI step.



10 (10A) Clip plane functionality to better visualize BOLD activations within the VRT segment. (10B) fMRI activations as displayed on a gray-scale VRT-like visualization within the VRT segment.

- Assignment of color palettes to the activation maps. Different modes are available:
 - ‘Individual Mode’ to assign different color palettes to each activation map.
 - ‘Uniform Mode’ to assign the same color palette to all activation maps.
 - ‘Highlight Mode’ to assign a specific color palette to the activation map resulting from a primary task and another color palette to the secondary tasks.
- Adjustment of statistical threshold levels
- Optional interpolation and specification of cluster size. This can be found in the ‘function properties’ menu (bottom right corner of each MPR segment)
- In the VRT segment:
 - Clip plane for visualization of the BOLD activation specific to a plane (upper left corner). Several planes can be activated simultaneously.

- Split plane for visualization of BOLD activation in the whole imaging volume up to the specified anatomical plane (upper left corner)
- Brain mask for skull removal to better visualize brain surface cortical structures

- Synchronization of MPR and VRT segments: Clicking on the VRT automatically brings the MPR segments to the corresponding reference point.

First, examine the activated areas for the different tasks in the MPR segments. If necessary, adjust the statistical threshold values for each paradigm. Highlight the corresponding paradigm with a click in the function list and adjust the threshold located below (slider bar or keyboard input). The colors of each activation map can be individually specified by using the drop down menus of available color palettes. Within the VRT segment, activate the clip plane and split plane functionalities to help 3D visualization (Fig. 10A).

A list of important keyboard shortcuts is present in Appendix A. To translate a plane, position the cursor close to the plane, press and hold the right mouse button and move the mouse in the desired direction. To rotate a plane, position the cursor close to the spheres on its border, press and hold the left mouse button and move the mouse in the desired direction.

Should a VRT-like gray-scale visualization be preferred (Fig. 10B), please do these following steps:

1. Click on “Fused Volume Renderer” (lower left corner) to deactivate the VRT.
2. Click on the wrench within “Orthogonal MPR” (lower left corner) and click on “Orthogonal MPR Properties”. This will activate a pop-up window. Activate the “In-situ Display” option.
3. To translate or rotate the different planes within the VRT segment, simply modify the reference lines within the MPR segments.

Fourth step: Time Course Evaluation

To perform a quality check of the activation maps, click on the 'Time Course Evaluation' step to analyze signal-time curves.

Select the desired paradigm in the 'function list' by clicking on the corresponding white box. An eye icon will appear and the corresponding activation map is displayed. Time-course analysis can be performed for individual voxels or volumes of interest. Select your desired tool by clicking on the appropriate icon

'fMRI voxel' or 'fMRI VOI' within the control area or in the upper right corner of each MPR segment (Fig. 11A, highlighted with squares).

For single voxel analysis, select the 'fMRI voxel' tool and click on the appropriate voxels of interest within the MPR segments. Every click will create a voxel of a different color and the corresponding signal-time curve is displayed with the same color in the time-course segment. To modify the position of a voxel, first deactivate the 'fMRI voxel' tool and relocate the voxel with drag and drop.

For volume analysis, select the 'fMRI VOI' tool and draw a volume over an activated area of interest (Fig. 11B). By default, the VOI is restricted to the voxels which are activated above threshold. You can change this behavior with a right click on the VOI and de-selection of 'shrink to activation' option.

To delete any voxel or volume of interest, select the corresponding object and choose the 'delete measurement' option with a right mouse click.



11 (11A) Options for tool selection. (11B) Display of activation maps with signal-time curves in the Time Course Evaluation step.

Fifth step: Tractography

For visualization of diffusion tracts, click on the 'Tractography' step. Tractography data for the complete imaging volume have been automatically generated. They are displayed overlaid on the reference scan in a 3D MPR view and as a volume rendered image (Fig. 12). If you have performed the fMRI step as described above, the



tractography data is simply added to the currently available MPRs and VRT.

The tracts are generated using a deterministic approach with the FACT algorithm (Fiber Assignment by Continuous Tracking) [4]. Different parameters can be specified, for example seed points and angle threshold (see Appendix B). Specific settings can be saved to be applied for the initial automated whole volume tractography as well as for the more precise generation of refined tracts. Default settings are provided.

You can save your own settings, for this, please refer to the user manual.

The whole volume tractography may be useful for the immediate visualization of tracts displacement in the presence of tumors (Fig. 13).

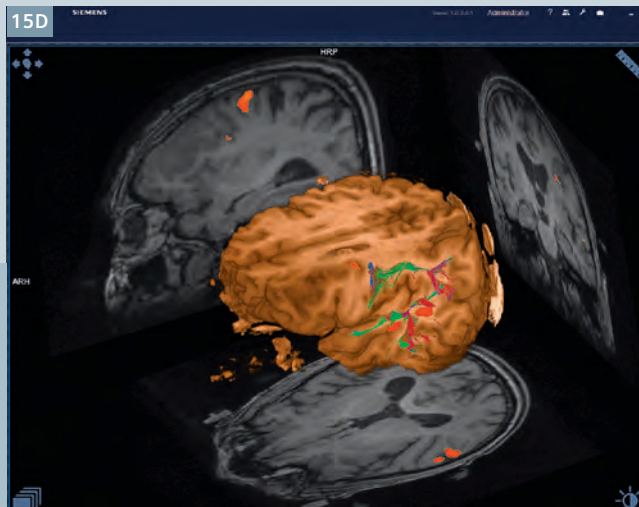
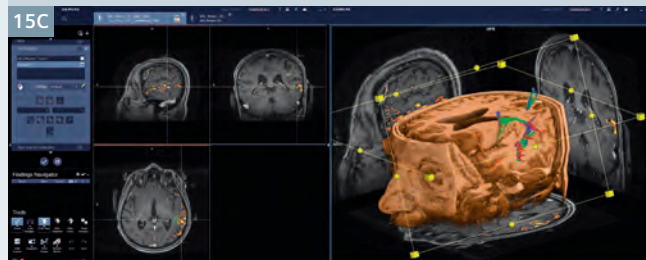
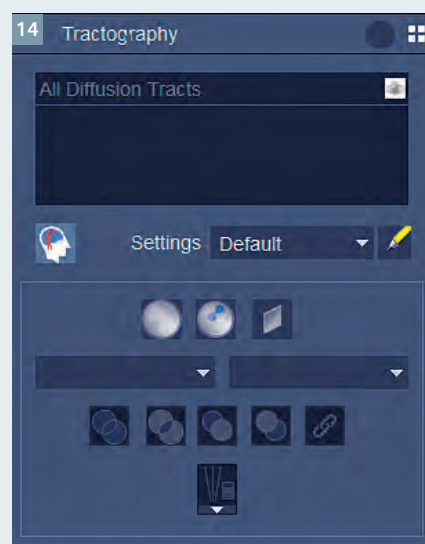
The whole volume tractography can be interactively refined through different options: volume of interest, volume of interest using activated voxels, planes, or logical combination (AND, OR ...) of these (Fig. 14):

1. Tractography VOI: selective visualization of tracts which traverses the VOI.
2. Tractography VOI (Shrink to activation): selective visualization of tracts within the vicinity of fMRI activated voxels in the VOI.
3. Tractography Plane: selective visualization of tracts which crosses the set plane.

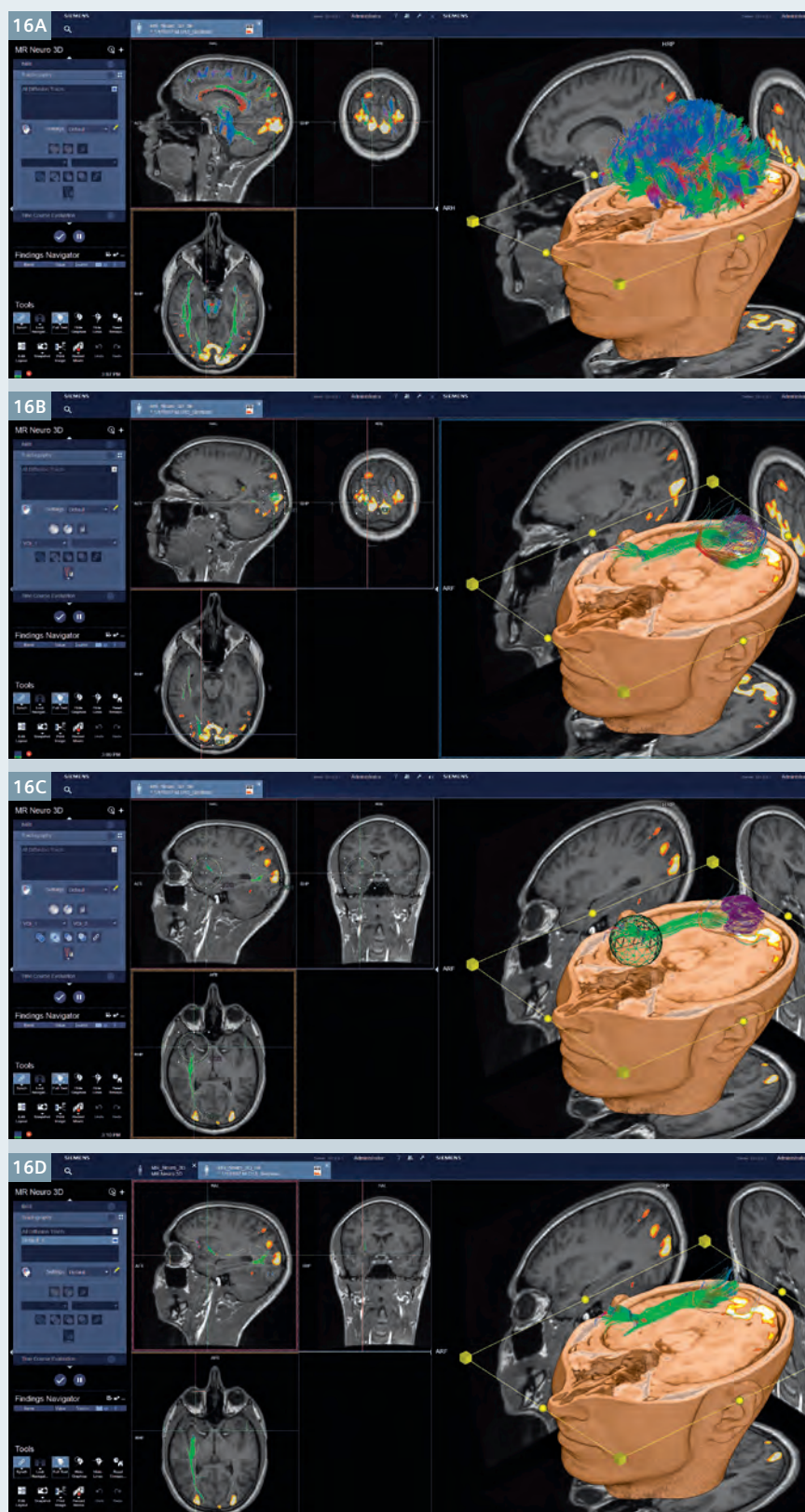
As there are many different approaches for tractography analysis, this article will focus on two use cases.



13 Visualization of whole volume tractography within the Tractography step (two clip planes have been used).



15 Visualization of the arcuate fasciculus in the tractography step. **(15A)** Initial whole brain tractography. **(15B)** Refined tracts after positioning of the VOI. **(15C)** Rendered Tracts with defined settings. **(15D)** Additional rendering with skull stripping.



16 Visualization of the connecting pathways for the visual system in the tractography step. **(16A)** Initial whole brain tractography. **(16B)** After fMRI VOI. **(16C)** After VOI 2, only tracts going through 1 and 2 are displayed. **(16D)** Rendered Tracts with defined settings.

1. Visualization of the arcuate fasciculus

Click on the 'Interactive Mode' icon (Fig. 14).

Visualization of this very important tract can be done by placing a Tractography VOI in the inferior frontal lobe or in the temporal lobe. However, in cases of lesions or tumors potentially displacing important functional language regions, it may be helpful to use fMRI activation voxels to guide placement of the VOI.

Select the 'Tractography VOI' or 'Tractography VOI (Shrink to activation)' by clicking on the corresponding icon. Draw the VOI in any MPR segment. This creates a VOI labeled 'VOI_1' (Fig. 15B). The color of the VOI reflects its function: green for a Tractography VOI, purple for a Tractography VOI (Shrink to activation). You can move the VOI by dragging and moving it in the different MPR segments. The VRT is updated in real time.

In the VRT segment, use the clip planes and split planes as described in the fMRI step. Once you are satisfied with the rendering, hide the seed volumes, if desired, with a right click and further selection of 'Hide seed points'. Save your result by clicking the 'Create and Save Diffusion Tract Bundle' icon in the control area. This generates the finalized tract bundle using the settings highlighted in the drop down menu 'Settings' (Fig. 15C).

2. Visualization of the connecting pathways for the visual system

Click on the 'Interactive Mode' icon.

First, select the 'Tractography VOI (Shrink to activation)' by clicking on the corresponding icon and draw a VOI encompassing the visual cortex on the axial plane. This creates a purple VOI labeled 'VOI_1' (Fig. 16B). Manipulate the shape of the VOI in the different planes to capture the visual cortex selectively for the left or right hemisphere.

Second, select the 'Tractography VOI' and draw a VOI next to the optic chiasm, usually best identified on the axial plane. This creates a green



17 Tractography displayed on a VRT-like gray-scale visualization with single seed point (17A) and multiple seed points (17B).

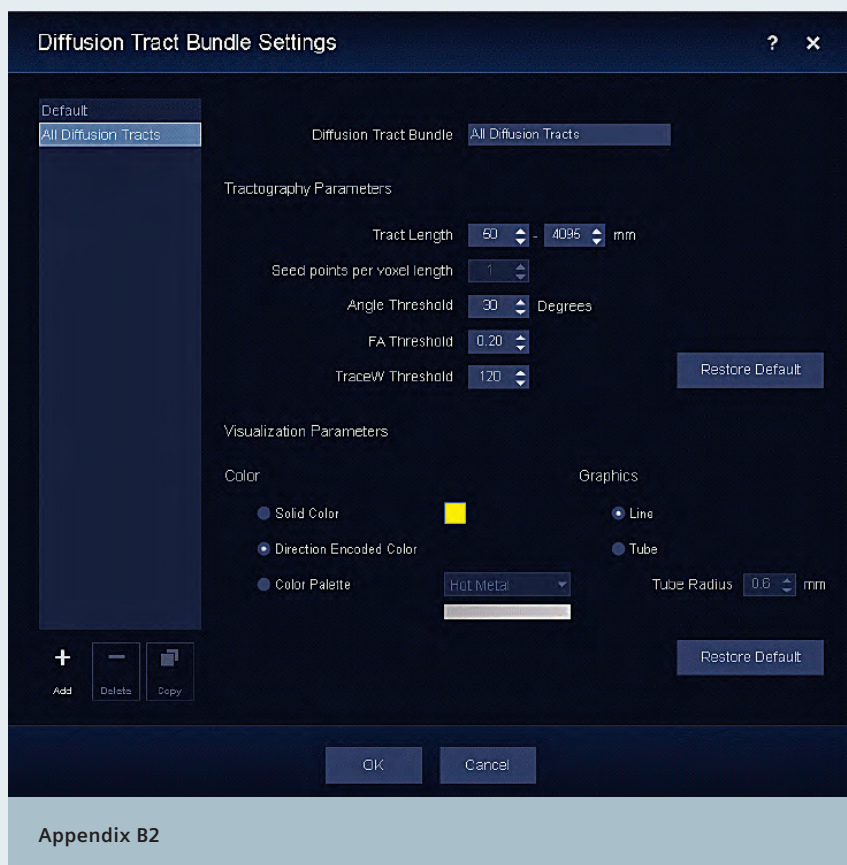
VOI labeled 'VOI_2' (Fig. 16C). By default, the logical combination 'A AND B' is selected (Fig. 16C, arrow), and therefore only the tracts going through the VOI_1 and the VOI_2 are displayed. You can change the position and shape of both VOIs in all planes in order to best capture the connecting pathways. Use the clip planes and split planes in the VRT segment to fine-tune the rendering.

Save your result by clicking the 'Create and Save Diffusion Tract Bundle' icon in the control area. This generates the finalized tract bundle using the settings highlighted in the drop down menu 'Settings'.

Should a VRT-like gray-scale visualization be preferred (Figs. 17A, B), please refer to the end of the fMRI section for the necessary steps.

Export:

To export the processing results, a dedicated 'Export' step is available. Please refer to the user manual.



References

- 1 Benzinger TL, McKinstry III RC, Chen CI, Priatna A. Clinical applications of Diffusion Tensor Imaging. MAGNETOM Flash. 2007;37:74-86.
- 2 Pillai JJ, Zaca D. Case series: Presurgical planning with fMRI/DTI. MAGNETOM Flash. 2011; 48: 14-17.
- 3 Bartsch AJ. Simultaneous Multi-Slice (SMS) Imaging for Pre-Surgical BOLD fMRI and Diffusion Tractography: Case Illustrations. MAGNETOM Flash Special Simultaneous Multi-Slice Supplement. 2015; 63: 58-64.
- 4 Mori S, van Zijl PCM. Fiber tracking: Principles and strategies—A technical review. NMR in Biomedicine. 2002;15:468–480.

Clip Planes	
Action	Keyboard Shortcut
Left Clip Plane	Shift+ L
Right Clip Plane	Shift + R
Head (Dorsal) Clip Plane	Shift + H
Foot (Ventral) Clip Plane	Shift + F
Anterior Clip Plane	Shift + A
Posterior Clip Plane	Shift + P
Home all Clip Planes (Orientation Reset)	Shift + 0 (zero)
Show/Hide all Clip Planes	Shift + 1
Orthogonal MPRs	
Action	Keyboard Shortcut
Action Increase offset of orthogonal MPRs	Shift + ↑
Decrease offset of orthogonal MPRs	Shift + ↓
Show/Hide orthogonal MPR frames	Shift + 2
Show/Hide orthogonal planes	Shift + 3
Others	
Action	Keyboard Shortcut
Show/Hide VRT	Shift + 4
Show/Hide Split Plane	Shift + 5
Toggle between Clip Plane and Split Plane	Shift + s
Appendix A: Important keyboard shortcuts for syngo.MR Neuro 3D	

Tract Length	
larger range = more tracts	smaller range = less tracts
It is defined as the length of the tracts that will be shown as tracts.	
Seed points per voxel length	
smaller value = less tracts	higher value = more tracts
value 1 = 1^3 = tract, value 2 = 2^3 = 8 tracts, value 3 = 3^3 = 27 tracts ...	
Angle Threshold	
smaller value = less tracts	higher value = more tracts
Fiber tracking stops at a certain position if the resulting fiber tract would bend by more than "Angle Threshold" degrees at this position.	
FA Threshold	
smaller value = more tracts	higher value = less tracts
It is defined as the degree of Anisotropy: 0 = low anisotropy, 1 = very strong anisotropy; typical values are between 0.05 and 0.2. Fiber tracking stops at voxel position with an FA value lower than the given FA threshold.	
TraceW Threshold	
smaller value = more tracts	higher value = less tracts
The trace-weighted image is obtained by taking the average of the individual diffusion weighted images from the DTI scan. This generates an image comparable to orthogonal DWI, yet is derived from the full diffusion sampling. The TraceW threshold value is set to 120 as default based on internal experience.	
Appendix B1	



Contact

Siemens Healthcare GmbH
 HC DI MR CRM AW
 Lisa Chuah, Ph.D.
 Global Segment Manager Neurology,
 Pediatrics and Orthopedics
 Postbox 32 60
 91050 Erlangen
 Germany
lisa.chuah@siemens.com



Contact

Siemens Healthcare GmbH
 HC DI MR CRM AW
 Julien Gervais
 Global Marketing Manager
 syngo.via for MR
 Postbox 32 60
 91050 Erlangen
 Germany
Julien.Gervais@siemens.com

Simultaneous Multi-Slice:

Accelerating advanced neuro applications for clinical routine

The common complaint – My MRI takes too long! – may soon be a thing of the past.

Simultaneous Multi-Slice (SMS) is an exciting new technique designed for unprecedented speed in imaging to shorten patient's table time. Developed under collaboration between Siemens and several partners including Athinoula A. Martinos Center for Biomedical Imaging, Massachusetts General Hospital/Harvard Medical School and the Centre for Magnetic Resonance Research (CMRR), University of Minnesota, SMS significantly speeds up imaging and circumvents the SNR loss associated with conventional parallel imaging (iPAT) techniques such as SENSE and GRAPPA.

Unlike iPAT techniques, which speed up acquisition by reducing the number of sampled data points, SMS speeds up imaging through a different method: the simultaneous excitation and acquisition of multiple imaging slices. This enables reduction in image acquisition time up to the factor of slice acceleration, that is, the number of slices excited and acquired in parallel. For diffusion-weighted and diffusion-tensor imaging, image acquisition time can be reduced by up to 68%. Alternatively, this increase in speed can be reinvested in higher spatial/diffusion resolution or anatomical coverage. The technology combines multiband RF pulses with a new, innovative technique – blipped CAIPIRINHA. This minimizes SNR loss and enables an effective combination of slice and in-plane acceleration, further reducing scan time, susceptibility artifacts, and/or enabling higher image resolution. With a slice acceleration factor of up to 8 for BOLD imaging, the BOLD signal can be sampled more intensively for higher sensitivity and statistical power and/or higher spatial resolution/coverage.

Find out more about this exciting new technique in a special MAGNETOM Flash issue on Simultaneous Multi-Slice, guest edited by Professor Peter Jezzard (FMRIB, University of Oxford). This issue covers all topics from technical details to clinical and research applications. Read articles from the developers of this technique (M. Griswold, K. Ugurbil, L. Wald) for technical details on SMS. Leading clinicians and scientists around the world share their clinical and research experiences with SMS Diffusion and BOLD in neuroimaging (A. Bartsch, C. Eichner, R. Hoge, K. Miller, T. Shepherd, S. Smith, E. Yacoub,) and beyond, to orthopedics, body, cardiology, and pediatric imaging (G. Andreisek, H. Chandarana, C. Mekkaouri, D. Staeb). This issue also provides a vision into the expansion of SMS to fast and high-resolution anatomical imaging with SMS TSE* (J. Cui, J. Ellermann, M. Kean, S. Kralik) and more advanced diffusion techniques with SMS RESOLVE* (R. Frost, D. Porter, V. Runge).



Download the SMS issue of MAGNETOM Flash at www.siemens.com/magnetom-world

Case Report: High-Resolution Simultaneous Multi-Slice (SMS) RESOLVE Diffusion Neurography for Evaluation of Peripheral Nerve Entrapment Syndrome and Neuropathy

Andreas J. Bartsch^{1,2,3}

¹ Radiologie Bamberg, Germany

² Depts. of Neuroradiology, Universities of Heidelberg and Wuerzburg, Germany

³ Oxford Centre for Functional MRI of the Brain (FMRIB), University of Oxford, UK

Abstract

Diffusion echo-planar imaging (EPI) using read-out segmentation of long variable echo trains (RESOLVE; [1]) has primarily been developed for high-resolution diffusion-weighted imaging with reduced susceptibility-based geometric image distortions as well as T2*-decay related blurring and robust correction for motion-induced phase artifacts. Notably, RESOLVE also reduces the echo time (TE) but increases the scan time of the acquisitions.

Simultaneous multi-slice (SMS) imaging has initiated a “new revolution” of accelerated MRI scanning [2], particularly for EPI. For diffusion EPI investigating structures with non-uniformly directed diffusion and areas of crossing fibers, like in the central nervous system, SMS principally allows to sample more diffusion directions and shells within a given acquisition time. In the peripheral nervous system with rather uniformly directed diffusion and few crossing fibers, however, substantial gains offered by SMS may be primarily related to increases in spatial image resolution and lower slice thicknesses. Thin slices reduce partial volume artifacts and facilitate isotropic recordings while an increased number of slices is able to maintain or extend the coverage.

As yet, SMS has primarily gained attention for brain examinations while RESOLVE has also been applied to extracranial (such as head-and-neck cancer) imaging. Here we illustrate the utility of high-resolution SMS RESOLVE¹ diffusion neurography for evaluation of peripheral neuropathies, exemplified by ulnar nerve compression at the Loge de Guyon.

Patient history

A 59-year-old left-handed woman presented with brachialgia paraesthetica nocturna of the left hand. It had developed about two months ago and consecutively worsened. She had been using a crutch due to severe, activated coxarthrosis on the left for six months and was originally transferred for MR evaluation of presumed carpal tunnel syndrome (median compression neuropathy).

Clinical examination revealed slight sensory loss of the left palmar hypothenar but not the thenar area. Phalen’s maneuver was negative on both sides while Froment’s sign was slightly positive on the left. Tapping the ulnar nerve at the level of the Loge de Guyon provoked paraesthesias of the fifth and the ulnar side of the fourth digit (positive Tinel’s sign).

There was slight left adductor- but also opponens-pollicis-weakness, compared to the right non-dominant hand, as manifested in the strength (4 out of 5) of key grip and thumb opposition. No muscular atrophy was detected, and fist closing was symmetric, with no claw hand. The thumb-to-little-finger and Schaeffer’s tests were intact.

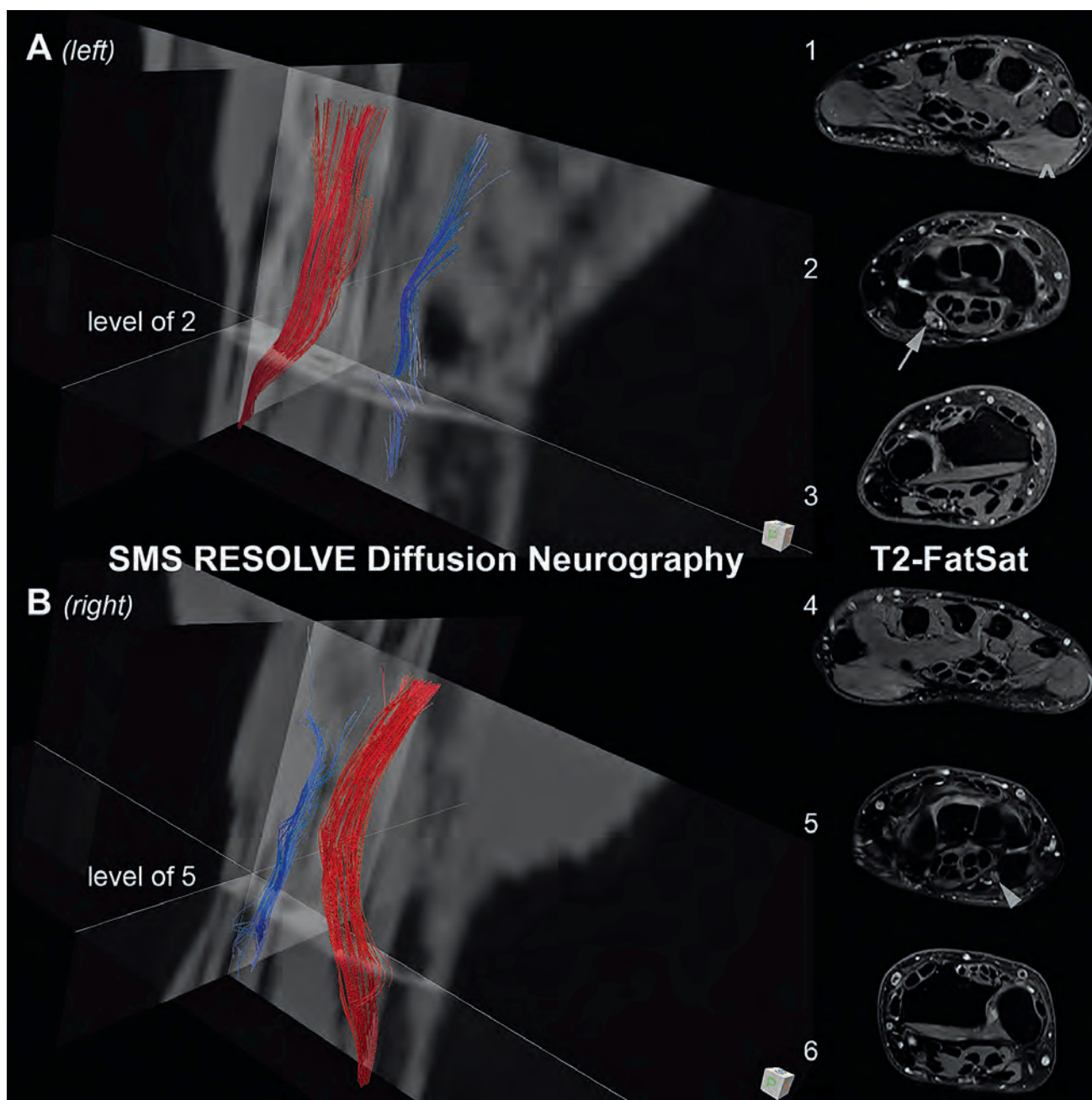
Imaging sequence and post-processing details

Imaging was performed on a 3 Tesla MAGNETOM Skyra scanner (Siemens Healthcare, Erlangen, Germany) running on software version syngo.MR E11C and using a 16-channel wrist coil.

Axial coplanar diffusion-, T2- as well as proton-density- and T1-weighted 2D-sequences were recorded, each with 30 slices at a slice thickness of 2.50 mm and a 10% interslice gap. For the relevant diagnostic diffusion- and T2-weighted sequences, an iPAT (GRAPPA) factor of 2 and fat saturation were used.

The diffusion-weighted acquisition was a simultaneous multi-slice (SMS) accelerated, high-resolution spin-echo echo-planar imaging (SE-EPI) sequence with read-out segmentation of long variable echo trains (RESOLVE), parallel imaging and a two-dimensional navigator-based reacquisition, recorded at a TR of

¹ The product is still under development and not commercially available yet. Its future availability cannot be ensured.



High-resolution SMS diffusion neurography in a patient with Loge-de-Guyon syndrome on the left. At the level of the left ulnar canal, fiber tracking was discontinuous and an increased angle threshold of interpolated streamlining was required to reconstruct the nerve. T2-weighted, fat-saturated imaging reveals focal hyperintensity and cross-sectional enlargement of the left ulnar nerve (arrow) compared to the right (arrowhead), consistent with distal ulnar compression neuropathy. (Note T2-hypointense flow void of the ulnar artery and T2-hyperintense ulnar veins, unambiguously allocated by T1-weighted contrast-enhanced images [not shown], in Guyon's canal on both sides.) Denervation edema of left thenar muscles normally innervated by the median nerve (abductor pollicis brevis and opponens pollicis) is also detected (caret), consistent with an innervation variant.

3000 ms, a TE of 50 ms, with a single measurement and 7 read-out segments, a SMS factor of 3, using monopolar diffusion-sensitizing gradients and 12 diffusion directions – isotropically distributed on the full sphere (generated using an optimiza-

tion for eddy-current correction by gps, version 1.0, part of FSL, <http://fsl.fmrib.ox.ac.uk/fsl/fslwiki/>, see below) – at $b = 800 \text{ s/mm}^2$ and with one b_0 -image with no diffusion weighting, 7/8 partial Fourier sampling, at a pixel bandwidth of

868 Hz/pixel, a flip angle of 180° , with a field-of-view (FOV) of 94 mm \times 75%, an effective matrix size of 80 \times 60, resulting in an in-plane resolution of 1.18 \times 1.18 mm, within a total acquisition time (TA) of 5.03 minutes.

The T2-weighted acquisition was a turbo-spin echo (TSE) sequence, recorded at a TR of 3000 ms, a TE of 95 ms, with 3 averages, an echo-train length of 11, a pixel bandwidth of 250 Hz/pixel, a flip angle of 120°, with a FOV of 100 mm x 60%, an effective matrix size of 256 x 152, resulting in an in-plane resolution of 0.39 x 0.39 mm, within a TA of 2.02 minutes.

Diffusion image post-processing was performed using tools from the Oxford Centre for Functional Magnetic Resonance Imaging of the Brain's Software Library (FMRIB Software Library FSL, version 5.0.9; <http://www.fmrrib.ox.ac.uk/fsl/>) [3] and consisted of (1) eddy current correction using eddy (part of FSL; [4]), (2) mask generation using fslmaths and fslview (version 3.2.0; both also part of FSL) and diffusion-tensor fitting with least squares using dtifit (again part of FSL).

Interpolated streamline diffusion neurography was performed using DiffusionToolkit (Version 0.6.3) and TrackVis (Version 0.6.0.1; <http://trackvis.org/>), using the default angle threshold of 35° (except for the Loge-de-Guyon segment of the left ulnar nerve, see below) and user-supplied masks (not shown) for seeding.

For comparison of the affected and unaffected side, both wrists were examined (Fig. 1A & 1B). On the affected left side (Fig. 1A), three cross-sectional seeds of the ulnar nerve – placed at the level of the Loge de Guyon (Fig. 1A – level of 2) as well as 15 mm proximally and distally to it – were required to reconstruct ulnar nerve fibers (displayed in blue-to-purple colors). Furthermore, the angle threshold had to be increased at the level Guyon's canal to enable fiber tracking on the left (90° were used here). On the unaffected right side (Fig. 1B), a single cross-sectional seed of the ulnar nerve – placed at the level of the Loge de Guyon (Fig. 1B – level of 5) – and the default angle threshold were sufficient for ulnar diffusion neurography

(shown in blue). For the median nerve (fibers shown in red), a single cross-sectional seed at the level of the carpal tunnel and the default angle threshold were sufficient on both sides for diffusion neurography.

Imaging findings

At the level of the Loge de Guyon, the left ulnar nerve revealed the following pathological changes on MR neurography (MRN):

- Increased signal of all fascicles on the high-resolution T2-weighted, fat suppressed sequence compared to the ipsilateral median nerve and the nerves of the contralateral wrist (Fig. 1A, arrow at 2),
- focally increased ('pseudoneuromalike') cross-sectional area by 38% compared to the ulnar nerve of the contralateral wrist (Fig. 1A & 1B, 2 vs. 5),
- decreased mean fractional anisotropy (FA) value by 43% compared to the ulnar nerve of the contralateral wrist (not shown),
- decreased and discontinuous 'trackability' compared to the ulnar nerve of the contralateral wrist (Fig. 1A vs. 1B), as evidenced by:
 - a) Interruption of fiber trackings at the level of the Loge de Guyon (three seeds were required to track the left ulnar nerve) and
 - b) increased uncertainty of fiber orientations (an increased angle threshold had to be chosen at the level of Guyon's canal; see Imaging Sequence and Post-Processing Details above).

These findings are consistent with distal ulnar compression neuropathy due to a Loge-de-Guyon syndrome.

Furthermore, there was increased signal of the left abductor pollicis brevis and opponens pollicis muscles consistent with denervation edema (Fig. 1A, caret at 1) but atypical for ulnar neuropathy because these muscles are typically innervated by the median nerve (see Discussion).

Discussion

Peripheral neuropathies constitute a significant source of debilitating morbidity, and focal compressions of peripheral nerves are one of the frequent etiologies. Median nerve neuropathy due to compression in the carpal tunnel and ulnar nerve neuropathy due to compression in the cubital tunnel are most common while compression of the ulnar nerve at the level of the Loge de Guyon is less frequent.

The MR anatomy of the ulnar canal or Loge de Guyon has been described in detail [5]. Guyon's canal is formed between the pisiform and hamate by the superficial flexor retinaculum, i.e. the volar carpal ligament or ligamentum carpi palmare (palmar margin), the deep flexor retinaculum, i.e. the transverse carpal ligament or ligamentum flexorum (latero-dorsal margin), and the flexor carpi ulnaris along with the pisiform (ulnar margin). It contains the ulnar nerve, artery and vein (Fig. 1A & 1B, 2 & 5). Originating from the medial cord of the brachial plexus, the ulnar nerve enters Guyon's canal medial (ulnar) to the ulnar artery, superficial to the deep flexor retinaculum and proximal to the pisiform (zone 1). Within the Loge de Guyon, it bifurcates at the level of the distal pisiform into superficial sensory and deep motor branches dorso-medially to the hook of the hamate (zone 2). The motor branches normally supply the abductor (et flexor) and opponens digiti minimi, flexor carpi ulnaris, the ulnar part of the flexor digitorum profundus (IV et V), interossei, adductor pollicis, and fourth (and third) lumbricals as well as the palmaris brevis. Sensory branches pass superficially to supply the skin of the hypothenar eminence, the fifth and the medial aspect of the fourth digit (zone 3). Thus, zone 1 contains both motor and sensory fibers. Here, compression typically results in both motor and sensory changes. Compression of deep motor branches in zone 2 distal to the bifurcation results in pure motor deficits, prolonged distal motor latencies to and eventually atrophy of the first dorsal interosseous and abductor digiti minimi, with no sensory changes. Compression of

superficial branches only in zone 3, resulting in pure sensory changes without motor deficits, are rare.

Compression can be due to fractures or fragments of the hook of the hamate, flexor tenosynovitis, atypical muscle bellies (esp. of the flexor digiti minimi brevis or abductor digiti minimi), space-occupying lesions including ganglion cysts from degenerative wrist disease or rheumatoid arthritis, lipomas or vascular pathologies such as (pseudo-) aneurysms of the ulnar artery or thrombosis. Compression can also result from chronic or repeated external pressure by push-ups, bicycle handle bars or, like in the presented case, from using crutches. Primary treatment consists of compression protection and, in refractory cases, of decompressive surgery. Regeneration tends to be slower and less successful for the ulnar compared to the median nerve.

High-resolution, fat-saturated pulse sequences sensitive to prolonged T2-relaxation times constitute the gold standard to detect neuropathic changes by MRN. However, diffusion MRI of peripheral nerves and derived parameter maps of fractional anisotropy (FA), radial (RD) and axial (AD) diffusivity from diffusion tensor imaging (DTI) have already been shown to correlate distinctly with electrophysiological parameters (distal motor latencies, nerve conduction velocities and compound muscle action potentials) even in clinically asymptomatic individuals and to improve diagnostic accuracy in detecting peripheral neuropathy in conjunction with T2-weighted fat-saturated imaging [6-8]. Previous studies were limited by in-plane resolutions and slice thicknesses, in particular, susceptible to profound partial volume contamination effects.

At a slice thickness of 4.0 mm and an interslice gap of 30% [6-8], peripheral nerve lesions of ≤ 1.2 mm may entirely fall into the gap and those ≤ 5.2 mm [1] are likely to be contaminated by partial volume effects of unaffected nerve tissue. In both situations, the measured FA values will be artificially increased which can lead to false-negative detec-

tions. At a low in-plane resolution, on the other hand, a thin peripheral nerve surrounded by fatty tissue in a canal, such as the cubital tunnel, will be contaminated by partial volume effects of tissue with no preference in the diffusion direction which will in turn artificially decrease the measured FA values. This situation can then lead to false-positive detections of 'abnormal' DTI parameters. For these reasons, a high spatial resolution, as offered by SMS RESOLVE, is essential to improve the diagnostic value of diffusion neurography of peripheral nerves.

High-resolution SMS RESOLVE now offers an unprecedented spatial resolution at low echo times and large coverage for diffusion neurography at clinically acceptable acquisition times to further improve its diagnostic performance. Such technology may also be instrumental to eventually detect previously unnoticed ischemic changes within peripheral nerves. Our case report illustrates the clinical utility of high-resolution SMS RESOLVE diffusion neurography in a patient with Loge-de-Guyon syndrome. Consistent with distal ulnar compression neuropathy, T2-weighted signal and cross-sectional area of the ulnar nerve was increased on the affected side while FA was profoundly decreased compared to the unaffected side. Streamline fiber tracking was impaired and discontinuous at the level of Guyon's canal (Fig. 1). As yet, very few studies have successfully reconstructed fiber pathways of peripheral nerves by diffusion neurography (emphasizing the high quality of our SMS RESOLVE data). Note that 'tractography' would be a misnomer in the peripheral nervous system.

Interestingly, there was denervation edema in thenar muscles normally supplied by the median nerve. Given that the median nerve showed no evidence of neuropathy, which virtually precludes muscular denervation due to median nerve lesions [9], this suggests (co-)innervation of the abductor pollicis brevis et opponens pollicis by the ulnar nerve in this particular case. Appreciation and

recognition of innervation variants, such as the Martin-Gruber anastomosis between the median and ulnar nerve or the Riche-Cannien anastomosis between the median nerve and deep ramus of the ulnar nerve, are essential to interpret such 'paradoxical' changes. Atypical nerve supply ranges from partial or total innervation of the opponens pollicis and abductor pollicis brevis by the ulnar nerve as a mild form [10] to the rare 'all ulnar' or 'all median' hand in the extremes [11]. The latter are more frequent in dysmelias.

Conclusion

Here, two recent advances in the development of MRI pulse sequences, namely diffusion EPI using read-out segmentation of long variable echo trains (RESOLVE) and simultaneous multi-slice (SMS) imaging, have been combined for diffusion neurography of peripheral nerves in a case with Loge-de-Guyon syndrome. At present, diffusion neurography has a primarily confirmatory diagnostic value. However, with this exciting progress in pulse sequence development diffusion neurography is now feasible at high-resolution, reduced partial voluming (due to reduced slice thicknesses), relatively large coverage and low echo-times in clinically acceptable scan times. This is anticipated to promote application and early diagnostic value of diffusion neurography in the peripheral nervous system.

Acknowledgement

... to Siemens Healthcare GmbH, Germany (Wei Liu, Thorsten Feiweier, Heiko Meyer and Thomas Illigen, in particular), for excellent support.

... to the Oxford Centre for Functional MRI of the Brain (FMRIB) for the outstanding image processing software (FSL) they are developing.

... to Optoacoustics', Israel (<http://www.optoacoustics.com/>), Active Noise Cancellation (ANC) system to cancel out EPI read-out noise making diffusion neurography much more comfortable.

References

- Porter DA, Heidemann R. High Resolution Diffusion-Weighted Imaging Using Readout-Segmented Echo-Planar Imaging, Parallel Imaging and a Two-Dimensional Navigator-Based Reacquisition. *Magn Res Med* 2009; 62:468-475.
- MAGNETOM Flash 2015; 63 (3, supplement issue on Simultaneous Multi-Slice Imaging): 2-110.
- Smith SM, Jenkinson M, Woolrich MW, Beckmann CF, Behrens TEJ, Johansen-Berg H, et al. Advances in functional and structural MR image analysis and implementation as FSL. *Neuroimage* 2004; 23(Suppl 1): S208-219.
- Anderson, J. L. R. (2014). Geometric distortions in diffusion MRI. In: *Diffusion MRI: from quantitative measurement to in-vivo neuroanatomy*. Johansen-Berg, H. & Behrens, T. E. (Eds.), 2nd edition, Elsevier Academic Press, Amsterdam (ISBN 978-0-12-396460-1), 2014. pp. 63-85.
- Zeiss J, Jakab E, Khimji T, Imbriglia J. The ulnar tunnel at the wrist (Guyon's canal): normal MR anatomy and variants. *AJRAmJRoentgenol* 1992; 158(5):1081-5.
- Baeumer P, Pham M, Ruetters M, Heiland S, Heckel A, Radbruch A, et al. Peripheral Neuropathy: Detection with Diffusion-Tensor Imaging. *Radiology* 2014; 273(1):185-193.
- Heckel A, Weiler M, Xia A, Ruetters M, Pham M, Bendszus M, et al. Peripheral Nerve Diffusion Tensor Imaging: Assessment of Axon and Myelin Sheath Integrity. *PLOS One* 2015; 10(6):e0130833.
- Breckwoldt MO, Stock C, Xia A, Heckel A, Bendszus M, Pham M, et al. Diffusion Tensor Imaging Adds Diagnostic Accuracy in Magnetic Resonance Neurography. *Invest Radiol*. 2015 Aug;50(8):498-504.
- Schwarz D, Weiler M, Pham M, Heiland S, Bendszus M, Bäumer P. Diagnostic signs of motor neuropathy in MR neurography: nerve lesions and muscle denervation. *Eur Radiol* 2015;25(5):1497-1503.
- von Lanz, T, Wachsmuth, W, *Praktische Anatomie. Arm* (1. Band, 3. Teil, 2. Auflage). Springer, Berlin, 1959. pp. 36-44, 214.
- Broser, F, *Topische und klinische Diagnostik neurologischer Krankheiten* (2. Auflage). Urban & Schwarzenberg, München, 1981. Pp. 49-50, 60-62.

Contact

Andreas Joachim Bartsch, MD
Radiologie Bamberg
<http://www.radiologie-bamberg.de/Heinrichsdamm6>
96047 Bamberg
Germany
bartsch@radvisory.net



Further Information

For MR Neurography protocols, case studies, clinical articles and expert talks please visit us at www.siemens.com/MR-Neurography

Case Report: 3D SPACE MR Acquisition in Genitourinary Tract Imaging

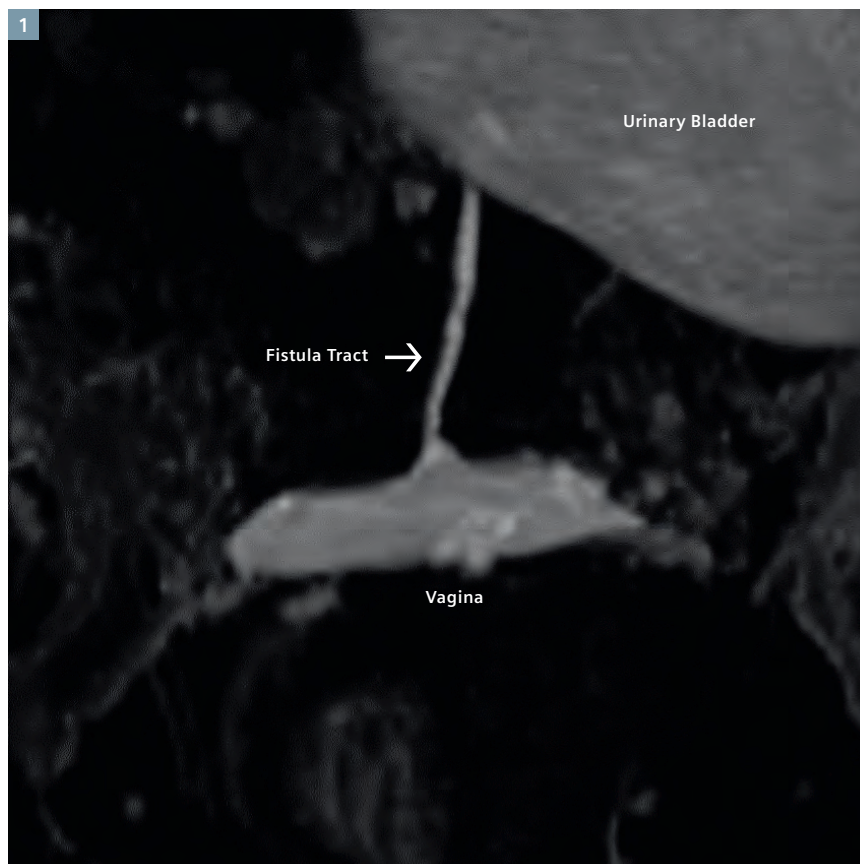
Dr. Wallabh Upasani; Dr. Priti Apte-Upasani

Sun Scan Center, Thane, India

Introduction

Advantages like the absence of ionizing radiation, the excellent soft-tissue contrast, the capability of multi-planar and 3D acquisitions as well as the ability to gain multi-parametric functional information have driven the increasing utilization of MRI in genitourinary (GU) tract imaging in clinical routine. For MRI systems, advances in hardware and software have enabled a reduction of motion artifacts, and helped acquire high-resolution 3D images in times acceptable to patients and clinicians.

The use of a versatile 3D sequence like T2-weighted 3D SPACE with fat suppression (fatsat) in this clinical example of vesico-vaginal fistula highlights the ability of MRI to provide excellent imaging information for complex clinical problems. MR imaging has helped the surgeon to accurately trace the fistulous tract during surgery, enabling complete excision of the tract. Furthermore, the acquisition of a 3D MRI dataset helped to avoid additional invasive pre-operative investigations like cystoscopy, which clearly works to the advantage of both, the patient and hospital resources.



1 Vesico-vaginal fistula with T2w fatsat 3D SPACE.

Case report

A 49-year-old female patient presented in our outpatient department with complaints of intermittent foul urinary smelling discharge per vaginum. She also presented a history of urinary urgency and of abdominal hysterectomy for myomas and resultant dysfunctional uterine bleeding (DUB) performed 9 months ago. She complained of urinary incontinence in the early post-opera-

tive period which was resolved by the third week post-operatively, but complains of subsequent intermittent vaginal discharge. There is no antecedent history of any other major medical illness.

The patient underwent routine blood investigations and pelvic ultrasound, with normal findings. On contrast-enhanced CT examination there was

no significant pelvic fluid and normal appearance of kidneys, ureter, and the urinary bladder. There was minimal vaginal contrast on the delayed images, suggestive of vesico-vaginal fistula. However, the exact location of fistula could not be demonstrated.

MR examination with a T2w fatsat 3D SPACE sequence with acquisition of very thin axial images was performed on our MAGNETOM Avanto 1.5T

system. Sagittal and coronal reconstructions of the 3D dataset demonstrated an approximately 2.75 cm long fistulous tract communicating between the urinary bladder and anterior wall of the vaginal vault (Fig. 1). Since SPACE is a 3D sequence, maximum intensity projection (MIP), and multiplanar reconstruction (MPR) images in different planes were generated from the original images. This enabled exquisite delineation of the pathologic anatomy of the fistulous tract.

Discussion

Analysis of the detailed patient history and a multimodality imaging approach helped us to identify the root cause of the patient's symptoms.

The MAGNETOM Avanto consistently provides excellent image quality. One key enabler is the excellent stability of the magnet and its large, homogenous field-of-view. With advances in shim

procedures and local shim options, the volume-of-interest is better prepared for sequences with fat suppression in presence of pathology (e.g. cysts/fluid) resulting in improved and consistent image quality. Improved signal-to-noise ratio (SNR) in short times is possible due to hardware like Tim (Total imaging matrix) technology, which allows to combine a 6-channel Body Matrix coil with the respective segments of the integrated spine coil to create a high-channel pelvic coil.

As a radiologist I decided to perform an MRI scan with T2w fatsat 3D SPACE after imaging. Post-processing and reformatting of the SPACE images in 3D as well as detailed reporting and correlation of the multi-modality image information helped to demonstrate the pathological anatomy to the surgeon.

Based on this information the surgeon was able to carefully plan the best approach for surgery, which ultimately helped to achieve the optimal outcome for the patient.

Contact

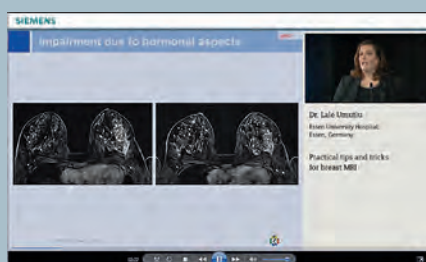
Dr. Priti Apte-Upasani
Sun Scan Center
Ground Floor, Shanti Niwas, Dr Moose Road
Talaopali, Thane, Maharashtra 400602
India
pritiwallabh@yahoo.co.in



Learn more!

Don't miss the talks of experienced and renowned experts on all aspects of MR breast imaging at:

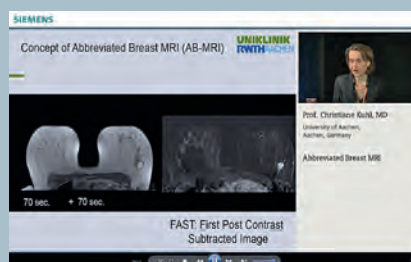
www.siemens.com/magnetom-world



Practical Tips and Tricks for Breast MRI

Lale Umutlu

University Hospital Essen
(Essen, Germany)



Abbreviated Breast MRI

Christiane Kuhl

University of Aachen
(Aachen, Germany)



Optimizing Breast MRI

Ritse Mann

Radboud University Medical Center
(Nijmegen, Netherlands)

Diffusion-Weighted MR Mammography (DWI-MRM) – Potential in the Clarification of Suspicious Lesions Detected by X-Ray Mammography

Sebastian Bickelhaupt¹; Frederik Laun²; Wolfgang Lederer³; Heidi Daniel⁴; Anne Stieber⁵; Stefan Delorme¹; Heinz-Peter Schlemmer¹

¹ German Cancer Research Center (DKFZ), Radiology Department, Heidelberg, Germany

² German Cancer Research Center (DKFZ), Medical Physics in Radiology Department, Heidelberg, Germany

³ Radiology Group Practice at the ATOS Clinic, Heidelberg, Germany

⁴ Mannheim Radiology Center (RZM), Mannheim, Germany

⁵ Department of Diagnostic and Interventional Radiology at the Heidelberg University Hospital, Heidelberg, Germany

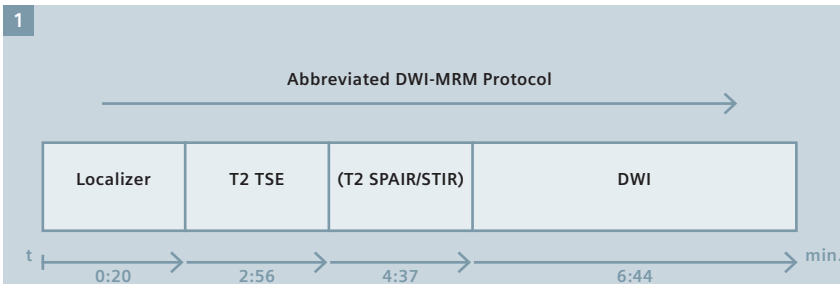
Introduction

False-positive findings in X-ray mammography may lead to further clarification examinations up to and including invasive measures such as tissue biopsies performed on healthy women [1, 2]. For the widely established breast cancer screening programs, this was described by the work group "International Agency for Research on Cancer (IARC)" in their Statement 2015 as a significant risk posed by breast cancer screening programs [3]. For women participating in breast cancer screening programs, the risk of obtaining a false-positive result in X-ray mammography is estimated to be 20% for those who undergo 10 screening examinations (in Germany, at two-year intervals and between the ages of 50 and 69 years) [1]. Based on the statistically processed biopsy results of the German breast cancer screening program, over 50% of the biopsies indicated in the context of the current clarification strategies result in benign histopathological findings [4]. It should be noted here that, especially in a screening program, continual balancing takes place between sufficient sensitivity and an optimally high specificity; moreover, the effects of a possible shift in this balance (belated detection vs. higher rate of false-positive findings) therefore have to be

Abstract

Diffusion-weighted MR mammography (DWI-MRM) maps the diffusion of water molecules in body tissue and could also contribute to a further increase in the diagnostic certainty of breast diagnostics. The advantages offered by DWI-MRM include short examination and evaluation times and the omission of administering contrast media containing gadolinium. In addition to its integration as a component of conventional MR mammography protocols, a shortened and contrast medium free DWI-MRM protocol (DWI,

T2 TSE, T2 SPAIR/STIR) might be of independent diagnostic value for specific indications, e.g. the noninvasive clarification of suspicious lesions in X-ray mammography. The establishment of a quality assurance concept and device-specific optimization for breast diagnostics has proved especially valuable in ensuring the data quality of such a shortened DWI-MRM protocol. The initially published data from a bicentric study indicate that a high level of sensitivity and specificity can be achieved for the clarification of suspicious lesions in X-ray mammography with this concept.

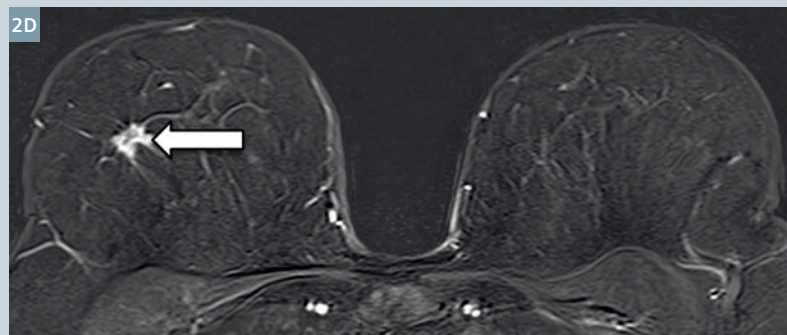
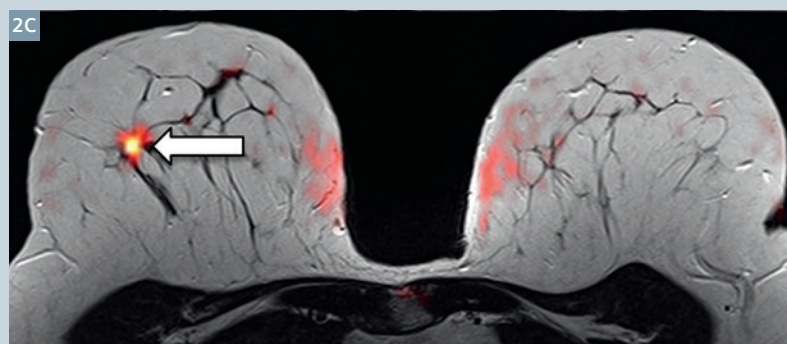
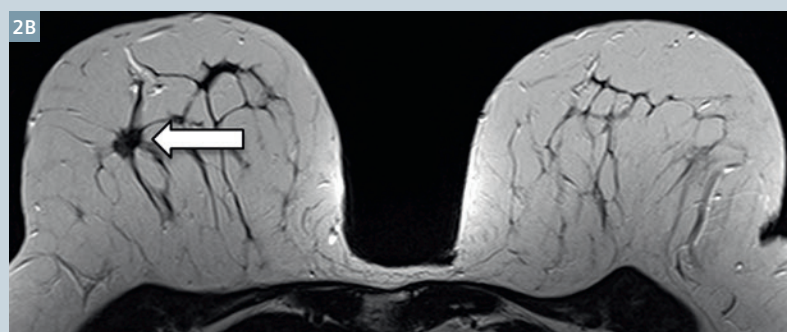
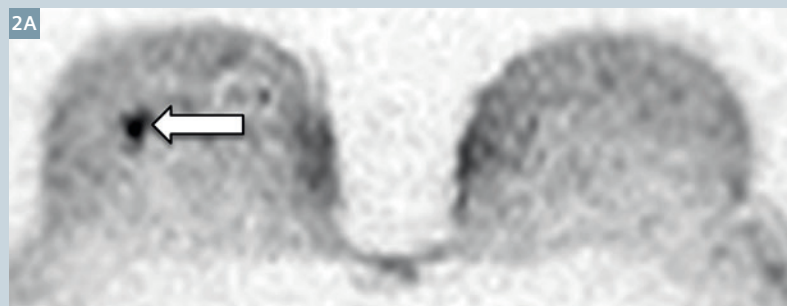


1 Sequence of the shortened, scientific DWI-MRM protocol in the study setting.

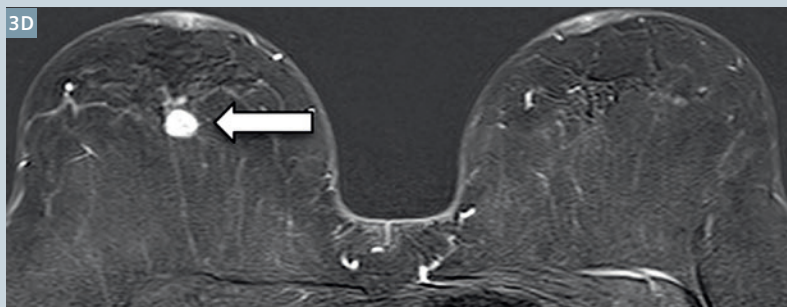
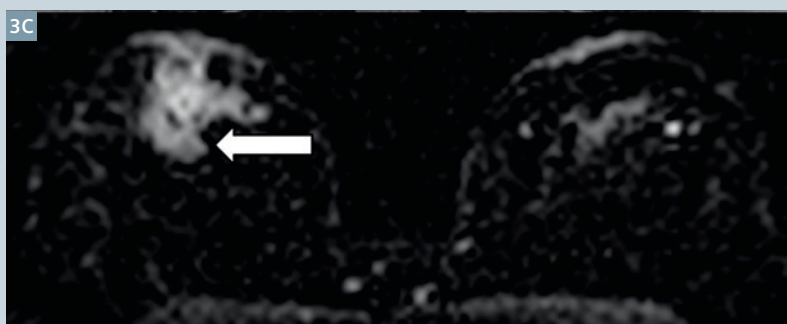
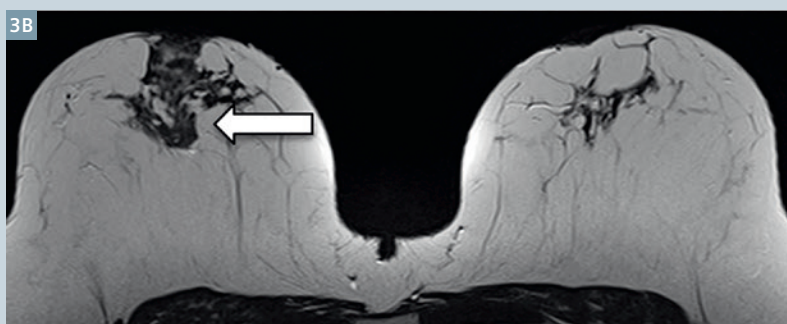
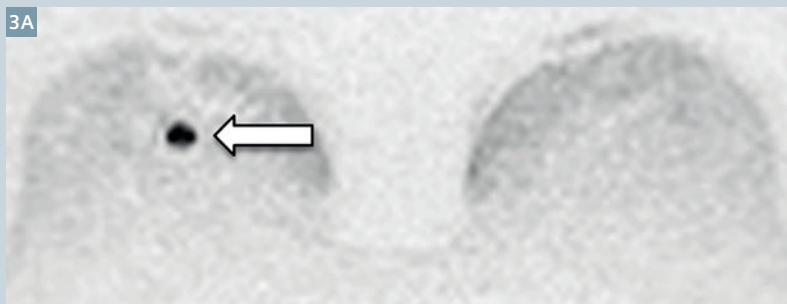
thoroughly discussed. The (further) development of imaging techniques in order to lower the rate of false-positive findings leading to the performance of invasive measures on the women concerned, and concurrently, in order to obtain a high sensitivity for the detection of malignant tumors, is therefore an essential task of radiological research. Further technical developments of existing techniques, e.g. modern ultrasound procedures by means of elastography, could further increase the diagnostic certainty in breast imaging under certain conditions [5]. Newer complementary techniques not previously considered in the breast cancer screening program on a regular basis, e.g. magnetic resonance imaging (MRI), also could lead to an improvement of diagnostic certainty if optimally adapted for screening purposes. The auspicious use of shortened contrast agent enhanced sequences in a screening collective has recently been demonstrated [6]. However, in addition to conventional sequences (T1, T2 TSE, T2 SPAIR/STIR, contrast agent enhanced), the contrast medium free, diffusion-weighted (DWI) sequence might also contribute to the further improvement of breast cancer screening [7, 8].

Diffusion-weighted MR mammography

Diffusion-weighted magnetic resonance imaging (DWI-MRI) enables the visual display and quantification of the Brownian motion of water molecules in body tissue [9]. Since the diffusion of water molecules in body tissue enables us to draw conclusions regarding tissue characteristics beyond the limits of pure image morphology, this technology is increasingly gaining interest, especially for the characterization of tissue in the field of oncological imaging [10]. In this way, DWI has established itself as an integral component of many oncological MRI protocols and has been integrated in the PI-RADS classification. It is used e.g. in the diagnostics of prostate carcinomas as the leading sequence for the detection of carcinomas of the peripheral zone [11].



2 Example of a lesion radiologically detected as BIRADS 5 in a mammography screening. **(2A)** RESOLVE DWI with b-value of 1500 s/mm² and clear demarcation of a diffusion-restricted focal lesion. **(2B)** T2-TSE sequence with suspiciously configured, spiculated lesion. **(2C)** Fusion imaging from T2-TSE and DWI (PET-CLUT) with congruent focus. **(2D)** DCE-MRI with likewise clear, contrast-enhanced lesion. Histopathology: Invasive ductal mammary carcinoma.



3 Participant in the mammography screening program with conspicuous lesion in the right breast. **(3A)** RESOLVE DWI with b-value of 1500 s/mm² and distinct, diffusion-restricted focal lesion. **(3B)** T2-TSE sequence with corresponding lesion, somewhat difficult to delimit in the gland tissue. **(3C)** Apparent diffusion coefficient (ADC) map. **(3D)** DCE-MRI with contrast-enhanced lesion. Histopathology: Invasive ductal mammary carcinoma.

The DWI-MRI technique allows for insights into various different biophysiological compartments: The determination of intravoxel incoherent motion (IVIM) enables conclusions concerning the perfusion behavior of the tissue under examination and uses low b-values [12]. The diffusion in the tissue can be quantified with the apparent diffusion coefficient (ADC) [13]. With high b-values, the free perfusion of the water begins to play a less predominant role and, based on the signal intensity curves, conclusions can be made regarding the spatial restriction of motion (kurtosis) [14].

The evaluation of diffusion-weighted sequences (DWI) as an integral module or as an additive component in breast diagnostics was the objective of several studies in recent years, which were partially summarized in a review by Thomassin-Naggara et al. in 2013 [13]. As an additive technique, DWI is chiefly researched as a means of increasing the specificity of conventional contrast agent enhanced (dynamic contrast enhanced) DCE-MRM protocols [13]. Recently published studies have shown that, in terms of a contrast medium free, shortened MRM using only DWI and morphological (T2-weighted-TSE, T2-weighted-SPAIR) sequences, DWI-MRM could exhibit its own diagnostic value under certain conditions [7, 8, 15]. The advantages offered by DWI-MRM include short examination times and dispensing with the administering of contrast media containing gadolinium. The latter benefit is especially important in light of the ongoing discussion concerning the accumulation of contrast media containing gadolinium in the brain after repeated application [16-18]. Scientific studies have provided morphological image-based and histopathological evidence of deposits of gadolinium in the brains of patients following repeated intravenous application in which preparation-dependent differences between linear and macrocyclic contrast media appeared [19]. The clinical relevance of these findings is currently still the controversial

subject of multiple studies. However, in the case of screening programs involving recurring examinations of participants primarily regarded as healthy, a technique which is as gentle as possible and at the same time of high diagnostic quality is very important for the guidance and acceptance of the measure.

In an initial study concerning the use of a contrast medium free DWI-MRM protocol (DWI, STIR, T2-TSE) as a diagnostic technique in breast cancer diagnostics, the work of Telegrafo et al. showed a sensitivity of 94% and a specificity of 79% [8]. DWI-MRM might prove especially valuable in the clarification of lesions previously detected and classified as suspicious by means of other diagnostic techniques. The possibilities offered by DWI-MRM for quantification with independent multiparametric aspects (IVIM, kurtosis, ADC) could play a role here. In a multicenter study concerning the application of DWI-MRM as an additional measure for clarifying conspicuous findings in the mammography screening program, a study project involving the German Cancer Research Center (DKFZ) and regional screening units was implemented to evaluate the diagnostic significance of a contrast medium free, shortened DWI-MRM performed prior to biopsies. A multi-level study concept enabled the translational establishment of a quality-assured DWI-MRM with subsequent implementation of the actual study project here.

Challenges and establishment of the quality-assured DWI-MRM

In addition to the advantages of DWI-MRM, methodic and technical challenges and limitations must be observed. Despite the use of DWI sequences in breast diagnostics in the scientific and clinical setting, no national or international standardization has occurred yet regarding the decisive sequence parameters. The b-values and slice thicknesses/resolutions selected in routine

clinical protocols thus vary greatly and the values are not infrequently selected too low. However, the selection of the b-values is very significant, especially for achieving a sufficient suppression of normal tissue and the T2 shine-through effect. Since the spatial resolution also is much lower than for DCE-MRM, e.g. partial volume effects must be considered in the optimization and standardization. Device-specific optimization of DWI-MRM is therefore an essential prerequisite for its effective and diagnostically significant application in breast diagnostics. If suboptimal parameters without a dedicated device-specific optimization are selected, this can influence the diagnostic significance substantially. Thus, for example, with b-values that are selected inadequately low, due to the missing suppression of the breast parenchyma and any possible benign compactions, false-positive lesions which complicate diagnostic assessment often can be found. For this reason, numerous b-values covering a broad spectrum should be acquired in order to have reliable data points for the calculation of the ADC. Moreover, a very high b-value in the range of 1000-1500 mm/s² should also be included in the protocol [20]. Therefore, device-optimized standardization of the MRI systems was performed in the study centers participating in the study project as part of a multilevel standardization process. Furthermore, a dedicated DWI-MRI phantom was developed by the Medical Physics Department and then established in all study centers with a quality assurance program. The phantom comprises a hollow cylindrical body containing several inserted tubes of varying diameter. A solution with high and low ADC values is placed in these tubes, thus simulating benign and malignant lesions of varying size. Device-optimized, comparable DWI-MRM findings as well as consistent quality could be ensured throughout the course of the study via regular check measurements.

Perspectives of DWI-MRM

The initial data of our multicenter study project indicated the possibility that a significant percentage of the false-positive findings from the breast cancer screening program can be detected as such only by using DWI-MRM as an additional clarification modality [7]. The number of unnecessary invasive biopsies could possibly be reduced considerably hereby. Although this method exhibited a high sensitivity in the first study evaluation, it still was apparent that lesions (e.g. DCIS lesions) also could be missed. The published early results here refer to a collective of 50 women with BI-RADS 4/5 lesions and a biopsy indication which subsequently resulted from the screening clarification. A sensitivity of 92% and a negative predictive value of 92% resulted for DWI-MRM [7]. DWI-MRM did not appear to be less advantageous compared to contrast agent enhanced DCE-MRM for this indication. Just as single-image MIPs (maximum intensity projections) can be evaluated for DCE-MRM, we tested the MIP display technique in the early data evaluation. This showed that high b-values ($b = 1500 \text{ mm/s}^2$) resulted in a sufficient suppression of the regular mammary gland tissue and fatty tissue, thus enabling a MIP projection. Regarding the reading function, the MIP technique shows the benefit a shorter evaluation time offers to the radiologist in contrast to the use of single slices. These were used for further morphological assessment in conjunction with the T2-weighted sequences only in cases involving anomalies.

No statement could be made to date or can possibly be made in the future within the scope of our study project as to what extent DWI-MRM could represent a possible alternative screening modality. Likewise, the objective of the study is not to evaluate the universal comparability of DWI-MRM and DCE-MRM, but rather, to investigate a dedicated indication, the clarification of suspicious findings

by means of noninvasive imaging where other diagnostic techniques have been exhausted. The initial results encourage us to perform further studies in order to evaluate use of the DWI-MRM technique as a procedure in breast cancer diagnostics.

Summary

Apart from the use of DWI as an additional component of conventional contrast agent enhanced MRM a shortened and contrast medium free DWI-MRM protocol (DWI, T2 TSE, T2 SPAIR/STIR) might be singularly significant in breast cancer diagnostics for specific indications. This concerns e.g. the noninvasive clarification of suspicious lesions from (screening) X-ray mammography before diagnosing an indication for biopsy. The advantages offered by DWI-MRM here include short examination and interpretation times, as well as the omission of any intravenous administering of contrast media containing gadolinium. In particular, the establishment of the quality assurance concept escribed above has proved valuable as a means of ensuring data quality. A device-specific optimization of imaging quality has proven indispensable in the preliminary stages of multicenter study projects. The initially published results from our first bicentric study project indicate that a high level of sensitivity and specificity can be achieved for the further clarification of suspicious lesions in X-ray mammograms with this concept.

The implementation of further studies dealing with DWI-MRM in breast cancer diagnostics is therefore appropriate.

References

- Hofvind S, Ponti A, Patnick J, et al. False-positive results in mammographic screening for breast cancer in Europe: a literature review and survey of service screening programmes. *Journal of Medical Screening* 2012;19:57-66.
- Payne JL, Martin T, Caines JS, Duggan R. The Burden of False-Positive Results in Analog and Digital Screening Mammography: Experience of the Nova Scotia Breast Screening Program. *Canadian Association of Radiologists Journal* 2014;65:315-20.
- Lauby-Secretan B, Scoccianti C, Loomis D, et al. Breast-Cancer Screening—Viewpoint of the IARC Working Group. *New England Journal of Medicine* 2015;372:2353-8.
- Berlin CMgKM. Evaluation-Report 2010. Results of the Mammography-Screening-Program in Germany. 2014.
- Golatta M, Schweitzer-Martin M. Evaluation of virtual touch tissue imaging quantification, a new shear wave velocity imaging method, for breast lesion assessment by ultrasound. 2014;2014:960262.
- Kuhl CK, Schrading S, Strobil K, Schild HH, Hilgers R-D, Bieling HB. Abbreviated Breast Magnetic Resonance Imaging (MRI): First Postcontrast Subtracted Images and Maximum-Intensity Projection—A Novel Approach to Breast Cancer Screening With MRI. *Journal of Clinical Oncology* 2014;32:2304-10.
- Bickelhaupt S, Laun FB, Tesdorff J, et al. Fast and Noninvasive Characterization of Suspicious Lesions Detected at Breast Cancer X-Ray Screening: Capability of Diffusion-weighted MR Imaging with MIPs. *Radiology* 2015;150425.
- Telegrafo M, Rella L, Stabile Ianora AA, Angelelli G, Moschetta M. Unenhanced breast MRI (STIR, T2-weighted TSE, DWIBS): An accurate and alternative strategy for detecting and differentiating breast lesions. *Magn Reson Imaging* 2015;33:951-5.
- Le Bihan D, Breton E. Imagerie de diffusion in-vivo par résonance. *C R Acad Sci (Paris)* 1985; 301 (15):1109-12.
- Freitag MT, Bickelhaupt S, Ziener C, et al. [Selected clinically established and scientific techniques of diffusion-weighted MRI: In the context of imaging in oncology]. *Der Radiologe* 2016;56:137-47.
- Weinreb JC BJ, Choyke PL, Cornud F, Haider MA, Macura KJ, Margolis D, Schnall MD, Shtern F, Tempny CM, Thoeny HC, Verma S. Weinreb JC. PI-RADS Prostate Imaging-Reporting and Data System:2015,Version 2. *Eur Urol* 2016;69(1):16-40
- Panek R, Borri M, Orton M, et al. Evaluation of diffusion models in breast cancer. *Medical physics* 2015;42:4833-9.
- Thomassin-Naggara I, De Bazelaire C, Chopier J, Bazot M, Marsault C, Trop I. Diffusion-weighted MR imaging of the breast: Advantages and pitfalls. *European Journal of Radiology* 2013;82:435-43.
- Jensen JH, Helpert JA, Ramani A, Lu H, Kaczynski K. Diffusional kurtosis imaging: the quantification of non-gaussian water diffusion by means of magnetic resonance imaging. *Magnetic resonance in medicine* 2005;53:1432-40.
- Kul S, Oguz S, Eyuboglu I, Komurcuoglu O. Can unenhanced breast MRI be used to decrease negative biopsy rates? Diagnostic and interventional radiology (Ankara, Turkey) 2015;21:287-92.
- Errante Y, Cirimele V, Mallio CA, Di Lazzaro V, Zobel BB, Quattrocchi CC. Progressive increase of T1 signal intensity of the dentate nucleus on unenhanced magnetic resonance images is associated with cumulative doses of intravenously administered gadodiamide in patients with normal renal function, suggesting dechelation. *Invest Radiol* 2014;49:685-90.
- Kanda T, Ishii K, Kawaguchi H, Kitajima K, Takenaka D. High signal intensity in the dentate nucleus and globus pallidus on unenhanced T1-weighted MR images: relationship with increasing cumulative dose of a gadolinium-based contrast material. *Radiology* 2014;270:834-41.
- McDonald RJ, McDonald JS, Kallmes DF, et al. Intracranial Gadolinium Deposition after Contrast-enhanced MR Imaging. *Radiology* 2015;275:772-82.
- Radbruch A, Weberling LD, Kieslich PJ, et al. Gadolinium retention in the dentate nucleus and globus pallidus is dependent on the class of contrast agent. *Radiology* 2015;275:783-91.
- Tamura T, Murakami S, Naito K, Yamada T, Fujimoto T, Kikkawa T. Investigation of the optimal b-value to detect breast tumors with diffusion weighted imaging by 1.5-T MRI. *Cancer imaging : the official publication of the International Cancer Imaging Society* 2014;14:11.

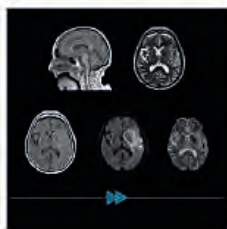


Contact

Sebastian Bickelhaupt, M.D.
German Cancer Research Center (DKFZ)
Im Neuenheimer Feld 280
69126 Heidelberg
Germany
Phone: +49 6221 422603
Fax: +49 6221 422615
S.Bickelhaupt@dkfz.de

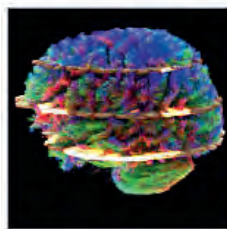
Try them on your system

Trial licenses for many of the applications featured in this issue of MAGNETOM Flash are available free of charge for a period of 90 days.



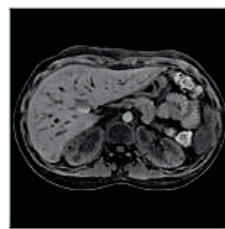
GOBrain

Push-button brain exam in 5 minutes.* >



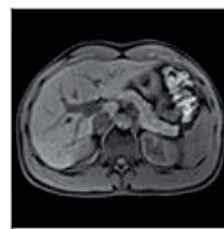
Simultaneous Multi-Slice

Accelerate advanced neuro applications for clinical routine. >



FREEZEit

Embrace motion in liver imaging. >



CAIPIRINHA

High-resolution 3D imaging with reduced breath-hold times. >

GOBrain

Simultaneous Multi-Slice

FREEZEit

CAIPIRINHA



Brain Dot Engine

The Brain Dot Engine increases productivity and standardization with guided and automated workflows. >



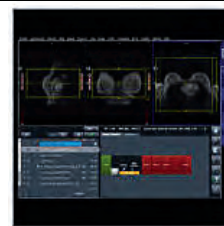
Abdomen Dot Engine

The Abdomen Dot Engine is customized for dynamic liver examinations and consistent contrast timing. >



Spine Dot Engine

The Spine Dot Engine optimizes cervical, thoracic, and lumbar spine imaging for a wide range of patients and conditions. >



Breast Dot Engine

The Breast Dot Engine supports consistent frequency selection for fat, water, saline or silicone. >

Brain Dot Engine

Abdomen Dot Engine

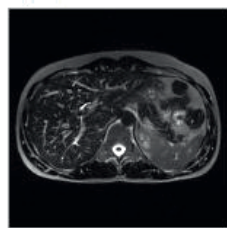
Spine Dot Engine

Breast Dot Engine



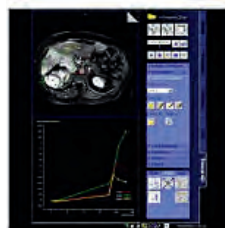
syngo.MR Neuro 3D Engine

Combine BOLD fMRI data with fiber tract information. >



SPACE

SPACE enables the acquisition of high resolution 3D datasets. >



Tissue 4D

Tissue 4D is an advanced postprocessing platform for pharmacokinetic modelling of dynamic-contrast enhanced (DCE), perfusion-weighted MRI datasets. >



RT Dot Engine

The RT Dot Engine provides a comprehensive package addressing specifically the requirements of MR imaging in Radiation Therapy. >

syngo.MR Neuro 3D

SPACE

Tissue 4D

RT Dot Engine

For further details, product overviews, image galleries, step-by-step videos and general requirements visit us at:

www.siemens.com/mri-options-overview

*Achieved on a MAGNETOM Skyra with the Head 32 coil. Total examination time can take up to 6 minutes depending on system field strength and coil density.

Multiparametric MRI at 3 Tesla for Prediction of Treatment Response in Rectal Cancer

Trang Pham^{1,3}; Michael Barton^{1,3}; Robba Rai¹; Dale Roach⁴; Karen Wong^{1,3}; Daniel Moses⁵; Christopher Henderson^{2,6}; Mark Lee^{1,2}; Benjamin Schmitt⁷; Gary Liney^{1,3}

¹ Liverpool Cancer Therapy Centre, Liverpool Hospital, Sydney, Australia

² Faculty of Medicine, University of New South Wales, Sydney, Australia

³ Ingham Institute for Applied Medical Research, Sydney, Australia

⁴ Faculty of Physics, University of Sydney, Sydney, Australia

⁵ Department of Radiology, Prince of Wales Hospital, Sydney, Australia

⁶ Department of Anatomical Pathology, Liverpool Hospital, Sydney, Australia

⁷ Siemens Healthcare, Macquarie Park, Australia

Introduction

Current functional MRI techniques have shown promising results for prediction and assessment of response to chemoradiotherapy (CRT) in rectal cancer [1,2], but lack sufficient accuracy for clinical use. There is a wide variation in performance of functional MRI in response prediction reported. Most studies describe single parameter values from either diffusion or perfusion MRI. Single parameter measurements, such as mean ADC or K^{trans} , do not adequately reflect tumor heterogeneity. Multiparametric MRI using quantitative diffusion-weighted and dynamic contrast-enhanced imaging in combination can assess tumor heterogeneity and its response to treatment. This strategy has the potential to better reflect tumor heterogeneity and improve the accuracy of therapeutic response prediction and assessment in rectal cancer.

Since 2014 we have been conducting treatment response studies on our dedicated MRI system ('MR-Simulator' shown in Figure 1) which was installed in our Radiation Oncology Centre to provide MRI planning and guidance in various tumor sites. This report describes our results in rectal cancer.

Imaging details

Patients with locally advanced rectal cancer undergoing preoperative CRT prospectively underwent multiparametric MRI on our 3T wide bore MAGNETOM Skyra (Siemens



1 The 3 Tesla MAGNETOM Skyra MR-Simulator at Liverpool Cancer Therapy Centre in Sydney, Australia.

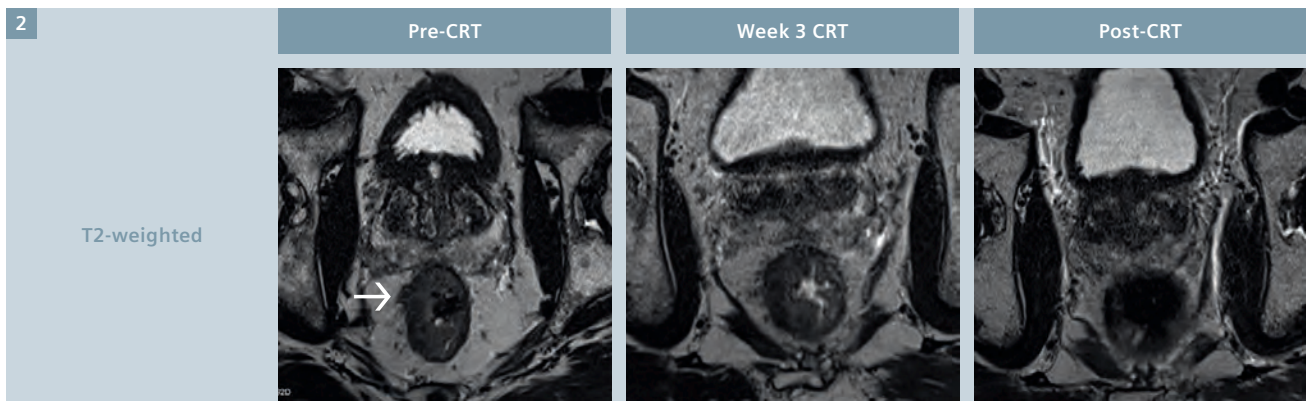
Healthcare, Erlangen, Germany) at 3 time-points: Pre-CRT, week 3 CRT, and post-CRT. The imaging protocol consisted of:

- (i) T2-weighted image.
- (ii) DWI using RESOLVE, which has been previously shown to be robust with respect to geometrical distortions [3]. Images were acquired with b-values 50 and 800 s/mm² and 1 & 3 averages. ADC maps and calculated b = 1400 s/mm² images were produced as part of protocol.
- (iii) DCE consisted of pre-contrast VIBE scans with flip angles 2° and 15° in order to calculate native T1, followed by gadoversetamide (0.1 mM/kg) injection and 60 phases using TWIST with a 5 s temporal resolution. Buscopan was administered intravenously prior to the functional sequences to reduce rectal peristaltic motion.

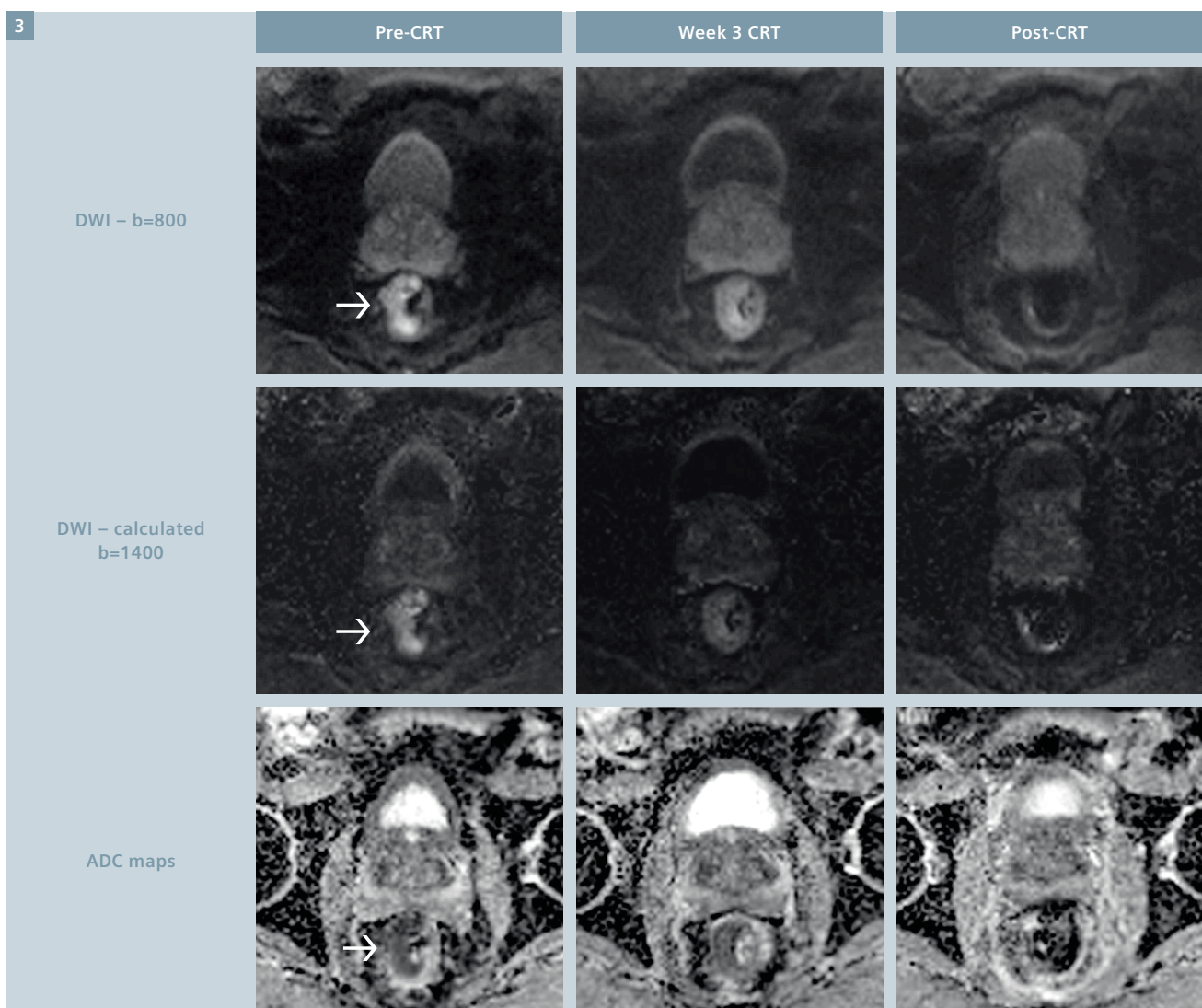
Multiparametric analysis and therapy monitoring

We developed a voxel-by-voxel multiparametric histogram analysis strategy to assess tumor heterogeneity and its changes in response to combined chemotherapy and radiotherapy. A complete protocol and analysis strategy was developed which has utilized commercial, in-house developed and works-in-progress (Siemens' OncoTreat¹) software. For DCE analysis, registration of the pre-contrast flip angle sequences to dynamic images was a crucial step in producing a pixel-by-pixel T1 map to ensure accurate voxel-by-voxel calculation of K^{trans} . Images were manually pre-registered in Siemens 3D fusion software and the headers of registered images were re-written with an in-house code to enable these images to be analyzed in

¹ The product is still under development and not commercially available yet. Its future availability cannot be ensured.



- 2 T2-weighted images for a rectal cancer patient at 3 time-points: pre-CRT, week 3 of CRT, and post-CRT. The rectal tumor (arrow) invades into the mesorectal fat. T2-weighted images alone cannot accurately assess treatment response, because of difficulty detecting residual tumor deposits within areas of radiation-induced necrosis or fibrosis.

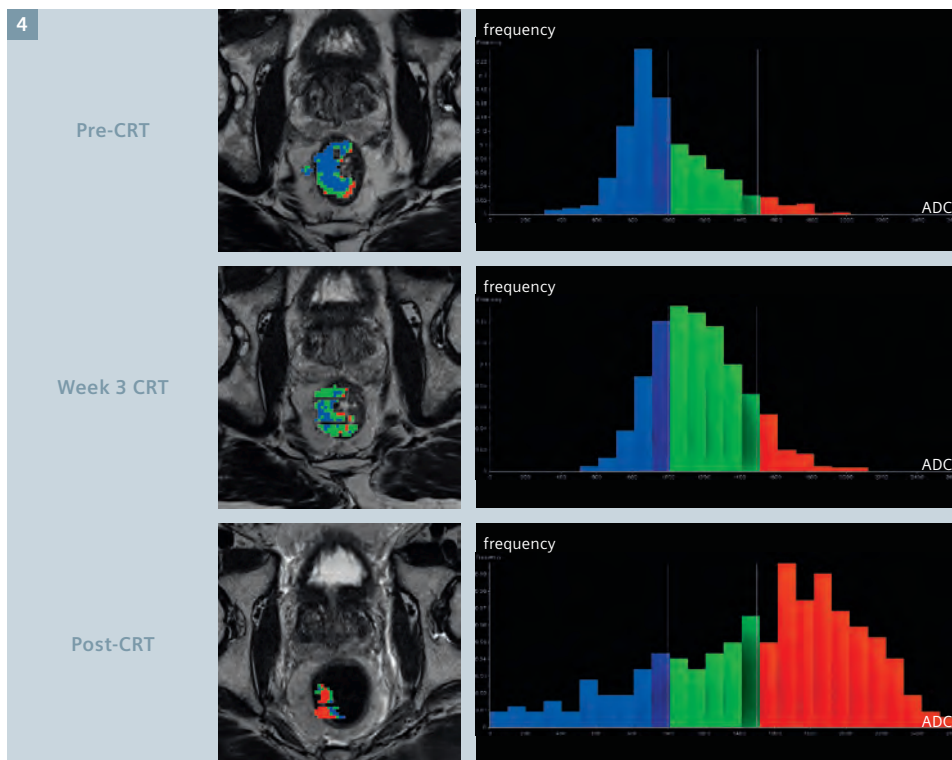


- 3 Diffusion-weighted RESOLVE images for the same rectal cancer patient at 3 time-points. The top panel shows the $b = 800 \text{ s/mm}^2$ images, the middle panel shows the calculated $b = 1400 \text{ s/mm}^2$ images and the bottom panel shows the ADC maps. Response to treatment can be seen on the diffusion images, with the level of tumor hyperintensity decreasing across the time-points. The histopathology demonstrated AJCC tumor regression grade 1 indicating a good response to preoperative CRT.

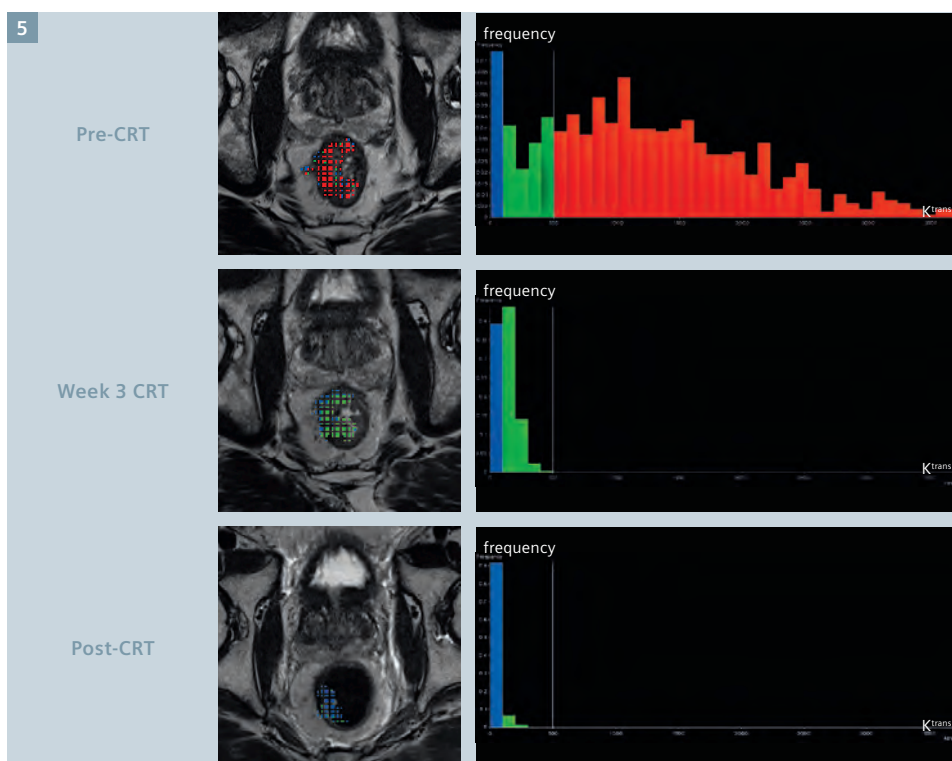
Tissue 4D. We have found this provides better results than using the available deformable registration. ADC and K^{trans} parameter maps were subsequently exported to OncoTreat where they were registered to

T2-weighted images. Semi-automated segmentation was used to define the volume of interest from the hyperintense tumor on the calculated $b\text{-value} = 1400 \text{ s/mm}^2$ images. We have found this dataset

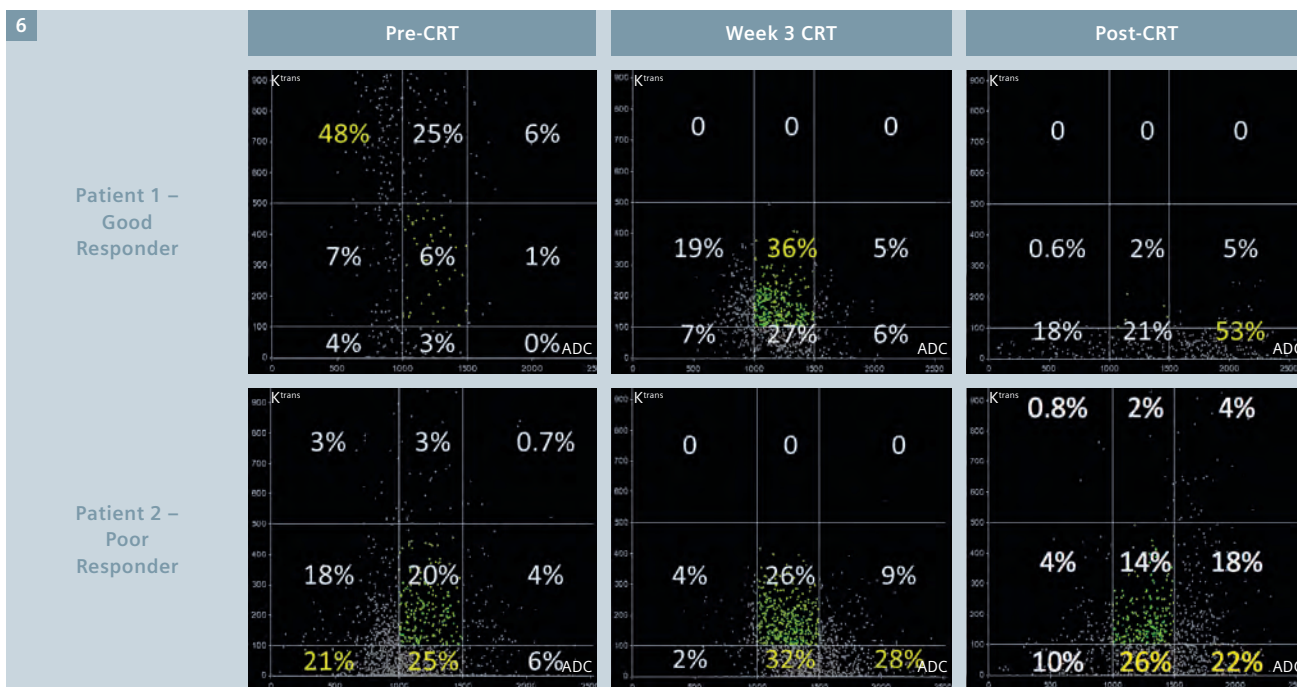
particularly useful – gaining both from the extra sensitivity and reduced noise of a calculated high $b\text{-value}$. A voxel-by-voxel technique was used to produce color-coded histograms of ADC and K^{trans} , as well as combined



4 Example of the color-coded ADC maps and voxel-by-voxel histograms for a patient with good response to CRT. This patient had AJCC tumor regression grade 1 (moderate response, single cells or small groups of cancer cells) on histopathology. The histograms demonstrated an increase in the absolute ADC values of voxels over the time-points.



5 K^{trans} color-coded maps and voxel-by-voxel histograms for the same patient, who had a good response to CRT (AJCC TRG 1). The majority of K^{trans} voxel values were high (red) pre-CRT. A possible explanation for this is that the high K^{trans} is due to a well perfused oxic tumor, which is predictive of good radiotherapy response. By week 3-CRT the K^{trans} histogram demonstrated a marked reduction in the absolute K^{trans} values of voxels.



6 The scatterplots demonstrating changes in combined ADC and K^{trans} of voxels of segmented region over the time-points for a good responder with AJCC TRG 1 (top panel) and a poor responder with AJCC TRG2 (bottom panel). Percentages of voxels in each quadrant are shown. The scatterplots show different patterns of shift in the distribution of plots between the two patients. For Patient 1, the week 3 histograms and maps showed both a shift in distribution of ADC of voxels to higher values and K^{trans} of voxels to lower values compared to the pre-CRT histogram. In contrast, Patient 2 had low K^{trans} values pre-CRT, without much change in the values of voxels over the time-points. The low K^{trans} values in this patient may be due to poor perfusion representing a hypoxic tumor, which is predictive of a radio-resistant tumor and poor response to radiotherapy.

scatterplots for each time-point. CRT response was defined according to histopathology tumor regression grade (TRG) (AJCC 7th Edition) [4].

Conclusions

We have successfully integrated a multiparametric MRI technique in our clinic to monitor response to treatment in patients with rectal cancer. This is a particularly challenging anatomy to image and provide robust functional datasets that can be examined in a serial manner. A voxel-by-voxel multiparametric analysis strategy has been adopted and early results show this is important in quantitatively assessing heterogeneity within the entire tumor region, and the changes in response to CRT in rectal cancer.

Acknowledgement

This work was partially funded by the Royal Australian and New Zealand College of Radiologists (RANZCR) Withers and Peters Research Grant 2014.

References

- 1 van der Paardt et al. Patients who undergo preoperative chemoradiotherapy for locally advanced rectal cancer restaged by using diagnostic MR imaging: a systematic review and meta-analysis. *Radiology*. 2013;269:101-12.
- 2 Beets-Tan R and Beets G. MRI for assessing and predicting response to neoadjuvant treatment in rectal cancer. *Nat Rev Gastroenterol Hepatol*. 2014;11:480-88.
- 3 Liney G et al. Quantitative evaluation of diffusion-weighted imaging techniques for the purposes of radiotherapy planning in the prostate. *Br J Radiol*. 2015. DOI <http://dx.doi.org/10.1259/bjr.20150034>.
- 4 Edge S, Byrd D, Compt C et al (Eds). *AJCC Cancer staging manual 7th edition*. New York Springer 2010.



Contact

Dr. Trang Pham
Radiation Oncologist
Liverpool Cancer Therapy Centre
2170, 1 Campbell Dr,
Liverpool NSW 2170
Australia
Phone: +61 2 87389806
trangpham283@gmail.com

Significant Benefit of Optimized 3D SPACE Sequences in Radiation Therapy Treatment

Maja Sohlín, Ph.D.¹; Karin Petruson, M.D., Ph.D.²

¹ Sahlgrenska University Hospital, Medical Physics and Biomedical Engineering, Gothenburg, Sweden

² Sahlgrenska University Hospital, Department of Oncology, Gothenburg, Sweden

MR images used in radiation therapy have other requirements than conventional diagnostic MR images. In radiation therapy, the exact extent and position of lesions in relation to critical structures have to be determined in order to ensure an effective and safe treatment of the patient. This requires high in-plane spatial resolution, thin slices without slice gaps, and a minimal geometric distortion. In addition, due to image registration and patient fixation, a sub-optimal patient set-up is often required, including flexible coil solutions and a flat table top.

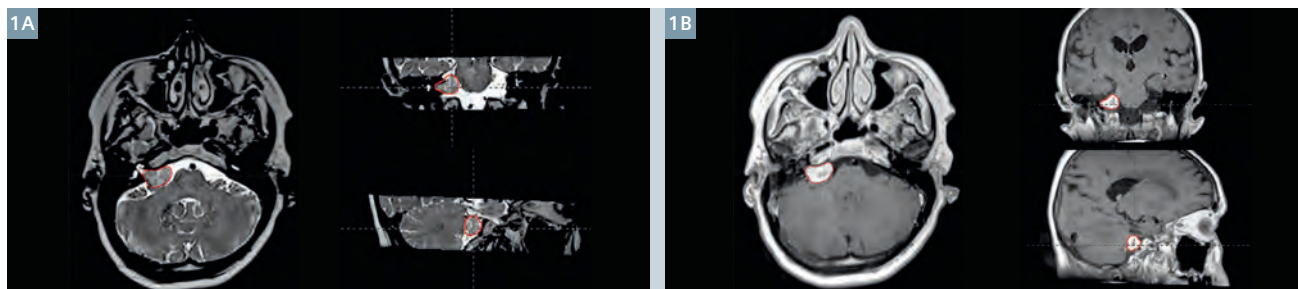
MR imaging struggles with system-related and patient-induced geometric distortions. For radiation therapy, the imaging protocols must be optimized to give minimal geometric distortions in the imaging volume. In general, the geometric integrity is best preserved by using spin-echo based sequences with high acquisition bandwidth. In the current workflow, MR images used for therapy planning have to be registered to a CT dataset. The imaging protocol must thus also be optimized to give sufficient image contrast and adequate spatial resolution to ensure an accurate image registration, with

a trade-off between registration accuracy and image quality. Acquiring thin slices (<2-3 mm) without slice gaps using standard 2D multi-slice acquisitions results in either low signal-to-noise ratio or unreasonably long acquisition times, the latter not only inconvenient for the patient but also an increased risk of introduction of motion artefacts in the images.

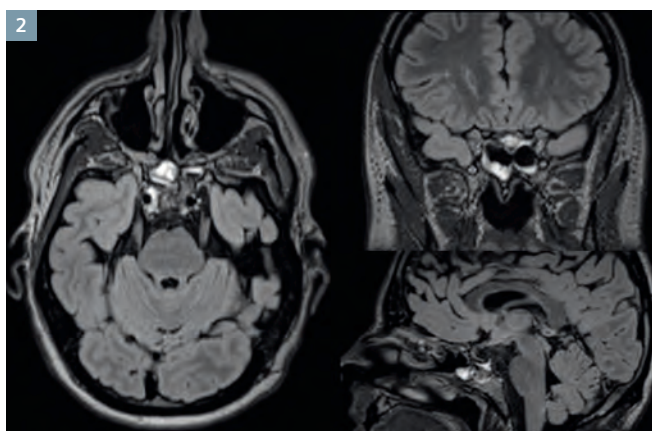
Although still not optimal for all applications, we found several examinations to benefit from the use of optimized fast isotropic 3D acquisitions. Utilization of the SPACE sequence for therapy planning has increased the possibilities we have to delineate small tumors intended for treatment with high-dose radiotherapy. The sequence has shown to be very helpful in defining small benign as well as malignant brain tumors. At our clinic, these tumors are treated with stereotactic radiotherapy that involves a very narrow margin between the gross tumor volume and the planning target volume intended for treatment, which makes an exact tumor volume definition essential for successful treatment.

Further, we are in the initial stages of incorporating MRI in the workflow

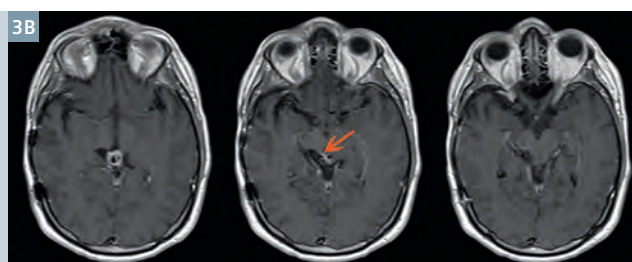
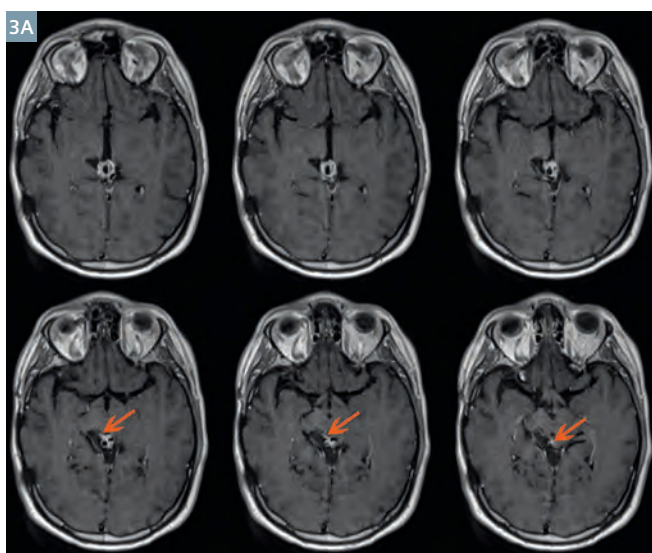
for brachytherapy for head-and-neck cancer patients. At our clinic, patients with cancer in the tongue and the base of tongue without nodal spread receive external radiotherapy combined with chemotherapy to the primary tumor site and to non-engaged lymph node sites. Some of the patients also receive an additional brachytherapy boost to the primary tumor site. The volume intended to receive the boost has been decided by the head-and-neck radio oncologist after a digital examination prior to brachy loop implantation. We have seen a great benefit of using a T1 3D SPACE MRI after the brachy loop implantation to reconstruct the loops and to verify that the tumor remnant is within reach of the radiotherapy. The possibility to reconstruct images in any arbitrary plane combined with the excellent image quality will increase the possibilities for us to offer patients a more exact treatment, sparing the salivary glands and mandibular bone. In conclusion, we are so far very satisfied with the SPACE sequence for several applications in radiation therapy and we see a great advantage of investing further optimization work to introduce the sequence in the treatment of other anatomical areas.



1 The gross tumor volume of a vestibular schwannoma on the T2-weighted SPACE (1A), and T1-weighted contrast enhanced SPACE (1B). The high (1 mm) and isotropic resolution of the SPACE sequence is highly beneficial for therapy planning of vestibular schwannoma as many schwannoma are as small as a few millimeters. The excellent image contrast on the T2-weighted SPACE may eliminate the need for contrast enhanced acquisitions.

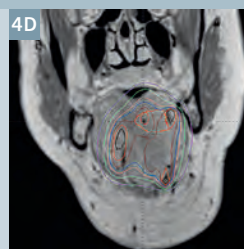
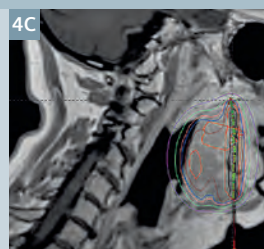
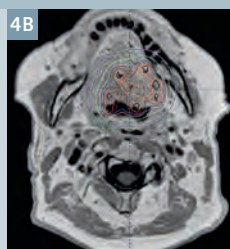
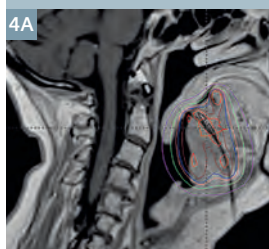


- 2** A patient diagnosed with a chordoma. Initial surgery was due to technical difficulties not completely radical and the patient will receive adjuvant radiotherapy to the remaining chordoma. Due to the close vicinity to the optical nerves it is extremely important to be able to define the exact volume of the tumor in order to minimize negative treatment effects of the radiotherapy. A T2-weighted SPACE dark fluid.



- 3** A patient who was diagnosed with a germinoma of the corpus pineale five years ago. He was initially treated with radio-chemotherapy and now shows a local recurrence. T1-weighted contrast-enhanced SPACE (**3A**) and standard T1-weighted contrast enhanced 2D TSE with a slice thickness of 3 mm (**3B**). The standard 2D TSE was not sufficient to determine the extent of the recurrent tumor.

- 4** Dose distribution for a brachytherapy patient on a T1-weighted SPACE (**4A-C**), and with an applicator reconstructed (**4D-E**).



Contact

Karin Petruson, M.D., Ph.D.
Radiation Oncologist
Sahlgrenska University
Hospital
Department of Oncology
Blå stråket 2
413 45 Gothenburg
Sweden
karin.petruson@vgregion.se



Contact

Maja Sohlin, Ph.D.
Medical Physicist
Sahlgrenska University
Hospital
Medical Physics and
Biomedical Engineering
Bruna stråket 13
413 45 Gothenburg
Sweden
maja.sohlin@vgregion.se

The Potential Role of Ultrashort Echo Time Sequences in MRI Guided Radiotherapy

Soumya Ghose³; Robba Rai¹; Jason Dowling³; Sankar Arumugam¹; Benjamin Schmitt⁴; Gary Liney^{1,2}

¹ Liverpool Cancer Therapy Centre, Liverpool Hospital, Sydney, Australia

² Ingham Institute for Applied Medical Research, Sydney, Australia

³ CSIRO, The Australian e-Health & Research Centre, Brisbane, Queensland

⁴ Siemens Healthcare, Australia

Introduction

An increasing number of Oncology Centers are implementing MRI into the planning and monitoring of radiation treated patients so that the benefits of improved soft-tissue contrast can be utilized in both the tumor target and organs-at-risk. The effects of geometric distortion both from the system and the patient are well documented and can be mitigated to acceptable levels of accuracy. However CT is still required to provide the electron density correction that is needed in the dose calculation. The current treatment workflow therefore involves the patient undergoing both a CT and MRI examination and the state-of-the-art solution is to acquire both of these in the same treatment position to facilitate registration in a treatment planning system. Nevertheless there are inherent differences between CT and MRI contrast that makes registration of certain structures and materials difficult. Furthermore, the require-

ment of a CT each time a plan is calculated, means that the potential of MRI for informing and adapting treatment at any point is never fully exploited.

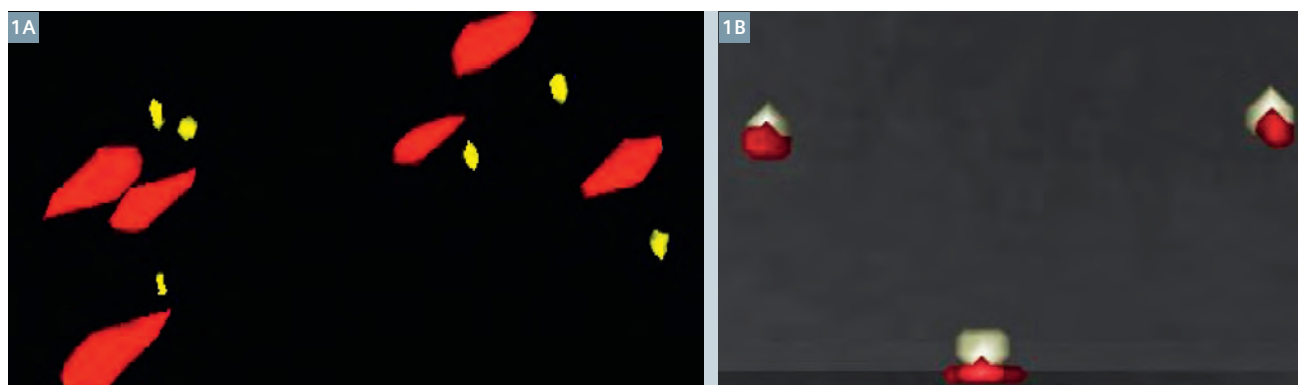
One of the key attractions of MRI for Oncologists is the variety of imaging techniques that can be acquired in a single examination. Ultrashort echo time (UTE) sequences¹ [1] are now being added to the list and finding new clinical applications with their ability to image at tens of microseconds. Recently developed sequences are able to achieve the shortest possible TEs limited only by transmit/receive switching times and gradient performance and requiring no hardware upgrades. These have the potential to generate signal in previously invisible structures and/or reduce susceptibility artefacts both of which could hold advantages for radiotherapy (RT) planning; either providing better registration between the two modalities or moving towards replacing CT altogether.

This commentary describes two phantom studies that were performed to explore the potential application of UTE sequences for RT planning. All imaging was undertaken on our current 3 Tesla wide-bore MAGNETOM Skyra system, which is used as a dedicated 'MR-simulator' at Liverpool Cancer Therapy Centre in South West Sydney.

¹ The product is still under development and not commercially available yet. Its future availability cannot be ensured.

MR-CT registration: a gold marker study

Fiducial marker insertion is a common clinical practice for radiotherapy (RT) to improve target localization in the prostate. Marker position on the planning CT can be aligned with daily cone beam CT (CBCT) image by table shifts prior to RT treatment. Fiducial marker appearance on CT can include areas of streak artefacts due to their



1 (1A) 3D rendering of artefacts in the 6 seeds for the FLASH (red) and UTE (yellow) sequences which show a 15 fold difference in volume. (1B) Seeds imaged with UTE show an excellent agreement compared to positions in CT.

high electron density and large Hounsfield units (HU). On MRI, these markers produce no signal but due to the difference in magnetic susceptibility, they can create signal voids and distortions that are not truly representative of the marker dimension [2]. In the prostate, these markers can be hard to visualize on anatomical T2-weighted images which are used in RT planning. An additional gradient-echo sequence such as fast low angle shot (FLASH) is currently used to increase the conspicuity of markers due to the enhanced susceptibility artifact however this is at the cost of accuracy of the marker size and location. Susceptibility artifacts are known to depend on material, orientation to the magnetic field, imaging sequence as well as echo time (TE). With the increased use of MRI for target localization and soft tissue delineation, the MRI appearance of these markers needs to be carefully characterized, particularly for new pulse sequences which may be beneficial for imaging markers. The purpose of the first study was to evaluate the appearance of two commercial fiducial markers using the current departmental protocol and compare it to various types of imaging sequences not currently used in our clinic. Five sequences were performed including the current clinical gradient echo sequence (FLASH), T2-weighted turbo spin echo (TSE), turbo gradient spin echo (TGSE), and two versions of ultra short echo time imaging (UTE and PETRA [3]). The final two sequences enabled a comparison of two minimum TEs of 0.04 ms and 0.06 ms respectively.

To evaluate these effects in a controlled manner, an in-house gelatine phantom was constructed containing three gold soft tissue markers (CIVCO Medical Solutions, Coralville, IA, USA) and 3 polymer markers (Polymark™, Portland, OR, USA). The gold marker dimensions are 1.2 x 3 mm. The Polymark™ dimensions are 1 x 3 mm and made of a PEEK-Optima polymer and medical grade stainless steel core. The fiducial markers were positioned parallel to each other and the phantom was imaged both with CT and MRI with the latter repeated so that the markers were aligned both

perpendicular and parallel to the B₀ field. Results showed that the marker-induced susceptibility artifacts in the FLASH sequence were 15 times greater in total volume compared to the UTE sequence which produced the smallest artifacts (Fig. 1A). The susceptibility artifacts of the (steel cored) polymer markers were larger in dimension compared to gold markers in all cases. The FLASH sequence increased the apparent size of the polymer marker to 5.5 x 10 mm (diameter x length) perpendicular and 4.5 x 10 mm parallel to the main magnetic field. As expected, the TSE sequence reduced susceptibility artifacts compared to the FLASH for both gold and polymer in the perpendicular direction, to 2 x 5.5 mm and 2.5 x 7 mm respectively. The TGSE sequence showed a further reduction in marker artefacts to 3 x 5 mm (gold/perpendicular orientation) and 3.5 x 6.5 mm (polymer/perpendicular). PETRA demonstrated reduced artefacts of 2.5 x 3.5 mm for gold and 2.5 x 4.5 mm for polymer in the perpendicular directions. Overall the UTE images exhibited the smallest dimensions (2 x 3 mm for gold/parallel and 3 x 3 mm for polymer/perpendicular) and was comparable to the actual marker size. The Euclidean distance between the centroids of each automatically contoured UTE gold marker were sub-voxel (mean distance 1.2 mm) when compared to the CT (Fig. 1B).

Direct MR to CT conversion: validation in animal tissue

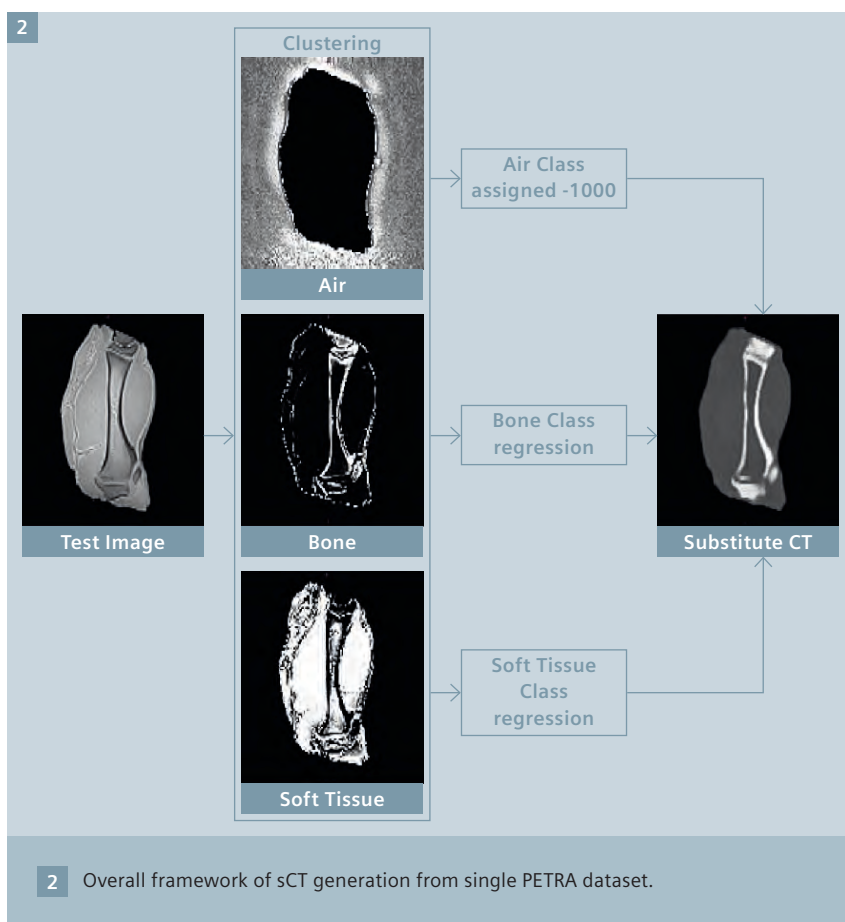
The necessity of a CT scan in the patient workflow has often hindered the flexibility and usefulness of MRI and led to many research centers turning towards MR-only planning² solutions – where the need for CT in the process is replaced altogether with the generation of a substitute (sCT) CT dataset from the MRI. The methods for the generation of substitute CT images to date may be broadly categorized into and atlas-based methods [4] and direct conversion or regression-based methods [5].

Atlas based methods have received most attention thus far and have been shown to produce accurate results. They work by first acquiring a representative set of co-registered patient CT and MR images. Registering these atlas MR images to a new patient MRI enables the co-registered CT Hounsfield Units to be mapped (and combined) into an MRI-based substitute CT. However atlas methods can fail in extreme cases not represented by the atlas population. The goal of regression based methods is to establish a relationship between CT and MR signal generated from one or more contrast weightings. In this next study we describe a regression-based approach to generate substitute CT images from just a single PETRA sequence². Whereas soft tissue is easily seen on MRI, cortical bone which is highly electron dense is invisible on routine imaging; at ultrashort echo times signal can be detected with the potential ability to provide a tissue classification model of soft tissue, air and bone. Compared to a purely atlas-based method, the model is computationally efficient and fast.

MRI and CT scans of a porcine leg were used to validate the proposed method – this provides us with cortical bone, fat and muscle in a convenient phantom. The approach may be broadly divided into two parts: (a) an expectation maximization (EM) based clustering of the soft tissues, bone and the air class followed by (b) random forest regression based prediction of CT intensities for every voxels from class probabilities.

A 3D PETRA sequence (TE/TR 0.07/10 ms; 0.93 mm isotropic pixels) was co-registered to the corresponding CT image [6] (1.17 x 1.17 x 2 mm) to build tissue specific regression models. The MRI signal intensity was normalized between zero mean and

² Radiotherapy Planning where MR data is the only imaging information is ongoing research. The concepts and information presented in this article are based on research and are not commercially available. Its future availability cannot be ensured.



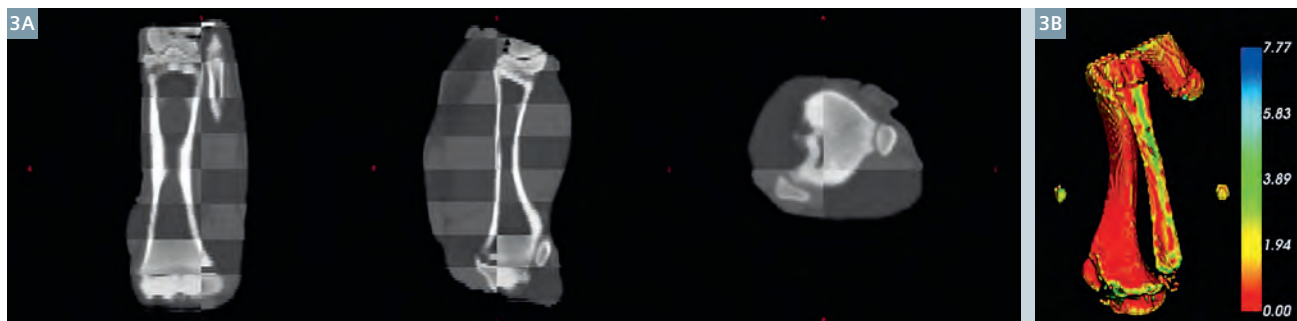
unit variance for faster convergence of the EM algorithm. A 3 class EM based clustering was performed on the co-registered PETRA image to identify the soft tissues, dense bone and air class. Unlike T2-weighted MRI the PETRA sequence is useful in separating the bone and the air classes. For each of the tissue classes (soft tissue, air and bone) the class probabilities and corresponding CT intensities were sampled from

the co-registered CT/PETRA images to build tissue-specific regression models. Thus we model separate random forest regression models for soft tissue and bone. Unlike other regression models used for HU prediction we do not use signal intensities for building the regression model but instead use class probabilities (bone, soft tissues and air probabilities) for a voxel in the random forest regression model to

predict the corresponding HU. The proposed approach is intuitive as there may not be any direct relationship between CT HU and MRI intensities. There is, however, a direct relationship between class probabilities of air, bone and soft tissues and corresponding HU maps. In our model we propose to exploit this relation. Air identified from the EM model is directly assigned a value of -1000 HU.

Further the degree of the regression curve is directly learnt from the class probability distribution.

For validation, an EM based clustering identified the soft tissue, the bone and the air in the phantom. Tissue specific regression models of the soft tissues and the bone were generated from half of the image to predict the other half of the image. The three classes (air, soft tissue and bone) were combined to generate the sCT. Use of half of the bone information during the training stage ensures that the training and the testing voxels were segregated. The entire substitute CT is reconstructed in less than 180 seconds. The entire framework of substitute CT image generation is illustrated in Figure 2. Checkerboard images of the CT and the substitute CT are presented in Figure 3A. The CT and the substitute CT were both thresholded at 500 HU to segment cortical bone. The surface distance difference map of the bone in mm is presented in Figure 3B. Results showed the desired level of accuracy for dosimetry calculations with a mean HU error of 15.6 HU (within the phantom skin boundary) when com-



3 (3A) Checkerboard overlay between the actual CT and PETRA-derived sCT shows good approximation of the CT.
(3B) The surface distance error map between bone segmented from CT and sCT.

pared to CT. The proposed approach also achieves a 1.3 mm bone surface reconstruction error when compared to CT bone.

Summary

This very early work shows the potential of ultra-short TE sequences to play an important role in MR guided Radiotherapy. Acquiring signal intensity at this vastly reduced echo time opens up new imaging contrasts and many possibilities. In this report two investigations were performed; Firstly ultrashort TE was used to reduce susceptibility artifacts from fiducial marker seeds. This showed a much closer agreement with known dimension and demonstrated an improved localization accuracy compared to currently used clinical sequences. In

the second example, a single ultra-short sequence was used to generate the substitute CT data directly using a novel modelling approach. This method of generating sCT shows great promise for the generation of fast MRI based sCT radiation therapy planning and PET attenuation correction. Both these methods will need further investigation *in vivo*.

References

- 1 Robson MD, Gatehouse PD, Bydder M, Bydder GM. Magnetic Resonance: An Introduction to Ultrashort TE (UTE) Imaging. *Journal of Computer Assisted Tomography*. 2003;27:825-46.
- 2 Wachowicz K, Thomas SD, Fallone BG. Characterization of the susceptibility artifact around a prostate brachytherapy seed in MRI. *Medical Physics*. 2006;33:4459-67.
- 3 Grodzki DM, Jakob PM, Heismann B. Ultra short echo time imaging using pointwise encoding time reduction with radial acquisition (PETRA), *Proc ISMRM* (2011):2815.
- 4 Jason A. Dowling et al. (2015). Automatic substitute CT generation and contouring for MRI-alone external beam radiation therapy from standard MRI sequences, *Int. J. Radiat. Oncol. Biol. Phys.*, DOI: <http://dx.doi.org/10.1016/j.ijrobp.2015.08.045>.
- 5 Hsu et al. (2013). Investigation of a method for generating synthetic CT models from MRI scans of the head and the neck for radiation therapy. *Phy. Med. Biol.*, 58(23), 8419-35.
- 6 David Rivest-Hénault et al. (2015). Robust inverse-consistent affine CT-MR registration in MRI-assisted and MRI-alone prostate radiation therapy. *Med Image Anal*. 2015 Jul;23(1):56-69.



Soumya Ghose



Robba Rai



Gary Liney

Contact

Associate Professor Gary Liney (UNSW)
Hon Principal Fellow, University of Wollongong
Ingham Institute for Applied Medical
Research & Radiation Oncology
Liverpool Hospital, 1 Campbell Street
Liverpool NSW 2170, Australia
Phone: +61 2 8738 9221
gary.liney@sswahs.nsw.gov.au

Further Reading

For further articles, application tips and clinical talks from experts focusing on the role of MRI in Radiation Therapy, please visit us at:

www.siemens.com/magnetom-world-rt

Cardiac Diffusion Tensor MRI

Daniel B. Ennis^{1,2,3}; Eric Aliotta^{1,2}; Holden H. Wu^{1,2,3}

¹ Department of Radiological Sciences, University of California, Los Angeles, CA, USA

² Biomedical Physics Interdepartmental Program, University of California, Los Angeles, CA, USA

³ Department of Bioengineering, University of California, Los Angeles, CA, USA

Introduction

Cardiac motion occurs at many scales. Fast and slow. Big and small. MRI has developed over several decades to freeze the motion of the heart or capture its dynamics all of which has led to advanced diagnostic methods for evaluating heart function. Central to our ability to freeze cardiac motion has been increasingly advanced gradient hardware [1]. Initially, this permitted capturing the dynamics of the beating heart in a breath-hold [2]. More recently, the fast and ultrafast gradient hardware permits encoding the diffusive motion of water molecules in a beating heart!

What can we measure?

Imaging the self-diffusion of water in the beating heart – termed cardiac diffusion weighted imaging (cDWI)¹ – presents numerous challenges, but also makes available new mechanisms for generating image contrast. cDWI is poised to provide molecular-

level, quantitative insight to micro-structural organization and changes in organization (i.e. remodeling) that occur with disease. For example, sensitivity to changes in the apparent diffusion coefficient (ADC, mm²/s) provides information about how freely water molecules diffuse. Another measure, termed fraction anisotropy (FA), characterizes the directional dependence of the diffusion and is zero for tissues that have isotropic microstructure and can be as high as one for highly anisotropic tissues [3].

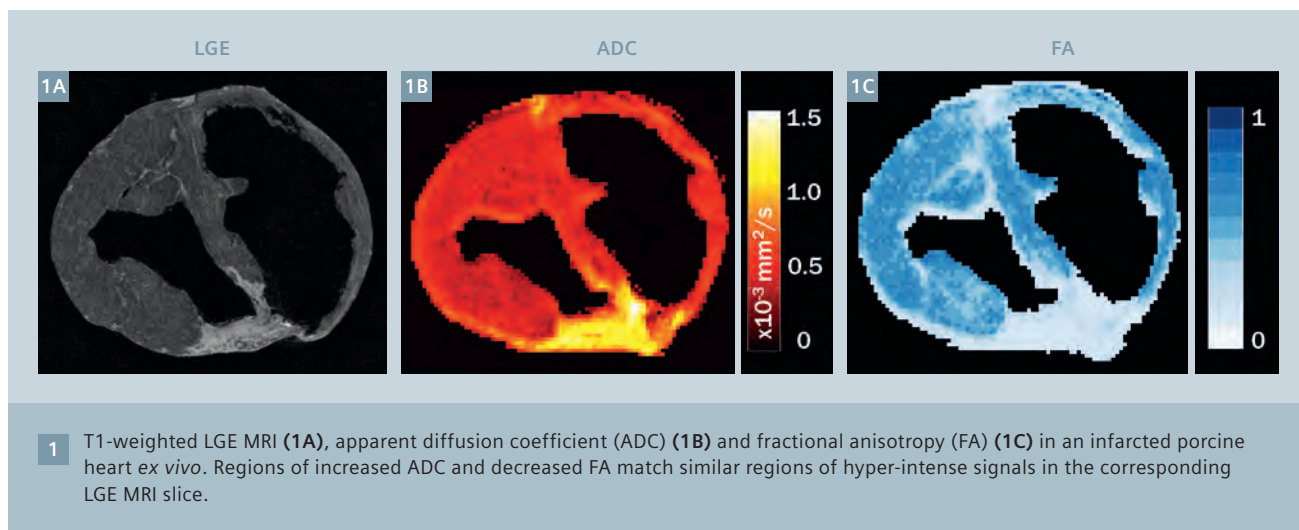
How do cDWI parameters change?

Much of what we know about *in vivo* changes in ADC comes from the neuro literature wherein it is widely appreciated that ADC decreases in acute strokes, pseudo-normalizes within weeks, and subsequently increases above baseline [4]. Currently, less is known about *in vivo* changes to ADC in areas of acute myocardial infarction, but similar findings have been reported [5]. ADC is known to increase significantly in diffuse fibrosis [6] and more so in chronic infarcts [7]. In fact, because

ex vivo cardiac DT-MRI has been practical already for several years we can easily observe the diffusive-level changes in chronic infarcts. Our detailed *ex vivo* work in chronic swine infarcts clearly demonstrates that the ADC is significantly elevated and that the FA is significantly decreased within the infarct, both of which show excellent correlation to the region identified using post-contrast T1-weighted MRI (Fig. 1). As *in vivo* cardiac diffusion weighted imaging becomes more widely available these findings are sure to be reported.

cDWI for myocardial infarcts?

Myocardial infarctions (MI) are the most common form of heart disease and a leading cause of death worldwide [8]. Non-invasive imaging methods for identifying and characterizing affected regions are critical to the diagnosis of MI and the management of post-MI ventricular remodeling [9, 10]. LGE MRI has demonstrated significant clinical value as the gold standard in detecting the location and extent of MI [11]. However, the injection of a GBCA is contraindicated in



patients with poor renal function, which poses a significant limitation because this group comprises ~40% of patients with cardiovascular disease and also exhibits increased cardiovascular mortality rates [12]. There does not currently exist a clinically acceptable imaging method for detecting and evaluating MI in this large and high-risk patient group. cDWI may be able to fill this role.

How is the heart microstructurally organized?

The heart is comprised of billions of individual myocytes coordinated into a highly organized network best described as a continuously branching syncytium. In the healthy heart, the organized myocytes are grossly characterized by a transmural change in orientation. The myocytes are further organized into bundles termed sheetlets [13] whose dynamics give rise to ventricular wall thickening [14]. Shortening along the myocyte's long-axis and shearing between the sheetlets are both critical to ventricular performance.

How does cDWI estimate directional information?

cDWI can be used to estimate the local diffusion tensor which comprises information about the magnitudes of diffusion (e.g. ADC and FA) and also the directionality of diffusion. We know from careful *ex vivo* work that the primary eigenvector of the diffusion tensor corresponds to the long axis of the myocytes [15] and that the tertiary eigenvector is generally related to the surface normal of the local sheetlets [16]. Consequently, *in vivo* measurement of the diffusion tensor provides direct insight to changes in microstructural orientations in health and disease [17].

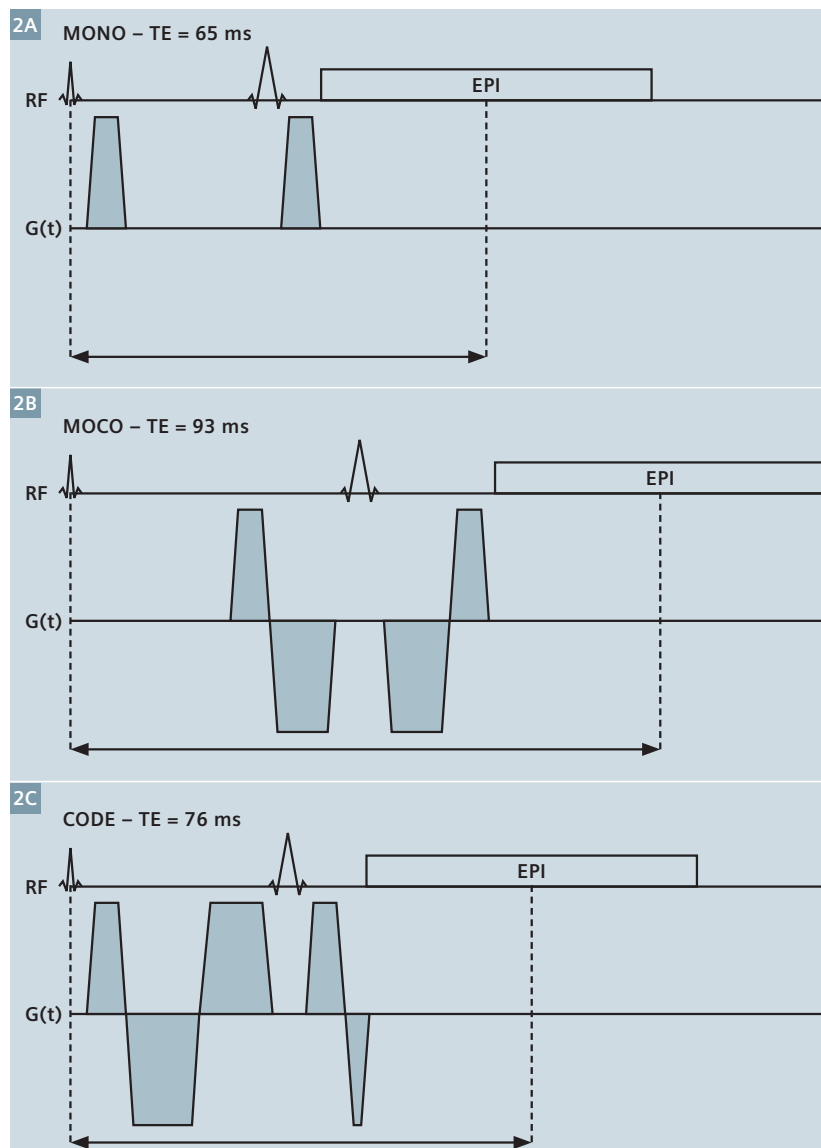
What about the bulk motion sensitivity of DWI?

cDWI measures diffusive motion on the microscopic scale using diffusion encoding gradients with large amplitudes (40 to 80 mT/m) and significant durations (5-10 ms is typical). Consequently, even subtle cardiac bulk motion can significantly corrupt the cDWI measurements unless steps are taken to carefully mitigate bulk motion artifacts. Several approaches have been proposed to address this issue.

For example, diffusion encoding with STimulated Echo Acquisition Mode (STEAM) [18] limits bulk-motion sensitivity by using very short diffusion encoding gradients distributed across two heartbeats. This approach has been widely adopted and is quite promising, but necessarily has a longer scan time due to two heart-beat encoding, modest SNR because of the stimulated echo, and is confounded by cardiac strain sensitivity and heart rate variability [19].

cDWI with SE-EPI as an alternative to STEAM?

An alternative is single-shot spin-echo (SE) echo planar imaging (SE-EPI) which is insensitive to strain and has better SNR performance and shorter scan times than STEAM [20]. However, SE-EPI cDWI with traditional monopolar encoding is highly sensitive to cardiac bulk motion and requires customized acquisition strategies and post



2 cDWI pulse sequence diagrams for (2A) bulk-motion sensitive, monopolar (MONO) encoding; (2B) non-optimized motion compensated (MOCO) encoding and (2C) Convex Optimized Diffusion Encoding encoding with M_1 and M_2 motion compensation (CODE) ($b = 350 \text{ s/mm}^2$ and $1.5 \times 1.5 \text{ mm}$ in-plane resolution) which eliminates sequence dead time and reduces TE compared to MOCO.

processing to achieve acceptable image quality [21].

How can bulk motion sensitivity be mitigated?

One approach to mitigating bulk motion artifacts is to use diffusion encoding gradient waveforms that are insensitive to bulk motion, but still sensitive to diffusive motion. Recent work has shown that motion compensated (MOCO) diffusion gradient waveforms with nulled first (M_1) and second (M_2) moments (time-weighted gradient waveform integrals) that are unaffected by bulk linear velocities and accelerations, can also encode diffusion in the presence of cardiac motion [22–24]. When applied to SE-EPI cDWI, MOCO gradients combine bulk motion robustness with strain insensitivity and short scan times. However, moment nulling for the diffusion encoding gradients (i.e. MOCO) necessarily increases the total diffusion encoding duration as compared to monopolar waveforms (Fig. 2). Consequently, conferring bulk motion insensitivity unavoidably

increases the echo time (TE), which reduces SNR. This is exacerbated in high-resolution imaging with long EPI readout intervals, which introduces lengthy dead times within the sequence before the refocusing pulse (Fig. 2). This generally limits cDWI to ~2.5 mm in-plane resolution, which is insufficient for evaluation of myocardial infarcts per cardiac MRI guidelines [25]. Herein we describe a technique that we have found to largely overcome this limitation.

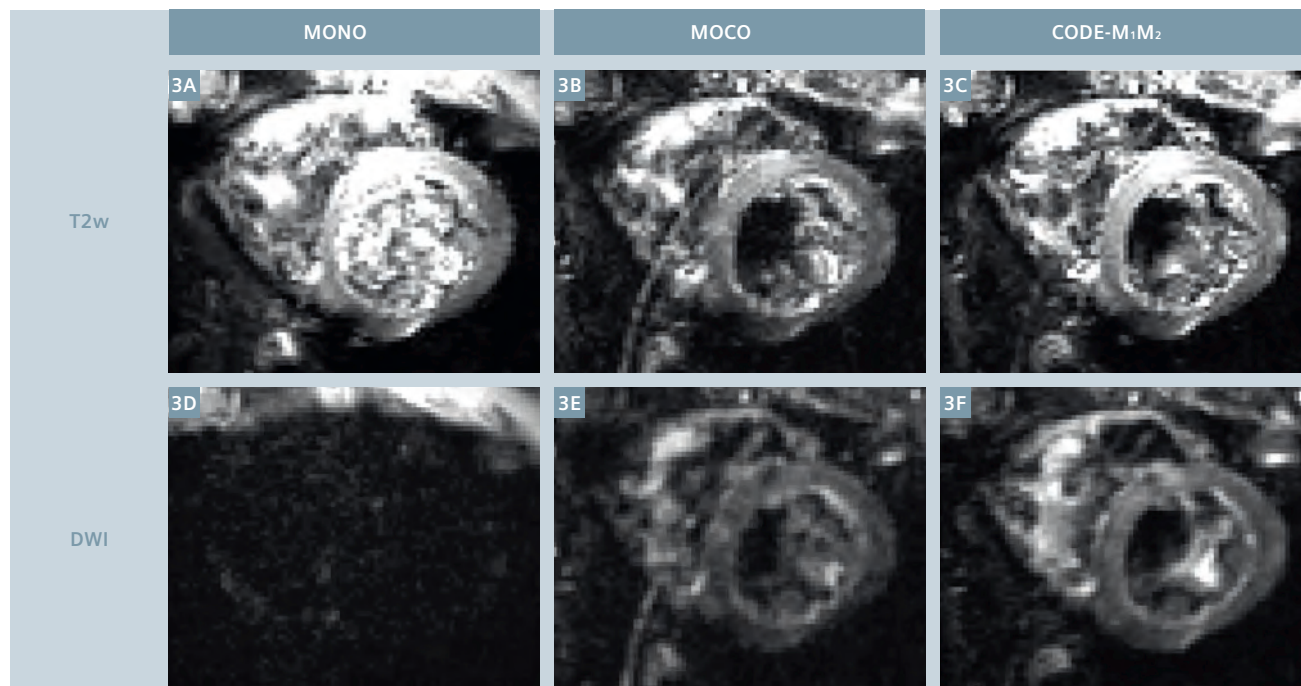
Methods

How are the diffusion encoding gradients designed?

Traditional diffusion encoding gradient waveform design uses an ad hoc approach that involves combining trapezoidal gradient waveforms with closed-form definitions that meet hardware constraints (G_{Max} and SR_{Max}) and ensure the desired properties (M_0 , M_1 , M_2 , b-value), but are agnostic to changes in sequence timing. This tends to lead to inefficiencies in pulse sequence timing that can extend TEs (Fig. 2).

How did we optimize diffusion encoding gradients design?

A general approach to gradient design has been proposed [26] which uses numerical optimization to select the most time-efficient waveform that adheres to all hardware (G_{Max} and SR_{Max}), gradient waveform (M_0 , M_1 , M_2 , b-value, etc.) and pulse sequence (field-of-view, bandwidth, resolution, etc.) constraints. This approach was recently used to design the fastest possible velocity encoding gradients for measuring through plane blood flow [27]. We have applied this concept to more efficiently encode diffusion in the beating heart using convex optimized diffusion encoding (CODE) gradients [28]. This approach calculates the diffusion encoding gradient waveform that minimizes TE for any spatial resolution (Fig. 2). By optimizing the diffusion encoding gradient waveform we can remove all diffusion encoding dead time and achieve M_1 and M_2 moment compensated diffusion encoding in shorter TEs than any previous method. This development permits bulk-motion



3 cDWI images with $b = 0$ (3A–C) and $b = 350 \text{ s/mm}^2$ (3D–F) are shown for a healthy volunteer at a systolic cardiac phase with MONO, MOCO, and CODE. MONO cDWI had the highest SNR with $b = 0$ but were severely motion corrupted with diffusion encoding. MOCO and CODE were both robust to cardiac motion with $b = 350 \text{ s/mm}^2$ but CODE had higher SNR due to its shorter TE.

insensitive cDWI with 1.5 mm in-plane spatial resolution that matches clinical LGE MRI and enables cDWI to be a practical GBCA-free method for the clinical evaluation of MI.

How are CODE cDWI images acquired?

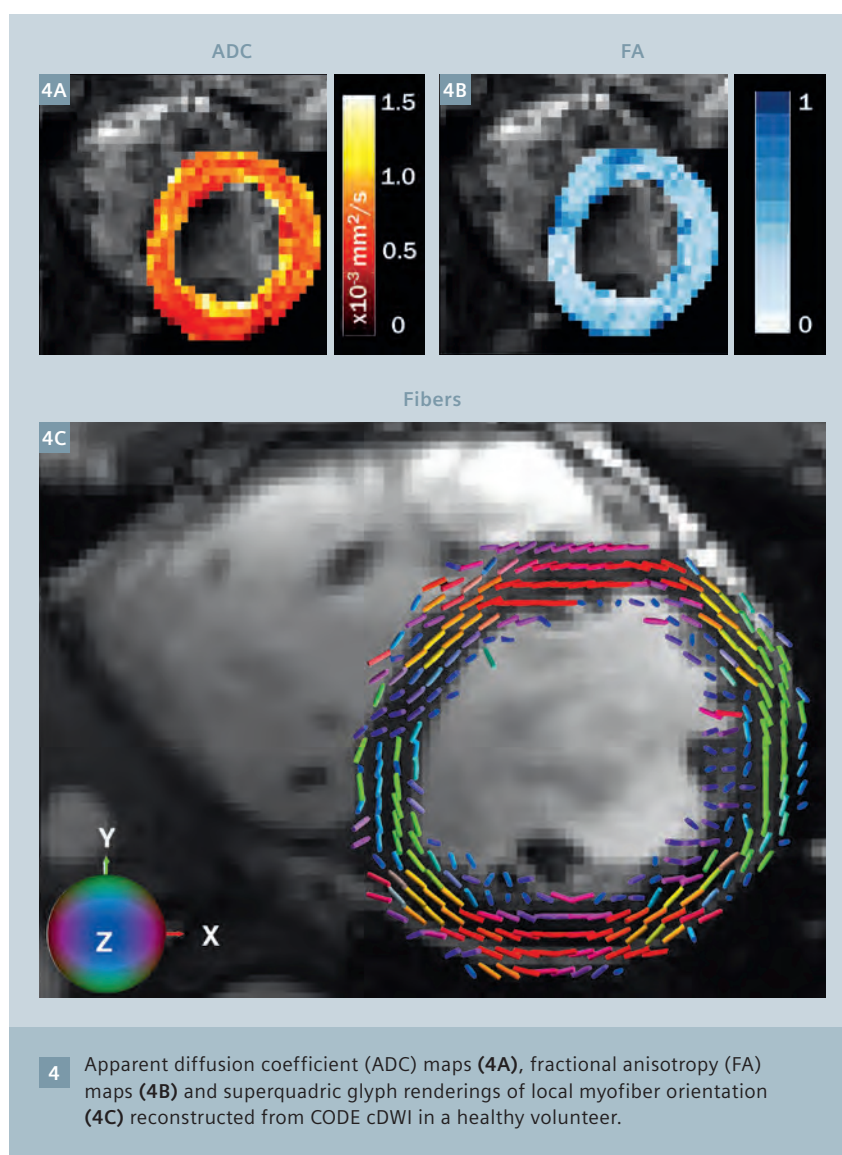
High resolution (1.5 x 1.5 x 5.0 mm) cDWI images ($b = 350 \text{ s/mm}^2$) were acquired in healthy volunteers on a 3T scanner (MAGNETOM Prisma) using three encoding schemes: monopolar (TE = 65 ms), non-optimized MOCO (TE = 93 ms) and CODE (TE = 76 ms) encoding. Diffusion was encoded along three orthogonal directions and three averages were acquired to improve image SNR. Imaging was performed under free breathing with navigator triggering (scan time: ~1 minute per technique). An additional CODE cDTI dataset was acquired with coarser resolution (2.5 x 2.5 x 5.0 mm) for fiber mapping (TE = 59 ms). This acquisition included six diffusion encoding directions and ten signal averages (scan time: ~10 minutes).

How does CODE cDWI compare with other approaches?

Monopolar cDWI resulted in dramatic bulk motion signal dropouts (Fig. 3) that were eliminated with MOCO and CODE. CODE also improved the SNR compared to conventional MOCO (Fig. 3). ADC, FA, and myocyte orientation maps were reconstructed from the CODE cDTI data and demonstrate the high SNR and high quality of the parametric and orientation maps (Fig. 4).

Discussion

We have developed, implemented, and demonstrated a novel approach to cDWI using convex optimized diffusion encoding (CODE) gradients. This approach is robust to cardiac bulk motion and enables sensitivity to diffusion in the beating heart. With the ability to routinely measure diffusion in the beating heart a number of quantitative imaging metrics become available. While the apparent diffusion coefficient (ADC) and the fractional anisotropy (FA) are the principal measures reported in the neuro literature, there are many additional metrics that



may prove specifically useful in the heart [29]. In particular, measures of local myocyte coherence and/or disarray, and changes to myocyte and sheetlet orientations may provide exceptional insight about myocardial function and dysfunction.

Future work will see broader application of CODE cDWI in both healthy volunteers and patients with a variety of clinical indications. Moving forward cDWI may lead directly to insights about microstructural organization in the healthy heart and may become a routine method for evaluating changes to cardiac microstructure without the need for GBCA. Central to the pursuit of this goal is a partnership between

physicists and physicians that enables novel insights arising from the latest MRI technologies.

Acknowledgements

The authors are grateful to receive research support from the Department of Radiological Sciences at UCLA, the National Institutes of Health, the American Heart Association, and Siemens Healthcare.

References

- 1 Fisher D, Eberlein E. The New, High-Performance MR Gradient System XR 80/200. Design; Benefits and Safe Operation. MAGNETOM Flash 52 (2/2013): 160-163.

- 2 Atkinson DJ, Edelman RR. Cineangiography of the heart in a single breath hold with a segmented turboFLASH sequence. *Radiology* 1991;178(2):357-360.
- 3 Ennis DB, Kindlmann G. Orthogonal tensor invariants and the analysis of diffusion tensor magnetic resonance images. *Magn Reson Med* 2006;55(1):136-146.
- 4 Schlaug G, Siewert B, Benfield A, Edelman RR, Warach S. Time course of the apparent diffusion coefficient (ADC) abnormality in human stroke. *Neurology* 1997;49(1):113-119.
- 5 Hsu EW, Xue R, Holmes A, Forder JR. Delayed reduction of tissue water diffusion after myocardial ischemia. *Am J Physiol* 1998;275(2 Pt 2):H697-702.
- 6 Abdullah OM, Drakos SG, Diakos NA, Wever-Pinzon O, Kfoury AG, Stehlik J, Selzman CH, Reid BB, Brunisholz K, Verma DR, Myrick C, Sachse FB, Li DY, Hsu EW. Characterization of diffuse fibrosis in the failing human heart via diffusion tensor imaging and quantitative histological validation. *NMR Biomed* 2014;27(11):1378-1386.
- 7 Nguyen C, Fan Z, Xie Y, Dawkins J, Tseliou E, Bi X, Sharif B, Dharmakumar R, Marban E, Li D. In vivo contrast free chronic myocardial infarction characterization using diffusion-weighted cardiovascular magnetic resonance. *J Cardiovasc Magn Reson* 2014;16:68.
- 8 Roger VL. Epidemiology of myocardial infarction. *The Medical clinics of North America* 2007;91(4):537-552; ix.
- 9 Kim RJ, Wu E, Rafael A, Chen EL, Parker MA, Simonetti O, Klocke FJ, Bonow RO, Judd RM. The use of contrast-enhanced magnetic resonance imaging to identify reversible myocardial dysfunction. *N Engl J Med* 2000;343(20):1445-1453.
- 10 Kelle S, Roes SD, Klein C, Kokocinski T, de Roos A, Fleck E, Bax JJ, Nagel E. Prognostic value of myocardial infarct size and contractile reserve using magnetic resonance imaging. *Journal of the American College of Cardiology* 2009;54(19):1770-1777.
- 11 Flett AS, Hasleton J, Cook C, Hausenloy D, Quarta G, Ariti C, Muthurangu V, Moon JC. Evaluation of techniques for the quantification of myocardial scar of differing etiology using cardiac magnetic resonance. *JACC Cardiovascular imaging* 2011;4(2):150-156.
- 12 Sarnak MJ, Levey AS, Schoolwerth AC, Coresh J, Culleton B, Hamm LL, McCullough PA, Kasiske BL, Kelepouris E, Klag MJ, Parfrey P, Pfeffer M, Raij L, Spinosa DJ, Wilson PW, American Heart Association Councils on Kidney in Cardiovascular Disease HBPCC, Epidemiology, Prevention. Kidney disease as a risk factor for development of cardiovascular disease: a statement from the American Heart Association Councils on Kidney in Cardiovascular Disease, High Blood Pressure Research, Clinical Cardiology, and Epidemiology and Prevention. *Hypertension* 2003;42(5):1050-1065.
- 13 LeGrice IJ, Hunter PJ, Smaill BH. Laminar structure of the heart: A mathematical model. *Am J Physiol-Heart C* 1997;272(5):H2466-H2476.
- 14 Costa KD, Takayama Y, McCulloch AD, Covell JW. Laminar fiber architecture and three-dimensional systolic mechanics in canine ventricular myocardium. *Am J Physiol* 1999;276(2 Pt 2):H595-607.
- 15 Hsu EW, Muzikant AL, Matulevicius SA, Penland RC, Henriquez CS. Magnetic resonance myocardial fiber-orientation mapping with direct histological correlation. *Am J Physiol* 1998;274(5 Pt 2):H1627-1634.
- 16 Kung GL, Nguyen TC, Itoh A, Skare S, Ingels NB, Jr., Miller DC, Ennis DB. The presence of two local myocardial sheet populations confirmed by diffusion tensor MRI and histological validation. *J Magn Reson Imaging* 2011;34(5):1080-1091.
- 17 Ferreira PF, Kilner PJ, McGill LA, NIELLES-Vallespin S, Scott AD, Ho SY, McCarthy KP, Haba MM, Ismail TF, Gatehouse PD, de Silva R, Lyon AR, Prasad SK, Firmin DN, Pennell DJ. In vivo cardiovascular magnetic resonance diffusion tensor imaging shows evidence of abnormal myocardial laminar orientations and mobility in hypertrophic cardiomyopathy. *Journal of cardiovascular magnetic resonance : official journal of the Society for Cardiovascular Magnetic Resonance* 2014;16:87.
- 18 Dou J, Reese TG, Tseng WY, Wedeen VJ. Cardiac diffusion MRI without motion effects. *Magn Reson Med* 2002;48(1):105-114.
- 19 Fischer SE, Stuber M, Scheidegger MB, Boesiger P. Limitations of stimulated echo acquisition mode (STEAM) techniques in cardiac applications. *Magn Reson Med* 1995;34(1):80-91.
- 20 Gamper U, Boesiger P, Kozerke S. Diffusion imaging of the in vivo heart using spin echoes--considerations on bulk motion sensitivity. *Magn Reson Med* 2007;57(2):331-337.
- 21 Pai VM, Rapacchi S, Kellman P, Croisille P, Wen H. PCATMIP: enhancing signal intensity in diffusion-weighted magnetic resonance imaging. *Magn Reson Med* 2011;65(6):1611-1619.
- 22 Stoeck CT, von Deuster C, Genet M, Atkinson D, Kozerke S. Second-order motion-compensated spin echo diffusion tensor imaging of the human heart. *Magnetic resonance in medicine : official journal of the Society of Magnetic Resonance in Medicine / Society of Magnetic Resonance in Medicine* 2015.
- 23 Welsh C, Di Bella E, Hsu E. Higher-Order Motion-Compensation for In Vivo Cardiac Diffusion Tensor Imaging in Rats. *IEEE transactions on medical imaging* 2015.
- 24 Nguyen C, Fan Z, Sharif B, He Y, Dharmakumar R, Berman DS, Li D. In vivo three-dimensional high resolution cardiac diffusion-weighted MRI: A motion compensated diffusion-prepared balanced steady-state free precession approach. *Magnetic resonance in medicine : official journal of the Society of Magnetic Resonance in Medicine / Society of Magnetic Resonance in Medicine* 2013;72(5):1257-1267.
- 25 Kramer CM, Barkhausen J, Flamm SD, Kim RJ, Nagel E, Society for Cardiovascular Magnetic Resonance Board of Trustees Task Force on Standardized P. Standardized cardiovascular magnetic resonance imaging (CMR) protocols, society for cardiovascular magnetic resonance: board of trustees task force on standardized protocols. *J Cardiovasc Magn Reson* 2008;10:35.
- 26 Hargreaves BA, Nishimura DG, Conolly SM. Time-optimal multidimensional gradient waveform design for rapid imaging. *Magn Reson Med* 2004;51(1):81-92.
- 27 Middione MJ, Wu HH, Ennis DB. Convex gradient optimization for increased spatiotemporal resolution and improved accuracy in phase contrast MRI. *Magn Reson Med* 2014;72(6):1552-1564.
- 28 Aliotta E, Wu HH, Ennis D. Convex Optimized Diffusion Encoding (CODE) Gradient Waveforms for Minimum Echo Time and Bulk Motion Compensated Diffusion Weighted MRI. *Magnetic Resonance in Medicine* 2016.
- 29 Kindlmann G, Ennis DB, Whitaker RT, Westin CF. Diffusion tensor analysis with invariant gradients and rotation tangents. *IEEE Trans Med Imaging* 2007;26(11):1483-1499.

Contact

Daniel B. Ennis, Ph.D.
University of California
Peter V. Ueberroth Building, Suite 1471, Room B
10945 Le Conte Avenue
Los Angeles, CA 90095, USA
Phone: +1 310 206 0713
Fax: +1 310 825 5837
daniel.ennis@ucla.edu



The entire editorial staff at New York University Langone Medical Center and at Siemens Healthcare extends their appreciation to all the radiologists, technologists, physicists, experts and scholars who donate their time and energy – without payment – in order to share their expertise with the readers of MAGNETOM Flash.

MAGNETOM Flash – Imprint

© 2016 by Siemens Healthcare GmbH,
All Rights Reserved

Publisher:

Siemens Healthcare GmbH
Magnetic Resonance,
Karl-Schall-Straße 6, D-91052 Erlangen,
Germany

Editor-in-chief:

Antje Hellwich
(antje.hellwich@siemens.com)

Guest Editor:

Daniel K. Sodickson, M.D., Ph.D.
Vice-Chair for Research,
Department of Radiology
Director, Bernard & Irene Schwartz Center
for Biomedical Imaging
Principal Investigator, Center for
Advanced Imaging Innovation and
Research (CAI²R)
New York University Langone Medical
Center New York, NY, USA

Editorial Board:

Reto Merges; Wellesley Were;
Sunil Kumar S.L., Ph.D.;
Gary R. McNeal, MS (BME);
Peter Kreisler, Ph.D.

Review Board:

Lisa Chuah, Ph.D.; Berthold Kiefer, Ph.D.;
Matthias Lichy, M.D., M.Sc.;
Heiko Meyer, Ph.D.; Edgar Müller;
Gregor Thörmer, Ph.D.; Heike Weh

Production:

Norbert Moser,
Siemens Healthcare GmbH

Layout:

Agentur Baumgärtner,
Friedrichstraße 4, D-90762 Fürth,
Germany

Printer:

G. Peschke Druckerei GmbH,
Taxetstrasse 4,
D-85599 Parsdorf b. Munich,
Germany

Note in accordance with § 33 Para.1 of
the German Federal Data Protection Law:
Despatch is made using an address file
which is maintained with the aid of an
automated data processing system.

MAGNETOM Flash is sent free of charge
to Siemens MR customers, qualified
physicians, technologists, physicists and
radiology departments throughout the
world. It includes reports in the English
language on magnetic resonance:
diagnostic and therapeutic methods and
their application as well as results and ex-
perience gained with corresponding sys-
tems and solutions. It introduces from
case to case new principles and proce-
dures and discusses their clinical poten-
tial. The statements and views of the
authors in the individual contributions
do not necessarily reflect the opinion of
the publisher.

The information presented in these
articles and case reports is for illustration
only and is not intended to be relied
upon by the reader for instruction as to
the practice of medicine. Any health
care practitioner reading this information
is reminded that they must use their
own learning, training and expertise in
dealing with their individual patients.
This material does not substitute
for that duty and is not intended by
Siemens Healthcare to be used for any
purpose in that regard. The drugs and
doses mentioned herein are consistent
with the approval labeling for uses and/or

indications of the drug. The treating
physician bears the sole responsibility for
the diagnosis and treatment of patients,
including drugs and doses prescribed in
connection with such use. The Operating
Instructions must always be strictly
followed when operating the MR system.
The sources for the technical data are the
corresponding data sheets. Results may
vary.

Partial reproduction in printed form of
individual contributions is permitted,
provided the customary bibliographical
data such as author's name and title of
the contribution as well as year, issue
number and pages of MAGNETOM Flash
are named, but the editors request that
two copies be sent to them. The written
consent of the authors and publisher is
required for the complete reprinting of
an article.

We welcome your questions and
comments about the editorial content of
MAGNETOM Flash. Please contact us at
magnetomworld.med@siemens.com.

Manuscripts as well as suggestions,
proposals and information are always
welcome; they are carefully examined
and submitted to the editorial board for
attention. MAGNETOM Flash is not
responsible for loss, damage, or any
other injury to unsolicited manuscripts
or other materials. We reserve the right
to edit for clarity, accuracy, and space.
Include your name, address, and phone
number and send to the editors, address
above.

MAGNETOM Flash is also available online:

www.siemens.com/magnetom-world

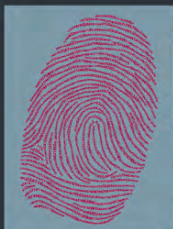
MAGNETOM Flash

The Magazine of MRI

Issue Number 2/2016 | ISMRM Edition

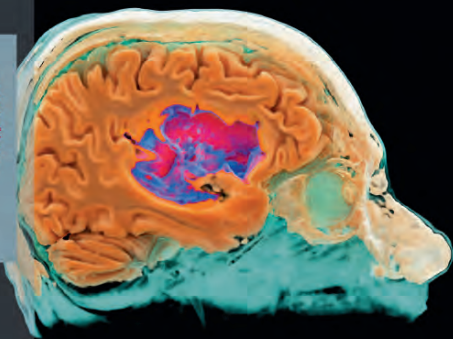
Not for distribution in the US

Overview of MR-Fingerprinting
Vikas Gulani et al.
Page 12



Editorial Comment
The Rapid Imaging Renaissance
Daniel K. Sodickson
Page 02

New Strategies
for Protocol Optimization
Otto Rapallino
Page 22



65

Please enter your business address

Institution

Department

Function

Title

Name

Street

Postal Code

City

State

Country

MR system used

Please include me in your mailing list for the following Siemens Healthcare customer magazine(s):

☐ Medical Solutions

☐ MAGNETOM Flash

☐ SOMATOM Sessions

☐ AXIOM Innovations

Stay up to date with the latest information

Register for:

E-mail

Please print clearly!

☐ Yes, I consent to the above information being used for future contact regarding product updates and other important news from Siemens.

☐ unsubscribe from info service

MAGNETOM Flash

The Magnetom® 400

Serial Number 2 2018 (SIEMENS Edition)

Serial Number 2 2018 (SIEMENS Edition)

Access to the top performing
MAGNETOM Flash 400

Access to the top performing
MAGNETOM Flash 400

Access to the top performing
MAGNETOM Flash 400

65

Siemens Healthcare GmbH
Antje Hellwich
HC DI MR CRM SCI
Karl-Schall-Straße 6
91052 Erlangen
Germany



– and get your free copy of future
MAGNETOM Flash! Interesting information from
the world of magnetic resonance – gratis to your
desk. Send us this postcard, or subscribe online at
www.siemens.com/MAGNETOM-World

On account of certain regional limitations of sales rights and service availability, we cannot guarantee that all products included in this brochure are available through the Siemens sales organization worldwide.

Availability and packaging may vary by country and is subject to change without prior notice. Some/All of the features and products described herein may not be available in the United States.

The information in this document contains general technical descriptions of specifications and options as well as standard and optional features which do not always have to be present in individual cases, and which

may not be commercially available in all countries. Due to regulatory reasons their future availability cannot be guaranteed. Please contact your local Siemens organization for further details.

Siemens reserves the right to modify the design, packaging, specifications, and options described herein without prior notice. Please contact your local Siemens sales representative for the most current information.

Note: Any technical data contained in this document may vary within defined tolerances. Original images always lose a certain amount of detail when reproduced.

Not for distribution in the US

Siemens Healthcare Headquarters

Siemens Healthcare GmbH
Henkestr. 127
91052 Erlangen
Germany
Phone: +49 9131 84-0
siemens.com/healthcare